Investigating the Solid-State Dynamics of 1D Coordination Polymers

by Lisa Mercene van Wyk

Dissertation presented in partial fulfilment of the requirements for the degree of Doctor of Philosophy

at

Stellenbosch University

Supervisor: Prof. Leonard J. Barbour
Department of Chemistry and Polymer Science
Faculty of Science
March 2021

Declaration

By submitting this dissertation electronically, I declare that the entirety of the work contained therein is my own, original work, that I am the sole author thereof (save to the extent explicitly otherwise stated), that reproduction and publication thereof by Stellenbosch University will not infringe any third party rights and that I have not previously in its entirety or in part submitted it for obtaining any qualification.

March 2021

Abstract

The aims of this study were twofold: (i) to produce a series of 1D materials exhibiting novel solid-state packing, and (ii), to study these materials with a view to gaining insight into their structure-property relationships. Studies of the ability of the materials to undergo several single-crystal to single-crystal transformations were prioritised. Both dynamic behaviours and transformations were observed in the series produced.

The first study describes the mechanochemical separation of two solvates that crystallise concomitantly under solvothermal conditions. Variation of the solvent water composition, and the introduction of aging periods before and after grinding provided various methods of preparing either solvate. A third solvate was prepared in a separate solvent system from the first two. Finally, solvent exchange allowed relatively facile interconversion between all three forms.

The second study focused on the transient porosity of two 1D coordination polymers. These materials show extreme contraction upon guest release equating to a reduction of up to 39% of the unit-cell volume. Importantly, these transformations progress in a single-crystal to single-crystal fashion and represent some of the largest reported lithotropic contractions. Consequently, the contortion of the conceptually linear ligand in one material far exceeds previous reports. These materials both resorb liquid guests, and one material sorbs vapours. Furthermore, greater ease of structural reopening occurs with each consecutive vapour sorption cycle.

In Chapter 5, the low-temperature phase-change behaviour and structural dynamics in terms of thermal expansion of a series of materials, where only the metal centre is varied, are studied. This yielded a series of materials with analogous packing motifs. In nearly all cases, colossal linear and volumetric thermal expansion were recorded in the temperature range 100–270 K. In some cases, supercolossal linear thermal expansion was exhibited, in addition to extreme anisotropy. The results are comparable to the largest linear and most anisotropic thermal expansion reported, but far exceed that reported for 1D coordination polymers. The largest anisotropic thermal expansion occurred in solid solutions, indicating that this behaviour is tuneable.

Studies of structure-property relationships and solid-state dynamics require firstly single-crystal to single crystal transformations and secondly bulk phase purity. In 1D coordination polymers both these criteria are often problematic. This work addresses both these concerns, providing methods to overcome or circumvent these hindrances. Furthermore, several of the outcomes in this work exceed or are comparable to the limits of similar solid-state dynamics reported in the literature.

Opsomming

Die doelstellings van hierdie studie was tweeledig: (i) om 'n reeks 1D-materiale te vervaardig wat nuwe vastetoestand verpakking toon, en (ii) om hierdie materiale te bestudeer met die oog op insig in hul struktuur-eiendomsverhoudinge. Studies oor die vermoë van die materiale om verskillende enkelkristal- tot enkelkristal-transformasies te ondergaan was geprioritiseer. Beide dinamiese gedrag en transformasies is waargeneem in die reeks wat geproduseer is.

Die eerste studie beskryf die meganochemiese skeiding van twee solvate wat gelyktydig kristaliseer onder solvotermiese toestande. 'n Variasie van die oplosmiddelwatersamestelling en die instelling van verouderingsperiodes voor en na die maalwerk het verskillende metodes vir die bereiding van elk van die vorme verskaf. 'n Derde solvaat is in 'n aparte oplosmiddelstelsel van die eerste twee berei. Laastens het die uitruil van oplosmiddels wisselwerking tussen al drie vorms moontlik gemaak.

Die tweede studie fokus op die kortstondige porositeit van twee 1D-koördinasiepolimere toegelig. Hierdie materiale toon 'n uiterse sametrekking met gasvrystelling, wat gelykstaande is aan 'n vermindering van tot 39% van die eenheidselvolume. Belangrikste is, is dat hierdie transformasies op 'n enkelkristal- tot enkelkristal-manier verloop en verteenwoordig van die grootste gerapporteerde litotropiese sametrekkings. Gevolglik is die vervorming van die konseptueel lineêre ligand in een materiaal baie groter as vorige verslae. Albei materiale resorbeer vloeibare gaste, en een materiaal absorbeer dampe. Verder vind 'n groter gemak van strukturele heropening plaas by elke opeenvolgende dampsorpsiesiklus.

In Hoofstuk 5 word die lae temperatuur faseveranderingsgedrag en strukturele dinamika in terme van termiese uitsetting van 'n reeks materiale waar slegs die metaalsentrum gevarieerd is bestudeer. Dus word 'n reeks materiale met analoog verpakkingsmotiewe vervaardig. In

bykans alle gevalle word kolossale lineêre en volumetriese termiese uitsetting aangeteken in die temperatuurreeks 100–270 K. In sommige gevalle word superkolossale lineêre termiese uitbsetting getoon, benewens ekstreme anisotropie. Die resultate is vergelykbaar met die grootste en mees anisotropiese termiese uitsetting wat gerapporteer is, maar is baie groter as wat vir 1D-koördinasiepolimere gerapporteer is. Die grootste anisotropiese termiese uitsetting vind in soliede oplossings plaas; wat aandui dat hierdie gedrag verstelbaar is.

Die studie van verhoudinge tussen struktuur-eiendom en vastetoestand-dinamika vereis eerstens enkelkristal tot enkelkristal transformasies en tweedens bulkfase suiwerheid. Met 1D-koördinasiepolimere is beide hierdie kriteria dikwels problematies. Hierdie werk spreek beide hierdie probleme aan, metodes word aangebied om hierdie hindernisse te oorkom of omseil. Verder oorskry of vergelyk die uitkomste in hierdie werk soortgelyke vastetoestanddinamika wat in die literatuur gemeld is.

Acknowledgements

It is near-impossible to give thanks without omitting some. Therefore, for those unnamed my eternal gratitude to you too. Your contribution is not overlooked.

First and foremost, I want to thank my supervisor, Professor Len Barbour, for his invaluable guidance and insights. The environment you have created has allowed me to gain vital confidence and experience related not only to the nitty-gritty of research, but also project management, writing and technical skills.

Personal thanks go to my mother, Lindie, for showing me the worth of a hard day's work. Moreover, you taught me to always look for what others may be able to teach me, no matter how unlikely it may seem. Although I still have not mastered the virtue of patience, I think two out of three lessons is satisfactory. Enormous thanks go to the entire Reekie family for the indelible mark they have left on my life, especially Malcolm. Your calm wisdom tames my sometimes frenetic energy. You taught me the value of a firm handshake, that a quick answer is always "no" and that mathematics makes the world go around (especially when my six times-tables were speculative at best). You have always been, and still are, there when I need advice or someone to hear my thoughts. I would like to thank my partner, Jaenrill, for supporting me in following my dreams – even when they sometimes came at the postponement of your own. You have had to deal with the fallout of bad experiments, lost data and the general frustrations of life, and never have you waivered in your conviction of my inevitable success.

Abundant thanks go to Varia for showing me the ropes when I was the 'new kid on the block', and not letting me sulk for too long when I made a mistake. I greatly enjoyed working with you and I even more enjoy your friendship. Similar thanks go to Leigh - you have taught me so much over the past few years and I feel there is so much more I can learn from you. Your outlook on life is marvellous and you always have a different perspective. Finally, I would like to thank Blossom for sharing my atrociously wonderful taste in music. Your wholesome attitude and trust in all is refreshing and reminds me daily to be a better person.

"As one person I cannot change the world, but I can change the world of one person."

Paul Shane Spear

Publications & Conferences

Publications forming part of this work:

1. L. M. van Wyk, L. Loots and L. J. Barbour. *J. Coord. Chem.,* 2021, 1–10

2. L. M. van Wyk and L. J. Barbour. *In preparation*.

3. L. M. van Wyk, L. Loots and L. J. Barbour. *In preparation*.

Publications not forming part of this work:

1. V. I. Nikolayenko, L. M. van Wyk, O. Q. Munro and L. J. Barbour. Supramolecular solvatochromism: mechanistic insight from crystallography, spectroscopy and theory, *Chem. Commun.,* 2018, **54**, 6975-6978.

2. L. M. van Wyk, V. J. Smith, M. Lusi, D. Das and L. J. Barbour. A Phase Change by Any Other Name: A Brief Guide to Identifying Subtle Phase Changes in Crystalline Materials. *In preparation.*

3. M. Shivanna, K. Otake, L. M. van Wyk, Q. Yang, W. K. Feldmann, S. Sanda, T. Pham, S. Suepaul, G. Beemer, B. Space, L. J. Barbour, S. Kitagawa and M. J. Zaworotko. Benchmark acetylene binding affinity and separation through induced fit in a flexible hybrid ultramicroporous material. *Submitted*.

4. N. Kumar, S. Mukherjee, N. C. Harvey-Reid, A. A. Bezrukov, K. Tan, M. Vandichel, T. Pham, L. M. van Wyk, K. Oyekan, A. Kumar, K. A. Forrest, L. J. Barbour, B. Space, P. E. Kruger, and M. J. Zaworotko. Breaking the trade-off between selectivity and adsorption capacity for gas separation. *Submitted*.

Conference Participation

1. *23rd International Conference on the Chemistry of the Organic Solid State (ICCOSS XXIII)*

STIAS, Stellenbosch, South Africa, 2-7 April 2017

Poster presentation: *Volatile Solvent Trapping by a Solvatochromic Metallocycle*

Abbreviations

1D	One Dimensional
2D	Two Dimensional
3D	Three Dimensional
ASU	Asymmetric Unit
ATR	Attenuated Total Reflectance
bdc	1,4-benzenedicarboxylic acid
bpdc	4,4′-biphenyldicarboxylic acid
bpy	2,2′-bipyridine
CIF	Crystallographic Information File
CP	Coordination Polymer
CPK	Corey-Pauling-Koltun
CSD	Cambridge Structural Database
DMA	*N,N*-Dimethylacetamide
DMF	*N,N*-Dimethylformamide
DSC	Differential Scanning Calorimetry
EDX	Energy-Dispersive X-Ray Spectroscopy
FT-IR	Fourier-Transform Infrared Spectroscopy
IUPAC	International Union of Pure and Applied Chemistry
IUCr	International Union of Crystallography
LAG	Liquid Assisted Grinding
MOF	Metal-Organic Framework
ndc	2,6-naphthalenedicarboxylic acid

NTE	Negative Thermal Expansion
PAS	Principal Axis Strain
PAV	Probe-Accessible Volume
PG-DSC	Pressure Gradient Differential Scanning Calorimetry
PTE	Positive Thermal Expansion
PXRD	Powder X-Ray Diffraction
SBU	Secondary Building Unit
$scCO_2$	Supercritical Carbon Dioxide
SC-SC	Single-Crystal to Single-Crystal
SCXRD	Single-Crystal X-Ray Diffraction
TGA	Thermogravimetric Analysis
VOC	Volatile Organic Compound
Z	Number of formula units per unit cell
ZTE	Zero Thermal Expansion

Atomic Colour Key

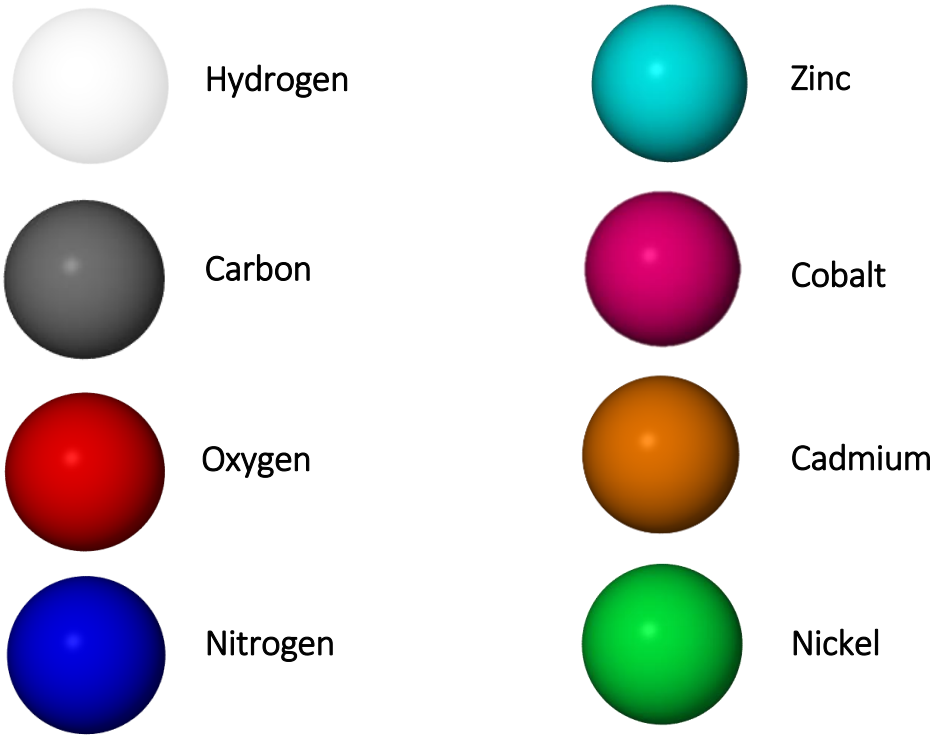

Table of Contents

Chapter 1 – Introduction

"The beginning is the most important part of the work." — Plato, *The Republic*

Aristotle wrote *"a whole is more than the sum of its parts."* Correspondingly, supramolecular chemistry can be seen as more than the additive effect of molecular chemistry. The term supramolecular chemistry was coined relatively recently; in 1978 Jean-Marie Lehn described it as *"the chemistry of molecular assemblies and of the intermolecular bond."*[1] Supramolecular chemistry has advanced the notion of properties beyond the molecular level, with compounds now showcasing a plethora of potential uses, including: catalysis,[2–4] sensing,[5,6] molecular separation[7,8] and storage,[9–11] and magnetism.[12–14]

1.1. Supramolecular Interactions

Supramolecular chemistry makes prodigious use of all manner of electrostatic interactions to achieve complex architectures. These may range from reasonably strong, directional interactions (*e.g.,* coordination linkages, hydrogen bonding and halogen bonding), to considerably weaker interactions, which lack compelling directionality (*e.g.,* π-interactions and van der Waals forces). It is seldom that any one of these interactions is found in isolation, and it is often the combined effect of numerous strong and/or weak interactions that results in a specific solid-state packing motif.

1.1.1. Coordination Bonding

Coordination linkages are strong interactions formed between metal centres and organic ligand donor atoms as the result of an ion-dipole interaction.[15] These bonds form when an organic ligand acts as a Lewis base and donates a lone pair into an empty coordination site on the metal centre (Lewis acid).[15] Coordination bonds are weaker than covalent bonds, but considerably stronger than hydrogen bonds. These interactions are the strongest directional, non-covalent interactions – with strengths ranging from 50–200 kJ mol^{-1} depending on the participating species.[16] As a result of this strength and rigidity, coordination bonds represent an important foundation from which coordination compounds can be engineered.[17]

1.1.2. Hydrogen Bonding

The hydrogen bond is a strong, directional interaction between a moiety that acts as the proton donor and another moiety that acts as the proton acceptor. Although it had already been studied for some time,[18,19] the hydrogen bond was comprehensively defined by Pauling in his book *"The Nature of the Chemical Bond"* in 1939.[20] Pauling noted that hydrogen atoms can only form a single covalent bond, subsequently recognising that hydrogen bonding can only result from some class of electrostatic interaction.[20]

Hydrogen bonding is an interaction between a hydrogen bond donor (D) and a hydrogen bond acceptor (A), which is denoted as D-H···A-X (where H is the proton participating in the hydrogen bond and X is any substituent group on the hydrogen bond acceptor). The hydrogen bond donor is electrostatically deficient while the hydrogen bond acceptor is electrostatically rich. IUPAC defined the hydrogen bond formally in 2011 as *"…an attractive interaction between a hydrogen atom from a molecule or a molecular fragment D-H in which D is more electronegative than H, and an atom or group of atoms in the same or different molecule in which there is evidence of bond formation."*[21] They also note that the closer the hydrogen bond angle (θ_{DHA}, Figure 1.1.) is to 180°, the stronger is the hydrogen bonding interaction.[21]

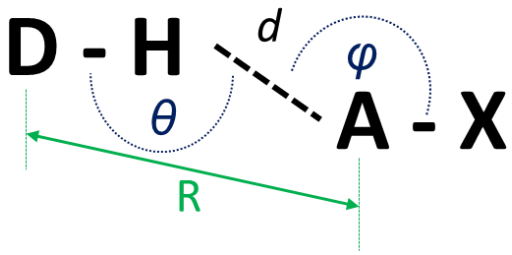

Figure 1.1. Geometries associated with hydrogen bonding. Adapted from Atwood and Steed.[22]

Strong hydrogen bonding occurs when D and A are both highly electronegative. However, weaker hydrogen bonding can also occur even when D and A are less electronegative. These weaker hydrogen bonds arise between hydrocarbon systems and heteroatoms, as well as between aromatic systems and heteroatoms (*e.g.,* C–H···O, C–H···N and C–H···π). Hydrogen bonds can vary in strength from 4–120 kJ mol^{-1}, but the majority of hydrogen bonds are less than 60 kJ mol^{-1} in strength.[16]

Determining the exact position of hydrogen atoms in crystal structures (especially those involved in hydrogen bonds) is problematic using only X-ray diffraction data because hydrogen atom assignment is frequently carried out by applying a riding model. For accurate hydrogen position assignment, neutron diffraction data are necessary. When accurate

hydrogen positions are available (*i.e.* obtained through neutron diffraction experiments), the distance between H and A (*d*) as well as the DHA angle (θ) are of importance for describing the hydrogen bonding interaction (Figure 1.1.).[22] If the positions of the hydrogen atoms are not accurately known, but were assigned using a riding model, then the distance *d* is also not accurately known and the distance between D and A (R) is used (Figure 1.1.).[22]

Hydrogen bonding is not limited to single donor-acceptor interactions; multifurcated hydrogen bonding readily takes place when more than one hydrogen bond acceptor is present. Similarly, more than one hydrogen bond donor can interact with an acceptor. Selected examples of multifurcated hydrogen bonding are shown in Figure 1.2.

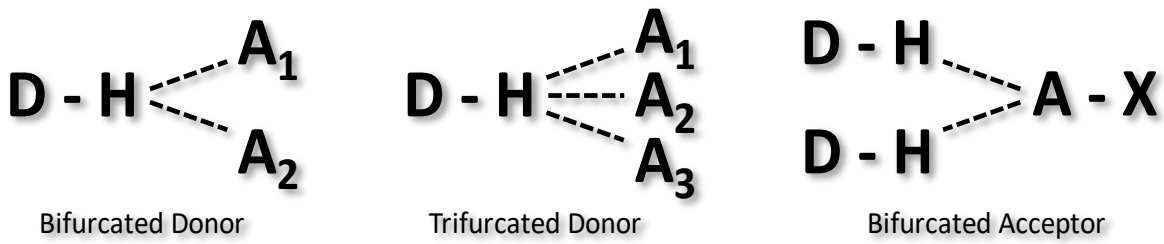

Figure 1.2. Examples of multifurcated hydrogen bonding. Adapted from Atwood and Steed.[22]

1.1.3. π-Interactions

The term *π-interaction* is an umbrella term describing a host of interactions of different compound classes with the delocalised π-electron cloud of a planar, aromatic moiety. While π-interaction can refer to any number of interactions (*e.g.,* C–H···π, O···π, N···π, *etc.*), π···π interactions are the most relevant. Of particular interest are the π···π interactions occurring between planar aromatic rings. These π···π interactions are non-directional interactions of weak to moderate strength (8–42 kJ mol^{-1}).[22]

Hunter and Sanders proposed a comprehensive model predicting π···π stacking of aromatic rings in 1990.[23] Their model demonstrated that a planar aromatic ring possesses a quadrupole when viewed side-on (Figure 1.3.).[23,24] This quadrupole is best illustrated by separating the σ-framework of the benzene ring from its delocalised π-electron cloud, where the σ-framework is electron rich (δ^-) while the π-electron cloud is electron deficient (δ^+).[23,24] Thus the σ-framework is effectively "sandwiched" between the two π-clouds (Figure 1.3.).[23] The resulting interaction geometry is then determined by the combination of the favourable (σ···π attraction) and the unfavourable interactions (π···π repulsion) occurring between two planar aromatic rings.[24] This model was subsequently termed the *polar/pi model* by Cozzi and Siegel,

who further demonstrated that the degree of polarisation of the π-electron cloud could be used to predict the interactions of aromatic compounds.[25–29]

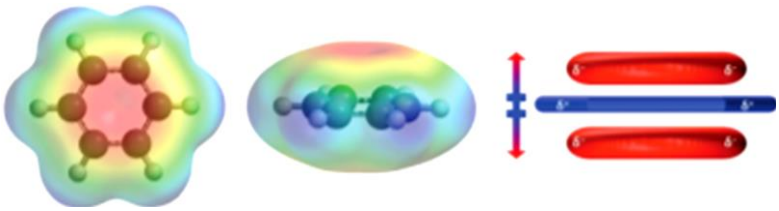

Figure 1.3. Electrostatic potential surface of benzene, alongside a cartoon representation of the σ-framework sandwiched by the π-electron clouds.[24]

A combined approach of the polar/pi model and electrostatics can be used to explain the different packing geometries of molecules in the solid-state. For example, this model explains why benzene prefers T-shaped packing (σ···π attraction, Figure 1.4c), but has an aversion to face-to-face stacking (π···π repulsion, Figure 1.4a).[24,30] In fact, the face-to-face alignment is not preferred for most aromatic compounds owing to the repulsive force of the π-electron clouds on one another.[31] However, once substituents are placed on the benzene ring (or heteroatoms are introduced), the subsequent polarisation of the quadrupole moment favours other packing geometries.[30,31] When the quadrupole moment is polarised by electron-withdrawing substituents, the π-character of the π-electron clouds is reduced.[30] This results in other π-interactions such as C–H···π and dipole···π type interactions determining packing geometry.[30] If this reduction in π-character is large enough, face-to-face alignment may be viable.[24] Conversely, polarisation of the quadrupole by electron-donating substituents will strengthen the π-character of the π-electron clouds, leading to greater repulsion in the face-to-face alignment.[30]

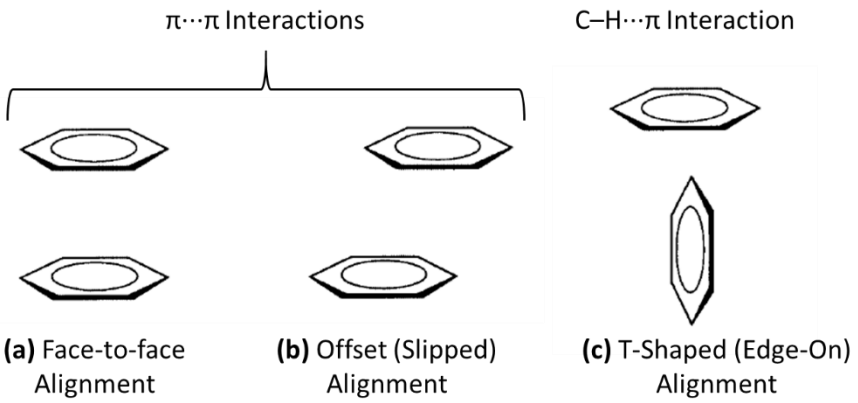

Figure 1.4. Principle geometries of π-interactions in benzene. Adapted from Janiak.[30]

Conventionally, the π···π interaction distance between two aromatic rings is reported as their centroid-to-centroid distance. Janiak asserts that facial π···π interactions (Figure 1.4a and b) generally fall within an interaction distance of 3.3–3.8 Å.[30]

1.1.4. Van der Waals Interactions

Van der Waals interactions (also known as London dispersion forces) are weak, non-directional interactions.[32,33] They occur between uncharged species where one electron cloud induces a momentary dipole in an adjacent species.[33] This momentary dipole is the result of short-lived electrostatic repulsion or attraction.[33] Owing to the fleeting duration of these dipoles, van der Waals interactions are the weakest electrostatic interactions and only act over very short distances. While these forces infrequently dictate supramolecular design, they are often of importance for inclusion compounds (§1.6.1.). Consequently, these interactions only have a meaningful contribution when there is a lack of other stronger electrostatic interactions and when there are a substantial number of van der Waals interactions.

1.2. Crystal Engineering

Crystal engineering is an approach describing the directed use of known supramolecular interactions and motifs to design novel supramolecular materials with desired physical and chemical properties.[34] Pepinsky is credited with the earliest use of the term *"crystal engineering"* in his 1955 article *"Crystal engineering: a new concept in crystallography."*[35] However, it was Schmidt who popularised the utility of crystal engineering in 1971 with his work on the solid-state photodimerisation of olefins.[36] Crystal engineering exploits various strategies to achieve desired supramolecular architectures and resulting properties, these include the use of supramolecular synthons,[34,37] self-assembly[16] and reticular synthesis.[38]

1.2.1. Supramolecular Synthons

Supramolecular synthons refer to the smallest structural unit obtained *via* molecular recognition to generate solid-state superstructures or crystals.[34,37] Supramolecular synthons are nearly always based on known hydrogen bonding motifs (Figure 1.5.). Thus, supramolecular synthons essentially define the solid-state packing by means of their specific configuration of electrostatic interactions. Along these lines, an organic crystal can be seen as a scaffold of nodes (the synthons) and linkers (the molecules).[17] Retrosynthetic study (*i.e.,* synthesis in reverse) of crystal structures allows for the extraction of key synthons, which

determine the supramolecular architecture achieved.[39] These can then be applied to the directed synthesis of crystals with predetermined packing motifs.

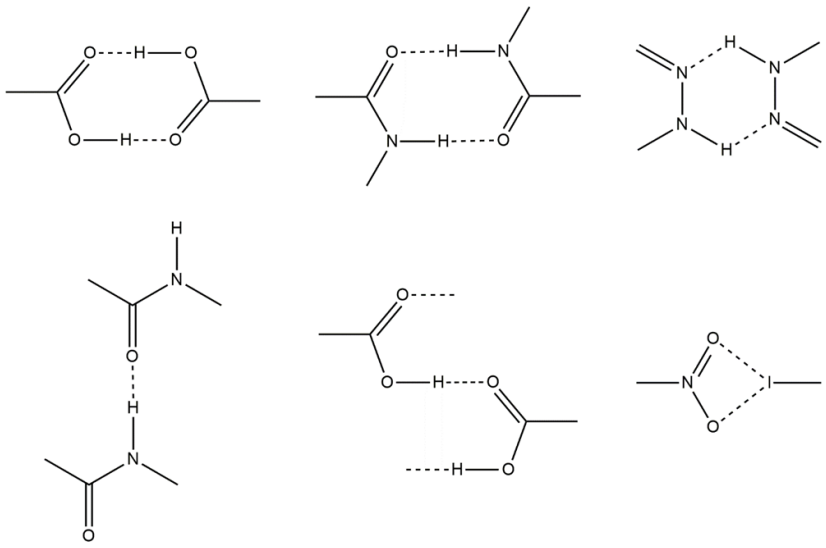

Figure 1.5. Representative supramolecular synthons. Adapted from Desiraju.[37]

1.2.2. Self-Assembly

Self-assembly describes the spontaneous association of two or more molecules to form aggregates by means of reversible, non-covalent interactions.[16] Although self-assembly is somewhat synonymous with the biological field, it is an invaluable supplement to supramolecular chemistry. During supramolecular self-assembly, synthons with complementary functionalities aggregate by means of non-covalent electrostatic interactions to pack regularly in the solid-state.[16] The reversible nature of the non-covalent interactions involved allows for spontaneous correction of any deviations from the most thermodynamically stable motif. By introducing more than one synthon, the complexity of the system can be exponentially increased as more than one self-assembly route becomes possible (where the most thermodynamically stable form prevails).

1.2.3. Secondary Building Units and Reticular Synthesis

Secondary building units (SBUs) represent a simplified approach to crystal engineering; organic ligands and metal nodes are regarded as molecular recognition sites and geometric forms.[38] SBUs generally make use of metal-carboxylate linkages because of their prevalence in solid-state chemistry.[40] The most common metal-carboxylate SBUs are shown in Figure 1.6. – illustrating how they may combine to create an array of complex 3D architectures.

Reticular synthesis involves the use of predetermined molecular units, or building blocks, to achieve desired topologies with specific chemical and physical material properties.[38] These building blocks are the aforementioned SBUs. Reticular synthesis utilises the deconstruction of desired motifs to progress forward in the way that retrosynthesis uses them to work backwards. It is, however, differentiated from retrosynthesis by the fact that the building blocks are not altered throughout the process of reticular synthesis.[38] Furthermore, reticular synthesis is distinguished from supramolecular self-assembly owing to the strong coordination linkages which connect SBUs to one-another.[38]

Isoreticular synthesis represents a sub-class of reticular synthesis, where the same SBUs are used with variable spacers.[38] Linker variation is achieved by using an analogous spacer of greater/shorter length or by functionalisation of the existing linker. Isoreticular synthesis creates motifs that exhibit the same topology,[38] but can differ in selectivity (in terms of size and chemoselectivity).[41]

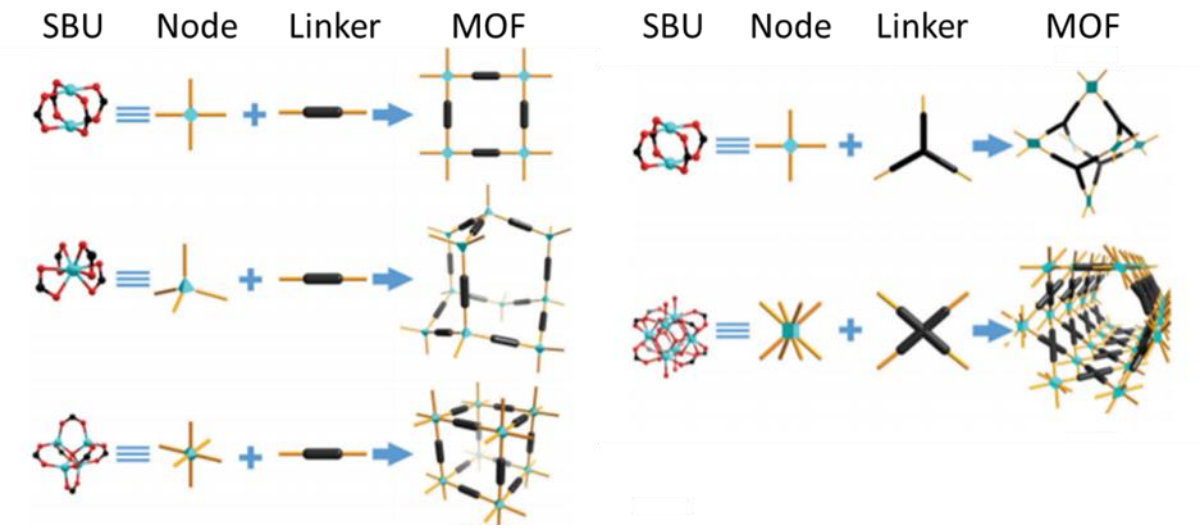

Figure 1.6. Graphical representation of the most common SBUs and how they combine into more complex motifs.[41]

1.3. Coordination Polymers and Metal-Organic Frameworks

Both coordination polymers and metal-organic frameworks (MOFs) represent conceptually infinite structures consisting of metal-ion nodes and organic ligands. The IUPAC has defined coordination polymers to include only coordination compounds that propagate in one-dimension.[42] For coordination compounds of higher dimensionality the term MOF is used.[43] The relevant terminology discussed above is represented in Figure 1.7.

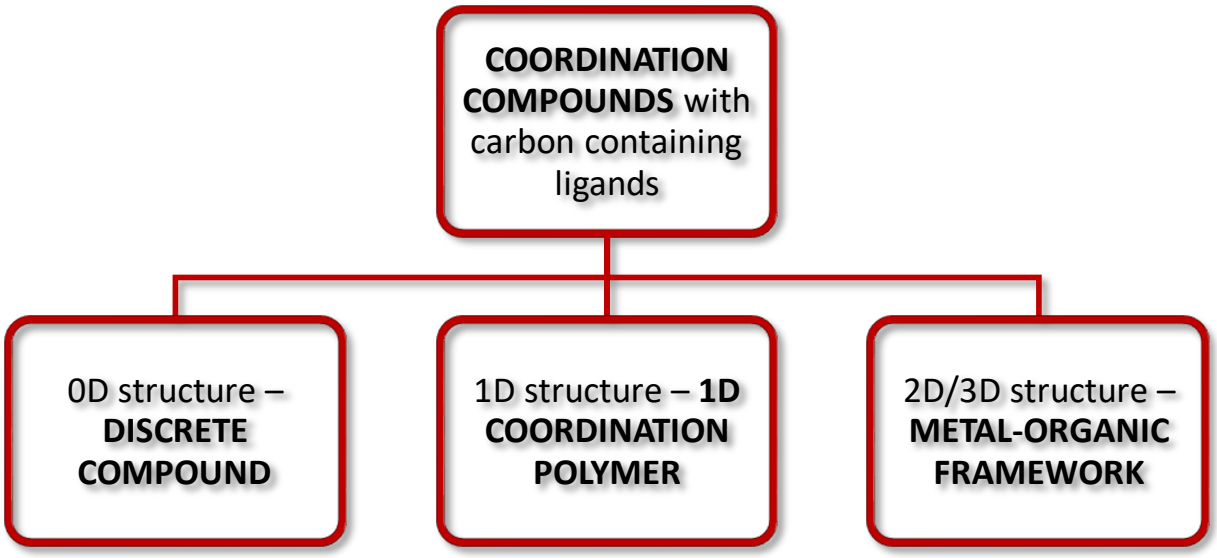

Figure 1.7. Representation of coordination compound nomenclature. Adapted from Batten *et al.*[43]

Coordination polymers predate MOFs and are defined by infinite 1D arrangements of metal ion nodes connected by organic ligands.[16] 1D coordination chains pack *via* directional electrostatic interactions, π···π interactions and short-range van der Waals interactions. The simplicity of their 1D connectivity allows for relatively facile structural modification by varying the metal-ion nodes and organic linkers. As a result, coordination polymers can adopt a number of different packing arrangements. These 1D motifs can include linear chains, zig-zag chains, helices, ladders, *etc*. (Figure 1.8a).[15] Their inherent flexibility is advantageous when designing complex hierarchical architectures. Although this creates the potential for large structural transformations, these changes often result in a dramatic decrease in crystal quality. Thus, despite being a promising avenue of exploration, such materials are frequently abandoned owing to the possible complications. Nonetheless, several examples of coordination polymers with striking applications have been published.[44–46]

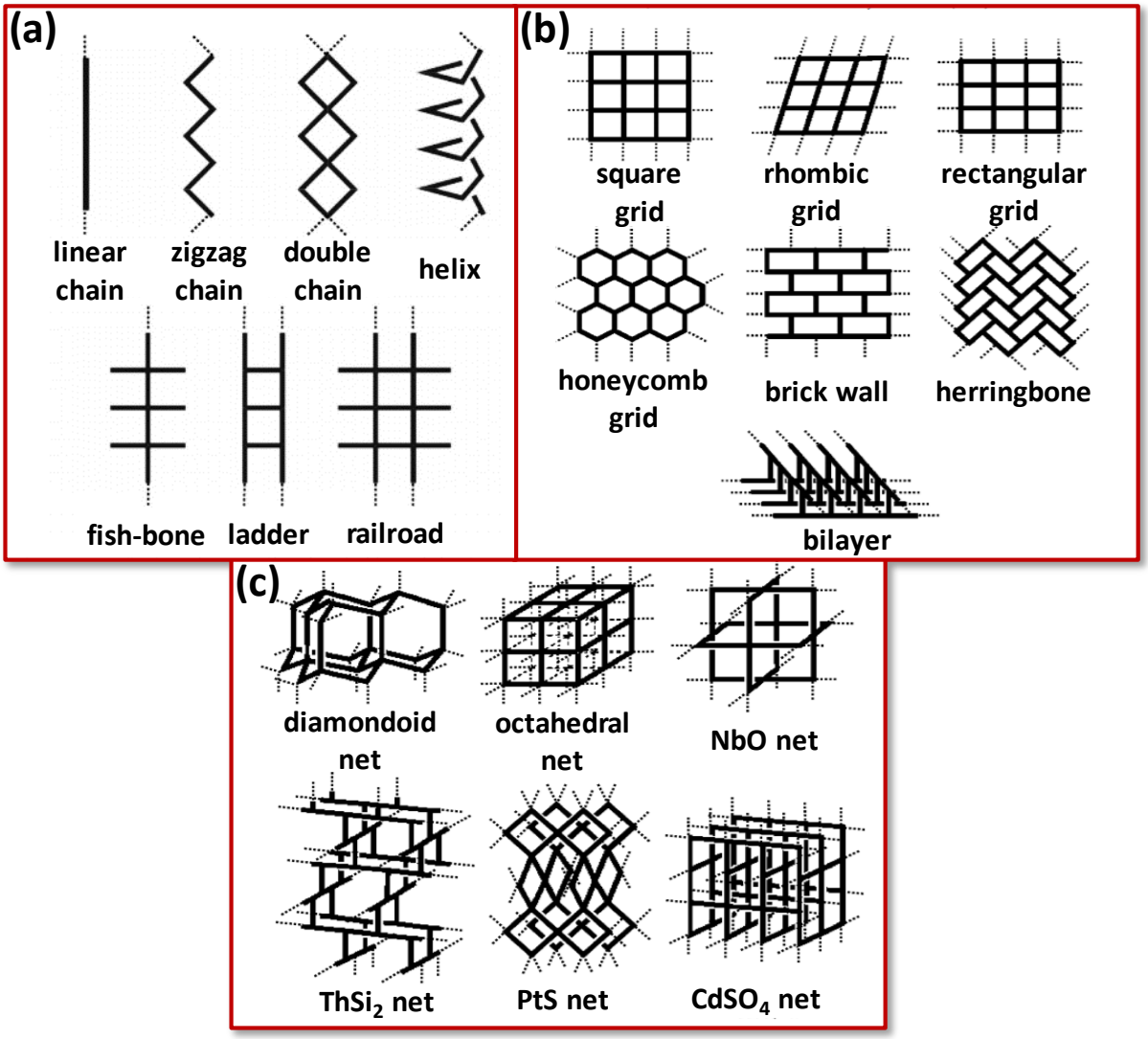

Figure 1.8. Common motifs in **(a)** 1D, **(b)** 2D and **(c)** 3D coordination compounds.[15]

1.4. Crystal Packing Phenomena

Crystals are composed of repeat units that pack in 3D in a conceptually infinite manner. It is possible for similar compounds to exhibit appreciably different crystal packing motifs. Conversely, it is possible for dissimilar compounds to display very similar crystal packing motifs. Elucidation of these phenomena assists with the characterisation and understanding of the architecture in question.

1.4.1. Close Packing

Molecular crystals favour packing arrangements that minimise intermolecular voids.[47,48] This *close packing principle* was introduced by Kitaigorodsky when he observed the tendency of molecules in the solid-state to pack in such a way that the "projection" of one molecule will fit into the "hollow" of another.[47,48] The close packing phenomenon is modulated by van der

Waals and other non-directional electrostatic interactions. However, when stronger directional electrostatic interactions are present, structures may deviate from the close packing principle.[48] Similarly, awkwardly shaped molecules generally do not form close-packed motifs.[47]

1.4.2. Supramolecular Isomerism

Solid-state motifs that are different from one another, but possess the same empirical formulae are often termed *supramolecular isomers*.[49] Following this line of reasoning, supramolecular isomerism can be divided into four sub-classes: catenane, optical, conformational and structural supramolecular isomers.[49] *Catenane isomerism* describes a dissimilarity in the level of structural interpenetration, while *optical isomerism* relates to a difference in chirality.[49] Conformational and structural isomers imitate their molecular counterparts. *Conformational supramolecular isomerism* describes structures with the same solid-state stoichiometry and connectivity, where the packing motif is different owing to changes in bond conformation in flexible ligands.[49] Lastly, *structural isomerism* describes differing supramolecular architectures generated from the same building block with the same empirical formulae.[49]

This simplistic classification is problematic as it creates ambiguity between supramolecular isomerism and polymorphism (**§1.4.3.**). Thus, to reduce the possiblity of any overlap between the terminology of structural phenomena, further constraints should be applied to the definition of supramolecular isomerism. Therefore, the distinction is made according to the materials described by each term; supramolecular isomerism is generally used for framework materials and polymorphism for discrete crystalline compounds.[50]

1.4.3. Polymorphism

Compounds that have different solid-state packing motifs, but give rise to the same liquid and vapour phases are *polymorphs* of each other.[51] Even though they are comprised of the same compound, owing to their differences in solid-state architecture, polymorphs can exhibit vastly different physical and chemical properties.[52,53] Polymorphs may differ from one another in terms of their solubility, density, diffraction, melting point, stability, *etc.*[53]

1.4.4. Concomitant Crystallisation

When two or more polymorphs, supramolecular isomers or solvates form during the same crystallisation experiment they are referred to as *concomitant.*[52,53] Concomitant crystallisation

is an interesting phenomenon from the perspective of fundamental science, as it presents great potential to investigate the relations between structure and thermodynamics.[52] While concomitant crystallisations are not rare, they are not necessarily common either. This may, in part, be as a result of underrepresentation, since the phenomenon is often avoided since phase-pure crystallisations are generally required in industry and pharma.[52]

For crystallisation to take place, thermodynamics necessitates that aggregation to form a solid-state compound results in a stabilisation of the system.[52] In other words, crystallisation must result in a lowering of the Gibbs free energy of the system.[52] It is possible for several different solid-state structures to be energetically accessible, wherein there may exist both kinetic and thermodynamic forms.[52,54] In these cases, the thermodynamic form represents the most stable overall packing configuration and the kinetic form represents the solid-state structure that the system can access with the most ease.[52] Furthermore, where more than two forms are present there may be multiple kinetic and thermodynamic forms.

In some instances, with the correct set of conditions (time, temperature, pressure, *etc.*), forms may interconvert (Figure 1.9a).[52,54] Alternatively, these materials may not interconvert, with each form representing a distinct local thermodynamic energy minimum (Figure 1.9b).[52,54] Materials that interconvert in the solid state are known as *enantiotropic,*[52] an example of which is shown in Figure 1.9a.[54] Figure 1.9a shows the energy *versus* temperature (E/T) diagram of two materials (denoted I and II), where II converts to I at a transition temperature (tp,II/I) that is lower than the melting points of the two materials (mpII and mpI).[52,54] It is at this transition point that concomitant forms may arise, and deviation from this point may result in one form being favoured over the other(s).[52] The degree of the shift in preference depends on the extent of the change in conditions as well as the energetic difference between the two forms.[52] Conversely, forms that do not interconvert are known as *monotropic,*[52] of which Figure 1.9b is an example.[54] Monotropic forms do not interconvert in the solid state. This is illustrated in Figure 1.9b (notation analogous to Figure 1.9a) where there is no crossing of the Gibbs free energy plots before the melting points of the materials.[52]

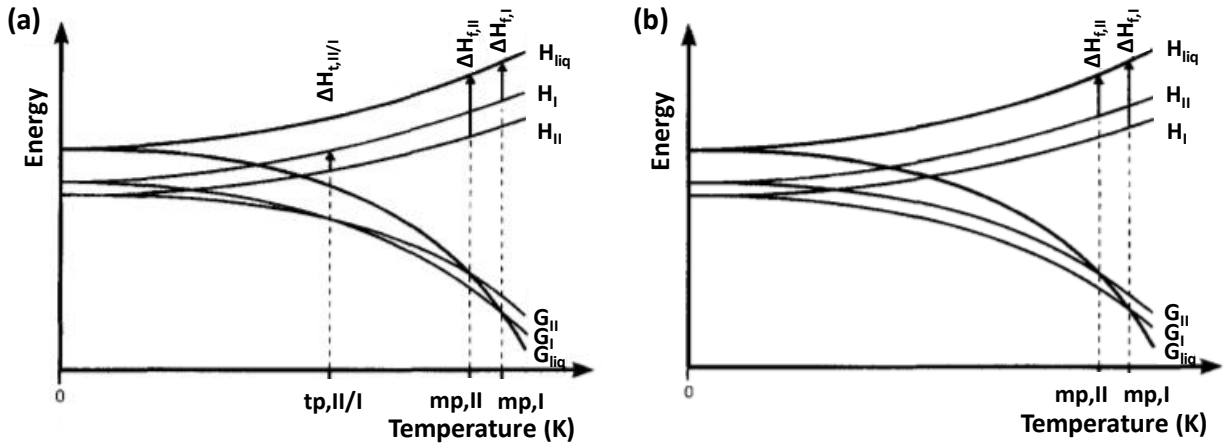

Figure 1.9. Energy *versus* temperature diagrams for examples of **(a)** enantiotropic and **(b)** monotropic systems, each consisting of two forms. In both graphs these forms are denoted by Roman numerals (I and II), mp indicates the melting points of the polymorphs, and G and H represent the Gibbs free energy and enthalpy plots, respectively. In **(a)** tp indicates a transition point between the two polymorphs. Adapted from Grunenberg *et al.*[54]

1.4.5. Phase Transitions

Some materials may interconvert between different packing architectures as a result of a change in a specific environmental factor (*e.g.,* temperature, pressure, *etc.*).[52,53] Phase changes can range from drastic to nearly imperceptible changes in packing. Thermally-induced phase transitions are known to occur spontaneously within a narrow temperature range.[54] In cases where structural changes are subtle and occur as a result of a temperature gradient, it may be difficult to determine whether a phase transition is occurring or if the material is simply undergoing thermal expansion (§1.4.6). Therefore, a distinction is made between these two phenomena on two accounts. Thermal phase transitions are characterised by (i) a peak in a differential scanning calorimetric thermogram and (ii) a discontinuity in a plot of unit-cell parameters as a function of temperature.[55,56]

1.4.6. Thermal Expansion

Generally, solids expand when heated. This is as a consequence of the increased thermal motion of the constituents and is known as *positive thermal expansion* (PTE).[57] When the opposite occurs (*i.e.,* contraction upon heating) it is known as *negative thermal expansion* (NTE).[57] The latter phenomenon is much rarer. *Anisotropic* thermal expansion describes thermal expansion coefficients of different magnitudes along the three axes and is generally observed in systems with lower crystal symmetry than cubic.[58] Furthermore, when a solid expands and contracts simultaneously along different directions, the thermal behaviour is

termed *anomalous*.[58] Some materials may exhibit no discernible change in dimensions over a temperature gradient; these materials display *zero thermal expansion* (ZTE).[57] In crystalline materials thermal expansion may be differentiated from phase change behaviour by continuous, gradual changes in the unit-cell parameters over a temperature gradient, and the absence of a heat of transition.[55,56]

The magnitude of thermal expansion can be expressed either as the percentage change in the axes or as an eigenvalue (referred to as the *expansion coefficient*).[59] The linear expansion coefficient along a direction *L* is calculated using Equation 1.1.[59,60]

$$\alpha_L = \frac{L_f - L_i}{L_i(T_f - T_i)} \tag{1.1.}$$

where the subscripts refer to the final (*f*) and initial (*i*) lengths and temperatures (*T*). Similarly, the volumetric expansion coefficient of a material with volume *V* is calculated using Equation 1.2.[59,60]

$$\alpha_V = \frac{V_f - V_i}{V_i(T_f - T_i)} \tag{1.2.}$$

Both volumetric and linear expansion coefficients are measured in K^{-1}.

Equations 1.1. and 1.2. are employed when the material crystallises in a space group possessing orthogonal unit-cell axes. If the material of interest crystallises in a space group with non-orthogonal unit-cell axes there may be a concurrent change in unit-cell axes and angles as a function of temperature. In these cases a set of orthogonal principal axes (typically denoted *X1*, *X2*, *X3*) are defined to simplify the description of the thermal expansion behaviour of the material.[59] These principal axes are reported together with the matrices relating them to the original unit-cell axes.[59] The thermal expansion of principal axes and the volumetric expansion may then be determined with equations 1.1. and 1.2., respectively.

An encompassing depiction of the thermal expansion behaviour experienced along all axes in a material can be visualised in various ways: expansivity indicatrix, thermal expansivity quadric, strain ellipsoid (Figure 1.10.).[59] In recent times the expansivity indicatrix has become favoured when representing thermal expansivity. This is as the directions and relative magnitudes of the thermal expansion are clearer in this representation.[59]

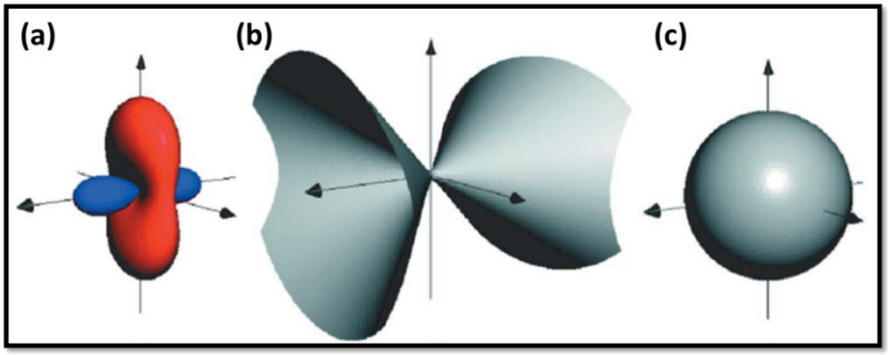

Figure 1.10. The expansivity tensor from variable temperature data of $Ag_3[Co(CN)_6]$-II represented as the **(a)** expansivity indicatrix (PTE shown in red and NTE in blue), **(b)** thermal expansivity quadric and **(c)** strain ellipsoid.[59]

1.4.7. Other Crystal Packing Phenomena

Compounds may exhibit similar crystal packing, but not be related in any of the ways discussed previously. Owing to the similarity of these structures, nomenclature often becomes conflated. Once more it is necessary, for clarity, to disentangle terms which are related. The terms in question are isomorphous, isostructural, isotypic and isoskeletal.

Isomorphism describes two or more crystals that display the same exterior morphologies, as first defined in 1819 by Mitscherlich.[61] However, the International Union of Crystallography (IUCr) has more recently extended the definition to encompass crystals that are essentially identical in all way except for their molecular composition.[62] The IUCr states that crystals are isomorphous if: "*(a) both have the same space group and unit-cell dimensions and (b) the types and the positions of atoms in both are the same except for a replacement of one or more atoms in one structure with different types of atoms in the other (diadochy), such as heavy atoms, or the presence of one or more additional atoms in one of them (isomorphous addition).*"[62]

Compounds with different chemical formulae, but identical (or nearly identical) crystal packing are deemed to be *isostructural.*[63] Isostructural crystals do not necessarily have the same unit-cell parameters or space group symmetry. However, atomic positions and identities are comparable.[63] In other words isostructural packing motifs should be virtually superimposable.[22] The terms *isostructural* and *isotypic* refer to structural similarities in organic and metal-organic compounds, respectively.[22] *Homeotypic* represents a more relaxed classification than *isostructural*. Compounds that pack in identical motifs, but whose atomic positions are not especially comparable (*e.g.,* differently substituted compounds), are considered to be *homeotypic*.[22,64]

Isoskeletal refers to inclusion compounds (**§1.6.1.**) where the host framework remains the same even when the guest varies.[64] Therefore, if the guests of isoskeletal materials are excluded, the materials become isostructural, and in essence it is only the variability in guest that differentiates isoskeletal from isostructural materials.[64] Isoskeletal materials may also be defined as homeotypic.[64]

1.5. Solid Solutions

Solid solutions (also termed *mixed crystals*) are produced when one component is dispersed within the crystal lattice in a non-stochiometric manner.[64,65] In coordination chemistry solid solutions are often employed to determine the selectivity of a system to one metal over another. Furthermore, even small amounts of doping (addition of a second, non-stochiometric component) may drastically alter the physical properties of a material (for example metal alloys are solid solutions).

1.6. Host-Guest Chemistry

Compounds sometimes pack in the solid-state in such a way that voids are formed. These voids are, more often than not, occupied by other molecules. Host-guest (inclusion) compounds consist of multicomponent systems where the individual components may be subjectively classified as either *host* or *guest*. The component possessing *convergent* binding sites is termed the *host*, while the component possessing *divergent* binding sites is termed the *guest*.[22] Binding sites may include hydrogen bonds, halogen bonds, π···π interactions, *etc.*

1.6.1. Solvates

Solvates are inclusion compounds where a host traps solvent guest molecules during crystallisation. There are no covalent bonds between the host and guest, and the guest is held in the channel or cavity by electrostatic interactions. These electrostatic interactions can range from strong hydrogen bonding and ionic interactions to weaker π-interactions and van der Waals forces.[66] Hydrogen bonding represents the most notable of these, owing to its prevalence, strength and directionality.[66]

A typical solvent inclusion/decomposition process is presented in Figure 1.11.[66] This process can also be formulated as shown in Equation 1.3.[66]

$$H\,(s,\alpha) + nG\,(l/g) \rightleftharpoons H{\cdot}G_n\,(s,\beta) \qquad \textbf{(1.3.)}$$

During the inclusion process, the host (H), initially in its pure phase (α), is introducted to a guest (G) in the liquid or vapour phase, resulting in formation of the host-guest phase (β or $H{\cdot}G_n$) – where *n* represents the host-guest stoichiometric ratio (Figure 1.11a,b).[66]

Once the inclusion compound (β phase) is formed, it can undergo several transitions upon desolvation. In some cases the host-guest inclusion compound will decompose and regenerate the original host α phase (Figure 1.11c).[66] A slightly more robust inclusion compound might only decompose partially, resulting in the formation of a new γ solvate phase (Figure 1.11d).[66] Robust host frameworks, which possess added rigidity, may not exhibit structural rearrangement at all when the solvent is removed.[66] In these cases a porous version of the β phase host is formed, and this is then termed the β_0 phase (Figure 1.11e).[66]

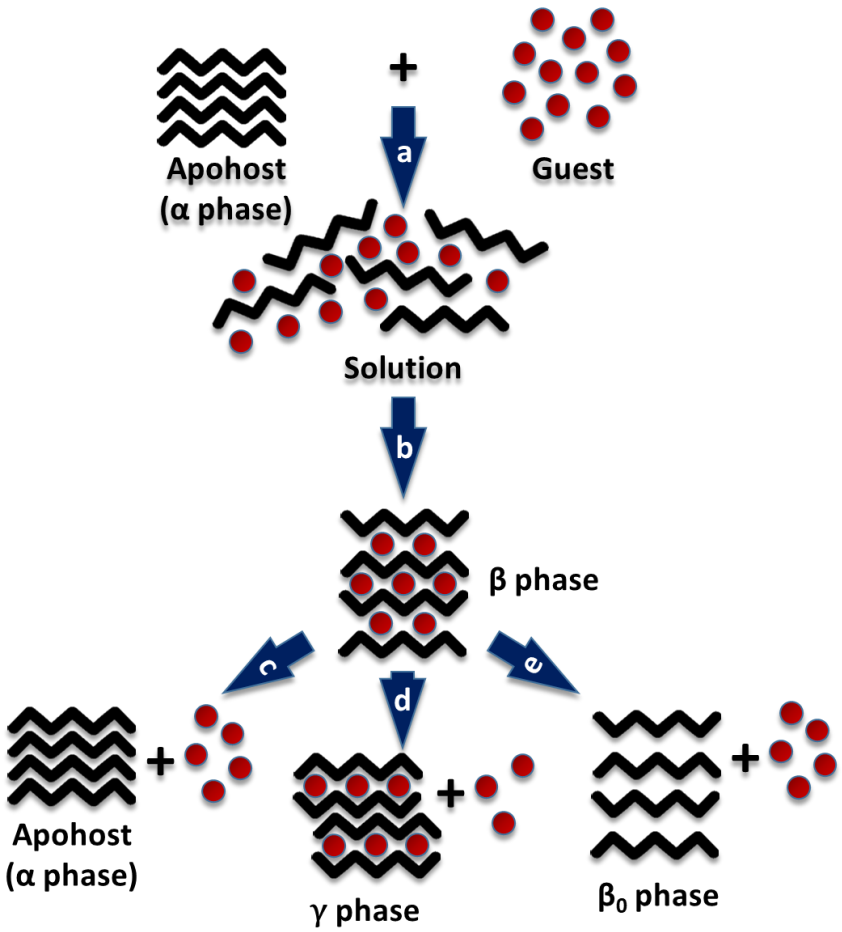

Figure 1.11. Representation of host-guest chemistry exhibiting **(a)** dissolution of host α phase (*i.e.,* the apohost) in liquid guest, **(b)** crystallisation of the β phase inclusion compound, **(c)** thermal decomposition resulting in desolvation to regenerate the host α phase, **(d)** partial thermal desolvation to produce a new γ phase inclusion compound, and **(e)** desolvation without host rearrangement to yield the empty host β_0 phase. Adapted from Nassimbeni.[66]

1.6.2. Guest Exchange and Solvatomorphism

As guests are often positioned in the host cavities/channels by weaker electrostatic interactions, it is frequently possible to exchange guest molecules. Guest exchange is carried out by immersion of the inclusion compound in a different guest solvent or vapour. In certain cases, the guest exchange process can occur as a single-crystal to single-crystal transformation (§1.9.) if the host structure is sufficiently robust to survive the structural deformation caused by the exchange.

Solvatomorphism is the phenomenon where a single host adopts different packing motifs depending on the ratio and identity of the guest(s).[53] In this dissertation the term *solvate* will be used to describe all compounds where the framework composition remains the same but the guest or guests differ.[64] The term *solvate* represents a broader scope than *solvatomorph* (as it does not require a difference in host packing upon solvent exchange), but fundamentally includes all solvatomorphs.

1.6.3. Selectivity

There are several potentially useful applications for host-guest chemistry, one of the most important being the separation of mixtures.[66,67] Hosts may display different selectivity for different guests owing to a number of chemical or physicochemical factors. Selectivity is governed by both size and chemical compatibility, and this can be complicated even further by concentration-dependent effects.[66]

1.7. Porosity

Porosity refers to the presence of guest-accessible voids or channels within a material.[68] However, owing to the close packing principle, porosity is not common in coordination compounds (and is quite rare in molecular compounds). Porosity in itself is not a recent discovery, with activated carbons and zeolites being well documented by the twentieth century. As a result of this, crystal engineering has developed numerous different strategies which engender porosity in MOFs and coordination polymers.

Owing to the relatively recent surge in the popularity of porous compounds, initiated by the rise of MOFs, the term *porous* is often applied indiscriminately. Barbour classifies compounds as porous if they subscribe to two fundamental criteria: (i) that the channels or voids are accessible to the new guest (*i.e.,* the material is permeable), and (ii) that the process of guest uptake should not result in degradation of the host structure.[68] Within this

classification of porosity, there are three sub-classes: virtual, transient and conventional porosity.[68]

Virtual porosity is generated computationally by deletion of guest molecules or counter ions from the crystallographic model.[68] This results in the misleading creation of empty voids or channels, which are not necessarily obtainable experimentally. This procedure can be used to visualise the solvent-accessible space in a host structure and is especially useful when comparing structural differences resulting from guest exchange. Virtual porosity is associated with how the structures are represented. Crystal structures are commonly visualised using the ball-and-stick or capped-stick representations for clarity. However, this is often misleading as these models do not represent the true sizes of the atoms relative to one another and the space that they occupy.[68] As a result, the observer might perceive voids/channels that are not actually present (an example of which is shown in Figure 1.12.).[68]

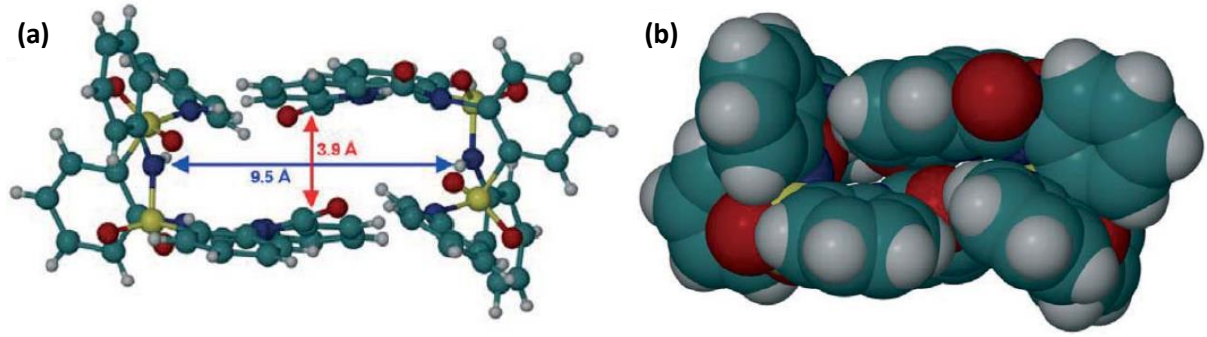

Figure 1.12. Dimer of two L-shaped molecules in the **(a)** ball-and-stick model and **(b)** space-fill representation.[68]

Transient porosity refers to guest diffusion in the absence of any permanent channels connecting internal voids to the external environment.[68] Even though the cavities do not extend to the crystal surface or interconnect, these materials may allow for a guest to travel through the structure.[68] In these cases, guest inclusion is achieved either by a single notable shift in the structure, which creates accessible channels, or by small continuous motions within the crystal structure, which allow for the guest to move from one pocket to the next. The latter thus results in a short-lived connection between two adjacent voids, which is then subsequently severed, with no permanent channel being formed.

The presence of permanent guest-accessible channels within a material is described as *conventional porosity*.[68] The orthodox approach to generating conventional porosity relies on growing inclusion compounds with solvent guest molecules located within the channels.[68]

These guest molecules should then be removed without disrupting the host framework, to yield a porous apohost analogous to the initial inclusion compound.[68]

Kitagawa and co-workers proposed further classification of porous materials into four classes based on the spatial identity of the voids/channels: 0D, 1D, 2D and 3D.[69] Zero-dimensional cavities are discrete voids within the host, and are often found in molecular crystals. One-dimensional channels are infinite passages which extend in only one direction throughout the crystal structure, whereas two-dimensional layers result from two sheets which are far enough apart to generate a void which extends in two directions. Two-dimensional porosity can also be created by intersecting 1D channels. Three-dimensional porosity arises when channels intersect in three directions (not necessarily all at once). A schematic representation of these pore dimensionalities is shown in Figure 1.13.

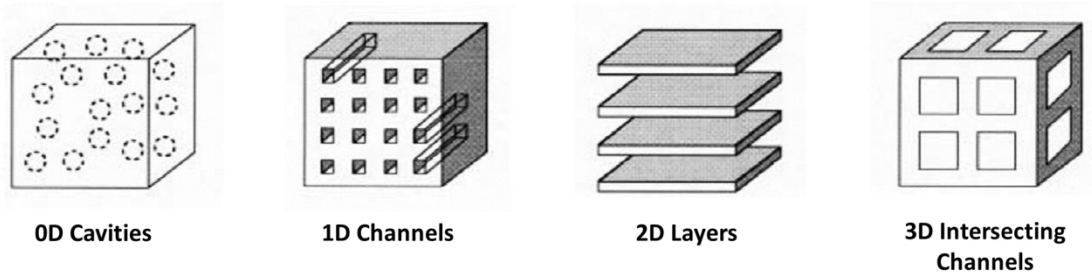

Figure 1.13. Classes of porosity based on pore dimensionality. Adapted from Kitagawa *et al*.[69]

Furthermore, porosity is also distinguishable on the basis of pore size. Pores can range from <5 Å (ultramicroporous), 5–20 Å (microporous), 20–500 Å (mesoporous) and >500 Å (macroporous).[69] There is essentially no difference between the adsorption properties of a discrete surface and a macropore (owing to relative size).[69] Mesopore adsorption is governed by the process of capillary condensation.[69] Adsorption in microporous compounds can be equated to the molecular filling of a nano-cavity.[69] These terms and their relation to sorption are further discussed in **§1.8.**

1.8. Sorption

Sorption is an all-encompassing term for both adsorption and absorption, and is usually applied where there is ambiguity as to which one is taking place. *Absorption* is the process of guest uptake into the host framework, while *adsorption* is a surface phenomenon.[70] The latter definition becomes problematic in instances where the interior surface of the pores/channels within a coordination compound may be considered as an extension of the external surface. As a result, the terms may occasionally cause confusion. Therefore, the all-encompassing

term sorption will be used in this document to avoid ambiguity. *Desorption* represents the reverse process of sorption.[70]

The sorbing material (host) is known as the *sorbent*, while the sorbed guest is known as the *sorptive*.[70] Sorptives can be gases, vapours or liquids. Sorption may occur by means of chemi- or physisorption. *Chemisorption* occurs when the sorptive and the host material form strong chemical bonds or interactions, whereas *physisorption* involves relatively weak interactions between host and guest.[70]

1.8.1. Gas Sorption

Gas sorption studies are generally carried out under isothermal conditions, where the amount of gas sorbed (in moles, grams or cubic centimetres) is plotted against the equilibrium relative pressure (P/P_0).[70] P_0 denotes the saturation pressure of the gas (sorptive) at the temperature chosen for the measurement.[70] However, if the temperature is above the critical temperature of the sorptive then P may be used as the abscissa of the plot.[70] In most cases, the desorption isotherm is plotted together with the sorption isotherm (where the experiments are run consecutively). *Hysteresis* occurs in cases where the sorption and desorption isotherms do not follow the same path.[70]

The IUPAC has designated six possible isotherm models for gas physisorption, labelled as Type I to VI (Figure 1.14a).[70] In addition to this they classify four idealised hysteretic loops, H1 to H4 (Figure 1.14b).[70] The isotherm is usually indicative of the pore size of the material. Type I isotherms generally occur for microporous materials, while non-porous and macroporous

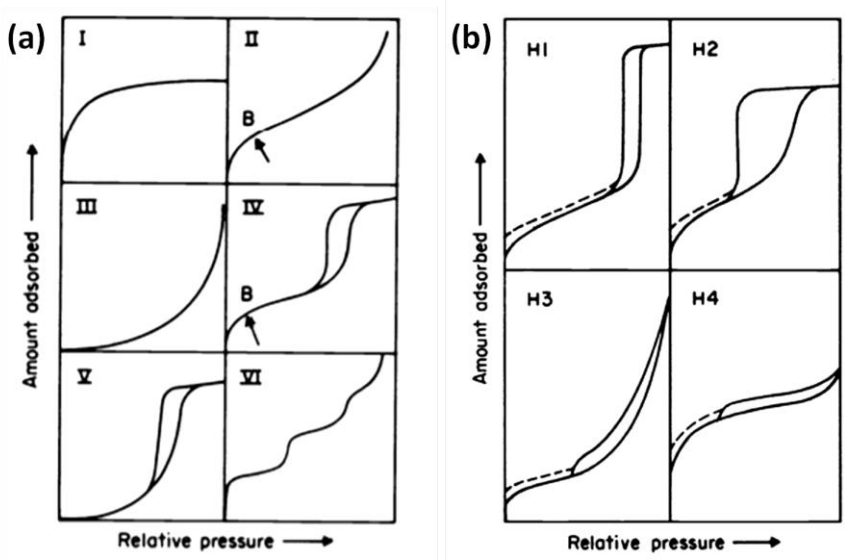

Figure 1.14. IUPAC definitions of **(a)** the gas physisorption isotherms and **(b)** idealised hysteretic loops.[70]

materials can generate isotherms of Type II, III or VI.[69] Lastly, Type IV and V isotherms are typical of mesoporous architectures.[69]

1.8.2. Vapour Sorption

The capture of volatile organic compounds (VOCs) is an imperative in both research and industry owing to the toxicity of many of these vapours.[71,72] Similarly, developing energy-efficient separations of industrially relevant compounds (such as xylene isomers) are of great interest.[67]

1.8.3. Sorption from Solution

While sorption is often associated with gases or vapours, some sorptives are only accessible in solution phase owing to either their own physicochemical properties or the conditions required for the experiment. Examples of such compounds include industrial dyes, iodine and bromine, as well as nitroaromatics. Many different kinetic and thermodynamic models describing liquid phase sorption exist, and it is by comparison of these that the best model for a specific sorption experiment is selected.

1.9. Single-Crystal to Single-Crystal Transformations (Lithotropism)

As mentioned throughout this chapter, coordination compounds may undergo a number of transformations in the solid-state. However, these transformations often result in a large amount of stresses on the crystal. As a result, it is common for crystals to disintegrate (*i.e.,* form crystalline powders) or even to become amorphous as a result of these stresses.[53] When a crystal maintains its single-crystal integrity during a structural transformation, this is known as a *single-crystal to single-crystal (SC-SC) transformation,* or *lithotropy*.[64] SC-SC transformations are useful as they allow for the study of structural dynamics and host-guest cooperativity. However, they are still rare in the literature.

1.10. Objectives and Dissertation Outline

The aim of this project was to synthesise an analogous series of novel coordination polymers from readily available organic ligands and metal salts, and to study the structure-property relationships of these compounds using various experimental techniques. Far fewer examples of SC-SC structural dynamics studies have been reported in CPs as compared to MOFs.[44–46,73,74] This may be due to two main influences. Firstly, CPs are more prone to close packing arrangements in the solid state. Secondly, the inherent flexibility of CPs may result in large

structural transformations such that the single crystals disintegrate into a polycrystalline powder.

Conceptually rigid ligands (Figure 1.15) were employed with a view to adding some support to the inherently flexible 1D strands and allow study of any structural transformation in a SC-SC manner. Finding a balance between structural flexibility and rigidity allows for the creation of dynamic materials, which do not undergo such dramatic transformations that they are not suitable for SC-SC study.

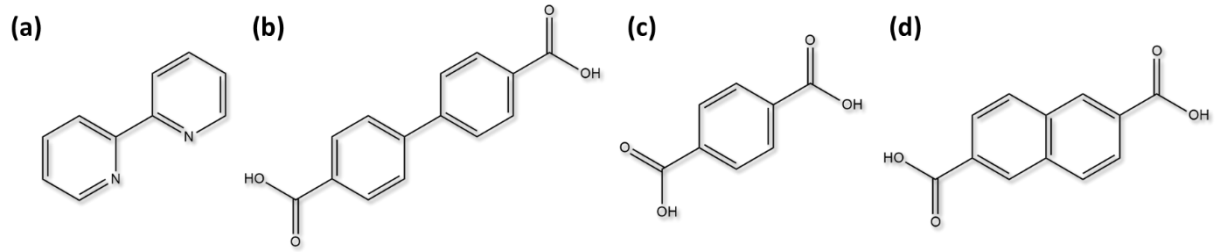

Figure 1.15. Organic ligands utilised during the studies described in this dissertation: **(a)** 2,2′-bipyridine, **(b)** 4,4′-biphenyldicarboxylic acid, **(c)** 1,4-benzenedicarboxylic acid (terephthalic acid) and **(d)** 2,6-naphthalenedicarboxylic acid.

All the materials studied display analogous crystal packing motifs comprising 1D “zig-zag" strands that pack in 3D to form trellis-like structural motifs with diamond-shaped apertures (Figure 1.16.). The 1D channels along the apertures contain the crystallisation solvent. The distinction is made between aperture and channel because, in some cases, an aperture may contain more than one guest-accessible channel.

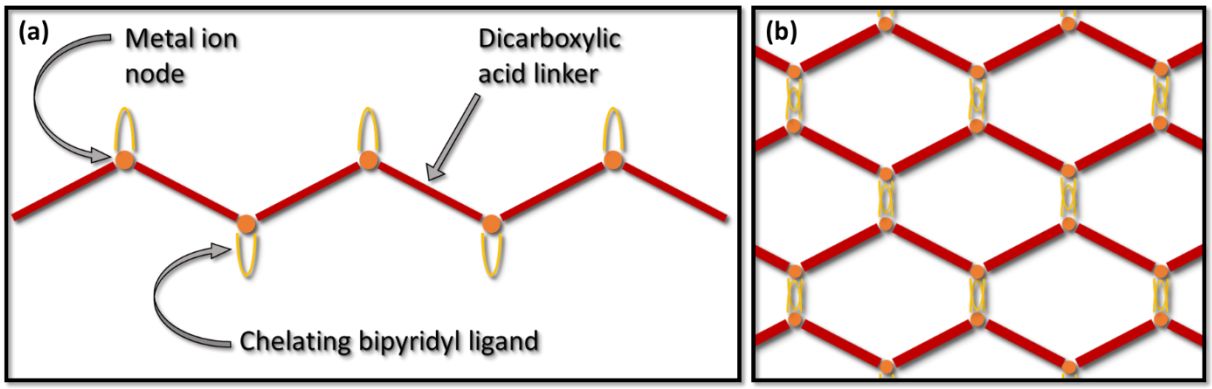

Figure 1.16. Cartoon representations of **(a)** the coordination linkages and **(b)** solid-state packing of the materials studied in this work (guests have been omitted for clarity). Note that, although it may appear in **(b)** that the strands are running parallel to the plane, they are actually traversing the plane.

The materials produced during this study were then exposed to multiple stimuli (*e.g.,* changes in temperature, guest exchange and pressure) and any changes observed were characterised using various techniques. These techniques included, but were not limited to:

single-crystal X-ray diffraction (SCXRD), differential scanning calorimetry (DSC), thermogravimetric analysis (TGA) and UV-visible spectrophotometry. Studies of how the synthetic method affects the material produced were also carried out.

1.10.1. Dissertation Outline

Chapter 2

All of the experimental techniques, equipment and software employed during this project are described.

Chapter 3

This chapter describes the successful isolation of two zinc CPs that crystallise concomitantly. This investigation focuses on the use of mechanochemical techniques when conventional solvothermal crystallisations result in complications.

Chapter 4

Studies of the activation and guest reintroduction behaviour of two zinc 1D coordination polymers are presented in this chapter. The crystal structure of the as-synthesised *N,N*-dimethylformamide (DMF) solvates exhibit great magnitudes of virtual porosity. However, upon desolvation (SC-SC) both compounds display dramatic contraction (uniaxial or biaxial), producing non-porous apohost phases. In one case, this contraction exceeds almost all previous reports for SC-SC contraction in the literature. Consequently, the dicarboxylic acid ligand becomes markedly distorted from its usual linear conformation. Vapour sorption of one of the non-porous apohost phases shows reopening to include the new guest, with subsequent cycles facilitating greater ease of reopening. Finally, the capacity of the material for the guest vapour is up to twice as much as expected because of cooperative surface deposition during sorption.

Chapter 5

The study of the thermal behaviour of a set of homeotypic CPs is described in this chapter. The CPs utilise the same organic ligands, but differ in the metal node selected. Certain solid solutions of two metal species were also prepared. Although these materials display slight thermal phase change behaviour, the thermal expansion properties are of greatest interest. The extreme anisotropic nature and magnitude of the thermal expansion in these materials surpasses almost all other accounts in the literature.

Chapter 6

This chapter consists of an overview and discussion of the results described in the dissertation. Some ideas for future work are also proposed.

References

1 J. M. Lehn, *Pure Appl. Chem.*, 1978, **50**, 871–892.

2 J. Liu, L. Chen, H. Cui, J. Zhang, L. Zhang and C.-Y. Su, *Chem. Soc. Rev.*, 2014, **43**, 6011–6061.

3 M. Raynal, P. Ballester, A. Vidal-Ferran and P. W. N. M. van Leeuwen, *Chem. Soc. Rev.*, 2014, **43**, 1660–1733.

4 M. Raynal, P. Ballester, A. Vidal-Ferran and P. W. N. M. van Leeuwen, *Chem. Soc. Rev.*, 2014, **43**, 1734–1787.

5 M. C.-L. Yeung and V. W.-W. Yam, *Chem. Soc. Rev.*, 2015, **44**, 4192–4202.

6 L. You, D. Zha and E. V. Anslyn, *Chem. Rev.*, 2015, **115**, 7840–7892.

7 X. Cui, K. Chen, H. Xing, Q. Yang, R. Krishna, Z. Bao, H. Wu, W. Zhou, X. Dong, Y. Han, B. Li, Q. Ren, M. J. Zaworotko and B. Chen, *Science*, 2016, **353**, 141–144.

8 J. Li, J. Sculley and H. Zhou, *Chem. Rev.*, 2012, **112**, 869–932.

9 K. Sumida, D. L. Rogow, J. A. Mason, T. M. McDonald, E. D. Bloch, Z. R. Herm, T. Bae and J. R. Long, *Chem. Rev.*, 2012, **112**, 724–781.

10 D. M. D'Alessandro, B. Smit and J. R. Long, *Angew. Chem., Int. Ed.*, 2010, **49**, 6058–6082.

11 J. A. Mason, M. Veenstra and J. R. Long, *Chem. Sci.*, 2014, **5**, 32–51.

12 T. Glaser, *Chem. Commun.*, 2011, **47**, 116–130.

13 J. Mihalčiak, P. Bertová, Z. Růžičková, J. Moncol, P. Segľa and R. Boča, *Inorg. Chem. Commun.*, 2015, **56**, 62–64.

14 M.-C. Dul, E. Pardo, R. Lescouëzec, Y. Journaux, J. Ferrando-Soria, R. Ruiz-García, J. Cano, M. Julve, F. Lloret, D. Cangussu, C. L. M. Pereira, H. O. Stumpf, J. Pasán and C. Ruiz-Pérez, *Coord. Chem. Rev.*, 2010, **254**, 2281–2296.

15 A. Y. Robin and K. M. Fromm, *Coord. Chem. Rev.*, 2006, **250**, 2127–2157.

16 J. W. Steed, D. R. Turner and K. Wallace, *Core Concepts in Supramolecular Chemistry and Nanochemistry*, Wiley, Chichester, 2007.

17 M. W. Hosseini, *CrystEngComm*, 2004, **6**, 318–322.

18 A. Werner, *Justus Liebigs Ann. Chem.*, 1902, **322**, 261–351.

19 L. Pauling, *J. Am. Chem. Soc.*, 1935, **57**, 2680–2684.

20 L. Pauling, *The Nature of the Chemical Bond and the Structure of Molecules and Crystals: An Introduction to Modern Structural Chemistry*, Cornell University Press, Cornell, 1939.

21 E. Arunan, G. R. Desiraju, R. A. Klein, J. Sadlej, S. Scheiner, I. Alkorta, D. C. Clary, R. H. Crabtree, J. J. Dannenberg, P. Hobza, H. G. Kjaergaard, A. C. Legon, B. Mennucci and D. J. Nesbitt, *Pure Appl. Chem.*, 2011, **83**, 1637–1641.

22 J. L. Atwood and J. W. Steed, *Encyclopedia of Supramolecular Chemistry*, Marcel Dekker, Boca Raton, 2004.

23 C. A. Hunter and J. K. M. Sanders, *J. Am. Chem. Soc.*, 1990, **112**, 5525–5534.

24 B. A. Ikkanda and B. L. Iverson, *Chem. Commun.*, 2016, **52**, 7752–7759.

25 F. Cozzi, M. Cinquini, R. Annunziata, T. Dwyer and J. S. Siegel, *J. Am. Chem. Soc.*, 1992, **114**, 5729–5733.

26 F. Cozzi, M. Cinquini, R. Annuziata and J. S. Siegel, *J. Am. Chem. Soc.*, 1993, **115**, 5330–5331.

27 F. Cozzi, F. Ponzini, R. Annunziata, M. Cinquini and J. S. Siegel, *Angew. Chem., Int. Ed.*, 1995, **34**, 1019–1020.

28 F. Cozzi and J. S. Siegel, *Pure Appl. Chem.*, 1995, **67**, 683–689.

29 F. Cozzi, R. Annunziata, M. Benaglia, M. Cinquini, L. Raimondi, K. K. Baldridge and J. S. Siegel, *Org. Biomol. Chem.*, 2003, **1**, 157–162.

30 C. Janiak, *J. Chem. Soc. Dalt. Trans.*, 2000, 3885–3896.

31 C. A. Hunter, K. R. Lawson, J. Perkins and C. J. Urch, *J. Chem. Soc. Perkin Trans. 2*, 2001, **2**, 651–669.

32 F. London, *Trans. Faraday Soc.*, 1937, **33**, 8b – 26.

33 A. Stone, *The Theory of Intermolecular Forces*, OUP Oxford, Oxford, 2013.

34 G. R. Desiraju, *Crystal engineering: the design of organic solids*, Elsevier, Amsterdam, 1989.

35 R. Pepinsky, *Phys. Rev.*, 1955, **100**, 971–971.

36 G. M. J. Schmidt, *Pure Appl. Chem.*, 1971, **27**, 647–678.

37 G. R. Desiraju, *Angew. Chem., Int. Ed.*, 1995, **34**, 2311–2327.

38 O. M. Yaghi, M. O'Keeffe, N. W. Ockwig, H. K. Chae, M. Eddaoudi and J. Kim, *Nature*, 2003, **423**, 705–714.

39 E. J. Corey, *Chem. Soc. Rev.*, 1988, **17**, 111–133.

40 M. Eddaoudi, D. B. Moler, H. Li, B. Chen, T. M. Reineke, M. O'Keeffe and O. M. Yaghi, *Acc. Chem. Res.*, 2001, **34**, 319–330.

41 W. Lu, Z. Wei, Z.-Y. Gu, T.-F. Liu, J. Park, J. Park, J. Tian, M. Zhang, Q. Zhang, T. Gentle III, M. Bosch and H.-C. Zhou, *Chem. Soc. Rev.*, 2014, **43**, 5561–5593.

42 L. G. Donaruma, B. P. Block, K. L. Loening, N. Platé, T. Tsuruta, K. C. Buschbeck, W. H. Powell and J. Reedijk, *Pure Appl. Chem.*, 1985, **57**, 149–168.

43 S. R. Batten, N. R. Champness, X. Chen, J. Garcia-Martinez, S. Kitagawa, L. Ohrstrom, M. O'Keeffe, M. Paik Suh and J. Reedijk, *CrystEngComm*, 2012, **14**, 3001–3004.

44 W. Mori, H. Hoshino, Y. Nishimoto and S. Takamizawa, *Chem. Lett.*, 1999, **28**, 331–332.

45 S. Takamizawa, E. I. Nakata and H. Yokoyama, *Inorg. Chem. Commun.*, 2003, **6**, 763–765.

46 K. Takahashi, N. Hoshino, T. Takeda, S. I. Noro, T. Nakamura, S. Takeda and T. Akutagawa, *Inorg. Chem.*, 2015, **54**, 9423–9431.

47 A. Kitaigorodsky, *Molecular crystals and Molecules*, Academic Press, New York, 1973.

48 G. R. Desiraju, J. J. Vittal and A. Ramanan, *Crystal Engineering: A Textbook*, World Scientific, Singapore, 2011.

49 J.-P. Zhang, X.-C. Huang and X.-M. Chen, *Chem. Soc. Rev.*, 2009, **38**, 2385–2396.

50 S. A. Bourne, in *Supramolecular Chemistry: From Molecules to Nanomaterials*, eds. P. Gale and J. Steed, John Wiley & Sons, Ltd., Hoboken, 2012.

51 J. Bernstein, *Polymorphism in Molecular Crystals*, Clarendon Press, Oxford, 2002.

52 J. Bernstein, R. J. Davey and J. O. Henck, *Angew. Chem., Int. Ed.*, 1999, **38**, 3440–3461.

53 D. Braga and F. Grepioni, *Chem. Soc. Rev.*, 2000, **29**, 229–238.

54 A. Grunenberg, O. Henck and W. Siesler, *Int. J. Pharm.*, 1996, **129**, 147–158.

55 J. D. Dunitz, *Pure Appl. Chem.*, 1991, **63**, 177–185.

56 J. D. Dunitz, *Acta Crystallogr. Sect. B*, 1995, **51**, 619–631.

57 J. Chen, L. Hu, J. Deng and X. Xing, *Chem. Soc. Rev.*, 2015, **44**, 3522–3567.

58 C. P. Romao, *Phys. Rev. B*, 2017, **96**, 1–8.

59 M. J. Cliffe and A. L. Goodwin, *J. Appl. Crystallogr.*, 2012, **45**, 1321–1329.

60 J. F. Nye, *Physical Properties of Crystals: Their Representation by Tensors and Matrices*, Clarendon Press, Oxford, 1958.

61 E. Mitscherlich, *Ann. Chim. Phys.*, 1822, **19**, 350–419.

62 International Union of Crystallography, Isomorphous Crystals, http://reference.iucr.org/dictionary/Isomorphous_crystals, (accessed 30 April 2018).

63 International Union of Crystallography, Isostructural Crystals, http://reference.iucr.org/dictionary/Isostructural_crystals, (accessed 30 April 2018).

64 L. J. Barbour, D. Das, T. Jacobs, G. O. Lloyd and V. J. Smith, in *Supramolecular Chemistry: From Molecules to Nanomaterials*, eds. P. A. Gale and J. W. Steed, John Wiley & Sons, Ltd., Hoboken, 2012.

65 C. R. R. Adolf, S. Ferlay and M. W. Hosseini, *CrystEngComm*, 2018, **20**, 2233–2236.

66 L. R. Nassimbeni, *Acc. Chem. Res.*, 2003, **36**, 631–637.

67 D. S. Sholl and R. P. Lively, *Nature*, 2016, **532**, 435–437.

68 L. J. Barbour, *Chem. Commun.*, 2006, 1163.

69 S. Kitagawa, R. Kitaura and S. I. Noro, *Angew. Chem., Int. Ed.*, 2004, **43**, 2334–2375.

70 K. S. W. Sing, *Pure Appl. Chem.*, 1985, **57**, 603–619.

71 A. S. Bale, C. A. Meacham, V. A. Benignus, P. J. Bushnell and T. J. Shafer, *Toxicol. Appl. Pharmacol.*, 2005, **205**, 77–88.

72 M. L. Boeglin, D. Wessels and D. Henshel, *Environ. Res.*, 2006, **100**, 242–254.

73 M. Nagarathinam and J. J. Vittal, *Angew. Chem., Int. Ed.*, 2006, **45**, 4337–4341.

74 B. Dutta, C. Sinha and M. H. Mir, *Chem. Commun.*, 2019, **55**, 11049–11051.

Chapter 2 – Experimental Techniques

"If I want to deprive you of your watch, I shall certainly have to fight for it; if I want to buy your watch, I shall have to pay for it; and if I want a gift, I shall have to plead for it; and, according to the means I employ, the watch is stolen property, my own property, or a donation. Thus we see three different results from three different means. Will you still say that the means do not matter?"

— Mahatma Gandhi, *Non-Violent Resistance*

This chapter describes all analytical techniques, instrumentation and computer software utilised during the course of this work. Brief descriptions are given for routine techniques, with more detailed descriptions of specialised or adapted techniques.

2.1. Single Crystal X-Ray Diffraction (SCXRD)

Crystals of appropriate size and morphology, and the ability to extinguish plane-polarised light were attached to the tip of a MiTeGen mount[1] using Paratone®N oil. The crystal mount was then attached to a goniometer head, which was in turn mounted on a diffractometer. X-ray intensity data were recorded using either a Bruker APEX II DUO or a Bruker D8 Venture diffractometer. The DUO instrument is equipped with Incoatec IμS molybdenum (λ = 0.71073 Å) and copper (λ = 1.5418 Å) microfocus X-ray sources and a CCD area detector. The Venture instrument is equipped with an Incoatec IμS 3.0 molybdenum (λ = 0.71073 Å) microfocus X-ray source and a Photon II CPAD detector. Each diffractometers is equipped with an Oxford Cryosystems cryostat (700 Series Cryostream Plus for the DUO instrument and 800 Series Cryostream Plus for the Venture instrument), which is used to control the sample temperature. Both the frame exposure time and the number of frames recorded for each experiment were varied, depending on the diffraction quality and characteristics of the crystal.

Data reduction and absorption corrections were carried out using the SAINT[2] and SADABS[3] programs, respectively. The unit-cell dimensions were refined on all data and space groups were assigned based on systematic absences and intensity statistics. The structures were solved with a dual-space algorithm or direct methods using SHELXT[4] or SHELXS-2016/1,[5] respectively. Structure refinement was carried out with SHELXL-2018/1[5] using the X-Seed[6,7] graphical user interface. Non-hydrogen atoms were refined anisotropically. Hydrogen atoms not belonging to water molecules were placed in calculated positions. In the case of water

molecules, where possible, these atoms were identified in the difference electron density maps and refined with an O–H bond-length restraint of 0.86(2) Å (based on a survey of the Cambridge Structural Database (CSD)).[8] Illustrations of all crystal structures were generated using the program POV-Ray.[9]

2.2. Powder X-Ray Diffraction (PXRD)

Diffractograms were collected with a Bruker D2 Phaser benchtop diffractometer. The diffractometer utilises Bragg-Brentano geometry and Cu Kα radiation (λ = 1.5418 Å) as the incident beam, captured by a LYNXEYE 1D detector. The diffractometer was operated at 30 kV and 10 mA. Intensity data were recorded using a rotating flat stage (30° min^{-1}). Where necessary samples were finely ground using a mortar and pestle, loaded onto a zero-background sample holder and levelled with a glass slide. The diffractograms were recorded under ambient conditions with a scanning range of 5–35° (or 5–40°), a step size of 0.018° and a 0.5 second scan speed.

2.3. Thermogravimetric Analysis (TGA)

Each thermogram was recorded by measuring the percentage mass (starting at 100%) as a function of temperature. A TA Instruments Q500 thermogravimetric analyser was used and sample weights typically ranged from 2-8 mg (placed in an aluminium crucible). A N_2 gas flow rate of 50 ml min^{-1} was used to purge the furnace. The temperature was ramped from ambient temperature (*ca* 25 °C) to *ca* 600 °C at a constant heating rate of 10 °C min^{-1}. The Universal Analysis 2000 software (TA Instruments) was used to analyse the thermograms.

2.4. Differential Scanning Calorimetry (DSC)

Differential scanning calorimetry (DSC) measures the change in heat flow of a sample over a temperature gradient, indicating were energetic events such as phase changes occur. Low temperature (to -173 °C) DSC thermograms were generated using a TA Instruments Q100 instrument equipped with a Liquid Nitrogen Cooling System (LNCS). For experiments only reaching -80 °C a TA Instruments Q20 was employed. The sample (2-5 mg) was placed in a non-hermetically sealed aluminium pan and the change in heat flow of the sample was recorded as a function of temperature (an empty, non-hermetically sealed pan was used as reference). Energetic events are recorded as either an endothermic or exothermic peak relative to temperature. The temperature was ramped from room temperature (*ca* 25 °C) to

100 K (*ca* -173 °C) and back at a rate of 5–10 °C min^{-1} depending on the sample. Dry N_2 gas was used to purge the furnace at a flow rate of 50 ml min^{-1}. Universal Analysis 2000 software (TA Instruments) was used to analyse the data.

2.5. Infrared Spectroscopy (IR)

IR absorption spectra were recorded using a Bruker Alpha P ATR-IR instrument. A background measurement was performed before each experimental spectrum was recorded.

2.6. Supercritical Drying

Supercritical drying is a technique most commonly known for its use in the preparation of aerogels,[10–12] but has recently been applied to the activation of various coordination compounds. For the activation of coordination compounds the supercritical medium is almost always carbon dioxide (CO_2). Activation of coordination compounds with the aid of supercritical CO_2 ($scCO_2$) is carried out by exposing the sample to liquid CO_2 at high pressure (*i.e.* >74 bar).[13] This allows for the liquid CO_2 to exchange with the current guest.[13] The sample containing the $scCO_2$ (still at high pressure) is then heated to above the supercritical temperature of CO_2 (*i.e.* >31 °C).[13] The $scCO_2$ is then slowly vented. This then allows the CO_2 to escape the host framework leaving it, ideally, unperturbed and guest free.[13] Consequently, $scCO_2$ activation (or supercritical drying) represents a gentler approach to conventional thermal activation methods, which may not always result in an activated species of single-crystal quality (due to partial activation or channel/pore collapse).[14,15] In some cases supercritical drying may result in a different, more porous, apohost form than thermal activation methods.[14] The greatest advantage of using supercritical drying is that the process circumvents liquid-to-gas phase guest extraction (by progressing directly to the gas phase from the supercritical phase), thus removing the impact of capillary forces and diminishing particle-to-particle aggregation.[13,14]

Supercritical drying was carried out using a Tousimis™ Samdri® PVT-30 critical point dryer. Each sample (contained in a sheared glass vial) was placed in the steel pressure chamber of the dryer, which was then sealed, filled with liquid CO_2, and warmed to 40 °C. At this point the chamber pressure is *ca* 100 bar. The chamber contents were kept above the critical point for *ca* 6 hours, after which the chamber was slowly vented.

2.7. Vapour Sorption

A modified version of the vapour balance setup reported by Barbour and co-workers[16] was used to carry out vapour sorption experiments (Figure 2.1.). The system provides an accurate measure of the change in sample mass as a function of time. A wooden cabinet encloses the system to aid temperature regulation using a temperature controller, two Edison light bulbs and a fan. The sample is placed in a steel mesh basket and suspended by a thin steel wire from the microelectronic balance, with a counterweight suspended at the adjacent end. A vacuum pump is used to evacuate the sample chamber (0.1 mbar). This reduced pressure environment allows both for the preparation of the sample vapour along with the evacuation of the apparatus and sample after an experiment is complete. Typically sample sizes range from 15–30 mg, and the temperature is maintained at 23 °C. After introduction of the sample vapour to the system the experiment is allowed to run until the sample mass reaches a plateau (indicating an equilibrium state). When required, the desorption profile can also be recorded by applying vacuum to a sorbed system at equilibrium. The sample mass is recorded until an equilibrium state is reached. For each experiment a plot of sample mass *versus* time is recorded.

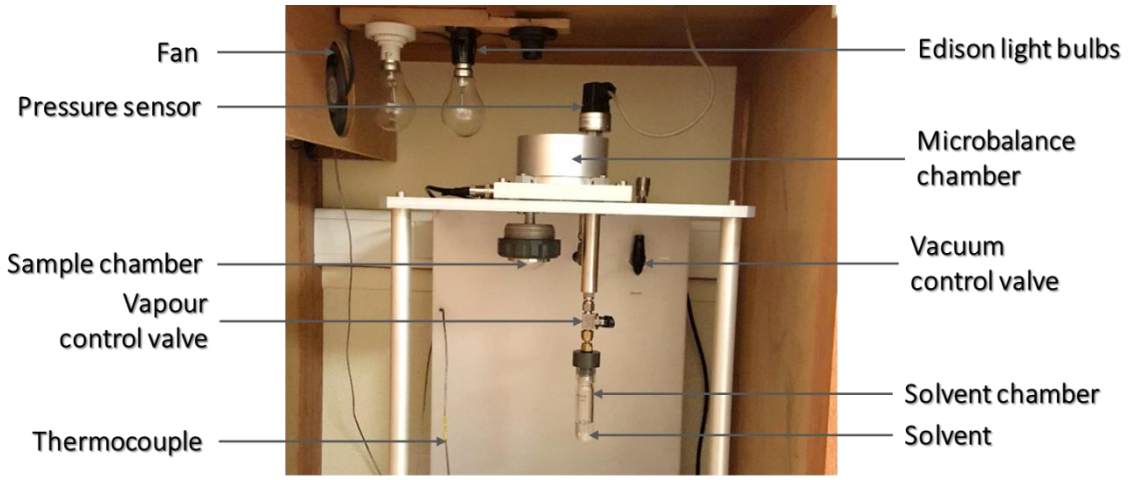

Figure 2.1. The vapour balance.

2.8. Principal Axis Strain Calculations

The web-based tool PASCal[17] (Principal Axis Strain Calculator, http://pascal.chem.ox.ac.uk) was used to determine a set of principal axes and calculates the linear and volumetric coefficients of thermal expansion. The thermal expansion coefficients were calculated from

the lattice parameters obtained from variable temperature single-crystal X-ray diffraction data.

2.9. Software Packages

Essential software packages employed throughout the course of this work are described below.

2.9.1. The Cambridge Structural Database (CSD)

The CSD[8] is a digital repository containing crystal structures (determined from both single crystal and powder diffraction data) for compounds that have been determined using X-ray or neutron diffraction studies and deposited as published or unpublished results. Therefore, the CSD represents a comprehensive database of known crystal structures and their associated literature.

2.9.2. Mercury

Mercury,[18–20] part of the CSD software package, can be used for structure exploration and visualisation. The program offers - amongst other features - powder diffractogram simulation, multiple structure overlay, probe-accessible volume[21] calculation and visualisation, in addition to morphology calculations.

2.9.3. Platon/SQUEEZE

Platon[22]/SQUEEZE[23,24] calculates the number of unmodelled electrons within the solvent-accessible space of a crystal structure. Additionally, the program is able to determine the volume of the solvent-accessible space *per* unit cell (*P*1 symmetry applied, probe radius 1.2 Å, grid spacing 0.2 Å). The electron count allows the user to calculate the approximate number of unmodelled guest molecules trapped in a host. For accurate results, high-quality high-completeness data with high and low-angle reflections are required (*i.e.,* the structural model should be as complete as possible).[24] Furthermore, disorder in the host and/or the guest molecules may affect the results. Finally, output accuracy decreases when solvent accessible voids comprise a large percentage of the unit-cell volume.[24]

References

1 MiTeGen, MiTeGen, https://www.mitegen.com/, (accessed 25 June 2018).

2 Bruker AXS Inc., 2016.

3 Bruker AXS Inc., 2016.

4 G. M. Sheldrick, *Acta Cryst.*, 2015, **A71**, 3–8.

5 G. M. Sheldrick, *Acta Cryst.*, 2015, **C71**, 3–8.

6 L. J. Barbour, *J. Supramol. Chem.*, 2001, **1**, 189–191.

7 L. J. Barbour, *J. Appl. Cryst.*, 2020, **53**, 1–6.

8 C. R. Groom, I. J. Bruno, M. P. Lightfoot and S. C. Ward, *Acta Crystallogr.*, 2016, **B72**, 171–179.

9 Persistence of Vision Raytracer Pty. Ltd., 2004.

10 P. H. Tewari, A. J. Hunt and K. D. Lofftus, *Mater. Lett.*, 1985, **3**, 363–367.

11 A. F. Bedilo and K. J. Klabunde, *Nanostructured Mater.*, 1997, **8**, 119–135.

12 D. J. Suh, T. J. Park, H. Y. Han and J. C. Lim, *Chem. Mater.*, 2002, **14**, 1452–1454.

13 J. E. Mondloch, O. Karagiaridi, O. K. Farha and J. T. Hupp, *CrystEngComm*, 2013, **15**, 9258–9264.

14 A. P. Nelson, O. K. Farha, K. L. Mulfort and J. T. Hupp, *J. Am. Chem. Soc.*, 2009, **131**, 458–460.

15 O. K. Farha and J. T. Hupp, *Acc. Chem. Res.*, 2010, **43**, 1166–1175.

16 L. J. Barbour, K. Achleitner and J. R. Greene, *Thermochim. Acta*, 1992, **5**, 171–177.

17 M. J. Cliffe and A. L. Goodwin, *J. Appl. Crystallogr.*, 2012, **45**, 1321–1329.

18 C. F. Macrae, P. R. Edgington, P. McCabe, E. Pidcock, G. P. Shields, R. Taylor, M. Towler and J. Van De Streek, *J. Appl. Crystallogr.*, 2006, **39**, 453–457.

19 C. F. Macrae, I. J. Bruno, J. A. Chisholm, P. R. Edgington, P. McCabe, E. Pidcock, L. Rodriguez-Monge, R. Taylor, J. Van De Streek and P. A. Wood, *J. Appl. Crystallogr.*, 2008, **41**, 466–470.

20 C. F. MacRae, I. Sovago, S. J. Cottrell, P. T. A. Galek, P. McCabe, E. Pidcock, M. Platings, G. P. Shields, J. S. Stevens, M. Towler and P. A. Wood, *J. Appl. Crystallogr.*, 2020, **53**, 226–235.

21 D. P. van Heerden and L. J. Barbour, *Chem. Soc. Rev.*, 2021, **50**, 735–749.

22 A. L. Spek, *Acta Crystallogr.*, 2009, **D65**, 148–155.

23 P. van der Sluis and A. L. Spek, *Acta Crystallogr.*, 1990, **A46**, 194–201.

24 A. L. Spek, *Acta Crystallogr.*, 2015, **C71**, 9–18.

Chapter 3 – Mechanochemical Control of Solvent Content in a 1D Coordination Polymer

"The most exciting phrase to hear in science, the one that heralds new discoveries, is not 'Eureka!' but 'That's funny…'" — Isaac Asimov

3.1. Article in *Journal of Coordination Chemistry*

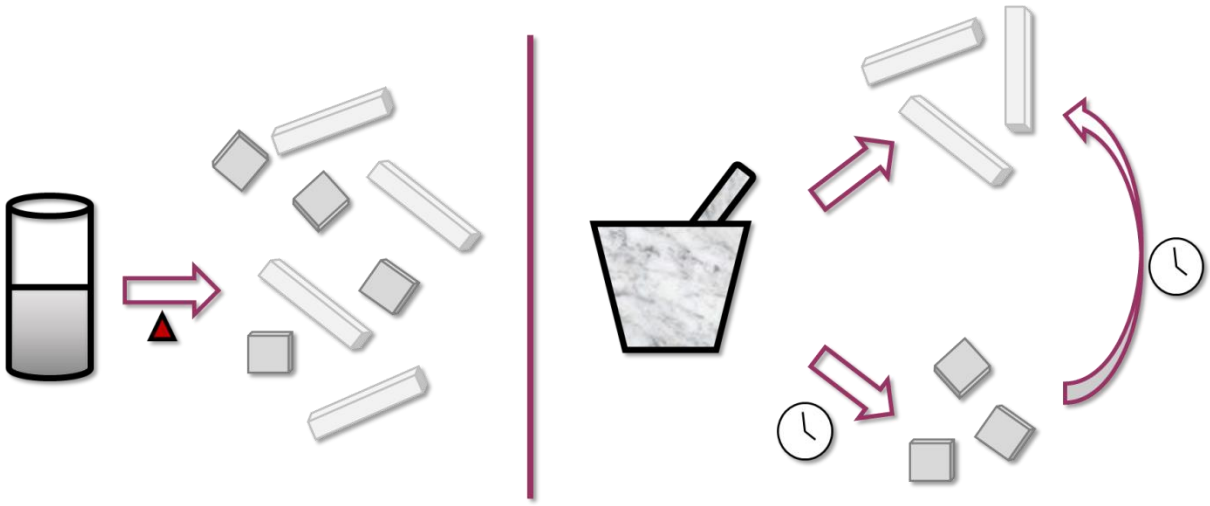

3.1.1. Contributions by author

- Design of the project
- Preparation and handling of crystals
- Collection of single-crystal X-ray diffraction data
- Structure solution and refinement
- Modelling of disorder
- Recording TGA and DSC thermograms
- Execution of mechanochemical experiments
- Collection of powder X-ray diffraction data
- Interpretation of powder X-ray diffraction results with Dr Leigh Loots
- Writing of the first draft of the article

JOURNAL OF COORDINATION CHEMISTRY
https://doi.org/10.1080/00958972.2021.1877688

Taylor & Francis
Taylor & Francis Group

Check for updates

Mechanochemical control of solvent content in a 1D coordination polymer

Lisa M. Van Wyk, Leigh Loots and Leonard J. Barbour

Department of Chemistry and Polymer Science, University of Stellenbosch, Matieland, South Africa

ABSTRACT

This study illustrates mechanochemical control over the formation of three coordination polymer solvates. Variation in the onset of grinding, aging after grinding and solvent water content leads to selective preparation of two solvates, which crystallize concomitantly when prepared solvothermally in DMF. A third solvate may be prepared with DMA. Finally, solvent exchange provides means of interconverting between the three solvates.

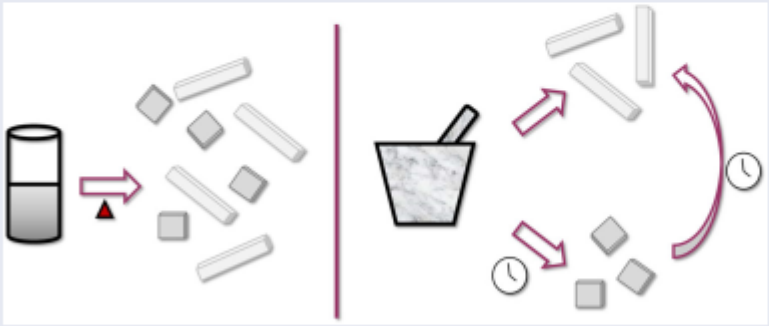

ARTICLE HISTORY
Received 3 December 2020
Accepted 7 January 2021

KEYWORDS
Coordination polymer; mechanochemistry; slurry grinding; aging; solvate

1. Introduction

Understanding the relationship between solid-state structure and the physicochemical properties of a material remains an active area of interest in crystal research [1]. This is particularly true for the well-known metal-organic frameworks (MOFs), a class of 3D polymeric metal-organic compounds that are generally understood to be porous [2] and have numerous potential applications, including sensing [3, 4], catalysis [5–7], separation [8, 9] and storage [10–12] of small guest molecules. MOF crystal structures comprise upwards of 8% Cambridge Structural Database (CSD) [1]. Coordination polymers (CPs), another subset of metal-organic materials, are compounds that propagate infinitely in one or two dimensions [2]. Although less thoroughly investigated for their

CONTACT Leonard J. Barbour ljb@sun.ac.za Department of Chemistry and Polymer Science, University of Stellenbosch, 7602 Matieland, South Africa.

Supplemental data for this article is available online at https://doi.org/10.1080/00958972.2021.1877688.

properties than MOFs, CPs often exhibit interesting structure-property relationships [13–16] as a result of the inherent flexibility due to their lower dimensionality [17].

Structural flexibility in crystals is difficult to characterize because large internal changes generally cause the crystals to disintegrate, thus precluding their analysis by single-crystal X-ray diffraction (SCXRD). Moreover, the potential for structural variety in combinations of CP components often results in formation of mixed phases consisting of polymorphs, structural isomers, homeotypes, solvates, *etc.* Phase purity is required for any credible investigation of the bulk properties of a material, while single crystals are required to elucidate the structural basis of these properties.

Although mechanochemical methods are more commonly employed to isolate polymorphs of molecular crystals (i.e. pharmaceuticals and co-crystals) [18–20], recent success with metal-organic materials has also been reported [20–22]. Mechanochemistry can be divided into three sub-categories, depending on the amount of solvent employed during the grinding or milling process. These are neat grinding, liquid-assisted grinding (LAG) and slurry grinding [23]. The η parameter (expressed in µL mg^{-1}) represents an empirical scale that is employed to differentiate mechanochemical techniques from one another (and from solution chemistry) [23]. Neat grinding requires $\eta = 0$ µL mg^{-1}, LAG $\eta = 0 < 2$ µL mg^{-1} and slurry grinding $\eta = 2 < 12$ µL mg^{-1} [23]. Therefore, apart from the potential for facilitating unique chemistry, mechanochemistry presents a more environmentally friendly way of approaching crystallization, owing to the significant reduction in solvent use [22].

2. Experimental

2.1. Materials

Unless otherwise indicated, all reagents were obtained from commercial suppliers (Sigma-Aldrich, Alfa Aesar, Merck) and were used without purification.

2.2. Solvothermal crystallization

Three solvates of [Zn(ndc)(bpy)] (**1**) were prepared solvothermally (80 °C) from a solution of $Zn(NO_3)_2{\cdot}6H_2O$, 2,6-naphthalenedicarboxylic acid (ndc) and 2,2′-bipyridine (bpy) in either *N,N*-dimethylformamide (DMF) or *N,N*-dimethylacetamide (DMA). The solvates have the general formulas $\{[Zn(ndc)(bpy)]{\cdot}DMF{\cdot}H_2O\}_n$ (**1a**), $\{[Zn(ndc)(bpy)]{\cdot}2DMF\}_n$ (**1b**) and $\{[Zn(ndc)(bpy)]{\cdot}2DMA{\cdot}0.5H_2O\}_n$ (**1c**).

2.2.1. Crystallization of 1a and 1b

$\{[Zn(ndc)(bpy)]{\cdot}DMF{\cdot}H_2O\}_n$ (**1a**) and $\{[Zn(ndc)(bpy)]{\cdot}2DMF\}_n$ (**1b**) were prepared solvothermally. In a scintillation vial, equimolar amounts of the ligands 2,6-naphthalenedicarboxylic acid (ndc, 0.10 mmol, 21.6 mg) and 2,2′-bipyridine (bpy, 0.10 mmol, 15.6 mg) along with $Zn(NO_3)_2{\cdot}6H_2O$ (0.15 mmol, 44.8 mg) were added to 3 ml *N,N*-dimethylformamide (DMF) and sonicated until partially dissolved. The vial was placed in an 80 °C preheated oven for approximately 3 days. Clear blocks (**1a**) and rods (**1b**) formed in approximately equal yield (determined by visual inspection, Figure S1). Single-crystal X-ray diffraction showed that the different morphologies belonged to individual concomitant solvates (Table S1).

2.2.2. Crystallization of 1b with dry DMF

Single crystals of **1b** were prepared similarly to the procedure in Sect. 2.2.1. However, the DMF utilized was first dried on molecular sieve for several days. Clear rods of various sizes were produced in a quantitative yield (Figure S2).

2.2.3. Crystallization of 1a and 1b with H_2O/DMF

Single crystals of **1a** and **1b** were prepared similarly to the procedure in Sect. 2.2.1, except five drops of water were added to the crystallization mixture. It was found that after relatively short periods of time (16 h) some crystals of **1b** had already formed. All crystallizations produced a mixture of clear blocks (**1a**) and rods (**1b**) (determined by visual inspection, Figure S3).

2.2.4. Crystallization of 1c

$\{[Zn(ndc)(bpy)]\cdot 2DMA\cdot 0.5H_2O\}_n$ (**1c**) was prepared solvothermally. The crystallization procedure was the same as in Sect. 2.2.1, except *N,N*-dimethylacetamide (DMA) was substituted for DMF. The crystallization produced clear blocks (and some needles) in a quantitative yield (Figure S4). Single crystal and powder X-ray diffraction (Figure S13) showed both morphologies to belong to the same material (**1c**).

2.2.5. Crystallization of 1c from dry DMA

To investigate if another solvate could be produced with DMA (without water as a secondary guest), a similar crystallization to that in Sect. 2.2.4. was carried out. However, the DMA used was first dried on molecular sieve for several days. The crystallization produced a low yield of small clear blocks (Figure S5). These were **1c**, as determined by SCXRD and PXRD (Table S1 and Figure S13). Small amounts of water from the metal salt hydrate or solvent (Figure S42) likely provide the water for the crystallization (resulting in the low yield).

2.3. Single-crystal X-ray diffraction

X-ray intensity data were recorded on a Bruker APEX II DUO or a Bruker D8 Venture diffractometer. The APEX II DUO is equipped with an Incoatec IμS molybdenum ($\lambda = 0.71073$ Å) microfocus X-ray source and a CCD area detector. The D8 Venture is equipped with an Incoatec IμS 3.0 molybdenum ($\lambda = 0.71073$ Å) microfocus X-ray source and a Photon II CPAD detector. The diffractometers are equipped with Oxford Cryosystems cryostats (Cryostream 700 Plus and Cryostream 800 Plus, respectively). Data reduction and absorption corrections were carried out using SAINT [24] and SADABS [25], respectively. The unit-cell dimensions were refined on all data and space groups were assigned based on systematic absences and intensity statistics. The structures were solved using a dual-space algorithm employed by SHELXT [26]. Structure refinement was carried out with SHELXL-2018/3 [27] using the X-Seed [28, 29] graphical user interface. Non-hydrogen atoms were refined anisotropically. Hydrogens not

belonging to water molecules were placed in calculated positions. In the case of water molecules, where possible, these atoms were identified in difference electron density maps and refined with O–H bond-length restraints of 0.86(2) Å (based on a survey of the CSD) [30]. Illustrations of all crystal structures were generated using the program POV-Ray [31].

CCDC 2046348–2046351 contain the supplementary crystallographic data for this paper. These data can be obtained free of charge via www.ccdc.cam.ac.uk/data_request/cif, or by emailing data_request@ccdc.cam.ac.uk, or by contacting The Cambridge Crystallographic Data Centre, 12 Union Road, Cambridge CB2 1EZ, UK; Fax: +44 1223 336033.

2.4. Powder X-ray diffraction (PXRD)

A Bruker D2 Phaser powder diffractometer was used to record experimental diffractograms. The diffractometer utilizes Bragg-Brentano geometry and Cu Kα radiation ($\lambda = 1.5418$ Å) as the incident beam. The diffractometer was operated at 30 kV and 10 mA. Samples were placed on a rotating (30° min^{-1}) flat stage and intensity data were recorded using a Lynxeye detector. Samples were finely ground (where necessary) using a mortar and pestle, loaded onto a zero-background sample holder and leveled with a glass slide (where possible). Diffractograms were recorded under ambient conditions using a scanning range of 5°–35°, a step size of 0.016° and a scan speed of 0.8 s *per* step.

3. Results and discussion

Herein we describe a study of three isoskeletal [32, 33] solvates of **1**, and the selective preparation of each. The forms **1a** and **1b** crystallize concomitantly when prepared solvothermally in DMF, while **1c** can be prepared using DMA. Form **1a** is a hydrate of another analogue that has been reported previously [34], but we note that the reported analogue was not encountered during this study.

All of the materials considered in this study crystallize in the monoclinic crystal system (**1a** *C*2/*c*, **1b** $P2_1/n$ and **1c** $P2_1/c$, Tables 1 and S1). They all exhibit analogous packing motifs comprising infinite 1D "zig-zag" strands (Figure S6) that form hourglass-shaped guest-accessible channels (Figure 1). These channels comprise *ca.* 39–44% of the total volume (probe-accessible volume [35]). Adjacent 1D strands are interdigitated and associate by means of offset $\pi\cdots\pi$ interactions between their bpy moieties.

Although all three materials pack similarly, subtle differences exist as a result of variation of the angles in the Zn coordination environment (Figure 2). The CPs **1a** and **1c** have very similar coordination geometries and disorder of the bpy moiety. This is most likely due to the presence of guest water molecules in both forms, which direct the packing arrangement. In **1b** the ndc moieties are disordered, but not the bpy moieties.

To study the effect on the outcome of solvothermal crystallization, we varied the temperature, duration and solvent composition. Fortunately, the crystal morphologies

Table 1. Crystallographic parameters for the materials studied.

	1a	1b	1c	1c (dry DMA)
Empirical formula	$C_{50}H_{46}N_6O_{12}Zn_2$[a]	$C_{56}H_{56}N_8O_{12}Zn_2$	$C_{30}H_{33}N_4O_{6.5}Zn$	$C_{30}H_{33}N_4O_{6.5}Zn$
Formula weight (g mol^{-1})	1053.66[a]	1163.82	619.00	619.00
Temperature (K)	100(2)	100(2)	100(2)	100(2)
Crystal system	Monoclinic	Monoclinic	Monoclinic	Monoclinic
Space group	*C2/c*	$P2_1/n$	$P2_1/c$	$P2_1/c$
a (Å)	14.581(4)	8.280(1)	7.549(1)	7.546(1)
b (Å)	27.777(8)	24.572(2)	27.766(1)	27.787(1)
c (Å)	7.794(2)	27.308(3)	13.850(1)	13.794(1)
α (°)	90	90	90	90
β (°)	118.051(3)	95.442(2)	90.666(2)	90.630(3)
γ (°)	90	90	90	90
V (Å^3)	2786.0(14)	5530.9(9)	2902.66(18)	2891.9(3)
Z	2	4	4	4
Calculated density (g cm^{-3})	1.251	1.398	1.413	1.420
Absorption coefficient (mm^{-1})	0.921	0.936	0.897	0.901
Reflections collected	16,434	68,676	48,535	50,267
Independent reflections	2487	9774	7197	5086
Data/restraints/parameters	2487/526/267	9774/2272/1038	7197/1053/503	5086/1151/503
Goodness-of-fit on F^2	1.042	1.098	1.140	1.243
Final *R* indices [$I > 2\sigma(I)$]	$R1 = 0.0777$ $wR2 = 0.2178$	$R1 = 0.0613$ $wR2 = 0.1404$	$R1 = 0.0875$ $wR2 = 0.2031$	$R1 = 0.1209$ $wR2 = 0.2483$
Largest diff. peak and hole (e Å^{-3})	1.054, −0.378	1.053, −0.507	1.576, −0.926	1.093, −0.877

[a]These values differ from those reported in the CIF owing to the unmodelled hydrogen atoms on water molecules.

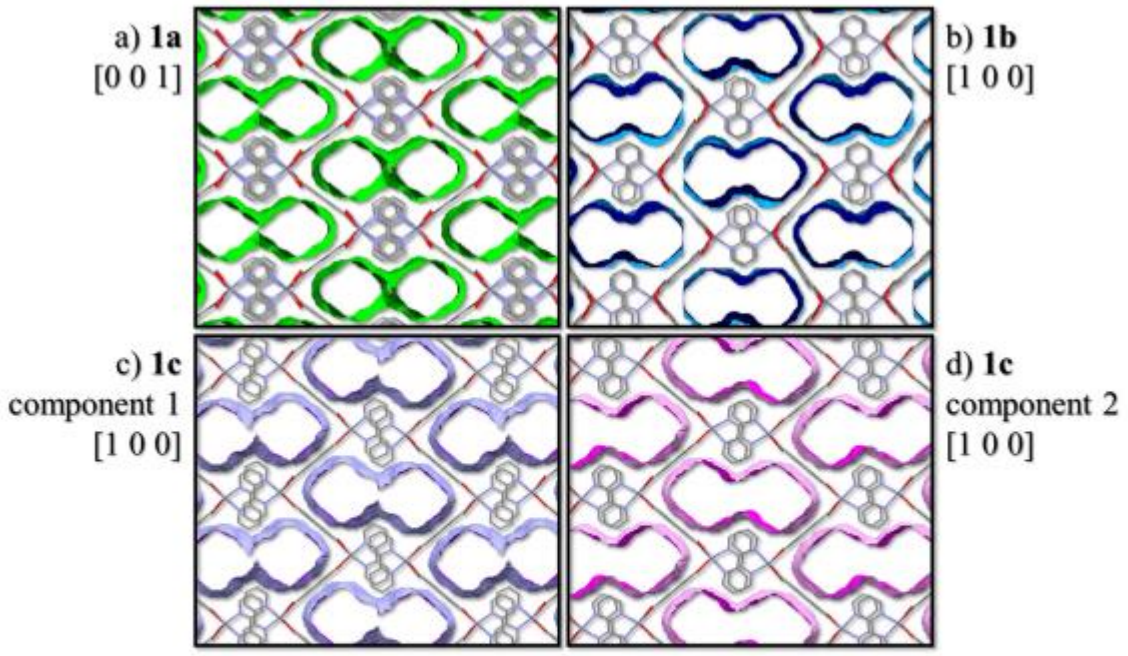

Figure 1. Probe-accessible volumes [35] (probe radius 1.5 Å, grid spacing 0.2 Å) of (a) 1a, (b) 1b, and (c) and (d) 1c viewed down the 1D channels of each material. In (a) both the components of the bpy disorder in 1a are shown as they are symmetry related. In (c) and (d) each component of the bpy disorder in 1c is shown separately as each component generates a slightly different shaped channel. The probe-accessible volumes comprise ca. 39, 38 and 44% of the unit-cell volumes of 1a, 1b and 1c, respectively. In all cases guest molecules and hydrogen atoms have been omitted for clarity.

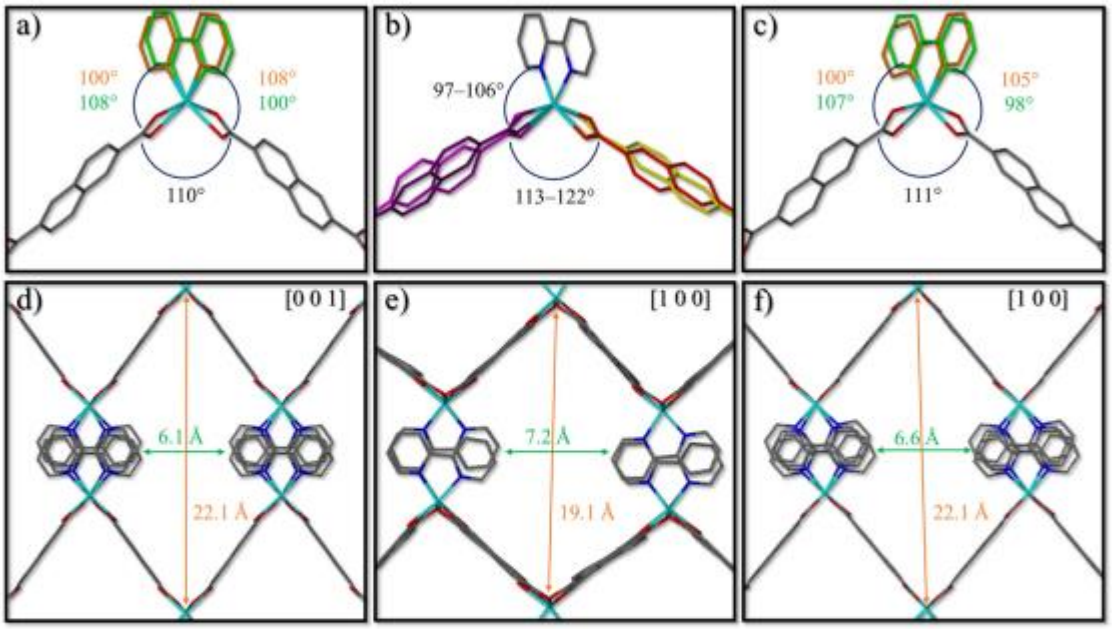

Figure 2. Comparison of the differences between the materials studied. The top row shows the coordination environments and the associated angles for (a) 1a, (b) 1b and (c) 1c. In (b) the angles are shown as ranges, owing to the various combinations possible as a result of disorder within the material. The bottom row shows the approximate atom-to-atom aperture dimensions of (d) 1a, (e) 1b and (f) 1c. In (a), (b) and (c) disorder is highlighted in non-CPK colors. The minor component of the disorder of the carboxylate moiety in 1a is omitted in (a) and (d) for clarity. Similarly, in all representations guest molecules and hydrogen atoms have been omitted for clarity.

of **1a** and **1b** are distinct, crystallizing as blocks and rods, respectively. This allows qualitative judgement of the composition of crystallizations based on visual inspection of crystal morphology. Variation of the temperature (between 80 and 150 °C) resulted in only slight changes in the relative amounts of **1a** and **1b**; the proportion of **1b** appears to increase with temperature. Similarly, increasing the duration of the heating step (between 16 hours and 5 days) appears to increase the ratio of **1b** slightly.

As expected, crystallizations carried out with DMF dried over molecular sieve for several days resulted in the exclusive formation of **1b** (Figures S2 and S11). Adding several drops of water resulted in the formation of a mixture of **1a** and **1b** (Figures S3 and S11). The addition of even more water (approximately 50:50 DMF:H_2O by volume) yielded a polycrystalline material of unknown structure (its diffractogram does not match that of **1a**, **1b** or **1c**, Figure S12). Therefore, using the solvothermal approach, we could obtain either phase-pure **1b** or a mixture of **1a** and **1b**, but not phase-pure **1a**.

When prepared solvothermally, form **1c** includes both DMA and water molecules and is phase pure. We attempted to form a solvate of only DMA (analogous to **1b**) by employing DMA dried over molecular sieve for several days. This resulted in a low yield of **1c** (Figures S5 and S13); the water molecules are likely derived from the metal salt hydrate (Figure S42).

Owing to limited success in controlling the outcome of the DMF system by varying the solvothermal parameters, we investigated mechanochemistry as an alternative

Table 2. Summary of the mechanochemical experiments carried out in this study (grinding period of 5 min).

Solvent/Method		Species formed
Slurry (*ca* 5 drops of solvent mixture $\eta \approx 9$ µl mg^{-1})	DMF (as received)	**1b**
	DMA (as received)	**1c**
	DMF (as received, aged 20 min prior to grinding)	**1a**
	DMF (as received, aged 20 min prior to grinding, after 2 days in fresh as received DMF)	**1b**
	H_2O/DMF (1:6 V:V)	**1a**
	H_2O/DMF (1:6 V:V) after 2 days in fresh H_2O/DMF	**1b**
	DMF (dried on molecular sieve)	**1b**
	DMF (dried on molecular sieve, aged 20 min prior to grinding)	**1b**
	DMF (dried on molecular sieve, aged 20 min prior to grinding. Left in fresh dry DMF for 2 days)	**1b**
	DMA (dried on molecular sieve)	**1c**
LAG (55 µl, $\eta = 1.98$ µl mg^{-1})	DMF (as received)	**1b**
	DMA (as received)	**1c**

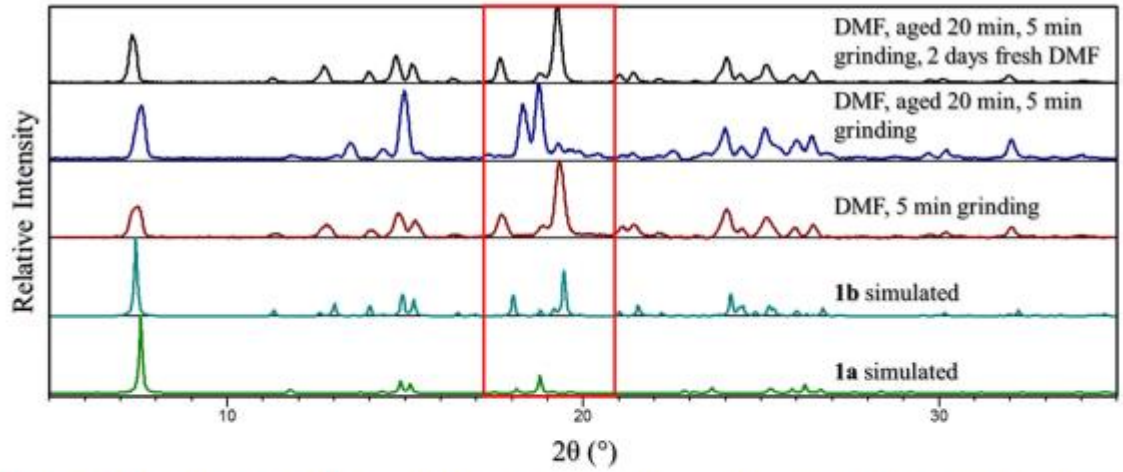

Figure 3. Diffractograms of the materials produced by mechanochemical techniques utilizing DMF of varying water content compared to those of **1a** and **1b** simulated from the single-crystal X-ray data. Dry DMF denotes DMF dried over molecular sieve for several days, while H_2O/DMF denotes a 1:6V:V mixture of water and DMF. Characteristic peak ranges are highlighted in red.

route. In each experiment the starting materials (0.05 mmol each) were ground together with the appropriate amount of solvent (5 drops for slurry grinding or 55 µL for LAG, see Table 2) for 5, 10 or 20 min (each period representing a separate experiment) using an agate pestle and mortar. Prior to grinding, some samples were aged at ambient conditions for 20 min. Some samples were also aged for several days after grinding to observe any further conversion between forms. Neat grinding, liquid assisted grinding (LAG) and slurry grinding were carried out. The results of the mechanochemical experiments are summarized in Table 2 (an expanded version of the table is provided in the Supplementary Information as Table S3).

Immediate grinding with a pestle and mortar of the starting materials in the presence of as-purchased DMF for 5 min resulted in the formation of **1b** (Figure 2). However, when the starting materials were allowed to age in the same DMF under ambient conditions for 20 min before grinding, **1a** was obtained (Figure 2). This sample of **1a**, when submerged in fresh as-purchased DMF for *ca.* 48 h, subsequently converted to **1b** (Figure 2). This apparently time-dependent conversion from **1a** to **1b** was not observed for the single-crystal samples (even over a period of several weeks).

Further mechanochemical investigations were carried out by varying the water content of the DMF. Grinding in the presence of DMF dried over molecular sieve for several days produced **1b** (Figure 3). Grinding in the presence of DMF doped with water (H_2O:DMF 1:6 by volume) produced **1a** (Figure 3). Conversion from **1a** to **1b** then occurred by either drying the sample under ambient conditions for 30 min, or by placing the sample in fresh H_2O/DMF for two days (Figure 3). Drying under ambient conditions (*i.e.*, leaving the sample exposed to the environment for *ca.* 30 min) may lead to conversion of **1a** to **1b** as a result of the material desolvating the lower boiling point guest (*i.e.* water) first. Thermogravimetric analysis of **1a** supports this assertion; there is a shoulder at *ca.* 100 °C in the first derivative that is attributed to the loss of water guest molecules (Figure S40). The conversion of **1a** to **1b** after addition of fresh solvent mixture is attributed to the aforementioned time-dependent effect. Differential scanning calorimetry of both **1a** and **1b** did not reveal any temperature-dependent phase transitions from −80 to 70 °C (Figures S43–S46). Therefore, the conversion from **1a** to **1b** is only observed over time and is not influenced by temperature.

Slurry grinding ($\eta \approx 9\,\mu L\ mg^{-1}$) was the most successful method; complete formation of each product occurred within the first 5 min of grinding. This control over the crystallization process is achieved within 5 min of grinding, with longer grinding periods yielding the same results. However, the DMF water content, aging the sample before grinding and aging after grinding are key regulators for selective preparation of either **1a** or **1b**. Pawley and Le Bail difference maps for **1a** and **1b** were used to determine the phase purity of the materials produced mechanochemically (Figures S29–S32, Tables S4 and S5). These show a reasonably good fit to either form, taking into account that the diffractograms are not well resolved. As observed for the solvothermal synthesis, **1c** forms consistently when DMA is used as the solvent during grinding (Figures S20 and S21). The results of the solvothermal and mechanochemical experiments carried out in this study are summarized in Scheme 1.

Finally, solvent exchange experiments with DMF and DMA were carried out to determine if the change in guest might effect a change in form. Both **1a** and **1b** converted to **1c** when immersed in DMA for 3 days (Figures S25 and S26). Moreover, when **1c** was immersed in dry DMF it converted to **1b** within 3 days (Figure S27). Interestingly, when **1c** was immersed in H_2O/DMF (1:6V:V) an approximately equal mixture of **1a** and **1b** formed after 3 days (Figure S28). After immersion for seven days a mixture was still obtained. Therefore, conversion from **1a** to **1b** occurs similarly to that observed for the slurry grinding experiments. We postulate that the decreased rate of conversion may be attributed to the higher water content in the system (owing to water contributions from both the solvent and the metal salt). Thus, it is reasonable to

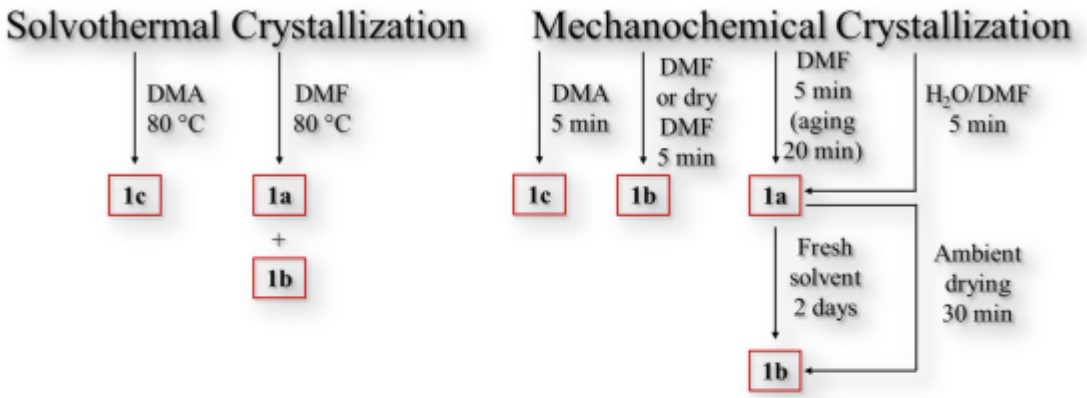

Scheme 1. Summary of the various solvothermal and mechanical experiments. Probe-accessible volumes [35] (probe radius 1.5 Å, grid spacing 0.2 Å) of (a) **1a**, (b) **1b**, and (c) and (d) **1c** viewed down the 1D channels of each material. In (a) both the components of the bpy disorder in **1a** are shown as they are symmetry related. In (c) and (d) each component of the bpy disorder in **1c** is shown separately as each component generates a slightly different shaped channel. The probe-accessible volumes comprise *ca.* 39, 38 and 44% of the unit-cell volumes of **1a**, **1b** and **1c**, respectively. In all cases guest molecules and hydrogen atoms have been omitted for clarity.

conclude that all forms interconvert in the presence of the appropriate combination of solvents.

4. Conclusions

While the materials in this study have similar host structures, they exhibit distinct solvation preferences, crystal morphology and crystal symmetry. In summary, this study illustrates how the crystallization outcome may be tailored by the use of mechanochemistry. In our case this control allowed for the selective preparation of phase-pure solvate (**1a**) not attainable by variation of the more conventional solvothermal method. Furthermore, conversions between these materials could be achieved by solvent exchange. Not only does the use of mechanochemistry promote the selective preparation of one material over another, but it also yields reproducible results on a much faster timescale.

Acknowledgement

We thank the National Research Foundation (NRF) of South Africa for financial support.

Disclosure statement

There are no conflicts of interest to declare.

References

[1] P.Z. Moghadam, A. Li, S.B. Wiggin, A. Tao, A.G.P. Maloney, A. Peter, S.C. Ward, D. Fairen-Jimenez. *Chem. Mater.*, **29**, 2618 (2017).

[2] S.R. Batten, N.R. Champness, X.-M. Chen, J. Garcia-Martinez, S. Kitagawa, L. Öhrström, M. O'Keeffe, M.P. Suh, J. Reedijk. *CrystEngComm*, **14**, 3001 (2012).
[3] M.C.-L. Yeung, V.W.-W. Yam. *Chem. Soc. Rev.*, **44**, 4192 (2015).
[4] L. You, D. Zha, E.V. Anslyn. *Chem. Rev.*, **115**, 7840 (2015).
[5] J. Liu, L. Chen, H. Cui, J. Zhang, L. Zhang, C.-Y. Su. *Chem. Soc. Rev.*, **43**, 6011 (2014).
[6] M. Raynal, P. Ballester, A. Vidal-Ferran, P.W.N.M. van Leeuwen. *Chem. Soc. Rev.*, **43**, 1660 (2014).
[7] M. Raynal, P. Ballester, A. Vidal-Ferran, P.W.N.M. van Leeuwen. *Chem. Soc. Rev.*, **43**, 1734 (2014).
[8] A. Cadiau, K. Adil, P.M. Bhatt, Y. Belmabkhout, M. Eddaoudi. *Science*, **353**, 137 (2016).
[9] J. Li, J. Sculley, H. Zhou. *Chem. Rev.*, **112**, 869 (2012).
[10] K. Sumida, D.L. Rogow, J.A. Mason, T.M. Mcdonald, E.D. Bloch, Z.R. Herm, T. Bae, R. Long. *Chem. Rev.*, **112**, 724 (2012).
[11] D.M. D'Alessandro, B. Smit, J.R. Long. *Angew. Chem. Int. Ed. Engl.*, **49**, 6058 (2010).
[12] J.A. Mason, M. Veenstra, J.R. Long. *Chem. Sci.*, **5**, 32 (2014).
[13] M. Kawano, M. Fujita. *Coord. Chem. Rev.*, **251**, 2592 (2007).
[14] J.J. Vittal. *Coord. Chem. Rev.*, **251**, 1781 (2007).
[15] G.K. Kole, J.J. Vittal. *Chem. Soc. Rev.*, **42**, 1755 (2013).
[16] B. Dutta, C. Sinha, M.H. Mir. *Chem. Commun. (Camb.)*, **55**, 11049 (2019).
[17] J.-P. Zhang, P.-Q. Liao, H.-L. Zhou, R.-B. Lin, X.-M. Chen. *Chem. Soc. Rev.*, **43**, 5789 (2014).
[18] S.M. Oburn, O.A. Ray, L.R. Macgillivray. *Cryst. Growth Des.*, **18**, 2495 (2018).
[19] J. Jones, V.T. Phuoc, L. Del Campo, N.E. Massa, C.M. Brown, S. Pagola. *Cryst. Growth Des.*, **19**, 4970 (2019).
[20] T. Stolar, S. Lukin, M. Tireli, I. Sović, B. Karadeniz, I. Kereković, G. Matijašić, M. Gretić, Z. Katančić, I. Dejanović, M. di Michiel, I. Halasz, K. Užarević. *ACS Sustainable Chem. Eng.*, **7**, 7102 (2019).
[21] B. Karadeniz, D. Žilić, I. Huskić, L.S. Germann, A.M. Fidelli, S. Muratović, I. Lončarić, M. Etter, R.E. Dinnebier, D. Barišić, N. Cindro, T. Islamoglu, O.K. Farha, T. Friščić, K. Užarević. *J. Am. Chem. Soc.*, **141**, 19214 (2019).
[22] T. Stolar, K. Užarević. *CrystEngComm*, **22**, 4503 (2020).
[23] T. Friščić. *J. Mater. Chem.*, **20**, 7599 (2010).
[24] Bruker AXS Inc. *SAINT Data Collection Software*, Bruker AXS Inc., Madison, WI (2016).
[25] Bruker AXS Inc. *SADABS data correction software*, Bruker AXS Inc.: Madison, WI (2016).
[26] G.M. Sheldrick. *Acta Crystallogr. C Struct. Chem.*, **71**, 3 (2015).
[27] G.M. Sheldrick. *SHELXS Version-2018/3 and SHELXL Version-2018/3: Programs for Crystal Structure Solution and Refinement*, University of Gottingen, Germany (2018).
[28] L.J. Barbour. *J. Supramol. Chem.*, **1**, 189 (2001).
[29] L.J. Barbour. *J. Appl. Cryst.*, **53**, 1 (2020).
[30] C.R. Groom, I.J. Bruno, M.P. Lightfoot, S.C. Ward. *Acta Crystallogr. B Struct. Sci. Cryst. Eng. Mater.*, **72**, 171 (2016).
[31] Persistence of Vision Raytracer Pty. Ltd. *POV-Ray for Windows*. Persistence of Vision Raytracer Pty. Ltd., Williamstone, VIC (2004).
[32] L.J. Barbour, D. Das, T. Jacobs, G.O. Lloyd, V.J. Smith. Concepts and nomenclature in chemical crystallography. In *Supramolecular Chemistry: From Molecules to Nanomaterials*, P.A. Gale, J.W. Steed (Eds.), John Wiley & Sons, Ltd., Hoboken, New Jersey, United States (2012).
[33] G.O. Lloyd, J. Alen, M.W. Bredenkamp, E.J.C. De Vries, C. Esterhuysen, L.J. Barbour. *Angew. Chem. Int. Ed. Engl.*, **45**, 5354 (2006).
[34] R. Haldar, K. Prasad, A. Hazra, T.K. Maji. *Cryst. Growth Des.*, **19**, 1514 (2019).
[35] D.P. van Heerden, L.J. Barbour. *Chem. Soc. Rev.*, **50**, 735 (2021). doi:10.1039/D0CS01040E

3.2. Supporting Information

Electronic Supplementary Information:

Mechanochemical Control of Solvent Content in a 1D Coordination Polymer

Lisa M. van Wyk, Leigh Loots and Leonard J. Barbour*

Department of Chemistry and Polymer Science, University of Stellenbosch, 7602 Matieland, South Africa.

* Correspondence to Professor Leonard J. Barbour (Email: ljb@sun.ac.za)

Contents

1. Preparation of single crystal samples

1.1. Crystallization of 1a and 1b

$\{[Zn(ndc)(bpy)]\cdot DMF\cdot H_2O\}_n$ (**1a**) and $\{[Zn(ndc)(bpy)]\cdot 2DMF\}_n$ (**1b**) were prepared solvothermally. In a scintillation vial, equimolar amounts of the ligands 2,6-naphthalenedicarboxylic acid (ndc, 0.10 mmol, 22 mg) and 2,2′-bipyridine (bpy, 0.10 mmol, 16 mg), along with $Zn(NO_3)_2\cdot 6H_2O$ (0.15 mmol, 45 mg) were added to 3 ml *N,N*-dimethylformamide (DMF) and sonicated until partially dissolved. The vial was placed in an 80 °C preheated oven for approximately 3 days. Clear blocks (**1a**) and rods (**1b**) formed in approximately equal yield (determined by visual inspection, **Fig. S1**). Single crystal X-ray diffraction showed that the different morphologies belonged to individual concomitant solvates (**Table S1**).

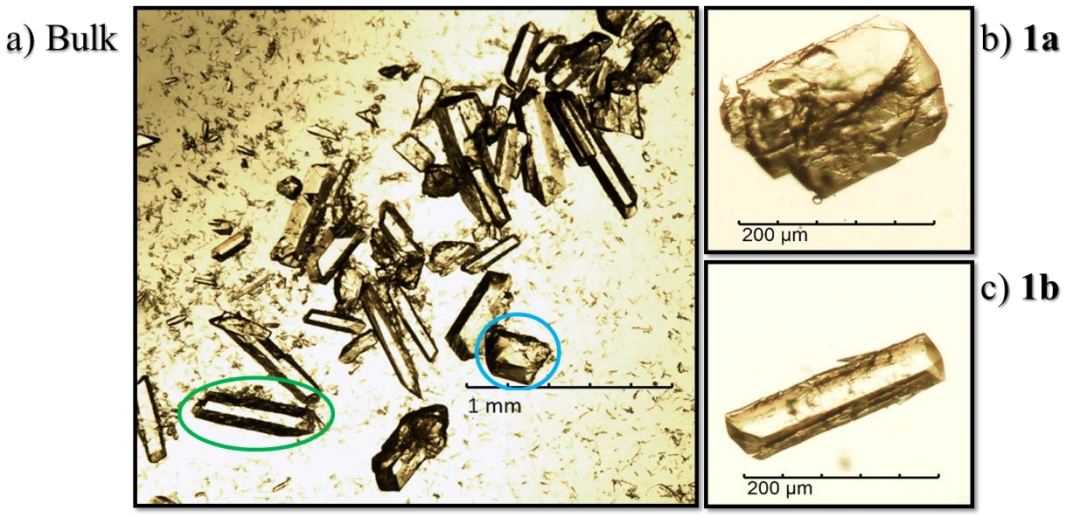

Figure S1: Photomicrographs of the bulk crystallization **(a)** and the concomitant solvates **1a (b)** and **1b (c)** from DMF. In **(a)** a crystal of **1a** is highlighted in blue and **1b** in green. Scale bars are shown in all photomicrographs.

1.2. Crystallization of 1b with dry DMF

Single crystals of **1b** were prepared similarly to the procedure in **§1.1**. However, the DMF utilized was first dried on molecular sieve for several days. Clear rods of various sizes were produced in a quantitative yield (**Fig. S2**).

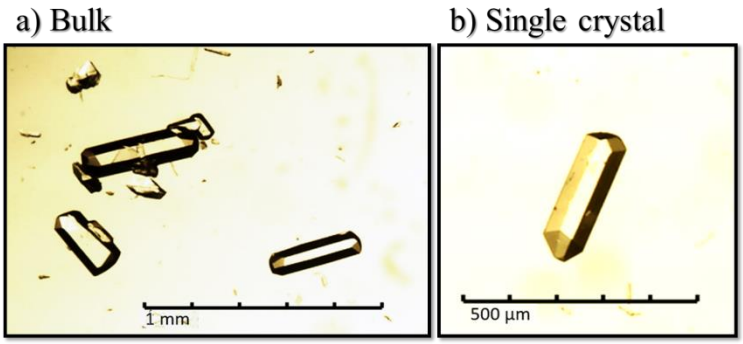

Figure S2: Photomicrographs of the bulk crystallization **(a)** and a single crystal **(b)** from DMF dried on molecular sieve for several days. Scale bars are shown in all photomicrographs.

1.3. Crystallization of 1a and 1b with H_2O/DMF

Single crystals of **1a** and **1b** were prepared similarly to the procedure in **§1.1**, except five drops of water was added to the crystallization mixture. It was found that after relatively short periods of time (16 hours) some crystals of **1b** had already formed. All crystallizations produced a mixture of clear blocks (**1a**) and rods (**1b**) (determined by visual inspection, **Fig. S3**).

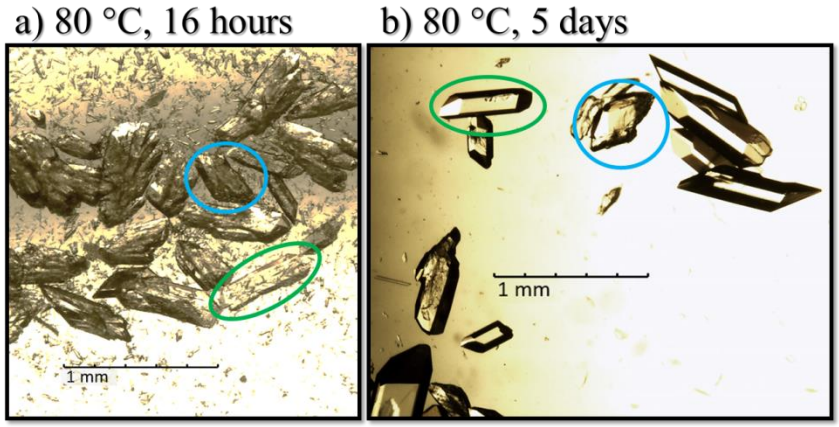

Figure S3: Photomicrographs of the bulk crystallization after 16 hours **(a)** and 5 days **(b)** from H_2O/DMF. In both photomicrographs a crystal of **1a** is highlighted in blue and **1b** in green. Scale bars are shown in all photomicrographs.

1.4. Crystallization of 1c

$\{[Zn(ndc)(bpy)]\cdot 2DMA\cdot 0.5H_2O\}_n$ (**1c**) was prepared solvothermally. The crystallization procedure was the same as in **§1.1**, except *N,N*-dimethylacetamide (DMA) was substituted for DMF. The crystallization produced clear blocks (and some needles) in a quantitative yield (**Fig. S4**). Single crystal and powder X-ray diffraction (**Fig. S13**) showed both morphologies to belong to the same material (**1c**).

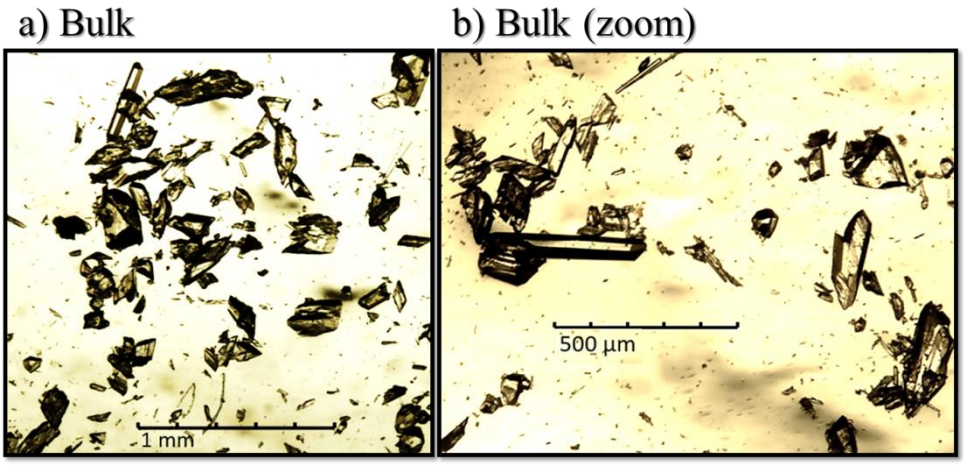

Figure S4: Photomicrographs of the bulk crystallization from DMA. Scale bars are shown in all photomicrographs.

1.5. Crystallization of 1c from dry DMA

To investigate if another solvate could be produced with DMA (without water as a secondary guest), a similar crystallization to that in §1.3 was carried out. However, the DMA used was first dried on molecular sieve for several days. The crystallization produced a low yield of small clear blocks (Fig. S5). These were **1c**, as determined by SCXRD and PXRD (Table S1 and Fig. S13). Small amounts of water from the metal salt hydrate or solvent (Fig. S42) likely provide the water for the crystallization (resulting in the low yield).

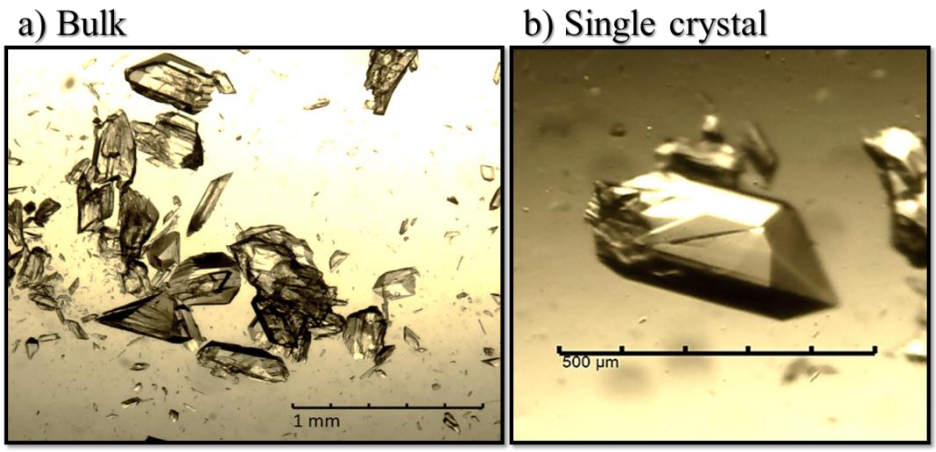

Figure S5: Photomicrographs of the bulk crystallization **(a)** and a single crystal **(b)** from DMA dried on molecular sieve for several days. Scale bars are shown in all photomicrographs.

2. Single-crystal X-ray diffraction (SCXRD)

Crystals of appropriate size possessing suitable morphology and ability to extinguish plane-polarized light were mounted onto the tip of a MiTeGen loop[1] using Paratone®N oil. The mounted crystal was then placed on a goniometer head attached to a diffractometer. X-ray intensity data were recorded on a Bruker APEX II DUO or a Bruker D8 Venture diffractometer. The DUO instrument is equipped with an Incoatec IμS molybdenum (λ = 0.71073 Å) microfocus X-ray source and a CCD area detector. The Venture instrument is equipped with an Incoatec IμS 3.0 molybdenum (λ = 0.71073 Å) microfocus X-ray source and a Photon II CPAD detector. All diffractometers are fitted with an Oxford Cryosystems cryostat (700 Series Cryostream Plus for the DUO instrument and 800 Series Cryostream Plus for the Venture instrument), which is used to control the sample temperature. Both the frame exposure time and the number of frames collected for each experiment were varied depending on the diffraction quality and characteristics of the mounted crystal.

Data reduction and absorption corrections were carried out using the SAINT[2] and SADABS[3] programs, respectively. The unit-cell dimensions were refined on all data and space groups were assigned based on systematic absences and intensity statistics. The structures were solved with a dual-space algorithm using SHELXT[4]. Structure refinement was carried out with SHELXL-2018/3[5] using the X-Seed[6,7] graphical user interface. Non-hydrogen atoms were refined anisotropically. Hydrogen atoms not part of water molecules were placed in calculated positions. In the case of water molecules, where possible, these atoms were identified in the difference electron density maps and refined with an O–H bond-length restraint of 0.86(2) Å (based on a survey of the Cambridge Structural Database (CSD)).[8] Illustrations of all crystal structures were generated using the program POV-Ray.[9]

Table S1. Crystallographic parameters for the materials studied.

	1a	1b	1c	1c (dry DMA)
Empirical Formula	$C_{50}H_{46}N_6O_{12}Zn_2$*	$C_{56}H_{56}N_8O_{12}Zn_2$	$C_{30}H_{33}N_4O_{6.5}Zn$	$C_{30}H_{33}N_4O_{6.5}Zn$
Formula weight ($g\ mol^{-1}$)	1053.66*	1163.82	619.00	619.00
Temperature (K)	100(2)	100(2)	100(2)	100(2)
Wavelength (Å)	0.71073	0.71073	0.71073	0.71073
Crystal system	Monoclinic	Monoclinic	Monoclinic	Monoclinic
Space group	*C*2/*c*	$P2_1/n$	$P2_1/c$	$P2_1/c$
a (Å)	14.581(4)	8.280(1)	7.549(1)	7.546(1)
b (Å)	27.777(8)	24.572(2)	27.766(1)	27.787(1)
c (Å)	7.794(2)	27.308(3)	13.850(1)	13.794(1)
α (°)	90	90	90	90
β (°)	118.051(3)	95.442(2)	90.666(2)	90.630(3)
γ (°)	90	90	90	90
V ($Å^3$)	2786.0(14)	5530.9(9)	2902.66(18)	2891.9(3)
Z	2	4	4	4
Calculated density / ($g\ cm^{-3}$)	1.251	1.398	1.413	1.420
Absorption coefficient (mm^{-1})	0.921	0.936	0.897	0.901
F_{000}	1080	2416	1288.4	1290.4
θ range for data collection (°)	1.47–25.14	1.12–25.06	2.65–28.31	1.47–25.02
Miller index ranges	$-17 \le h \le 17$ $-33 \le k \le 33$ $-9 \le l \le 9$	$-9 \le h \le 9$ $-29 \le k \le 29$ $-32 \le l \le 29$	$-10 \le h \le 10$ $-36 \le k \le 36$ $-18 \le l \le 18$	$-8 \le h \le 8$ $-32 \le k \le 33$ $-16 \le l \le 16$
Reflections collected	16434	68676	48535	50267
Independent reflections	2487	9774	7197	5086
Completeness to θ_{max} (%)	99.6	99.7	99.8	99.9
Max. and min. transmission	0.745, 0.654	0.745, 0.668	0.746, 0.640	0.745, 0.630
Refinement Method	Full-matrix least-squares on F^2	Full-matrix least-squares on F^2	Full-matrix least-squares on F^2	Full-matrix least-squares on F^2
Data / restraints / parameters	2487 / 526 / 267	9774 / 2272 / 1038	7197 / 1053 / 503	5086 / 1151 / 503
Goodness-of-fit on F^2	1.042	1.098	1.140	1.243
Final *R* indices [$I > 2\sigma(I)$]	$R1 = 0.0777$ $wR2 = 0.2178$	$R1 = 0.0613$ $wR2 = 0.1404$	$R1 = 0.0875$ $wR2 = 0.2031$	$R1 = 0.1209$ $wR2 = 0.2483$
Largest diff. peak and hole (e $Å^{-3}$)	1.054, -0.378	1.053, -0.507	1.576, -0.926	1.093, -0.877

*These values differ from those reported in the CIF owing to the addition of the hydrogen atoms on the water molecule which were not modelled.

Table S2. Niggli matrices and reduced cells for the materials studied; illustrating that they are different from one another.

	1a	1b	1c
Niggli Matrix	$\begin{pmatrix} a.a = 60.75 & b.b = 166.48 & c.c = 246.04 \\ b.c = -79.59 & a.c = -26.72 & a.b = -7.31 \end{pmatrix}$	$\begin{pmatrix} a.a = 68.56 & b.b = 603.77 & c.c = 745.72 \\ b.c = 0.00 & a.c = -21.45 & a.b = 0.00 \end{pmatrix}$	$\begin{pmatrix} a.a = 56.98 & b.b = 191.82 & c.c = 770.96 \\ b.c = 0.00 & a.c = 0.00 & a.b = -1.22 \end{pmatrix}$
Reduced Cell (platon/NEWSYMM)[10,11] *P*-1	$a = 7.794$ Å $b = 12.902$ Å $c = 15.686$ Å $\alpha = 113.16°$ $\beta = 102.63°$ $\gamma = 94.17°$ $V = 1393$ Å^3	$a = 8.280$ Å $b = 24.572$ Å $c = 27.308$ Å $\alpha = 90°$ $\beta = 95.44°$ $\gamma = 90°$ $V = 5531$ Å^3	$a = 7.549$ Å $b = 13.850$ Å $c = 27.766$ Å $\alpha = 90°$ $\beta = 90°$ $\gamma = 90.67°$ $V = 2903$ Å^3
Reduced Cell (APEX3)[12] *P*1	$a = 7.77$ Å $b = 14.49$ Å $c = 15.56$ Å $\alpha = 62.57°$ $\beta = 77.21°$ $\gamma = 61.82°$ $V = 1371$ Å^3	$a = 8.28$ Å $b = 24.58$ Å $c = 27.28$ Å $\alpha = 89.95°$ $\beta = 84.58°$ $\gamma = 89.95°$ $V = 5526$ Å^3	$a = 7.55$ Å $b = 13.85$ Å $c = 27.78$ Å $\alpha = 89.98°$ $\beta = 89.98°$ $\gamma = 89.33°$ $V = 2905$ Å^3

2.1. Structural comparisons of solvates

The following figures illustrate the structural variation between the solvates **1a**, **1b** and **1c**. In nearly all cases hydrogen atoms have been omitted for clarity, except where hydrogen bonding is illustrated.

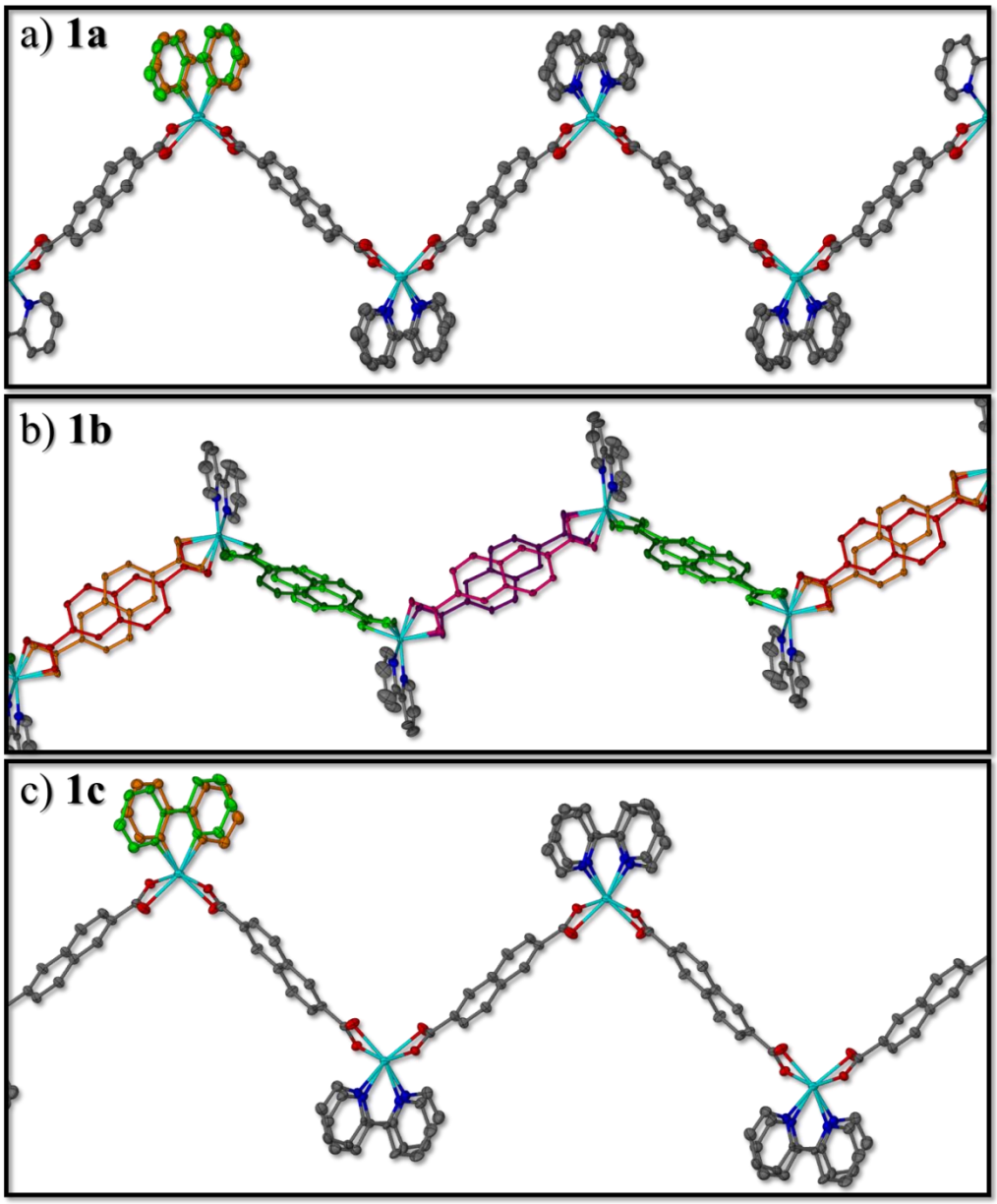

Figure S6: The infinite 1D zig-zag strands of **(a) 1a**, **(b) 1b** and **(c) 1c**. Thermal ellipsoids are shown at the 50% probability level. The site occupancies of all disordered moieties are approximately 50:50 and they are shown in non-CPK colors. In **(a)** and **(c)** only one disordered ligand set is show in non-CPK colors, while all disorder is shown in non-CPK colors in **(b)**. The minor component of the disorder of the carboxylate moiety in **1a** is omitted in **(a)** for clarity. Hydrogen atoms and guest molecules have also been ommitted for clarity.

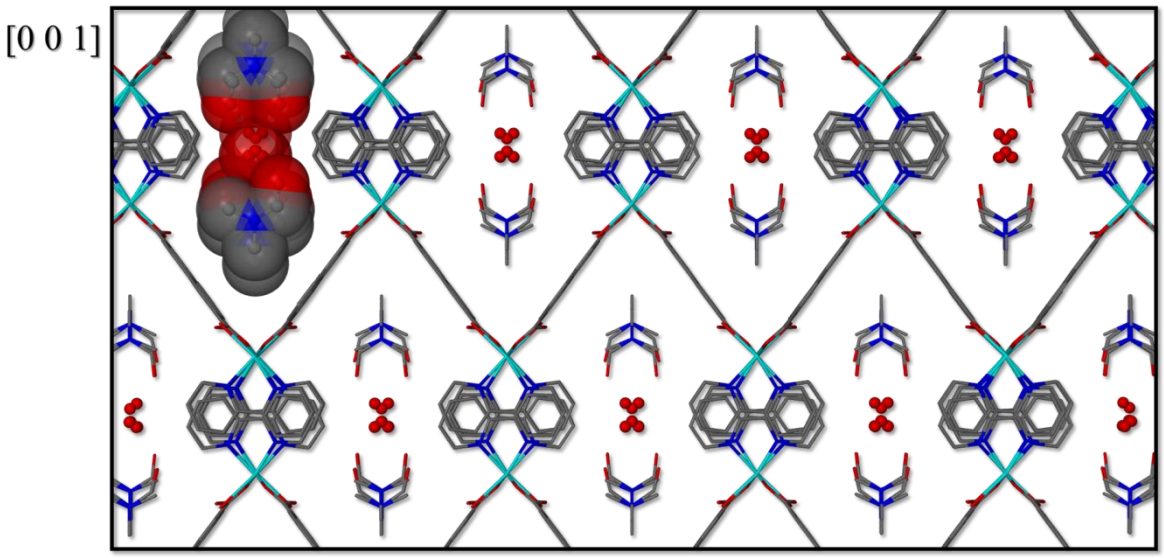

Figure S7: Packing of **1a** viewed down the *c* axis. The guest molecules in one channel are shown in spacefill representation, while the remainder of the packing diagram is shown in capped-stick representation (water molecules shown in ball-and-stick representation). Hydrogen atoms have been ommitted for clarity.

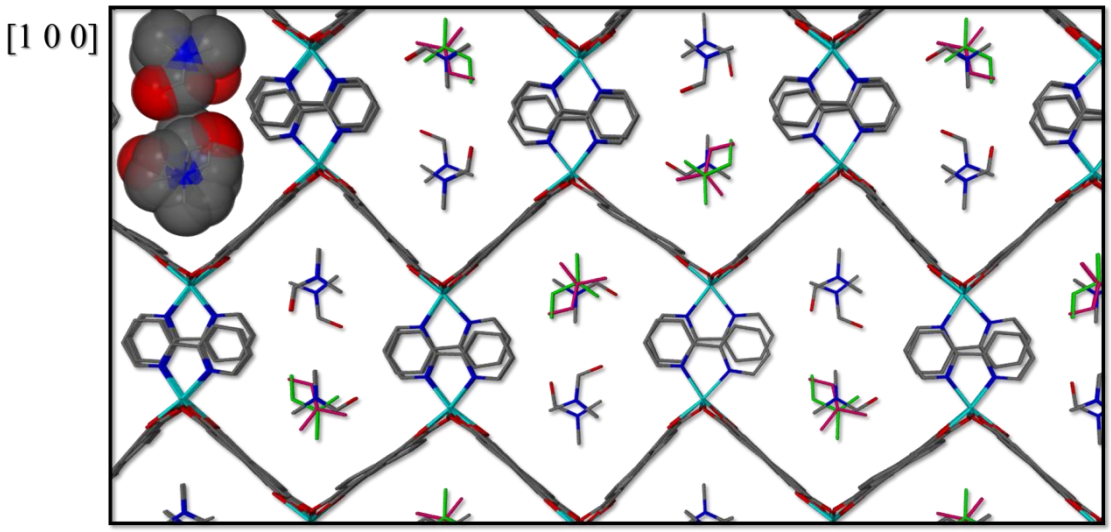

Figure S8: Packing of **1b** viewed down the *a* axis. The guest molecules in one channel are shown in spacefill representation, while the remainder of the packing diagram is shown in capped-stick representation. One DMF molecule, of the four present in the ASU, is disordered. This disorder is shown in non-CPK colors. Hydrogen atoms have been ommitted for clarity.

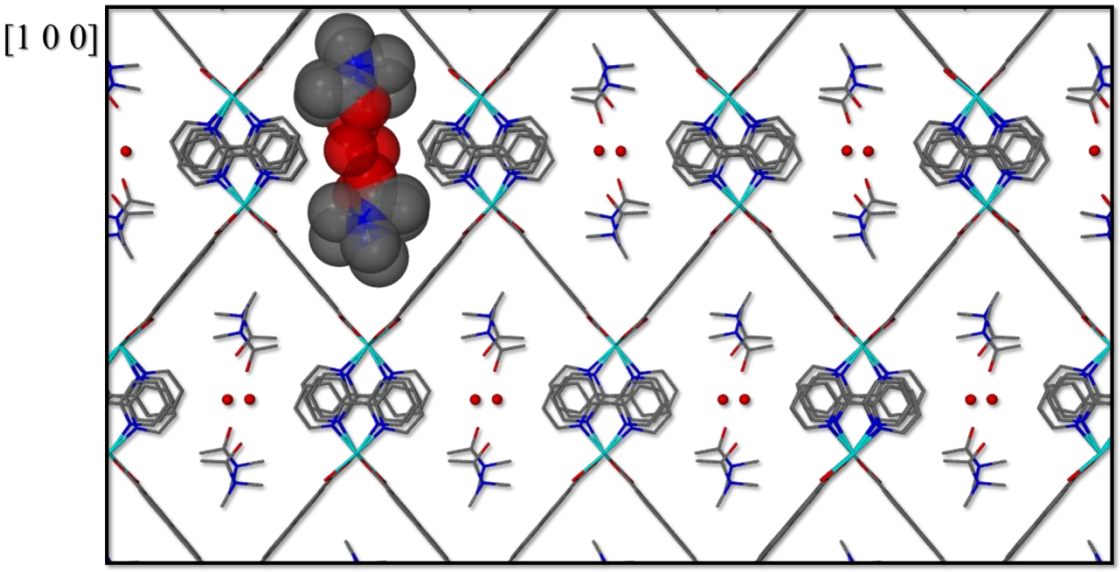

Figure S9: Packing of **1c** viewed down the *a* axis. The guest molecules in one channel are shown in spacefill representation, while the remainder of the packing diagram is shown in capped-stick representation. Hydrogen atoms have been ommitted for clarity.

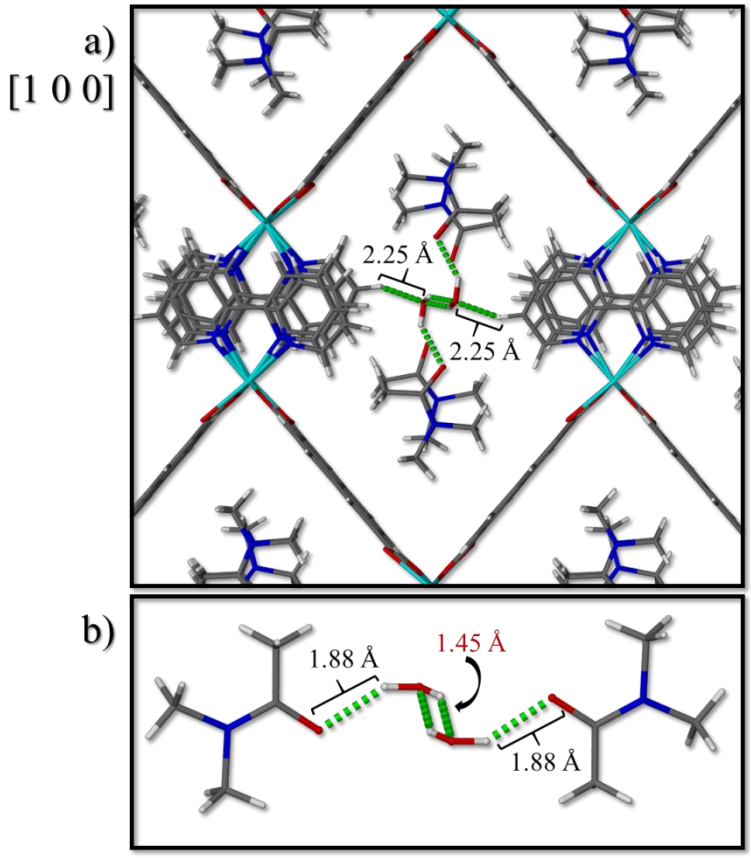

Figure S10: (a) Packing of **1c** viewed down the *a* axis showing the hydrogen bonding between the guest molecules as well as between the guest molecules and the host. **(b)** An isolated view of the hydrogen-bonding motif between the guest molecules. The short distance between the water molecules (1.45 Å) indicates that these are two symmetry generated positions for one water molecule. This is supported by the site occupancy of each being approximately 50%.

3. Mechanochemical preparation of samples

The mechanochemical experiments carried out during this study are summarised in **Table S3** (supporting powder X-ray diffraction data are found in **§4**). In each individual experiment 0.05 mmol of each of the starting materials (ndc (10.8 mg), bpy (7.8 mg) and $Zn(CH_3COO)_2$ (9.2 mg)) was ground with an agate pestle and mortar for 5, 10 or 20 minutes (with each time period representing a fresh sample). Aging prior to grinding was carried out by exposing the unground sample to ambient conditions for a specified period of time. Furthermore, aging was also carried out after grinding by prolonged exposure to different solvent systems. Neat grinding, liquid assisted grinding (LAG) and slurry grinding[13] were carried out. LAG was successful to an extent (*i.e.* when grinding for 5 minutes). However, extended periods of grinding with minimal solvent may have allowed for desolvation or degradation of any materials formed. Consequently, slurry grinding was the most successful preparation method, allowing for control of which solvate was prepared.

Table S3. Summary of the mechanochemical study illustrating which solvate predominated under different preparation conditions as determined by powder X-ray diffraction (visual identification of characteristic peaks).

Solvent/Method		Grinding duration		
		5 minutes	10 minutes	20 minutes
Slurry (*ca* 5 drops of solvent mixture $\eta \approx 9$ µl mg^{-1})	DMF (as received)	**1b**	**1b**	**1b**
	DMA (as received)	**1c**	**1c**	**1c**
	DMF (as received, aged 20 minutes prior to grinding)	**1a**	**1a**	**1a**
	DMF (as received, aged 20 minutes prior to grinding, after 2 days in fresh as received DMF)	**1b**	**1b**	**1b**
	H_2O/DMF (1:6 V:V)	**1a**		
	H_2O/DMF (1:6 V:V) after 2 days in fresh H_2O/DMF	**1b**		
	DMF (dried on molecular sieve)	**1b**	**1b**	**1b**
	DMF (dried on molecular sieve, aged 20 minutes prior to grinding)	**1b**		
	DMF (dried on molecular sieve, aged 20 minutes prior to grinding. Left in fresh dry DMF for 2 days)	**1b**		
	DMA (dried on molecular sieve)	**1c**		
	DMF ($Zn(OAc)_2$ and bpy added first, then ground for 2 minutes. Second ligand added and ground further)	**1b**		
	DMF ($Zn(OAc)_2$ and ndc added first, then ground for 2 minutes. Second ligand added and ground further)	**1b**		
LAG (55 µl, $\eta = 1.98$ µl mg^{-1})	DMF (as received)	**1b**	unknown	unknown
	DMA (as received)	**1c**		

*In all cases the reaction mixture progresses from translucent to opaque white after *ca* 90 seconds of grinding. This is attributed to the formation of the product.

4. Powder X-ray diffraction (PXRD)

A Bruker D2 Phaser powder diffractometer was used to determine experimental diffractograms. The diffractometer utilises Bragg-Brentano geometry and Cu Kα radiation (λ = 1.5418 Å) as the incident beam. The diffractometer was operated at 30 kV and 10 mA. Intensity data were recorded with a Lynxeye detector using a rotating flat stage (30° min^{-1}). Samples were finely ground (where necessary) using a mortar and pestle, loaded onto a zero-background sample holder and levelled with a glass slide (where possible). The diffractograms were determined under ambient conditions with a scanning range of 5–35°, a step size of 0.016° and a 0.8 second scan speed. Note that shifts may be observed between the experimental diffractograms (determined at ambient temperatures) and those simulated from the 100 K SCXRD data (especially in the peak situated at 7–8° 2θ). These are attributed to the discrepancies in temperature resulting in thermal shifts.

4.1. Solvothermal crystallizations

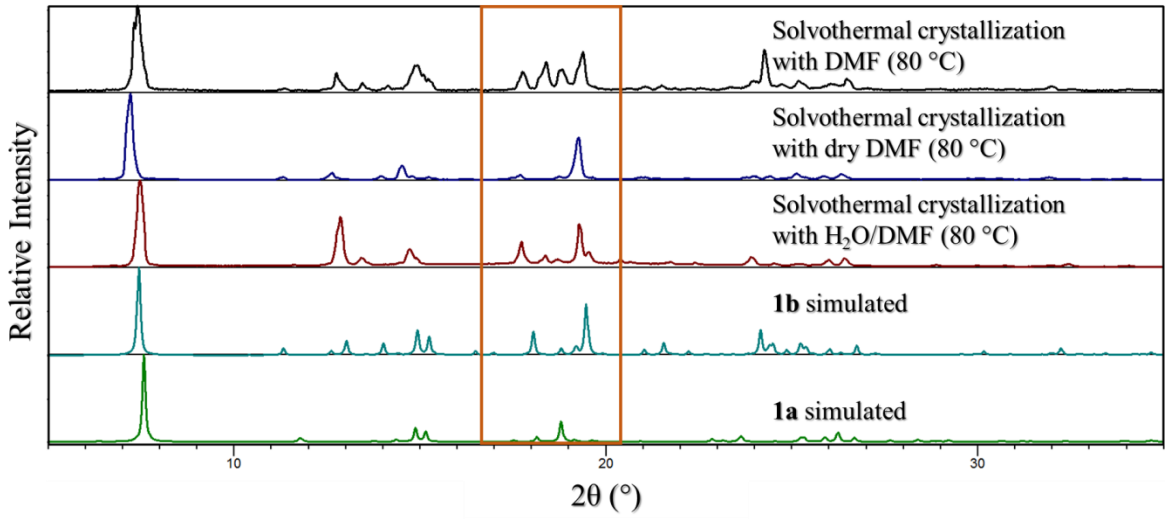

Figure S11: Diffractograms of solvothermal DMF crystallizations with variation in the water content of the solvent system compared to the diffractograms simulated for **1a** and **1b** from SCXRD data.

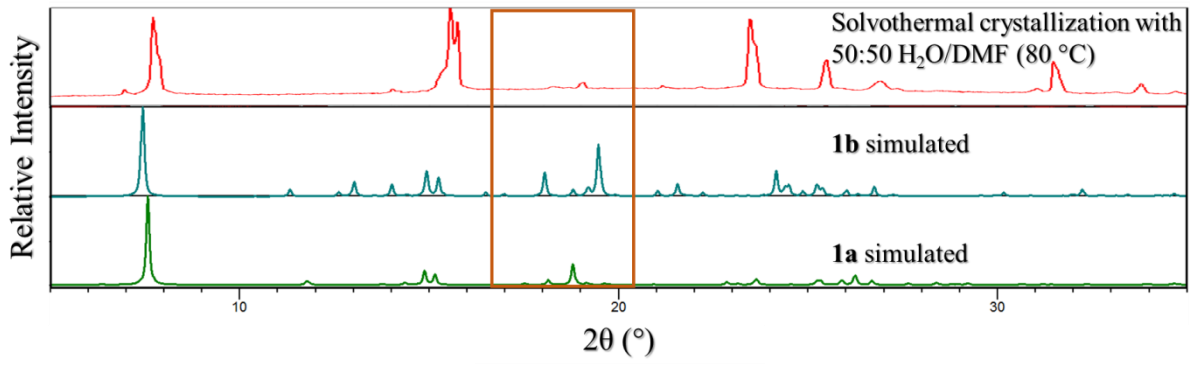

Figure S12: Diffractograms of solvothermal crystallizations with 50:50 H_2O:DMF by volume compared to the diffractograms simulated for **1a** and **1b** from SCXRD data.

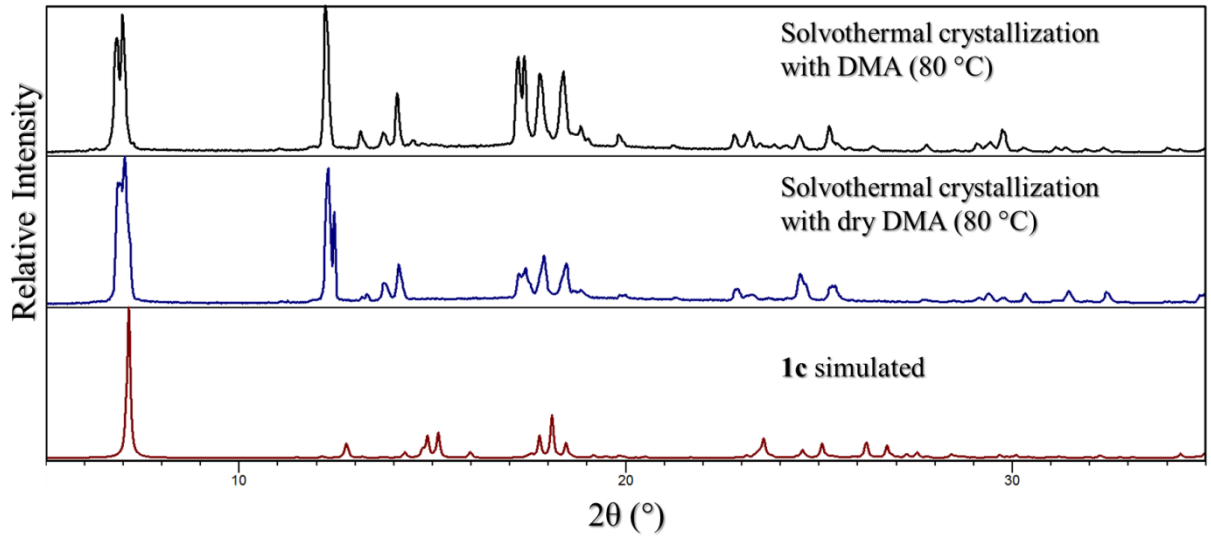

Figure S13: Diffractograms of solvothermal DMA crystallizations with variation in the water content of the solvent system compared to the diffractogram simulated for **1c** from SCXRD data. The crystallization with dry DMA produced crystals of **1c**. However, the yield was much lower. Either the water from the metal salt hydrate or water remaining in the solvent allowed for the material to form (explaining the low yield).

4.2. Slurry grinding experiments

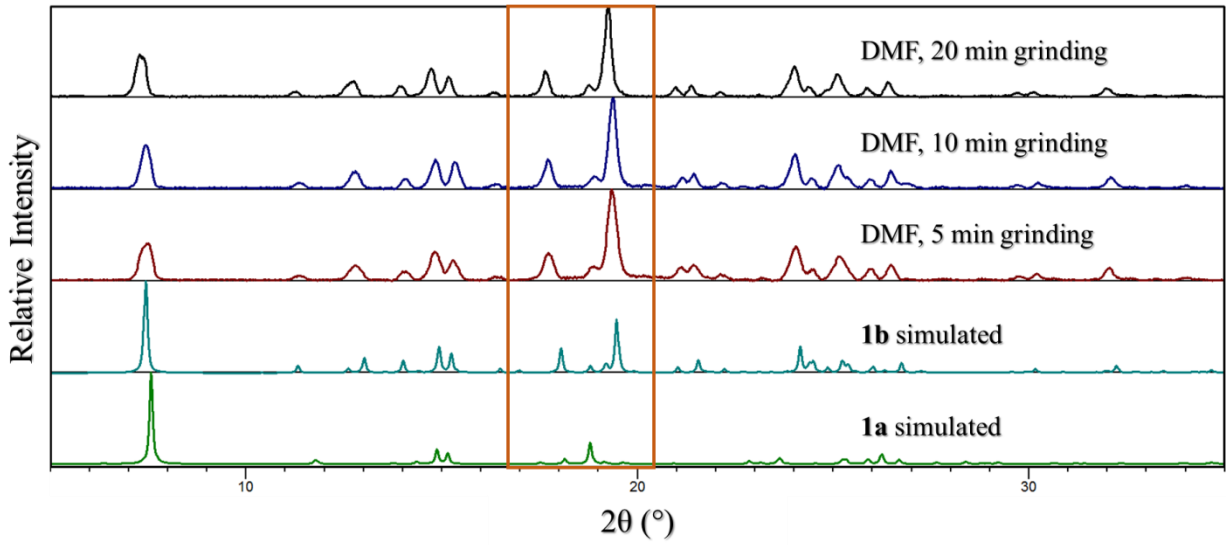

Figure S14: Diffractograms of the mechanochemical preparation (slurry) of **1b** with increasing grinding times compared to the diffractograms simulated from SCXRD data for **1a** and **1b**. DMF used as-purchased.

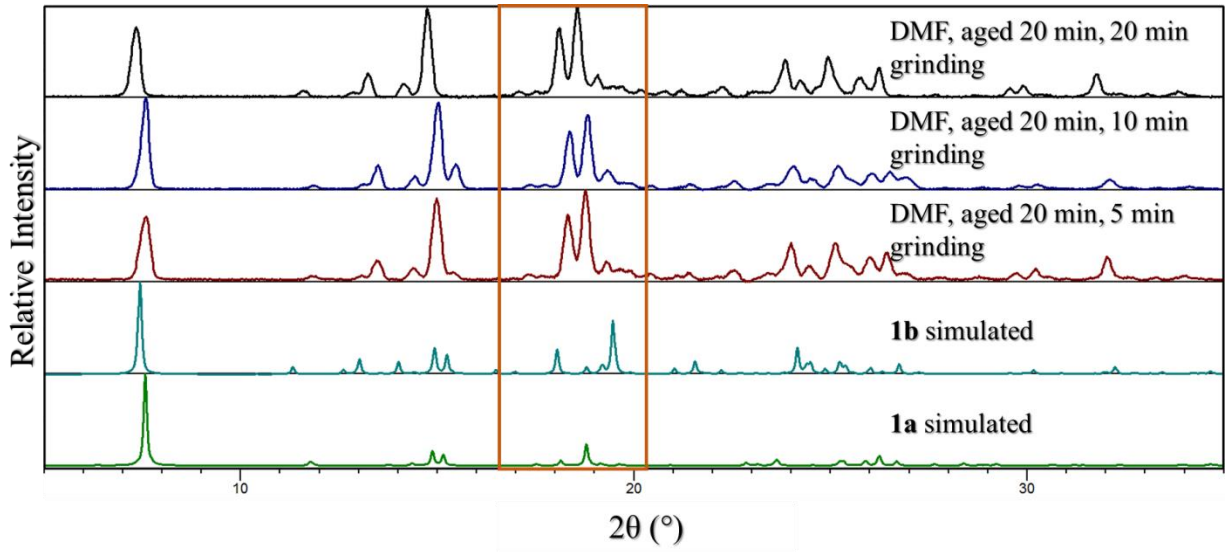

Figure S15: Diffractograms of the mechanochemical preparation (slurry) of **1a** with increasing grinding times compared to the diffractograms simulated from SCXRD data for **1a** and **1b**. In each case the sample was aged for 20 minutes (after addition of the solvent) before grinding. DMF used as-purchased.

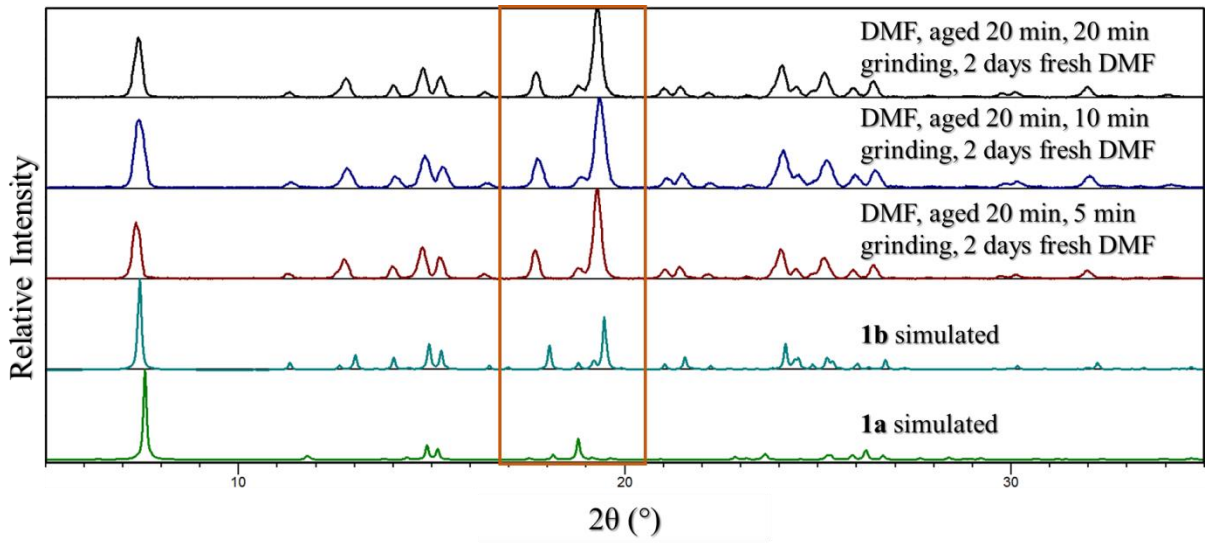

Figure S16: Diffractograms of the mechanochemically prepared (slurry) materials. Samples were aged, then ground and subsequently immersed in fresh as-purchased DMF for two days. The simulated diffractograms for **1a** and **1b** from SCXRD data are included for comparison. Initially after mechanochemical preparation the **1a** form dominated, whereas after soaking in fresh as-purchased DMF for two days conversion to the **1b** form has occurred.

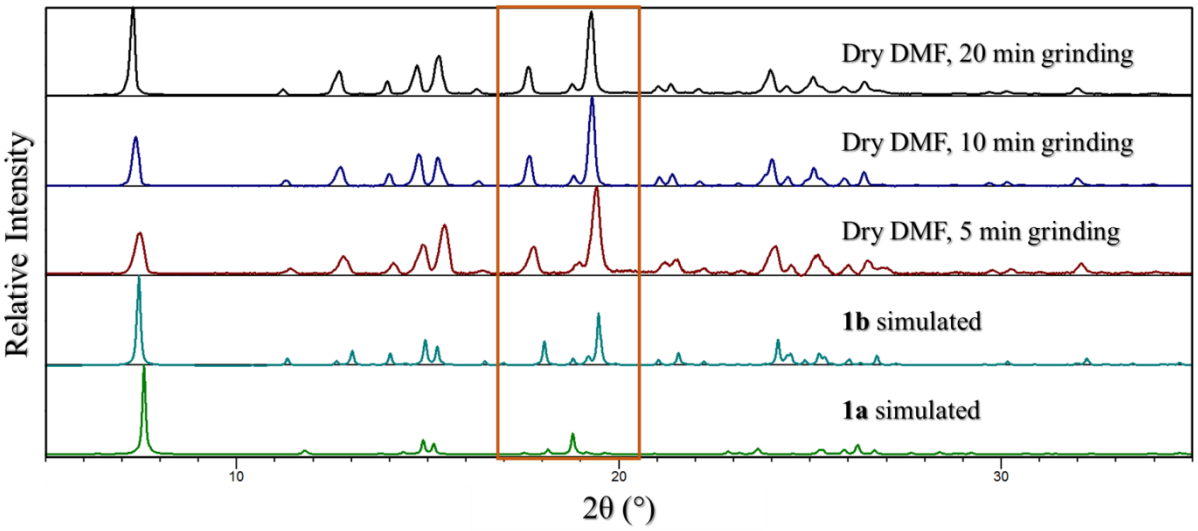

Figure S17: Diffractograms of the mechanochemical preparation (slurry) of **1b** with DMF (dried over molecular sieve for several days) compared to the diffractograms simulated from SCXRD data for **1a** and **1b**.

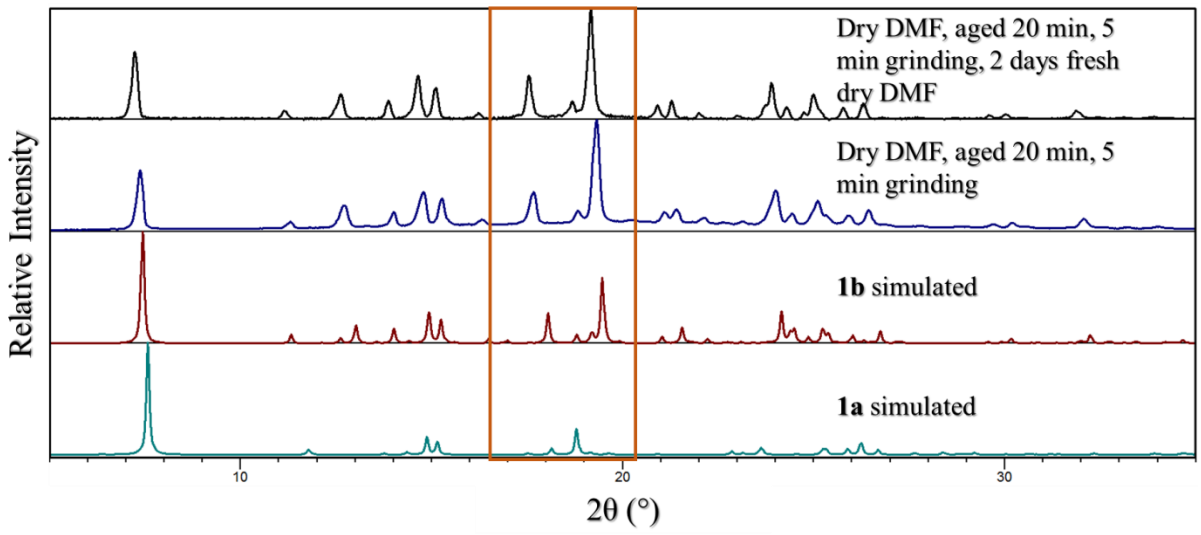

Figure S18: Diffractograms of the mechanochemical preparation (slurry) of **1b** with DMF dried over molecular sieve for several days, compared to diffractograms simulated for **1a** and **1b** from SCXRD data. The diffractogram in blue was achieved by first aging the sample (after the addition of solvent) before grinding for 20 minutes. Previously, when fresh DMF was employed this methodology produced **1a**. However, by reducing the water content of the solvent it seems that the **1b** form predominates. This sample was then immersed in additional dry DMF for two days, after which no change in diffractogram was observed (black diffractogram).

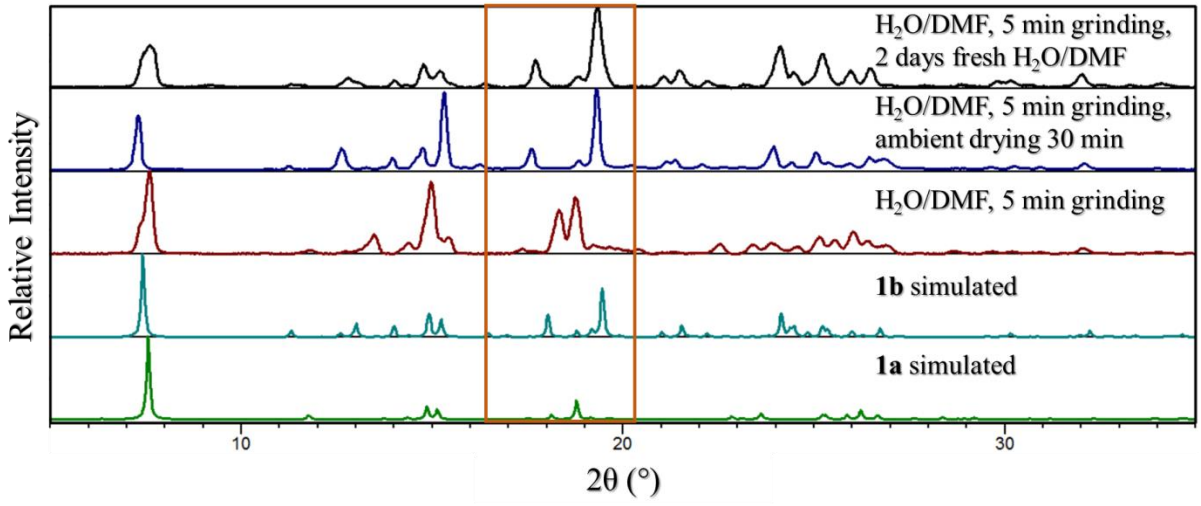

Figure S19: Diffractogram (red) of the mechanochemical preparation (slurry) of **1a** with H_2O/DMF (1:6 V:V) compared to the diffractograms simulated from SCXRD data for **1a** and **1b**. The sample was then dried in ambient conditions (*ca* 22 °C) for 30 minutes. The resulting diffractogram (blue) shows conversion to the **1b** form. Similarly, immersion of the sample after grinding in fresh H_2O/DMF (1:6 V:V) for two days also resulted in conversion to the **1b** form (black diffractogram).

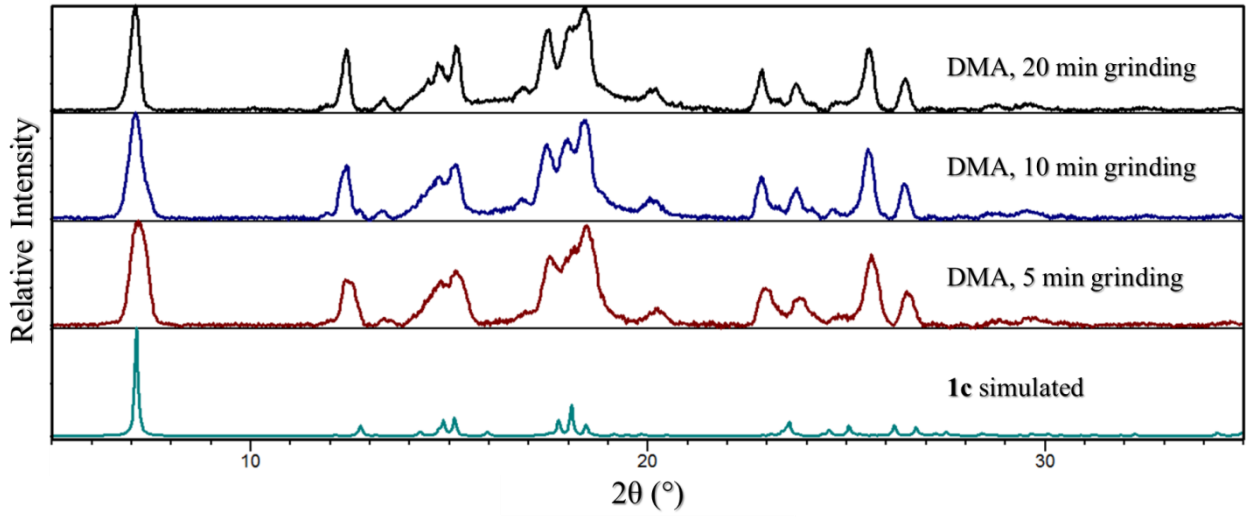

Figure S20: Diffractograms of the mechanochemical preparation (slurry) of **1c** with DMA with variation in the period of grinding compared to the diffractogram simulated from SCXRD data for **1c**.

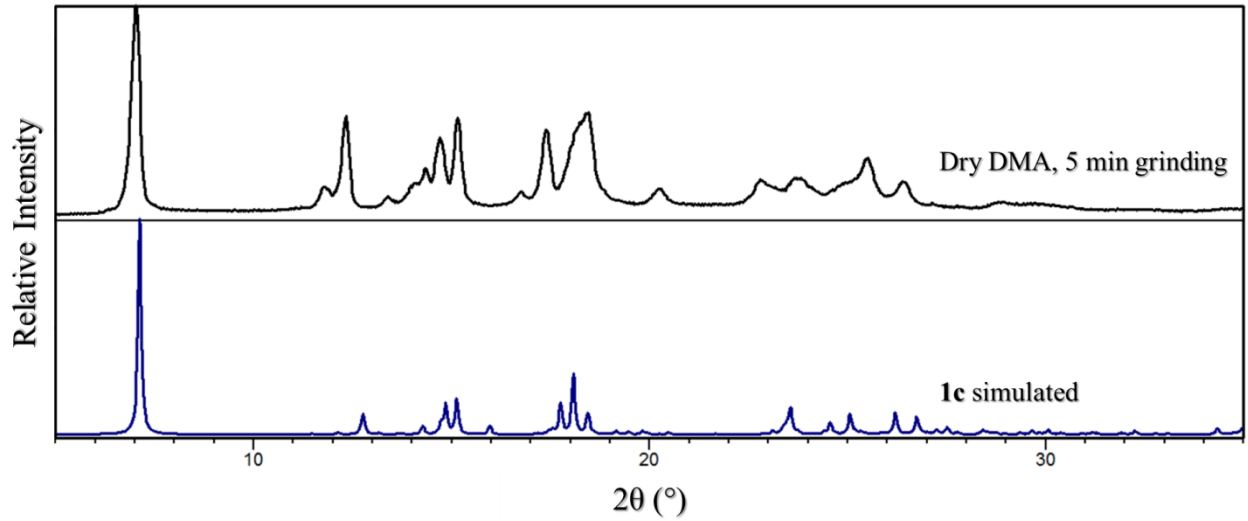

Figure S21: Diffractogram of the mechanochemical preparation (slurry) of **1c** with DMA dried on molecular sieve for several days, compared to the diffractogram simulated from SCXRD data for **1c**. Surprisingly, the **1c** form is still produced. Consequently, either the small amount of water present in the solvent or water from the ambient environment facilitated the formation of **1c**.

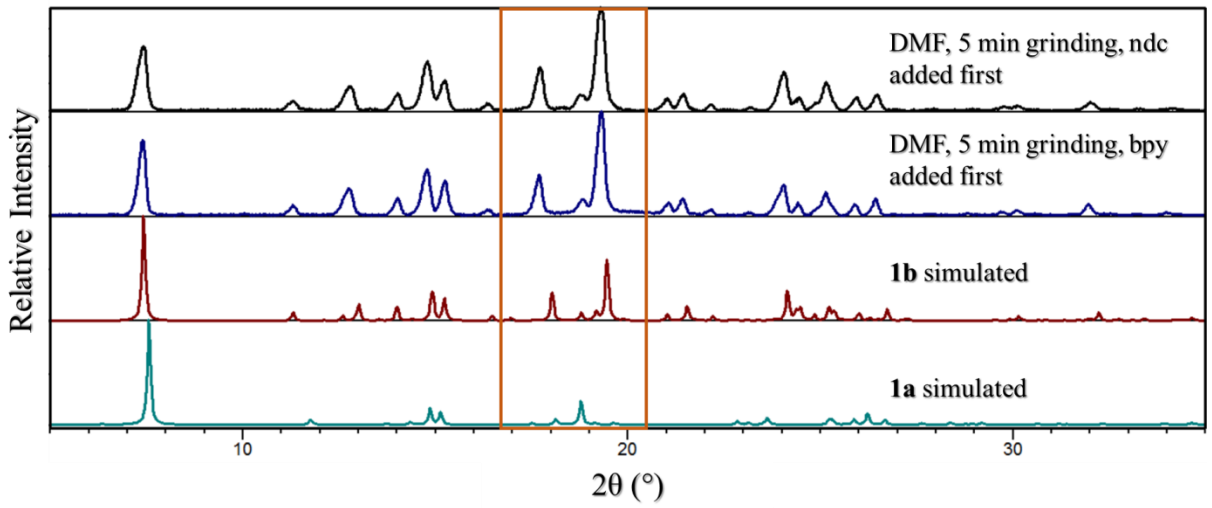

Figure S22: Diffractograms of the mechanochemical preparation (slurry) of **1b** with DMF compared to the diffractograms simulated from SCXRD data for **1a** and **1b**. Instead of adding both ligands at once, each ligand was added separately (varying the order in individual experiments). After the addition of the first ligand the sample was ground for two minutes. Once the second ligand was introduced grinding for a further three minutes was carried out. In both cases it was found that the **1b** form predominates.

4.3. LAG experiments

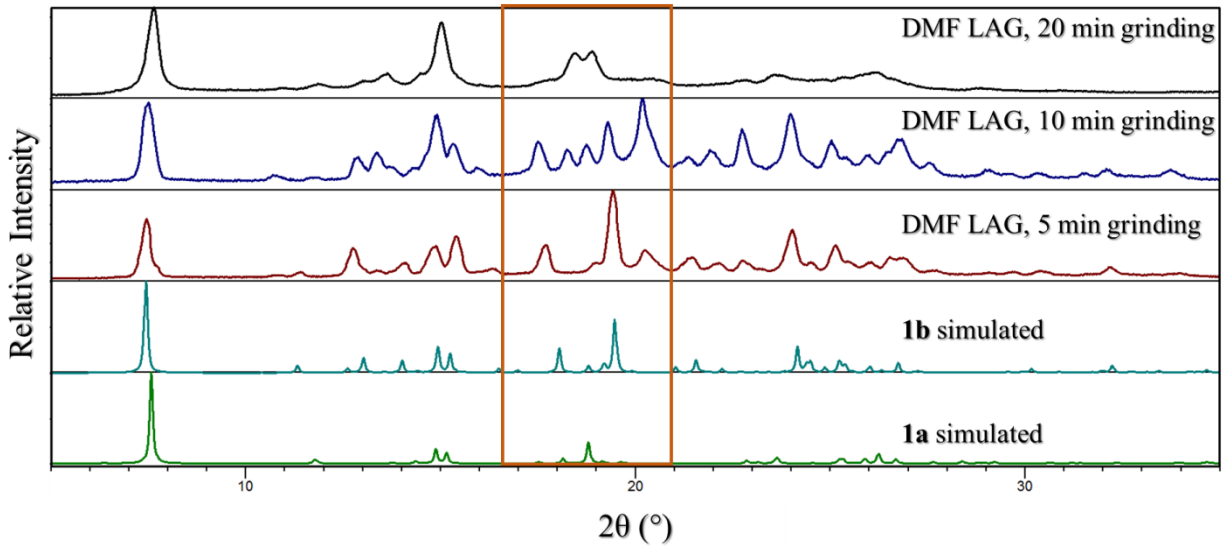

Figure S23: Diffractograms of the mechanochemical preparation (LAG) of **1b** with DMF compared to the diffractograms simulated from SCXRD data for **1a** and **1b**. Five minutes LAG (red diffractogram) produced the predominantly **1b** form. However, extended grinding produced more indistinguishable forms. This is likely as a result of desolvation during extended grinding.

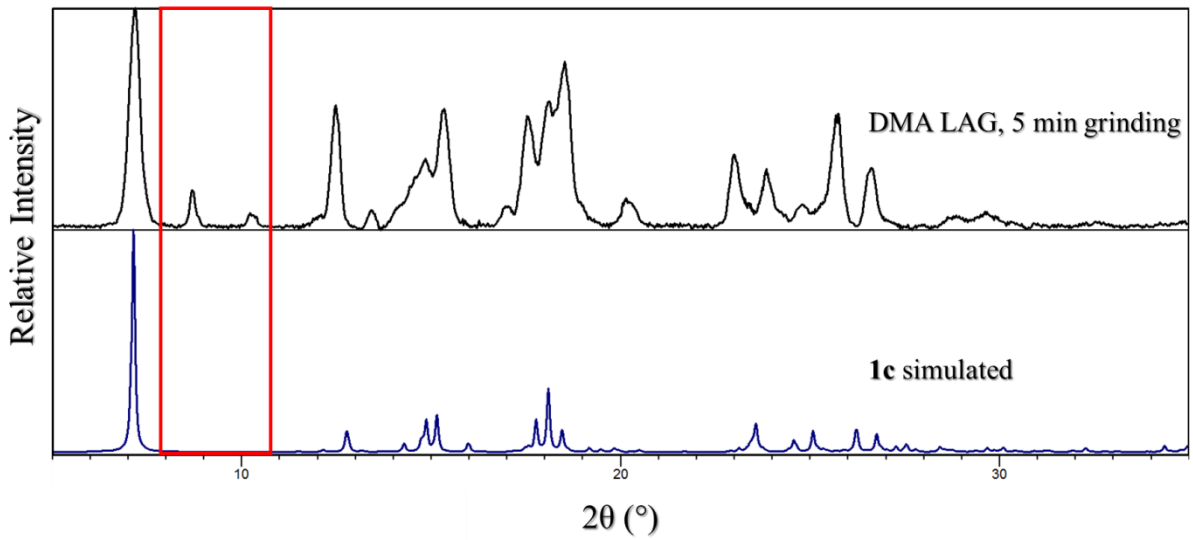

Figure S24: Diffractograms of the mechanochemical preparation (LAG) of **1c** with DMA compared to the diffractogram simulated from SCXRD data for **1c**. Five minutes LAG (black diffractogram) produced the predominantly **1c** form. However, some impurities were observed (highlighted in red). Extended grinding times were not carried out owing to the ambiguity obtained from similar experiments with DMF.

4.4. Solvent exchange experiments

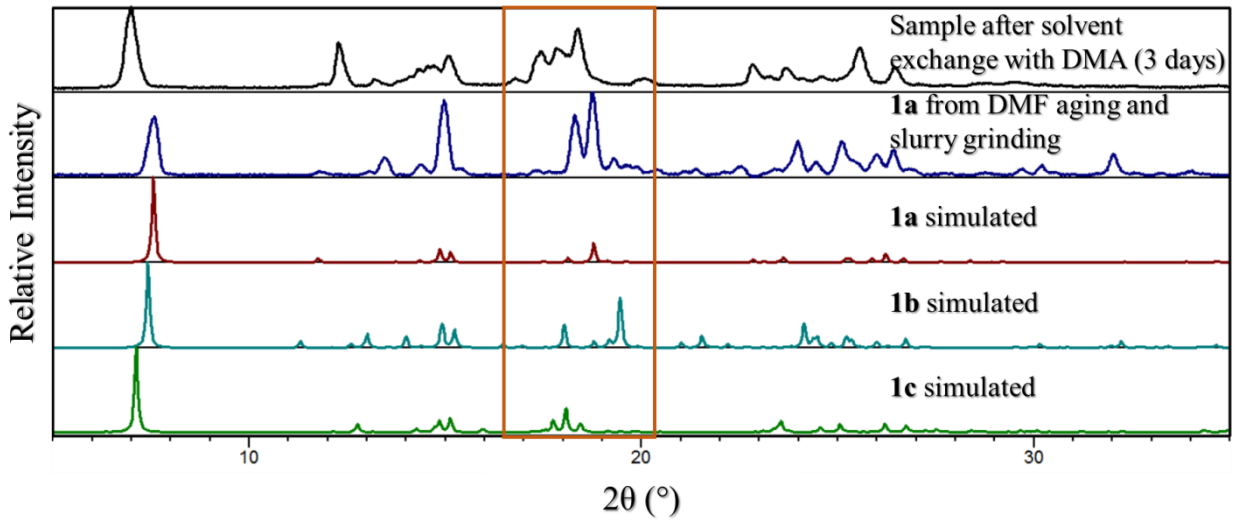

Figure S25: Solvent exchange of a sample of **1a** (prepared mechanochemically with the above mentioned aging and grinding procedure in DMF) with DMA. The diffractogram in black shows conversion to **1c** after immersion in DMA for three days.

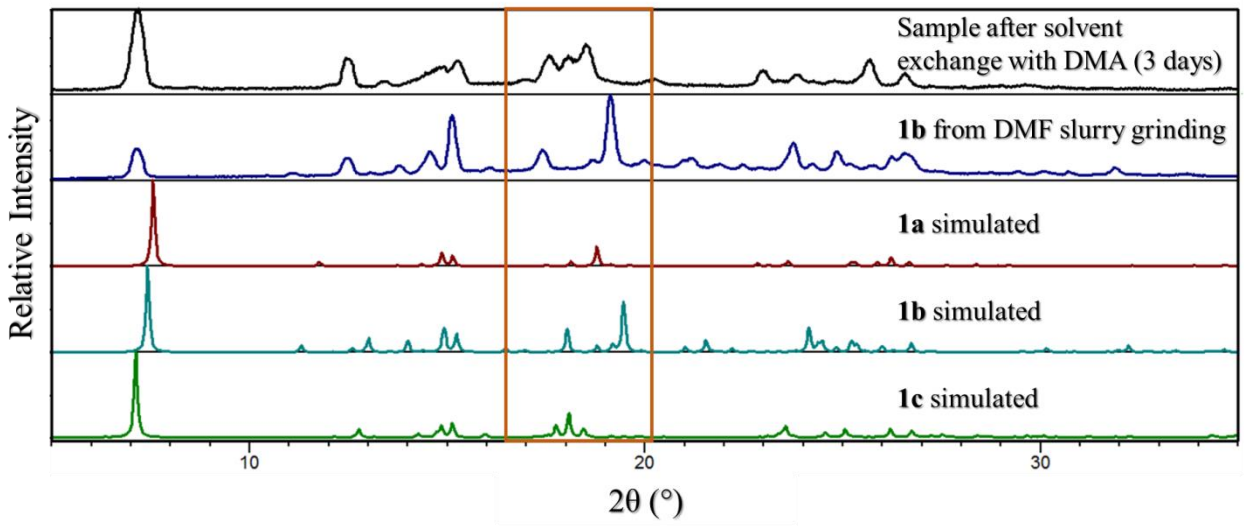

Figure S26: Solvent exchange of a sample of **1b** (prepared mechanochemically with the above mentioned grinding procedure in DMF) with DMA. The diffractogram in black shows conversion to **1c** after immersion in DMA for three days.

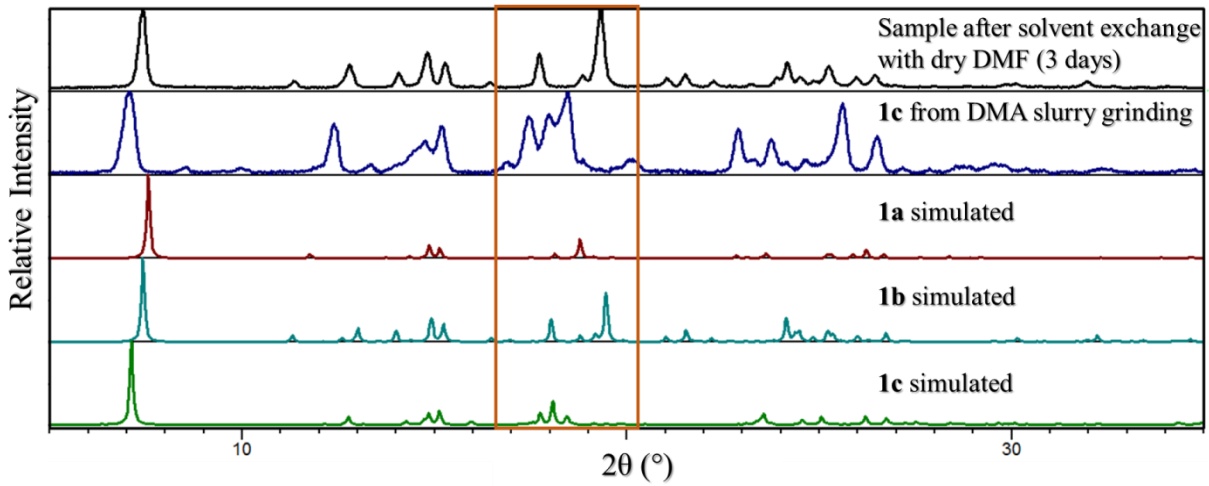

Figure S27: Solvent exchange of a sample of **1c** (prepared mechanochemically with the above mentioned grinding procedure in DMA) with DMF (dried on molecular sieve). The diffractogram in black shows conversion to **1b** after immersion in dry DMF for three days.

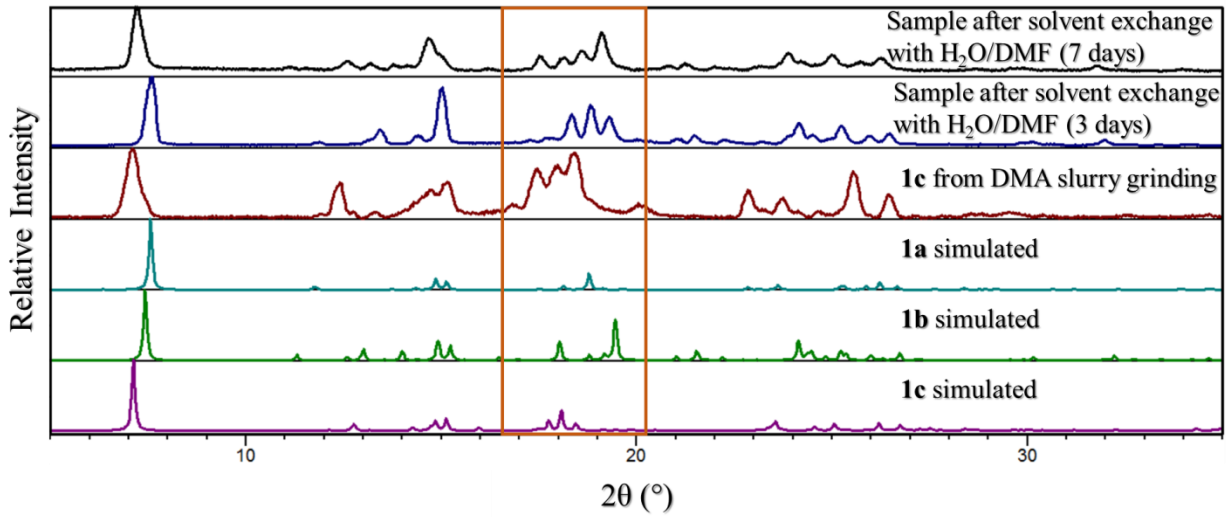

Figure S28: Solvent exchange of a sample of **1c** (prepared mechanochemically with the above mentioned grinding procedure in DMA) with H_2O/DMF (1:6 V:V). After three days immersed in H_2O/DMF a mixture of **1a** and **1b** is produced. After seven days a mixture is still obtained, but more of the **1b** form appears to be present. It is possible that **1a** forms first and then converts to **1b** (as observed previously). It may be postulated that the decrease in speed of the conversion is owing to the higher water content (both from the solvent and the original species).

5. Pawley and Le Bail fitting of powder diffractograms

The powder diffractograms of **1a** and **1b** can be distinguished by very subtle differences in the peak positions. Indexing of the experimental PXRD patterns using TOPAS[14,15] was attempted, however, because the quality of the experimental PXRD patterns is quite poor, results from indexing were not satisfactory. The best quality representative powder patterns that could be obtained for each of the phases (**1a** and **1b**) were refined using both Pawley and Le Bail fittings to obtain lattice parameters. The fit as well as difference plots are shown in Figs S32-S35 with the unit-cell parameters shown in Tables S4 and S5.

Table S4 Comparison of SCXRD and PXRD data of the **1a** solvate using Le Bail and Pawley fitting

Parameters from SCXRD	Parameters from Le Bail	Parameters from Pawley
Space group = *C*2/*c*	Space group = *C*2/*c*	Space group = *C*2/*c*
Temperature = 100 K	Temperature = 298 K	Temperature = 298 K
a = 14.581(4) Å	a = 14.3366 Å	a = 14.5658 Å
b = 27.777(8) Å	b = 25.948 Å	b = 26.4120 Å
c = 7.794(2) Å	c = 7.776 Å	c = 7.7916 Å
β = 118.051(3)°	β = 118.6438°	β = 118.4455°
V = 2786.0(14) Å^3	V = 2590.46 Å^3	V = 2635.61 Å^3
–	R_{exp} : 2.07	R_{exp} : 2.00
–	R_{wp} : 3.88	R_{wp} : 4.13
–	R_p : 2.81	R_p : 3.00
–	GOF : 1.88	GOF : 2.07
–	DW : 0.76	DW : 0.68

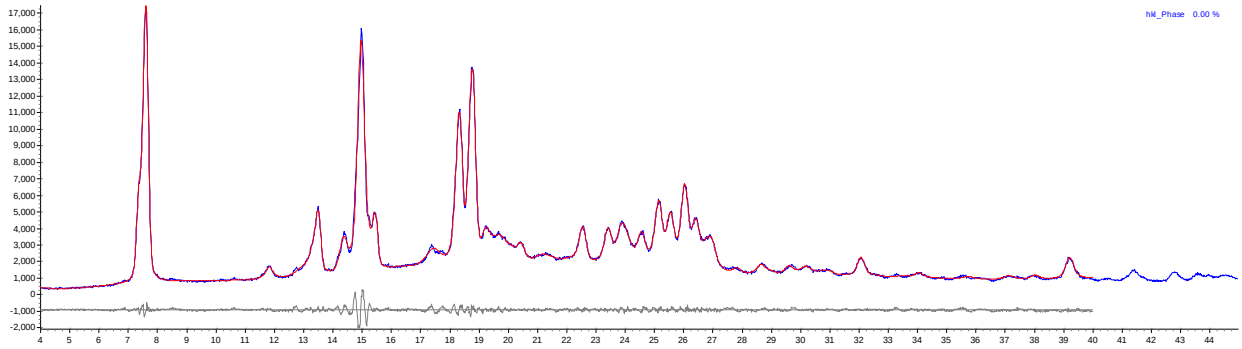

Figure S29 Experimental **1a** diffractogram (blue) compared to Pawley fitting (red), difference plot is shown in grey.

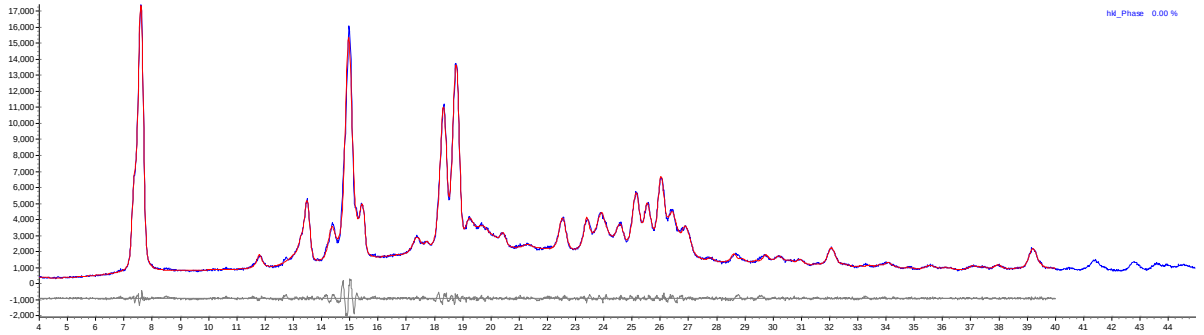

Figure S30 Experimental **1a** diffractogram (blue) compared to Le Bail fitting (red), difference plot is shown in grey.

Table S5 Comparison of SCXRD and PXRD data of the **1b** phase using Le Bail and Pawley fitting

Parameters from SCXRD	Parameters from Le Bail	Parameters from Pawley
Space group = $P2_1/n$	Space group = $P2_1/n$	Space group = $P2_1/n$
Temperature = 100 K	Temperature = 298 K	Temperature = 298 K
a = 8.280(1) Å	a = 8.410 Å	a = 8.261 Å
b = 24.572(2) Å	b = 24.474 Å	b = 23.993 Å
c= 27.308(3) Å	c = 25.904 Å	c = 27.157 Å
β = 95.442(2)°	β = 94.839 °	β = 95.028°
V = 5530.9(9) Å^3	V = 5312.967 Å^3	V= 5362.37 Å^3
–	R_{exp} : 5.71	R_{exp} : 4.87
–	R_{wp} : 7.65	R_{wp} : 6.07
–	R_p : 5.67	R_p : 4.44
–	GOF : 1.34	GOF : 1.25
–	DW : 1.34	DW : 2.05

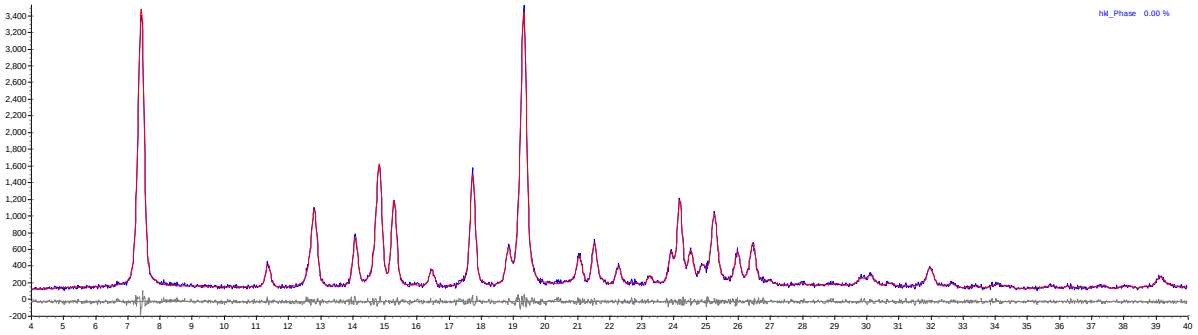

Figure S31 Pawley fitting of **1b** diffractogram. Experimental pattern (blue) and Pawley fit (red) and the difference plot (grey).

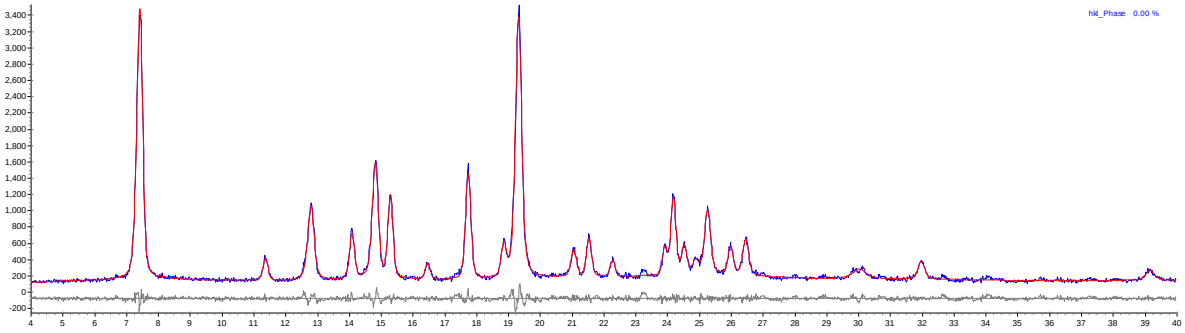

Figure S32 Le Bail fitting of **1b** diffractogram. Experimental pattern (blue) and Pawley fit (red) and the difference plot (grey).

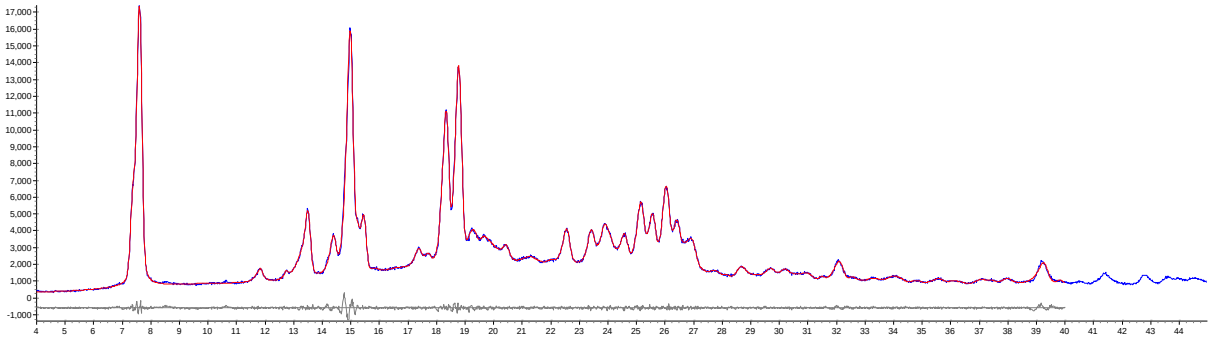

Figure S33 Rietveld refinement of experimental **1a** phase (blue) with the single-crystal data of **1a** (red).
R_{exp} : 1.86 R_{wp} : 3.05 R_p : 2.17 GOF : 1.65, DW: 1.16

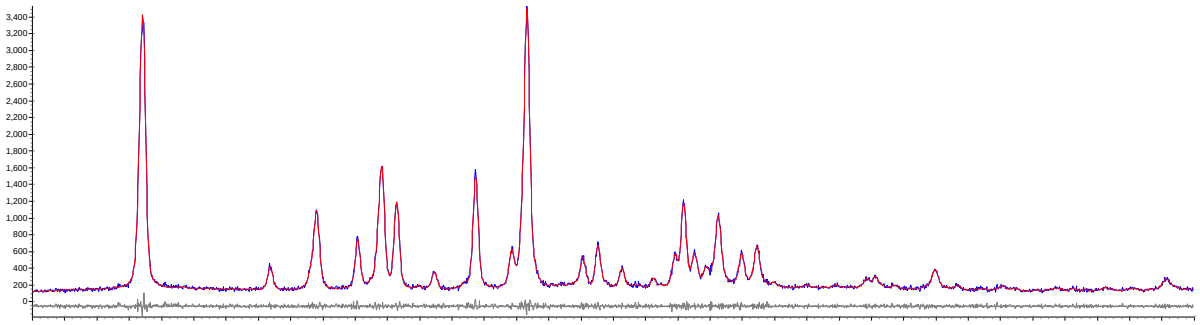

Figure S34 Rietveld refinement of experimental **1b** phase (blue) with the single-crystal data of **1b** (red). R_{exp} : 4.92 R_{wp} : 5.93 R_p : 4.30 GOF : 1.21, DW: 2.17

6. Fourier transform infrared spectrophotometry (FT-IR)

IR spectra were recorded using a Bruker Alpha P ATR-IR instrument. A background measurement was performed before each experimental spectrum was recorded. Samples were briefly dried on filter paper before measurement to remove any surface solvent.

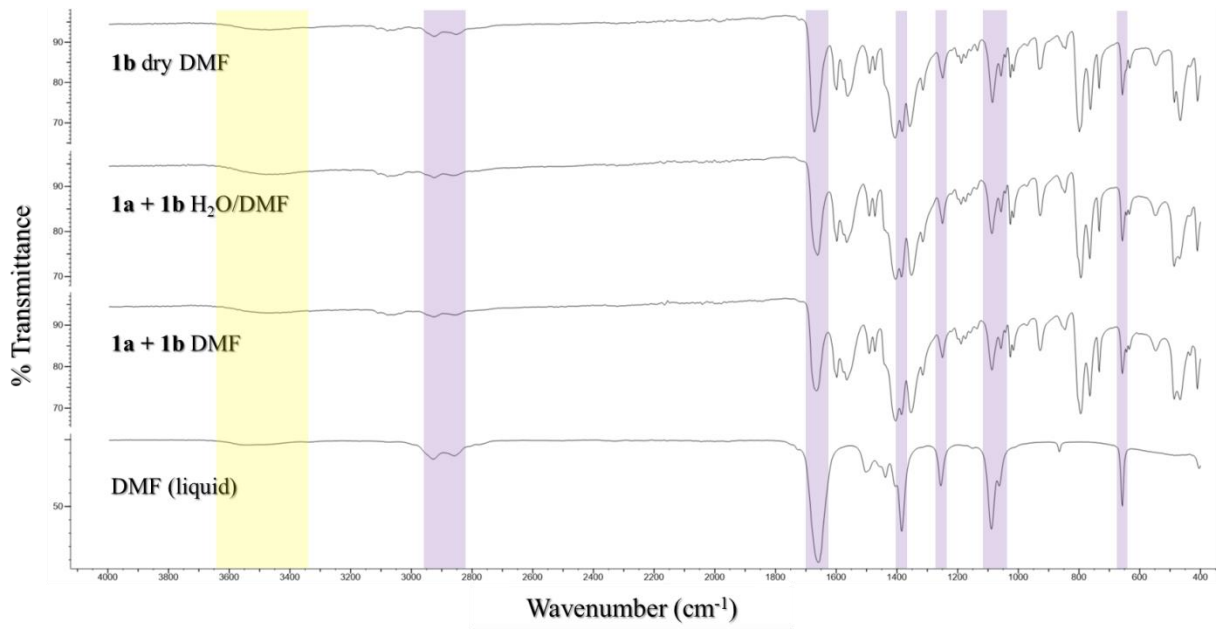

Figure S35: FT-IR spectra of single-crystal samples of the solvates prepared in DMF during this study. The IR spectrum for DMF is also included for comparison. The characteristic peaks of DMF are highlighted in purple. The yellow area indicates the water O–H stretching (hydrogen bonded). Even in the sample determined to be predominantly **1b** (from dry DMF) there is still seemingly a small amount of water present. This is likely as a result of small amounts of surface solvent containing water.

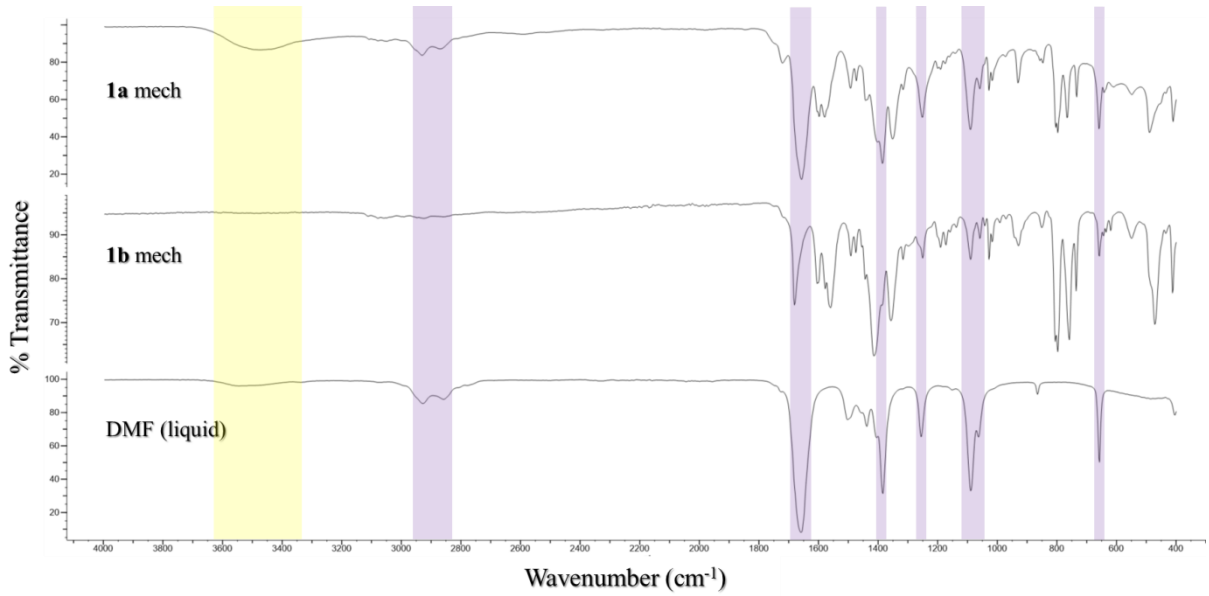

Figure S36: FT-IR spectra of the samples prepared mechanochemically in DMF. The IR spectrum for DMF is also included for comparison. The characteristic peaks of DMF are highlighted in purple. The yellow area indicates the water O–H stretching (hydrogen bonded). In this case the water stretching band is congruent with the guest identity of each solvate.

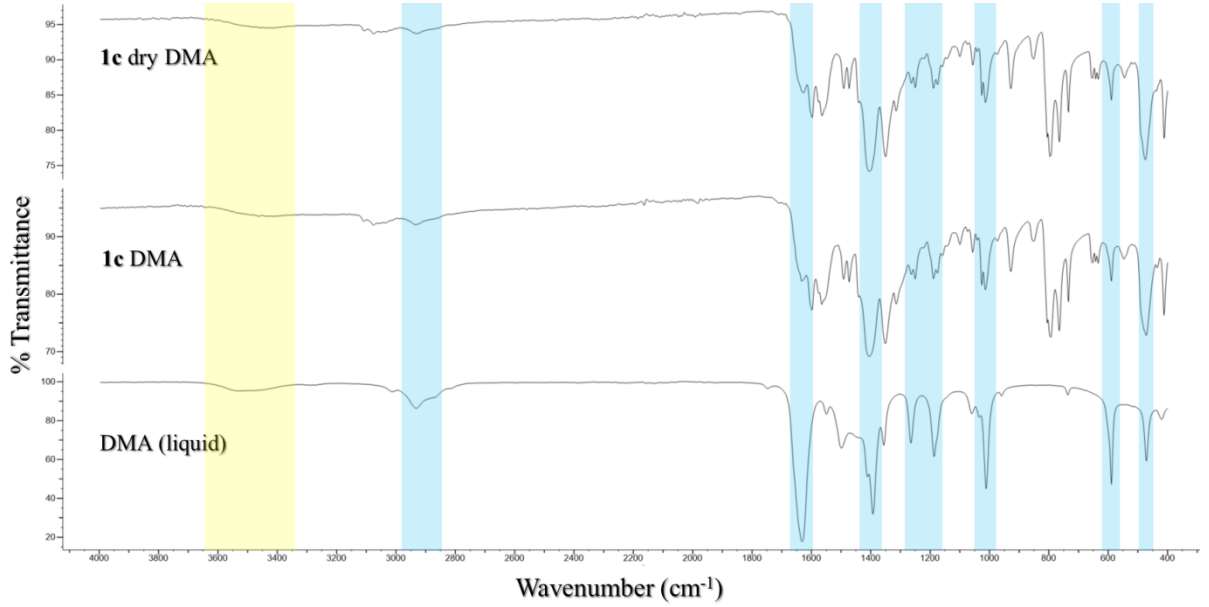

Figure S37: FT-IR spectra of single-crystal samples of **1c** prepared in DMA. The spectrum for DMA is also included for comparison. The characteristic peaks of DMA are highlighted in blue. The yellow area the possible water O–H stretching (hydrogen bonded). As expected all species exhibit the water stretching band.

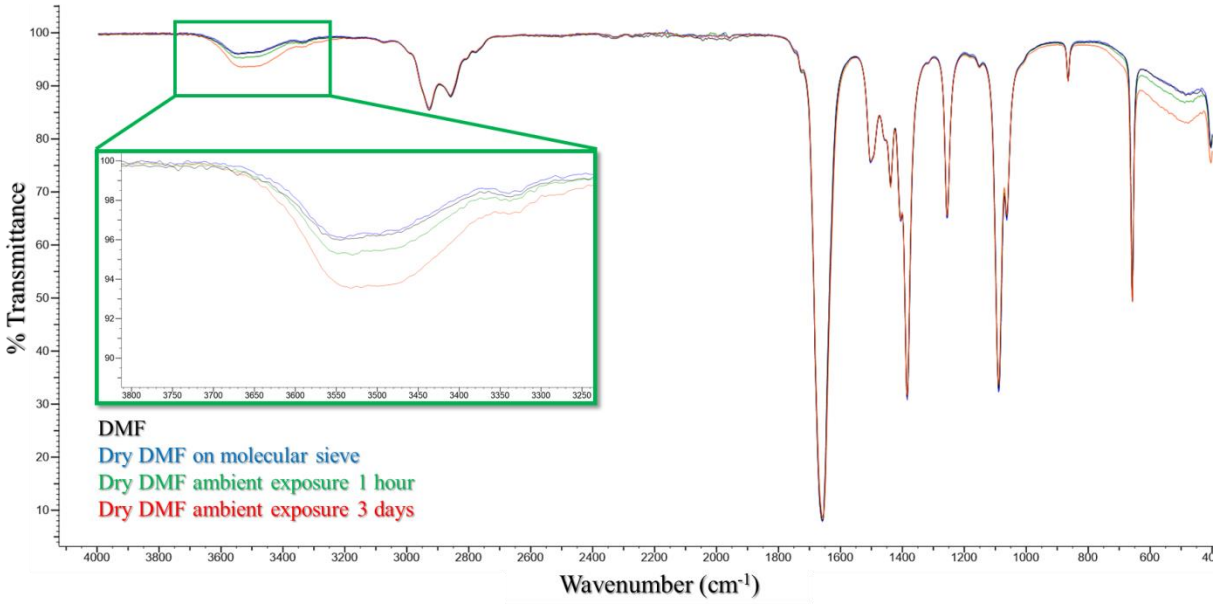

Figure S38: FT-IR spectra of DMF as purchased (black) and dried on molecular sieve (blue). To test the hygroscopic nature of the solvent the dry DMF was left under ambient conditions – 1 hour (green) and 3 day (red) exposures are shown. The water O–H stretching band is expanded to indicate the relative water content of the samples. The spectra indicate that the DMF is reasonably dry when purchased and molecular sieve reduce the water content only slightly. However, ambient exposure results in uptake of water from the environment and a reasonable amount of water is present after three days.

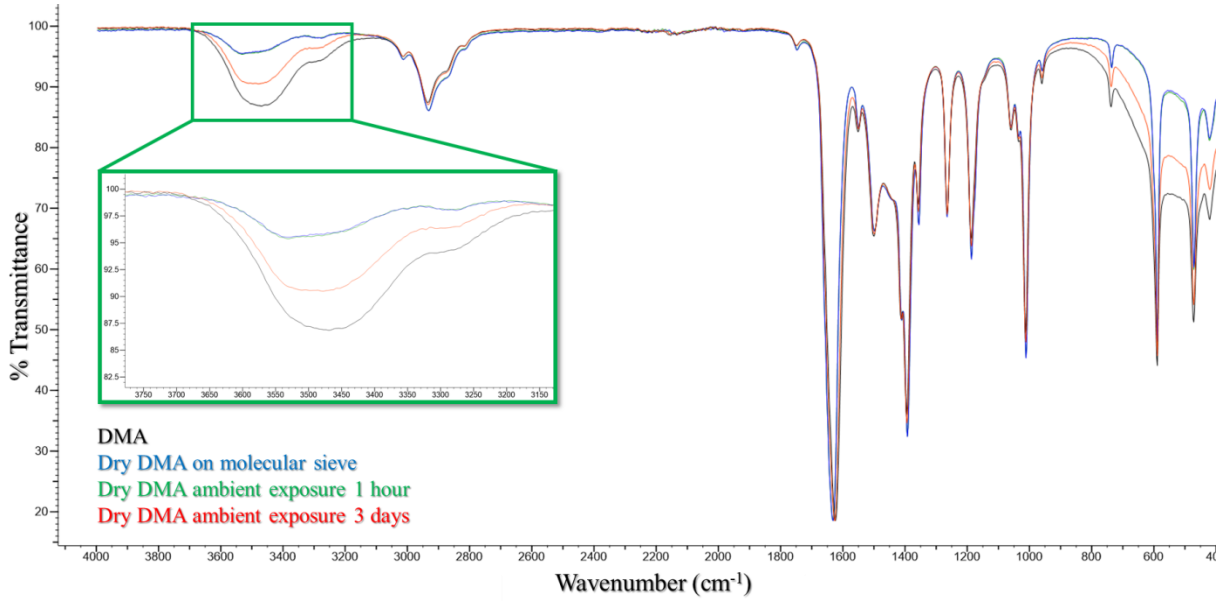

Figure S39: FT-IR spectra of DMA as purchased (black) and dried on molecular sieve (blue). To test the hygroscopic nature of the solvent the dry DMA was left under ambient conditions – 1 hour (green) and 3 day (red) exposures are shown. The water O–H stretching band is expanded to indicate the relative water content of the samples. The spectra indicate that the DMA has a notable water content when purchased, of which most is removed by the molecular sieve. Subsequent ambient exposure results in the uptake of water from the environment and a large amount of water is present after 3 days.

7. Thermogravimetric analysis (TGA)

A TGA trace was generated by measuring the percentage mass as the sample was heated at a constant rate. A TA Instruments Q500 thermogravimetric analyser was used. Samples were contained in aluminium pans and sample weights typically ranged from 1 to 5 mg. N_2 gas (flow rate 40 ml min^{-1}) was used to purge the furnace. The temperature was ramped from room temperature to *ca.* 600 °C at a constant heating rate of 10 °C min^{-1}. The resulting thermograms were analysed using the TA Instruments Universal Analysis program.

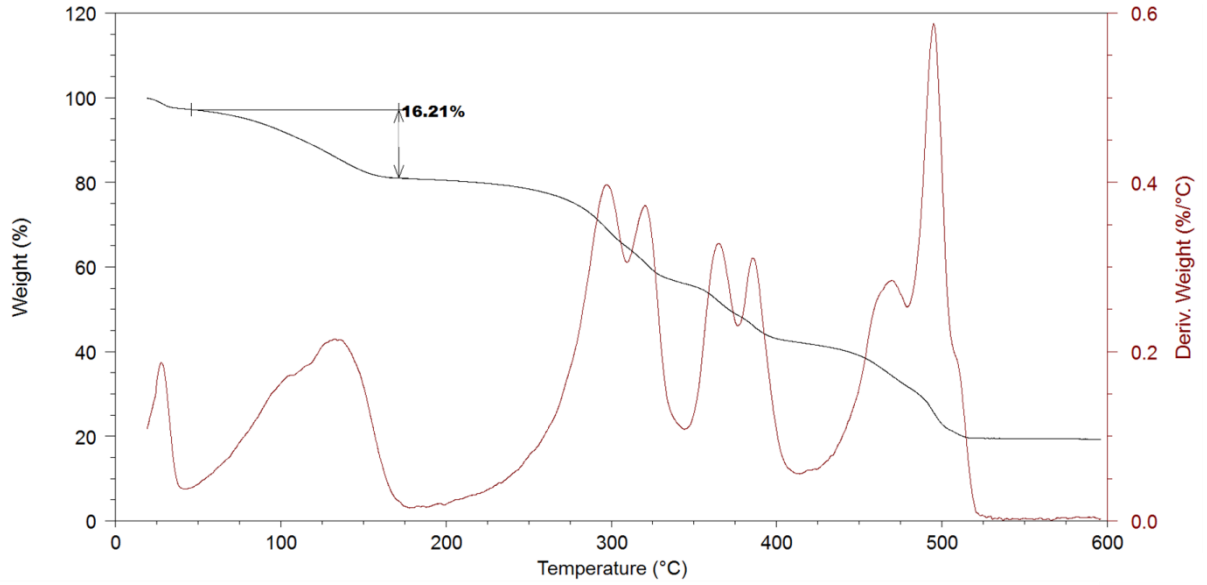

Figure S40: Thermogram of **1a** (prepared mechanochemically). The weight loss of 16.2% is equal to *ca* one DMF and *ca* one H_2O molecules per host formula unit (calculated 16.6%). The initial weight loss between onset and *ca* 45 °C may be attributed to excess surface solvent. The paste formed by the mechanochemical preparation proved difficult to dry adequately without initiating desolvation processes.

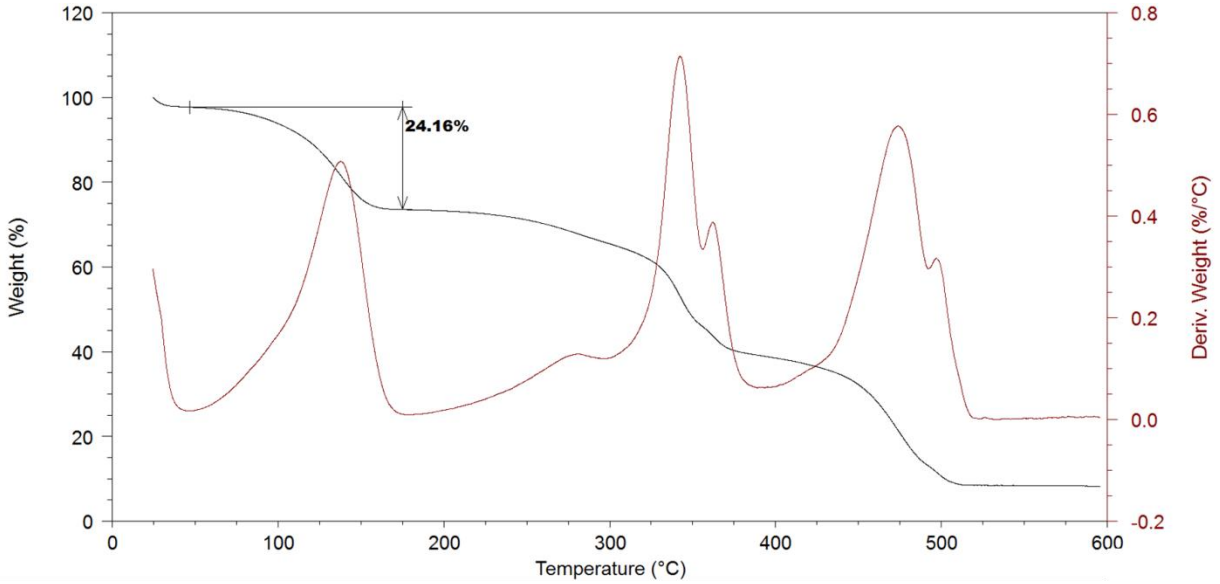

Figure S41: Thermogram of **1b** (prepared mechanochemically). The weight loss of 24.2% is equal to *ca* 2 DMF molecules per host formula unit (calculated 25.0%). The initial weight loss between onset and *ca* 45 °C may be attributed to excess surface solvent. The paste formed by the mechanochemical preparation proved difficult to dry adequately without initiating desolvation processes.

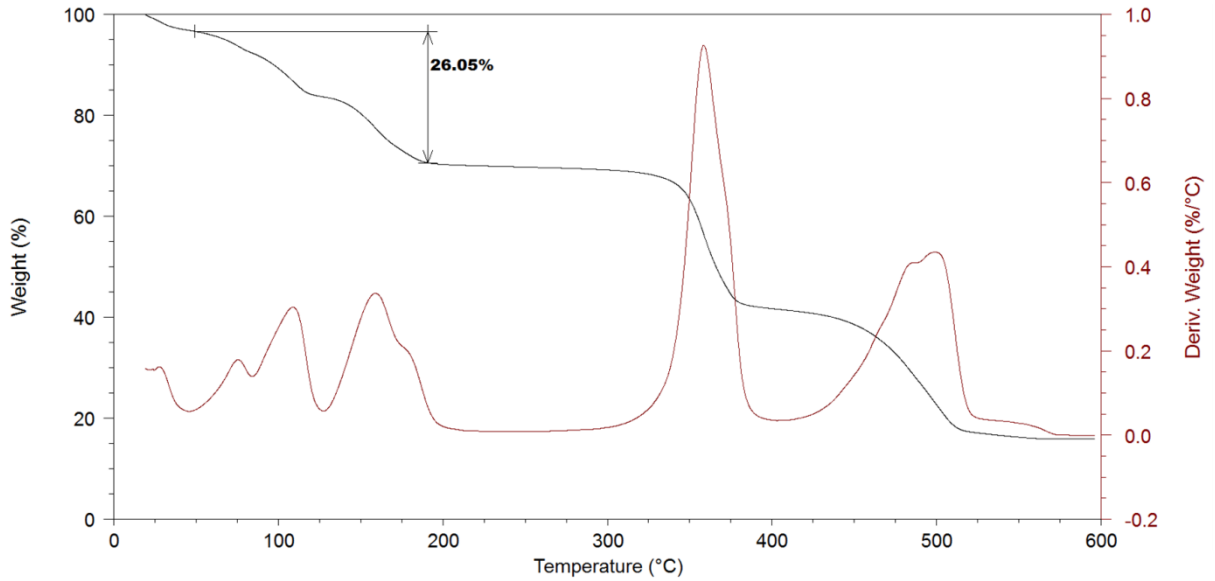

Figure S42: Thermogram of **1c** (single crystals). The weight loss of 26.1% is equal to *ca* two DMF and 0.5 H_2O molecules per host formula unit (calculated 25.1%). The initial weight loss between onset and *ca* 45 °C may be attributed to excess surface solvent. Care was taken not to excessively dry the sample before analysis as these materials desolvate quite rapidly, even under ambient conditions.

8. Differential Scanning Calorimetry (DSC)

DSC was performed on a TA Q20 instrument. Samples ranging in weight between 4 and 7 mg were placed in aluminium pans with perforated lids. An N_2 gas flow rate of 50 ml min^{-1} was used. The temperature was ramped between the upper and lower temperature bounds over three cycles with a heating rate of 5 °C min^{-1} for cooling and 10 °C min^{-1} for heating segments. The resultant data was analysed using the TA Instruments Universal Analysis program.

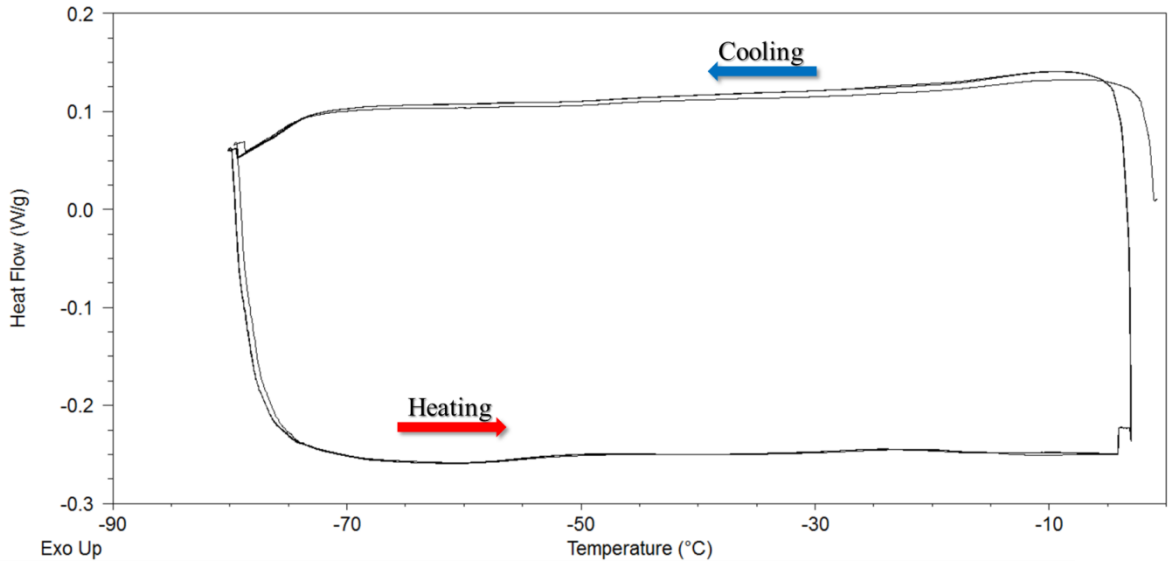

Figure S43: Low temperature DSC thermogram of **1a** (prepared mechanochemically) over three cycles. No events occurred in the temperature range scanned.

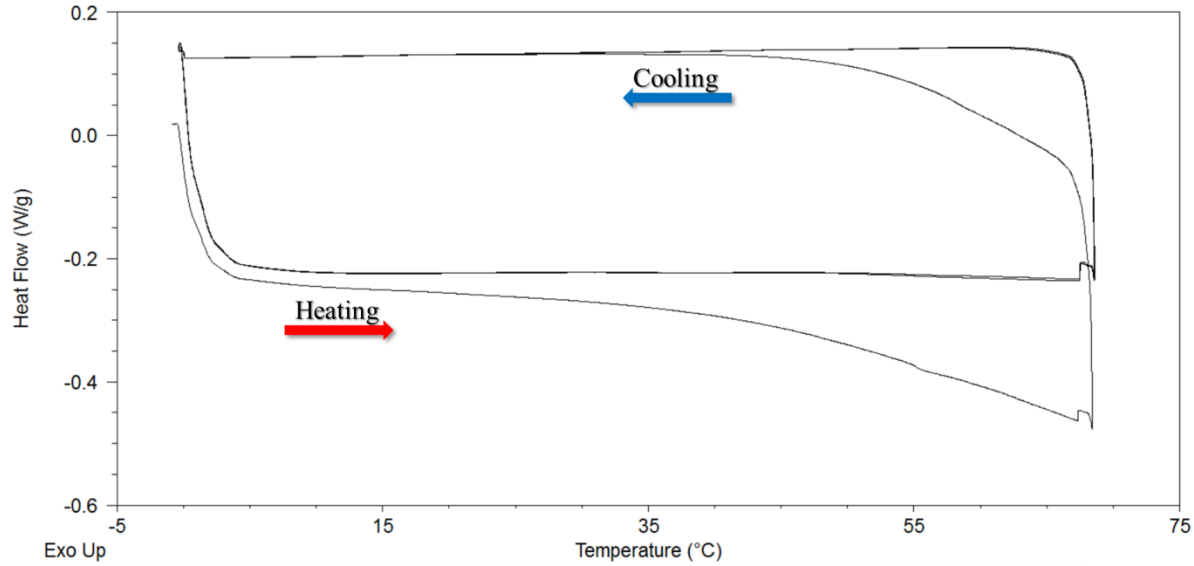

Figure S44: High temperature DSC thermogram of **1a** (prepared mechanochemically) over three cycles. No events occurred in the temperature range scanned.

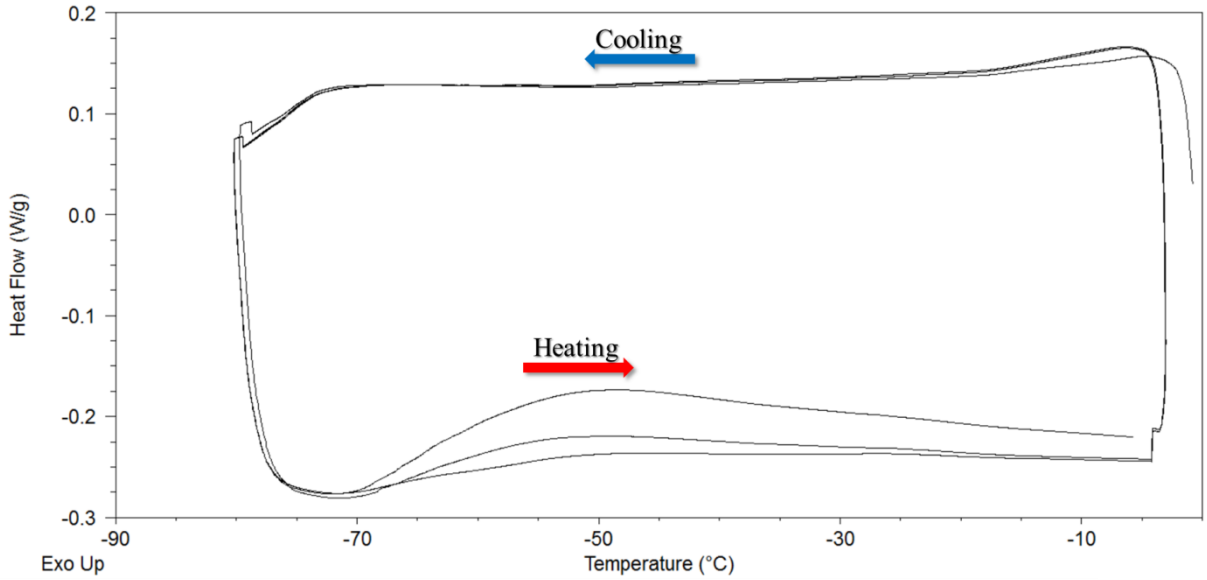

Figure S45: Low temperature DSC thermogram of **1b** (prepared mechanochemically) over three cycles. No events occurred in the temperature range scanned. The slight inflection below -60 °C is likely related to a small amount of surface DMF freezing.

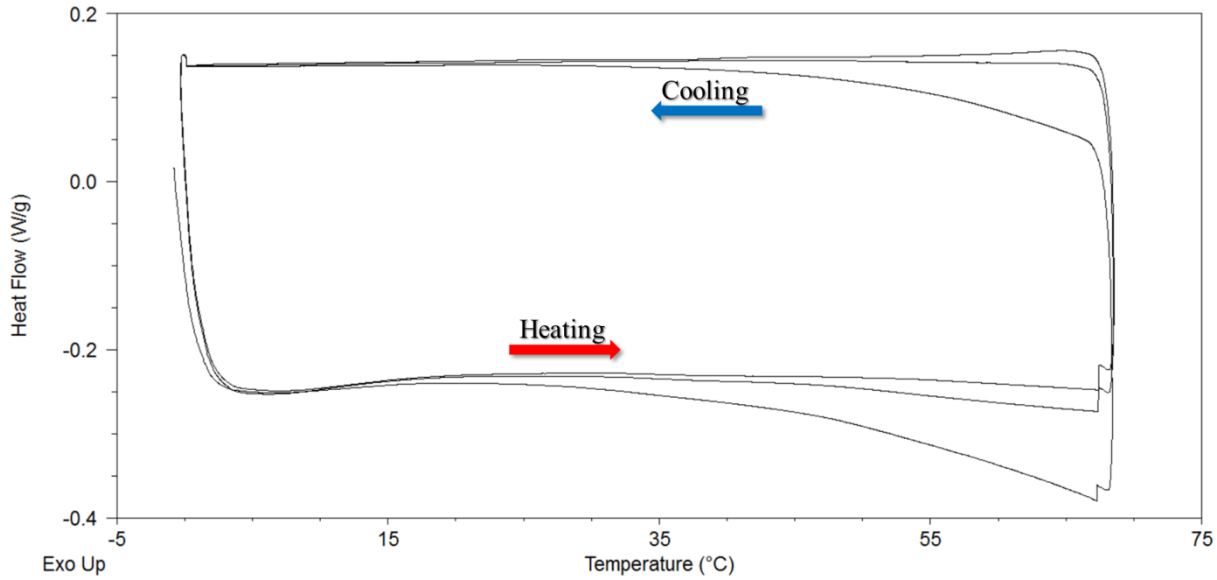

Figure S46: High temperature DSC thermogram of **1b** (prepared mechanochemically) over three cycles. No events occurred in the temperature range scanned.

References

1 MiTeGen, MiTeGen, https://www.mitegen.com/, (accessed 25 June 2018).

2 Bruker AXS Inc., 2016.

3 Bruker AXS Inc., 2016.

4 G. M. Sheldrick, *Acta Cryst.*, 2015, **A71**, 3–8.

5 G. M. Sheldrick, *Univ. Gottingen, Ger.*, 2018.

6 L. J. Barbour, *J. Supramol. Chem.*, 2001, **1**, 189–191.

7 L. J. Barbour, *J. Appl. Cryst.*, 2020, **53**, 1–6.

8 C. R. Groom, I. J. Bruno, M. P. Lightfoot and S. C. Ward, *Acta Crystallogr.*, 2016, **B72**, 171–179.

9 Persistence of Vision Raytracer Pty. Ltd., 2004.

10 A. L. Spek, *J. Appl. Crystallogr.*, 2003, **36**, 7–13.

11 A. L. Spek, *Acta Crystallogr.*, 2009, **D65**, 148–155.

12 Bruker AXS Inc., *Bruker AXS Inc., Wisconsin, USA*, 2016.

13 T. Friščić, *J. Mater. Chem.*, 2010, **20**, 7599–7605.

14 Bruker AXS Inc., 2008.

15 A. A. Coelho, *J. Appl. Crystallogr.*, 2003, **36**, 86–95.

Chapter 4 – Colossal Trellis-Like Single-Crystal to Single-Crystal Structural Transformations in Two 1D Coordination Polymers

"Equipped with his five senses, man explores the universe around him and calls the adventure Science."

— Edwin Powell Hubble

4.1. Article (submitted to a peer-reviewed journal)

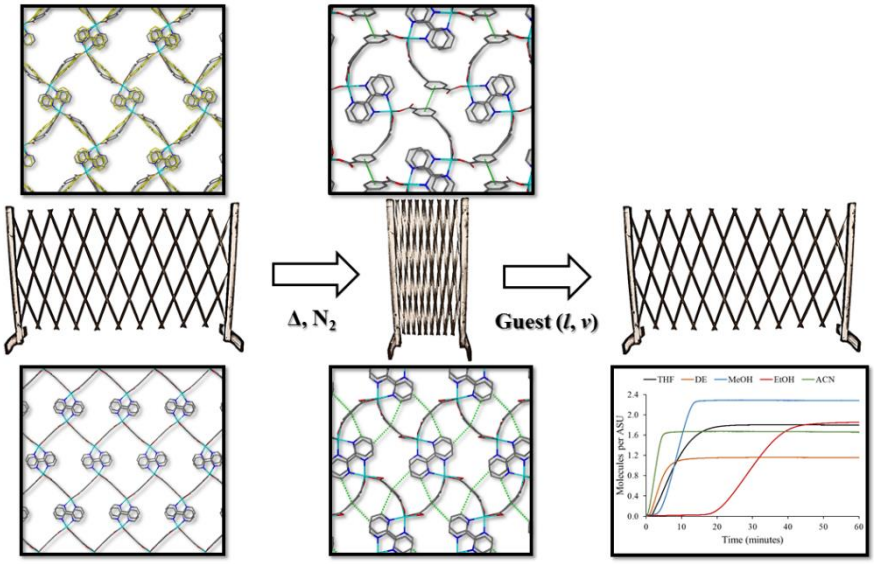

4.1.1. Contributions by author

- Design of the project
- Preparation and handling of crystals
- Collection of single-crystal X-ray diffraction data
- Structure solution and refinement
- Modelling of disorder
- Recording TGA thermograms
- Collection of powder X-ray diffraction data
- Execution of vapor sorption experiments
- Interpretation of results
- Writing of the first draft of the article

Colossal Trellis-Like Single-Crystal to Single-Crystal Structural Transformations in Two 1D Coordination Polymers

*Lisa M. van Wyk and Leonard J. Barbour**

Department of Chemistry and Polymer Science, University of Stellenbosch, 7602 Matieland, South Africa. Email: ljb@sun.ac.za

ABSTRACT

Two 1D coordination polymers exhibit dramatic trellis-like structural contraction during activation, resulting in the contortion of conceptually rigid ligands in the guest-free forms. Structural expansion may be effected by liquid guest in both cases, and by vapor in one. Vapor sorption behavior varies with changes in vapor pressure and kinetic diameter of the solvent in question.

INTRODUCTION

Coordination polymers (CPs) have attracted interest for more than three decades owing to their structural versatility, which often gives rise to distinctive chemical and physical properties.[1] As a result, CPs have a range of potential applications, including the storage,[2–4] separation[5,6] and sensing of small guest molecules,[7,8] as well as catalysis[9–11] and magnetism.[12–14] A fundamental understanding of the structure-property relationships of CPs is essential to the rational design of dynamic functional materials based on such systems. Typically, these studies benefit substantially from structural transformations that occur in a

single-crystal to single-crystal (SC-SC) manner. This is because routine structural solution from powder diffraction data using standard laboratory instrumentation is often a difficult process.[1,15] However, structural transformation of a crystal often introduces significant mechanical strain, leading to an increase in mosaicity or even to disintegration.[1] Therefore, SC-SC transformations are observed relatively infrequently for phase changes that involve large structural rearrangements at the molecular level.[16–18] Although some 1D CPs are known to undergo SC-SC transformations,[19–23] very few examples of substantial structural changes in such materials have been reported. Furthermore, many known 1D CPs do not possess large probe-accessible volumes (PAV)[24] because they often favor close-packed (or near close-packed) solid-state arrangements.

Owing to the toxicity of many volatile organic compounds (VOCs),[25,26] materials that can capture various vapors are of interest to both fundamental research and to industry. To mitigate costs, such materials should ideally be easy to prepare, and regenerable. Although viable low-cost options are available (e.g., activated carbons and zeolites), their preparation relies on calcination techniques and/or mining operations. Coordination compounds therefore present opportunities for cyclable and environmentally friendly capture of VOCs if their preparation and regeneration can be optimized.[27]

EXPERIMENTAL SECTION

2.1. Materials

Unless otherwise indicated, all reagents were obtained from commercial suppliers (Sigma-Aldrich, Alfa Aesar, Merck) and used without further purification.

2.2. Solvothermal crystallization

{[Zn(bpdc)(bpy)]·2DMF}*n* (**1**) was prepared solvothermally. In a scintillation vial, equimolar amounts of the ligands 4,4′-biphenyldicarboxylic acid (bpdc, 0.30 mmol, 73 mg) and

2,2′-bipyridine (bpy, 0.30 mmol, 47 mg), along with $Zn(NO_3)_2 \cdot 6H_2O$ (0.40 mmol, 119 mg) were added to 5 ml *N,N*-dimethylformamide (DMF) and sonicated until partially dissolved. The vial was heated at 80 °C in an oven for 4–7 days. Clear rod-shaped crystals were deposited in quantitative yield. {[Zn(bdc)(bpy)]·DMF}*n* (**2**) was prepared in similar manner to **1** from 1,4-benzenedicarboxylic acid (bdc, 0.1 mmol, 17 mg) and bpy (0.1 mmol, 16 mg) and $Zn(NO_3)_2 \cdot 6H_2O$ (0.15 mmol, 45 mg) in 3 ml DMF. Clear plates crystallized in quantitative yield.

2.3. Activation procedures

Crystals of **1** were activated in the furnace of a thermogravimetric analyzer (T_{max} = 180 °C, ramp rate = 5 °C min^{-1}, N_2 purge = 40 ml min^{-1}) to yield single crystals of the guest-free phase **1a**. Crystals of **2** were activated by supercritical CO_2 drying (T = 40 °C, P ≈ 100 bar, t ≈ 4–6 hours) to yield single crystals of the guest-free phase **2a**. Supercritical drying was carried out using a Tousimis™ Samdri® PVT-3D critical point dryer.

2.4. Single-crystal X-ray diffraction

X-ray intensity data were recorded on a Bruker APEX II DUO or a Bruker D8 Venture diffractometer. The APEX II DUO is equipped with an Incoatec IμS molybdenum (λ = 0.71073 Å) microfocus X-ray source and a CCD area detector. The D8 Venture is equipped with an Incoatec IμS 3.0 molybdenum (λ = 0.71073 Å) microfocus X-ray source and a Photon II CPAD detector. The diffractometers are equipped with Oxford Cryosystems cryostats (Cryostream 700 Plus and Cryostream 800 Plus, respectively). Data reduction and absorption corrections were carried out using the SAINT[28] and SADABS[29] programs, respectively. Unit-cell dimensions were refined on all data and space groups were assigned based on systematic absences and intensity statistics. The structures were solved using a dual-space algorithm employed by SHELXT.[30] Structure refinement was carried out with

SHELXL-2018/3[31] using the X-Seed[32,33] graphical user interface. Non-hydrogen atoms were refined anisotropically and hydrogen atoms were placed in calculated positions using riding models. Illustrations of all crystal structures were generated using the programs POV-Ray[34] and Mercury.[35–37]

2.5. Powder X-ray diffraction (PXRD)

A Bruker D2 Phaser powder diffractometer was used to record experimental diffractograms. The diffractometer utilizes Bragg-Brentano geometry and Cu Kα radiation (λ = 1.5418 Å) as the incident beam. The diffractometer was operated at 30 kV and 10 mA. Samples were placed on a rotating (30° min^{-1}) flat stage and intensity data were recorded using a Lynxeye detector. Samples were finely ground (where necessary) using a mortar and pestle, loaded onto a zero-background sample holder and levelled with a glass slide (where possible). Diffractograms were recorded under ambient conditions using a scanning range of 5–40°, a step size of 0.016° and a scan speed of 0.8 s per step.

2.6. Gravimetric Vapor Sorption

A modified version of the vapor balance setup reported by Barbour and co-workers[38] was used to carry out vapor sorption experiments. The system provides an accurate measure of the change in sample weight as a function of time. The vapor balance is enclosed in a temperature-controlled cabinet. The sample is placed in a perforated aluminum basket, which is suspended from the microbalance by a thin steel wire. A vacuum pump allows the system to be evacuated dynamically to a pressure of 0.1 mbar. Typical sample sizes range from 15-30 mg, and the temperature is maintained at 23 °C. After introduction of the sample vapor the experiment is allowed to run until the sample weight reaches a plateau (indicating equilibrium). If required, the desorption profile can also be recorded by applying dynamic vacuum.

RESULTS AND DISCUSSION

Here we report two analogous CPs, each consisting of irregular octahedral zinc(II) nodes linked by means of a linear dicarboxylate ligand (either 4,4′-biphenyldicarboxylic acid (bpdc) or 1,4-benzenedicarboxylic acid (bdc)), and with the remaining two coordination sites occupied by a chelating 2,2′-bipyridine (bpy) ligand. This arrangement facilitates propagation of the coordination compound in one dimension only. $\{[Zn(bpdc)(bpy)]\cdot 2DMF\}_n$ (**1**) and $\{[Zn(bdc)(bpy)]\cdot DMF\}_n$ (**2**) (DMF = *N*,*N*-dimethylformamide) were prepared solvothermally in DMF. CPs **1** and **2** crystallize in the same space group ($P2_1/n$ and $P2_1/c$, respectively) and exhibit analogous crystal packing motifs consisting of 1D "zig-zag" strands that intercalate by means of π···π interactions between offset bpy moieties of neighboring strands to form large 1D channels (Fig. 1).

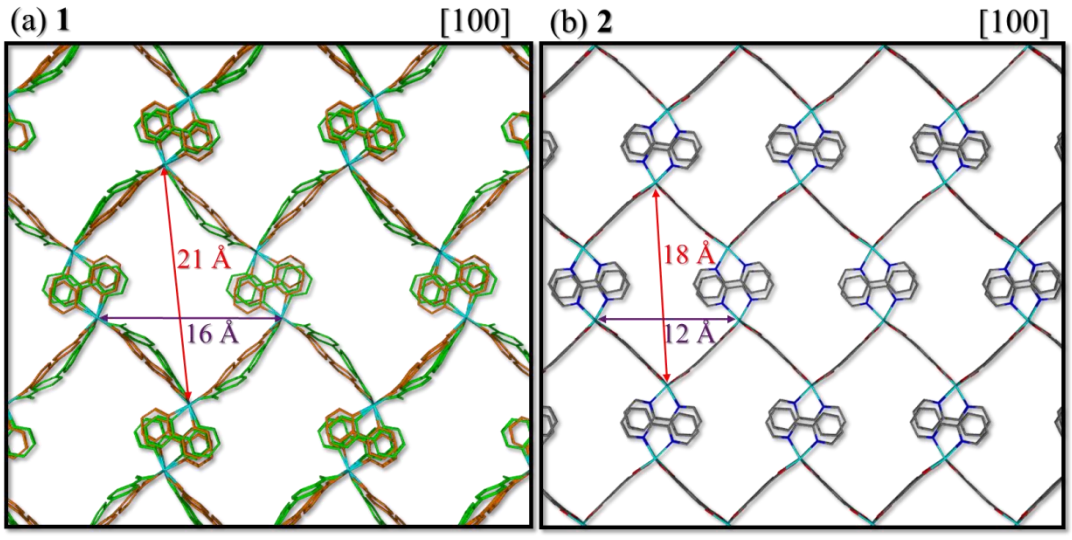

Figure 1. Crystal packing of (a) **1** and (b) **2** viewed along the crystallographic *a* axis. Guest molecules and hydrogen atoms are omitted. In (a) the major component of each ligand disorder is shown in green and the minor in orange. The approximate atom-to-atom dimensions of each solvent-accessible aperture are shown.

In **1** the channels propagate along [100] and contain DMF guest molecules. Although it was not possible to model the guest molecules crystallographically, their presence and

occupancies were determined by means of infrared spectroscopy and thermogravimetry (Figs. S5 and S7), respectively. Each of the bpdc and bpy moieties is disordered over two positions (with site occupancy distributions of 50:50 and 62:38, respectively). The PAV (considering either component of the bpdc disorder) consists of approximately 45–46% of the total volume (Fig. S2a, b).

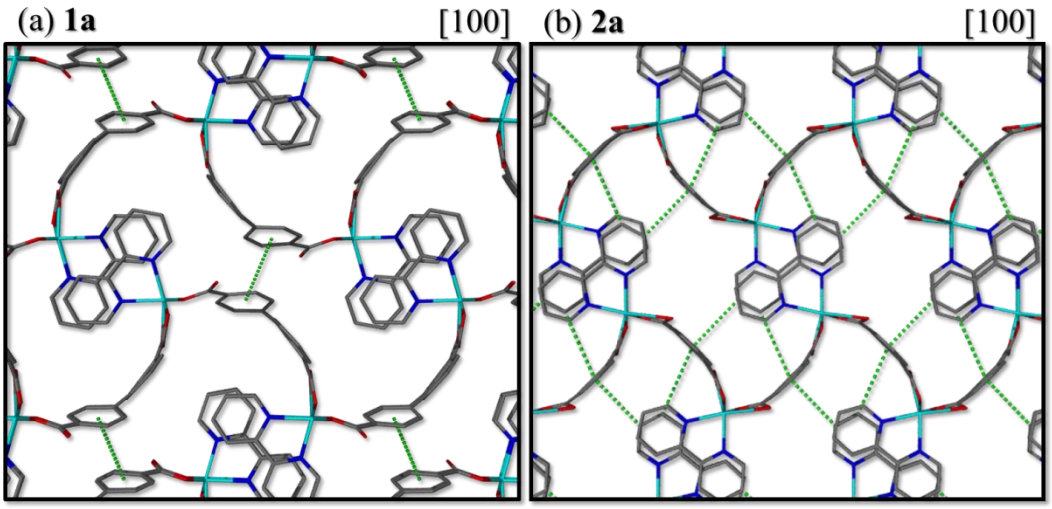

Figure 2. Crystal packing of (a) **1a** and (b) **2a** viewed along the *a* axis. Dotted green lines in (a) illustrate π···π interactions between adjacent bpdc ligands (centroid–centroid 3.663(6) Å) and in (b) C–H···π interactions between adjacent bpy and bdc ligands (centroid–C 3.509(11) and 3.963(11) Å) are shown. Hydrogen atoms have been omitted for clarity.

Based on this promising 'virtual porosity',[39] CP **1** was activated (see Experimental section and SI) with a view to investigating its guest inclusion properties. We note that precise control of the conditions is required to ensure that activation proceeds as a SC-SC process. Direct comparison of **1** with its apohost structure (**1a**) shows that activation preserves the space-group symmetry, but results in dramatic contraction of the crystal, which results in a 'virtually'[39] non-porous apohost form, with apparent collapse of the 1D channels upon guest removal (Fig. 2a).

During the transformation from **1** to **1a** the *b* axis contracts substantially (by 34%), along with slight contraction of the *c* axis (by 9%), with a total reduction of the unit-cell volume by *ca*

39%. There are relatively few examples of SC-SC transformations that result in a structural contraction of similar magnitude,[40–43] and even fewer examples exceeding this value.[44] Notably, very few of these examples involve CPs, with most being 2D and 3D framework materials. Furthermore, activation results in ordering of the previously disordered ligands, and could plausibly be due to the lack of free space in the close-packed apohost structure. To establish unequivocally that the transformation of **1** to **1a** occurs as a SC-SC process, a crystal of **1** was activated *in situ* while mounted on a single-crystal diffractometer (Table S2, Fig. S1). This experiment also illustrates that the change in size of the crystal corresponds to the changes in the unit-cell parameters (Table S3).

The translations that accompany activation result in the formation of π···π interactions between adjacent bpdc linkers in **1a.** These interactions cause unusual contortion of the conceptually rigid bpdc ligand (Figs. 2a, S3, S4). A search of the Cambridge Structural Database[45] revealed that **1a** exhibits the largest deviation from linearity observed to date for bpdc and analogous ligands (Fig. S4, Table S4).

To investigate whether the guest-free form **1a** would undergo further structural transformation upon reintroduction of guest molecules, a number of experiments (including exposure to possible guests in either gas, liquid or vapor form) were carried out, with various levels of success. Gas sorption was investigated using pressure-gradient differential scanning calorimetry (PG-DSC, see SI).[46] Exposure of **1a** to 50 bar of CO_2, CH_4 and N_2 gas resulted in no structural changes or guest sorption (as determined by PG-DSC, Fig. S26). Next, resolvation was carried out by immersing **1a** in fresh DMF overnight. The material undergoes structural transformation to an open form (**1′**) determined by means of powder X-ray diffraction (PXRD) to be structurally analogous to **1** (Fig. S21). Single-crystal X-ray diffraction (SCXRD) analysis of **1′** was not possible since the resolvation process resulted in disintegration of the crystals into a polycrystalline material. This is likely due to the large stress involved in structural transformation back to the open form **1′**. Finally, vapor sorption

was carried using a customized vapor balance,[38] which monitors sample mass as a function of time during exposure to solvent vapor. In each vapor sorption experiment two cycles were carried out, each entailing sorption for 90 minutes followed by the application of dynamic vacuum (desorption) for 90 minutes. A fresh sample of **1** was used for each vapor sorption experiment. Exposing **1a** to vapors of tetrahydrofuran (THF), 1,4-dioxane, *p*-xylene and toluene did not result in sorption (or structural transformation); no increase in sample mass was observed during 90 minutes of exposure and the PXRD pattern was similar to that of **1a**.

CP **2** packs in an analogous manner to **1**, with DMF containing paired channels that are periodically interconnected to each other (Fig. 3, S2c, 31.9% PAV), also extending along [100]. Both of the ligands in **2** are ordered. The structural transformation from **2** to **2a** involves considerable contraction along the *b* and *c* axes, resulting in a reduction in the unit-cell volume by *ca* 22%. As for **1,** activation of **2** produces a 'virtually nonporous' apohost form (**2a**). Structural translations accompanying activation result in the formation of C–H···π

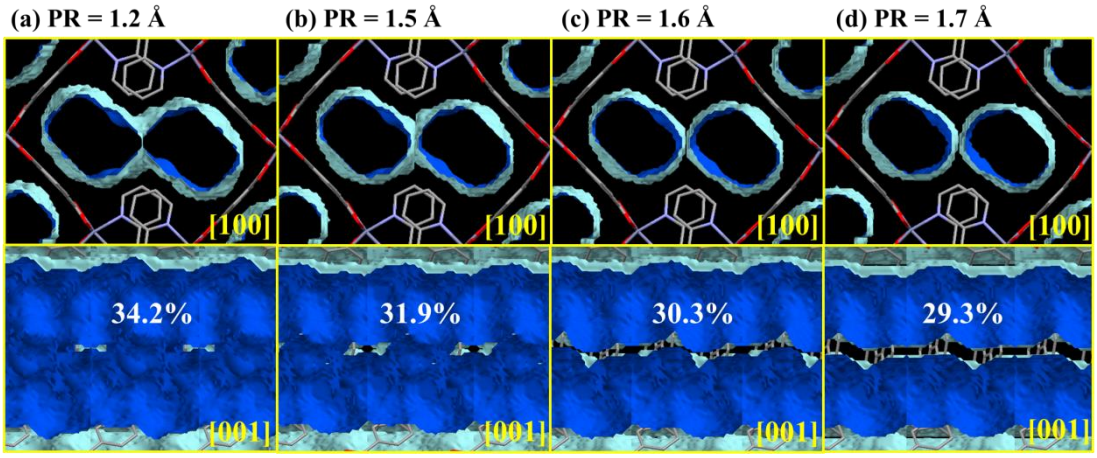

Figure 3. PAV surfaces generated with various probe radii (PR) for **2**: (a) 1.2 , (b) 1.5 , (c) 1.6 and (d) 1.7 Å. The upper row shows PAVs viewed down the *a* axis. The bottom row shows a cross-section of a channel set viewed down the *c* axis. The percentage of the crystal structure occupied by the PAV is shown. Hydrogen atoms and guest molecules are omitted for clarity.

interactions between adjacent bpy and bdc ligands in **2a** (Fig. 2b), which cause slight contortion of the conceptually rigid bdc ligands.

PG-DSC (1 to 50 bar of CO_2, CH_4 and N_2) of **2a**, showed no gas sorption or phase change events (Fig. S27). Similarly to **1a**, immersion of **2a** in fresh DMF overnight resulted in a polycrystalline structural transformation to an open phase denoted **2′** (Fig. S22). In each case, exposure of **2a** to vapors of THF, diethyl ether (DE), ethanol (EtOH), methanol (MeOH) and acetonitrile (ACN) resulted in uptake of the guest, from which we infer a structural transformation to an open phase denoted **2″** (Figs. 4, S23). However, **2a** did not appear to absorb vapors of 1,4-dioxane, *p*-xylene and cyclohexane within 90 minutes, implying that no structural transformation to an open form takes place in these instances. It is possible that

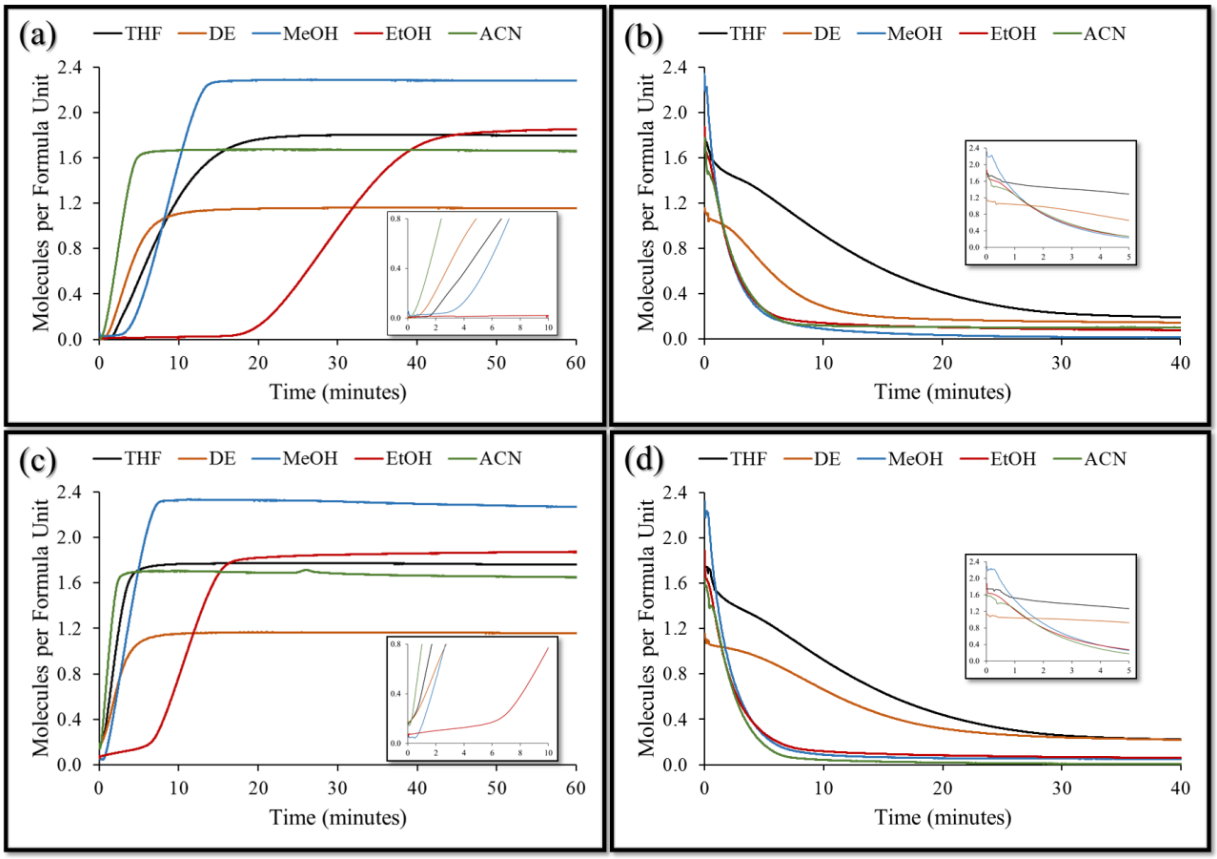

Figure 4. Vapor sorption (left) and desorption (right) profiles for **2a**. Two sorption-desorption cycles were carried out consecutively. Cycle 1 is shown in (a) and (b), and cycle 2 in (c) and (d). Insets show the first 10 minutes of sorption in (a) and (c), and the first 5 minutes of desorption in (b) and (d).

these compounds are too sterically bulky for inclusion in the guest-accessible space, since they have the largest kinetic diameters of all the VOCs tested (Table S6). Furthermore, these vapors also do not appear to exchange with the DMF of the as-synthesized material **2**, as determined by thermogravimetry (Fig. S16). This suggests that a size-exclusion effect may prohibit the uptake of larger cyclic compounds.

The first vapor sorption cycle shows a latent period where the channels of **2a** remain closed, after which the structure opens to allow uptake of the vapor (Fig. 4a). The desorption profiles for THF and DE are stepped; an initial drop in guest occupancy occurs within the first few minutes (Fig. 4b), followed by an inflection point after which the guest occupancy decreases more rapidly. For the other sorbed vapors there is no notable inflection point. However, this may also be due to the relative speed of desorption. In some cases the guest occupancy does not return to zero (*i.e.,* THF and DE), and thus the material might not revert completely to **2a** because some portion remains open (**2′′**). This was confirmed by PXRD of the desorbed materials in most cases (Fig. S23), with the exception of MeOH and ACN. The diffractogram for each desorbed sample shows peaks at *ca* 8° 2θ, which corresponds to the major characteristic peak of the open form **2**. However, the remainder of the diffractogram matches that of the guest-free material **2a**. The relative intensities of the characteristic peaks of each form (open and closed) indicate that the sample consists predominantly of **2a**. Heating the THF-desorbed sample at 75 °C under dynamic vacuum for several hours did not lead to any distinct change in the diffractogram (Fig. S24). Subsequent thermogravimetric analysis confirms that the material is guest-free at this point (Fig. S17). Thus, the consecutive structural transformations between the closed and open forms result in bulk **2a** never being entirely recovered. We believe that the remaining open phase then facilitates more rapid reopening to **2′′** in consecutive sorption cycles. This phenomenon is observed in the second sorption cycle, which shows a reduced or no initial latent period compared to that of the first cycle for each solvent vapor (Fig. 4c). The diffractograms of the samples post MeOH and

ACN sorption reveal that the materials have entirely collapsed to closed forms and match that of **2a** (Fig. S23). This may be explained by the facile desolvation of these solvates of **2**, which proved difficult to analyze via thermogravimetry (especially in the case of the MeOH solvate, Fig. S13). However, the latent period in the second cycle of MeOH vapor sorption was notably diminished relative to the first cycle.

Intriguingly, in all cases where vapor sorption occurred, the maximum guest occupancy attained far exceeded that expected (nearly double in some cases) from thermogravimetric analyses of the respective solvates. This was likely due to condensation of solvent on the sample during sorption (Fig. S18). The presence of surface solvent may explain the inflection point observed during the desorption of certain solvent vapors. Under dynamic vacuum the surface solvent is removed relatively easily from the material, after which the included guest is then desorbed. Condensation did not occur during experiments with vapors that were not included (namely 1,4-dioxane, cyclohexane and *p*-xylene). Thus, the process of solvent deposition on the surface of the material seems to be connected to guest uptake. Although solvent uptake occurs rapidly, both solvent components (surface and guest) are readily removed from the material under reduced pressure.

The trends observed in each vapor sorption experiment are comparable, with the principal dissimilarity being the duration of the latent period before the onset of sorption. This is likely a consequence of several factors, including host-guest affinity (confined to relatively weak interactions), guest vapor pressure (Table S5) and guest kinetic diameters (Table S6). THF and DE have the highest vapor pressures at ambient conditions, but also the largest kinetic diameters. Thus, relative to the other solvents investigated, these compounds display moderate latent periods for sorption and delayed desorption curves. Although ACN possesses one of the smallest kinetic diameters of the sorbed vapors, it also has one of the lowest vapor pressures. Since it is both sorbed and desorbed rapidly, its small kinetic diameter may facilitate its ease of movement in and out of the channels. MeOH and EtOH have the longest

latent periods during both of the consecutive sorption cycles and this is possibly related to their lower vapor pressures, since they also possess some of the smallest kinetic diameters. These vapors also desorb rapidly, which may also be attributed to the small kinetic diameters of these molecules. Thus small molecules with high vapor pressures appear to be associated with shorter latent periods before sorption occurs, and they desorb with relative ease, with the opposite being true for larger molecules with lower vapor pressures.

The fact that only liquid DMF induces framework reopening in **1a** but both liquid DMF and certain solvent vapors induce structural transformation in **2a** could be a consequence of the relative strengths of the supramolecular interactions that stabilize the two different structures. **1a** has notably stronger interactions (π···π interactions) than **2a** (C–H···π). Subsequently, it is possible that there exists a smaller energy barrier in **2a** to overcome the interactions keeping the channel closed than in **1a**.

CONCLUSION

We have prepared two novel CPs with large solvent-accessible volumes in their as-synthesized forms. Upon activation these materials undergo colossal trellis-like SC-SC contraction; the apohost forms display considerable contortion of the conceptually rigid dicarboxylic acid ligands, with **1a** exceeding all known examples of ligand contortion. Both apohost materials can be resolvated by immersion in DMF to recover their open phases. **2a** will also reopen when exposed to certain solvent vapors. The apohost material is largely or entirely regenerable, with consecutive sorption cycles occurring at lower vapor pressures. Condensation of solvent vapor on the surface of the material allows for much higher equilibrium capacity than expected. In some cases this increase is more than twice that expected. Furthermore, trends in the rapidity of the sorption and desorption cycles likely stem from trends in the kinetic diameter and vapor pressures of the individual solvents.

ASSOCIATED CONTENT

Supporting Information.

The Supporting Information is available free of charge at XXX.

Additional figures, synthesis and characterization information, including: crystallization and activation procedures, FT-IR, single-crystal X-ray diffraction, powder X-ray diffraction, vapor sorption, *etc.* (PDF).

Accession Codes

CCDC 1940574–1940578 contain the supplementary crystallographic data for this paper. These data can be obtained free of charge via www.ccdc.cam.ac.uk/data_request/cif, or by emailing data_request@ccdc.cam.ac.uk, or by contacting The Cambridge Crystallographic Data Centre, 12 Union Road, Cambridge CB2 1EZ, UK; fax: +44 1223 336033.

AUTHOR INFORMATION

Corresponding Author

*E-mail: ljb@sun.ac.za

Funding Sources

We thank the National Research Foundation (NRF) of South Africa for financial support.

ACKNOWLEDGEMENT

We acknowledge Dr. Peter Müller for his help with single-crystal structural solution and refinement.

REFERENCES

(1) Zhang, J.-P.; Liao, P.-Q.; Zhou, H.-L.; Lin, R.-B.; Chen, X.-M. Single-Crystal X-Ray Diffraction Studies on Structural Transformations of Porous Coordination Polymers. *Chem. Soc. Rev.* **2014**, *43* (16), 5789–5814. https://doi.org/10.1039/C4CS00129J.

(2) Sumida, K.; Rogow, D. L.; Mason, J. A.; McDonald, T. M.; Bloch, E. D.; Herm, Z. R.;

Bae, T.; Long, J. R. Carbon Dioxide Capture in Metal–Organic Frameworks. *Chem. Rev.* **2012**, *112* (2), 724–781. https://doi.org/10.1021/cr2003272.

(3) D'Alessandro, D. M.; Smit, B.; Long, J. R. Carbon Dioxide Capture: Prospects for New Materials. *Angew. Chem., Int. Ed.* **2010**, *49* (35), 6058–6082. https://doi.org/10.1002/anie.201000431.

(4) Mason, J. A.; Veenstra, M.; Long, J. R. Evaluating Metal–Organic Frameworks for Natural Gas Storage. *Chem. Sci.* **2014**, *5* (1), 32–51. https://doi.org/10.1039/C3SC52633J.

(5) Cadiau, A.; Adil, K.; Bhatt, P. M.; Belmabkhout, Y.; Eddaoudi, M. A Metal-Organic Framework-Based Splitter for Separating Propylene from Propane. *Science.* **2016**, *353* (6295), 137–140. https://doi.org/10.1126/science.aaf6323.

(6) Li, J.; Sculley, J.; Zhou, H. Metal–Organic Frameworks for Separations. *Chem. Rev.* **2012**, *112* (2), 869–932. https://doi.org/10.1021/cr200190s.

(7) Yeung, M. C.-L.; Yam, V. W.-W. Luminescent Cation Sensors: From Host–Guest Chemistry, Supramolecular Chemistry to Reaction-Based Mechanisms. *Chem. Soc. Rev.* **2015**, *44* (13), 4192–4202. https://doi.org/10.1039/C4CS00391H.

(8) You, L.; Zha, D.; Anslyn, E. V. Recent Advances in Supramolecular Analytical Chemistry Using Optical Sensing. *Chem. Rev.* **2015**, *115* (15), 7840–7892. https://doi.org/10.1021/cr5005524.

(9) Liu, J.; Chen, L.; Cui, H.; Zhang, J.; Zhang, L.; Su, C.-Y. Applications of Metal–Organic Frameworks in Heterogeneous Supramolecular Catalysis. *Chem. Soc. Rev.* **2014**, *43* (16), 6011–6061. https://doi.org/10.1039/C4CS00094C.

(10) Raynal, M.; Ballester, P.; Vidal-Ferran, A.; van Leeuwen, P. W. N. M. Supramolecular Catalysis. Part 1: Non-Covalent Interactions as a Tool for Building and Modifying Homogeneous Catalysts. *Chem. Soc. Rev.* **2014**, *43* (5), 1660–1733. https://doi.org/10.1039/C3CS60027K.

(11) Raynal, M.; Ballester, P.; Vidal-Ferran, A.; van Leeuwen, P. W. N. M. Supramolecular Catalysis. Part 2: Artificial Enzyme Mimics. *Chem. Soc. Rev.* **2014**, *43* (5), 1734–1787. https://doi.org/10.1039/C3CS60037H.

(12) Glaser, T. Rational Design of Single-Molecule Magnets: A Supramolecular Approach. *Chem. Commun.* **2011**, *47* (1), 116–130. https://doi.org/10.1039/C0CC02259D.

(13) Mihalčiak, J.; Bertová, P.; Růžičková, Z.; Moncol, J.; Segľa, P.; Boča, R. Structure and Magnetism of Novel Dinuclear Cobalt(II) Complexes. *Inorg. Chem. Commun.* **2015**, *56*, 62–64. https://doi.org/10.1016/j.inoche.2015.03.038.

(14) Dul, M.-C.; Pardo, E.; Lescouëzec, R.; Journaux, Y.; Ferrando-Soria, J.; Ruiz-García, R.; Cano, J.; Julve, M.; Lloret, F.; Cangussu, D.; Pereira, C. L. M.; Stumpf, H. O.; Pasán, J.; Ruiz-Pérez, C. Supramolecular Coordination Chemistry of Aromatic Polyoxalamide Ligands: A Metallosupramolecular Approach toward Functional Magnetic Materials. *Coord. Chem. Rev.* **2010**, *254* (19–20), 2281–2296. https://doi.org/10.1016/j.ccr.2010.03.003.

(15) Férey, G.; Serre, C.; Mellot-Draznieks, C.; Millange, F.; Surblé, S.; Dutour, J.; Margiolaki, I. A Hybrid Solid with Giant Pores Prepared by a Combination of Targeted Chemistry, Simulation, and Powder Diffraction. *Angew. Chem., Int. Ed.* **2004**, *43* (46), 6296–6301. https://doi.org/10.1002/anie.200460592.

(16) Kawano, M.; Fujita, M. Direct Observation of Crystalline-State Guest Exchange in Coordination Networks. *Coord. Chem. Rev.* **2007**, *251* (21–24), 2592–2605. https://doi.org/10.1016/j.ccr.2007.07.022.

(17) Vittal, J. J. Supramolecular Structural Transformations Involving Coordination Polymers in the Solid State. *Coord. Chem. Rev.* **2007**, *251* (13–14), 1781–1795. https://doi.org/10.1016/j.ccr.2007.02.002.

(18) Kole, G. K.; Vittal, J. J. Solid-State Reactivity and Structural Transformations Involving Coordination Polymers. *Chem. Soc. Rev.* **2013**, *42* (4), 1755–1775.

https://doi.org/10.1039/c2cs35234f.

(19) Mori, W.; Hoshino, H.; Nishimoto, Y.; Takamizawa, S. Synthesis and Gas Occlusion of New Micropore Substance Rhodium(II) Carboxylates Bridged by Pyrazine. *Chem. Lett.* **1999**, *28* (4), 331–332. https://doi.org/10.1246/cl.1999.331.

(20) Takamizawa, S.; Nakata, E. I.; Yokoyama, H. Synthesis of Novel Copper (II) Benzoate Pyrazine and Its Phase Transition Induced by CO2 Adsorption. *Inorg. Chem. Commun.* **2003**, *6* (6), 763–765. https://doi.org/10.1016/S1387-7003(03)00078-9.

(21) Takahashi, K.; Hoshino, N.; Takeda, T.; Noro, S. I.; Nakamura, T.; Takeda, S.; Akutagawa, T. Structural Flexibilities and Gas Adsorption Properties of One-Dimensional Copper(II) Polymers with Paddle-Wheel Units by Modification of Benzoate Ligands. *Inorg. Chem.* **2015**, *54* (19), 9423–9431. https://doi.org/10.1021/acs.inorgchem.5b01168.

(22) Nagarathinam, M.; Vittal, J. J. Anisotropic Movements of Coordination Polymers upon Desolvation: Solid-State Transformation of a Linear 1D Coordination Polymer to a Ladderlike Structure. *Angew. Chem., Int. Ed.* **2006**, *45* (26), 4337–4341. https://doi.org/10.1002/anie.200600376.

(23) Dutta, B.; Sinha, C.; Mir, M. H. The Sunlight-Driven Photosalient Effect of a 1D Coordination Polymer and the Release of an Elusive Cyclobutane Derivative. *Chem. Commun.* **2019**, *55* (74), 11049–11051. https://doi.org/10.1039/c9cc06016b.

(24) van Heerden, D. P.; Barbour, L. J. Guest-Occupiable Space in the Crystalline Solid State: A Simple Rule-of-Thumb for Predicting Occupancy. *Chem. Soc. Rev.* **2021**, *50* (2), 735–749. https://doi.org/10.1039/d0cs01040e.

(25) Bale, A. S.; Meacham, C. A.; Benignus, V. A.; Bushnell, P. J.; Shafer, T. J. Volatile Organic Compounds Inhibit Human and Rat Neuronal Nicotinic Acetylcholine Receptors Expressed in Xenopus Oocytes. *Toxicol. Appl. Pharmacol.* **2005**, *205* (1), 77–88. https://doi.org/10.1016/j.taap.2004.09.011.

(26) Boeglin, M. L.; Wessels, D.; Henshel, D. An Investigation of the Relationship between Air Emissions of Volatile Organic Compounds and the Incidence of Cancer in Indiana Counties. *Environ. Res.* **2006**, *100* (2), 242–254. https://doi.org/10.1016/j.envres.2005.04.004.

(27) Vellingiri, K.; Kumar, P.; Kim, K. Coordination Polymers: Challenges and Future Scenarios for Capture and Degradation of Volatile Organic Compounds. *Nano Res.* **2016**, *9* (11), 3181–3208. https://doi.org/10.1007/s12274-016-1230-7.

(28) Bruker AXS Inc. SAINT Data Collection Software. Bruker AXS Inc.: Madison, WI 2016.

(29) Bruker AXS Inc. SADABS Data Correction Software. Bruker AXS Inc.: Madison, WI 2016.

(30) Sheldrick, G. M. SHELXT – Integrated Space-Group and Crystal-Structure Determination. *Acta Cryst.* **2015**, *A71*, 3–8.

(31) Sheldrick, G. M. SHELXS Version-2018/3 and SHELXL Version-2018/3: Programs for Crystal Structure Solution and Refinement. *University of Göttingen, Germany*. 2018.

(32) Barbour, L. J. X-Seed - A Software Tool for Supramolecular Crystallography. *J. Supramol. Chem.* **2001**, *1* (4–6), 189–191. https://doi.org/10.1016/S1472-7862(02)00030-8.

(33) Barbour, L. J. X-Seed 4 : Updates to a Program for Small-Molecule Supramolecular Crystallography. *J. Appl. Crystallogr.* **2020**, *53* (4), 1141–1146. https://doi.org/10.1107/S1600576720007438.

(34) Persistence of Vision Raytracer Pty. Ltd. POV-Ray for Windows. Persistence of Vision Raytracer Pty. Ltd.: Williamstone 2004.

(35) Macrae, C. F.; Edgington, P. R.; McCabe, P.; Pidcock, E.; Shields, G. P.; Taylor, R.; Towler, M.; Van De Streek, J. Mercury: Visualization and Analysis of Crystal

Structures. *J. Appl. Crystallogr.* **2006**, *39* (3), 453–457. https://doi.org/10.1107/S002188980600731X.

(36) Macrae, C. F.; Bruno, I. J.; Chisholm, J. A.; Edgington, P. R.; McCabe, P.; Pidcock, E.; Rodriguez-Monge, L.; Taylor, R.; Van De Streek, J.; Wood, P. A. Mercury CSD 2.0 - New Features for the Visualization and Investigation of Crystal Structures. *J. Appl. Crystallogr.* **2008**, *41* (2), 466–470. https://doi.org/10.1107/S0021889807067908.

(37) MacRae, C. F.; Sovago, I.; Cottrell, S. J.; Galek, P. T. A.; McCabe, P.; Pidcock, E.; Platings, M.; Shields, G. P.; Stevens, J. S.; Towler, M.; Wood, P. A. Mercury 4.0: From Visualization to Analysis, Design and Prediction. *J. Appl. Crystallogr.* **2020**, *53*, 226–235. https://doi.org/10.1107/S1600576719014092.

(38) Barbour, L. J.; Achleitner, K.; Greene, J. R. A System for Studying Gas-Solid Reaction Kinetics in Controlled Atmospheres. *Thermochim. Acta* **1992**, *205*, 171–177. https://doi.org/10.1016/0040-6031(92)85258-W.

(39) Barbour, L. J. Crystal Porosity and the Burden of Proof. *Chem. Commun.* **2006**, No. 11, 1163. https://doi.org/10.1039/b515612m.

(40) Chen, C.; Goforth, A. M.; Smith, M. D.; Su, C.-Y.; zur Loye, H.-C. [Co2(Ppca)2(H2O)(V4O12)0.5]: A Framework Material Exhibiting Reversible Shrinkage and Expansion through a Single-Crystal-to-Single-Crystal Transformation Involving a Change in the Cobalt Coordination Environment. *Angew. Chem., Int. Ed.* **2005**, *44* (41), 6673–6677. https://doi.org/10.1002/anie.200502309.

(41) Kaneko, W.; Ohba, M.; Kitagawa, S. A Flexible Coordination Polymer Crystal Providing Reversible Structural and Magnetic Conversions. *J. Am. Chem. Soc.* **2007**, *129* (44), 13706–13712. https://doi.org/10.1021/ja074915q.

(42) Bernini, M. C.; Gándara, F.; Iglesias, M.; Snejko, N.; Gutiérrez-Puebla, E.; Brusau, E. V.; Narda, G. E.; Monge, M. Á. Reversible Breaking and Forming of Metal-Ligand Coordination Bonds: Temperature-Triggered Single-Crystal to Single-Crystal

Transformation in a Metal-Organic Framework. *Chem. Eur. J.* **2009**, *15* (19), 4896–4905. https://doi.org/10.1002/chem.200802385.

(43) Demessence, A.; Long, J. R. Selective Gas Adsorption in the Flexible Metal-Organic Frameworks Cu(BDTri)L (L=DMF, DEF). *Chem. Eur. J.* **2010**, *16* (20), 5902–5908. https://doi.org/10.1002/chem.201000053.

(44) Zhang, Y.; Zhang, X.; Lyu, J.; Otake, K.; Wang, X.; Redfern, L. R.; Malliakas, C. D.; Li, Z.; Islamoglu, T.; Wang, B.; Farha, O. K. A Flexible Metal–Organic Framework with 4-Connected Zr 6 Nodes. *J. Am. Chem. Soc.* **2018**, *140* (36), 11179–11183. https://doi.org/10.1021/jacs.8b06789.

(45) Groom, C. R.; Bruno, I. J.; Lightfoot, M. P.; Ward, S. C. The Cambridge Structural Database. *Acta Crystallogr. Sect. B Struct. Sci. Cryst. Eng. Mater.* **2016**, *72* (2), 171–179. https://doi.org/10.1107/S2052520616003954.

(46) Feldmann, W. K.; White, K.-A.; Bezuidenhout, C. X.; Smith, V. J.; Esterhuysen, C.; Barbour, L. J. Direct Determination of Enthalpies of Sorption Using Pressure-Gradient Differential Scanning Calorimetry: CO2 Sorption by Cu-HKUST. *ChemSusChem* **2020**, *13* (1), 102–105. https://doi.org/https://doi.org/10.1002/cssc.201902990.

4.2. Supporting Information

Electronic Supporting Information:

Colossal Trellis-Like Single-Crystal to Single-Crystal Structural Transformations in Two 1D Coordination Polymers

Lisa M. van Wyk and Leonard J. Barbour*

Department of Chemistry and Polymer Science, University of Stellenbosch, 7602 Matieland, South Africa.

* Correspondence to Professor Leonard J. Barbour (Email: ljb@sun.ac.za)

Contents

1. Crystallization & Activation

1.1. Crystallization of 1

{[Zn(bpdc)(bpy)]·2DMF}$_n$ (**1**) was prepared solvothermally. In a scintillation vial, equimolar amounts of the ligands 4,4′-biphenyldicarboxylic acid (bpdc, 0.30 mmol, 73mg) and 2,2′-bipyridine (bpy, 0.30 mmol, 47 mg), along with $Zn(NO_3)_2{\cdot}6H_2O$ (0.40 mmol, 119 mg) were added to 5 ml DMF and sonicated until partially dissolved. The vial was placed in an 80 °C preheated oven for 4–7 days. Clear, rod-shaped crystals were produced in a quantitative yield.

1.2. Activation of 1

Crystals of **1** were activated in a thermogravimetry furnace (T_{max} = 180 °C, ramp rate = 5 °C min^{-1}, N_2 purge = 40 ml min^{-1}) to produce single crystals of the guest-free phase **1a**. Where single crystals of **1a** were not required supercritical CO_2 drying may be used (see §1.4.).

1.3. Crystallization of 2

{[Zn(bdc)(bpy)]·DMF}$_n$ (**2**) was prepared solvothermally. In a scintillation vial, equimolar amounts of the ligands 1,4-benzenedicarboxylic acid (bdc, 0.1 mmol, 17 mg) and 2,2′-bipyridine (0.1 mmol, 16 mg), in addition to $Zn(NO_3)_2{\cdot}6H_2O$ (0.15 mmol, 45 mg) were added to 3 ml DMF and sonicated until partially dissolved. The scintillation vial containing the reaction mixture was then placed in a preheated oven at 80 °C for 4–7 days. The crystallization produced clear plates formed in a quantitative yield.

1.4. Activation of 2

Crystals of **2** were activated by supercritical CO_2 drying (T = 40 °C, P ≈ 100 bar, t ≈ 4–6 hours) to produce single crystals of the guest-free phase **2a**. Supercritical drying was carried out using a Tousimis™ Samdri® PVT-3D critical point dryer.

2. Single-crystal X-ray diffraction (SCXRD)

Crystals of appropriate size possessing suitable morphology and ability to extinguish plane-polarized light were mounted onto the tip of a MiTeGen loop[47] using Paratone®N oil.

The mounted crystal was then placed on a goniometer head attached to a diffractometer. X-ray intensity data were recorded on a Bruker APEX II DUO or a Bruker D8 Venture diffractometer. The DUO instrument is equipped with an Incoatec IμS molybdenum (λ = 0.71073 Å) microfocus X-ray source and a CCD area detector. The Venture instrument is equipped with an Incoatec IμS 3.0 molybdenum (λ = 0.71073 Å) microfocus X-ray source and a Photon II CPAD detector. All diffractometers are fitted with an Oxford Cryosystems cryostat (700 Series Cryostream Plus for the DUO instrument and 800 Series Cryostream Plus for the Venture instrument), which is used to control the sample temperature. Both the frame exposure time and the number of frames collected for each experiment were varied depending on the diffraction quality and characteristics of the mounted crystal.

Data reduction and absorption corrections were carried out using the SAINT[28] and SADABS[29] programs, respectively. Unit-cell dimensions were refined on all data and space groups were assigned based on systematic absences and intensity statistics. The structures were solved with a dual-space algorithm or direct methods using SHELXT[30] or SHELXS-2016/1,[48] respectively. Structure refinement was carried out with SHELXL-2018/1[48] using the X-Seed[32,33] graphical user interface. Non-hydrogen atoms were refined anisotropically. Hydrogen atoms were placed in calculated positions. Illustrations of all crystal structures were generated using the program POV-Ray[34] and Mercury.[35–37]

Table S1. Crystallographic parameters for both the as-synthesized and activated species.

	1	1a	2	2a
Empirical Formula	$C_{30}H_{30}N_4O_6Zn$	$C_{24}H_{16}N_2O_4Zn$	$C_{21}H_{19}N_3O_5Zn$	$C_{18}H_{12}N_2O_4Zn$
Formula weight ($g\ mol^{-1}$)	607.94	461.76	458.77	385.67
Temperature (K)	100(2)	100(2)	100(2)	100(2)
Wavelength (Å)	0.71073	0.71073	0.71073	0.71073
Crystal system	Monoclinic	Monoclinic	Monoclinic	Monoclinic
Space group	$P2_1/n$	$P2_1/n$	$P2_1/c$	$P2_1/c$
a (Å)	7.598 (1)	7.700(4)	7.362(1)	7.638(4)
b (Å)	26.508(5)	17.546(9)	23.320(4)	20.447(10)
c (Å)	16.115 (3)	14.651(8)	12.285(2)	10.566(5)
α (°)	90	90	90	90
β (°)	99.22(3)	100.10(1)	95.159(3)	95.873(7)
γ (°)	90	90	90	90
V ($Å^3$)	3204.0(11)	1948.7(18)	2100.5(6)	1641.3(14)
Z	4	4	4	4
Calculated density / ($g\ cm^{-3}$)‡	0.957	1.574	1.220	1.561
Absorption coefficient (mm^{-1})	0.788	1.296	1.189	1.522
F_{000}	944.0	944.0	784.0	784.0
θ range for data collection (°)	2.00–28.38	1.83–25.10	1.75–26.43	1.99–25.04
Miller index ranges	$-10 \le h \le 10$ $-35 \le k \le 35$ $-21 \le l \le 21$	$-9 \le h \le 9$ $-20 \le k \le 20$ $-17 \le l \le 17$	$-9 \le h \le 9$ $-29 \le k \le 29$ $-15 \le l \le 15$	$-9 \le h \le 9$ $-24 \le k \le 24$ $-12 \le l \le 12$
Reflections collected	85516	14393	28904	12597
Independent reflections	8016	3464	4296	2897
Completeness to θ_{max} (%)	99.8	99.7	99.5	99.8
Max. and min. transmission	0.746, 0.700	0.745, 0.597	0.745, 0.571	0.745, 0.565
Refinement Method	Full-matrix least-squares on F^2	Full-matrix least-squares on F^2	Full-matrix least-squares on F^2	Full-matrix least-squares on F^2
Data / restraints / parameters	8016 / 1837 / 552	3464 / 6 / 280	4296 / 30 / 226	2897 / 0 / 226
Goodness-of-fit on F^2	1.020	1.024	1.002	1.204
Final R indices [$I > 2\sigma(I)$]	$R1$ = 0.0405 $wR2$ = 0.1040	$R1$ = 0.0718 $wR2$ = 0.1420	$R1$ = 0.0396 $wR2$ = 0.1074	$R1$ = 0.0809 $wR2$ = 0.1558

‡Densities calculated with structures that have had the guest electron density removed by the Platon/SQUEEZE[49] routine

2.1. *In situ* single-crystal to single-crystal activation of 1

To critically assess whether this was in fact a single-crystal to single-crystal transformation, activation of a crystal of **1** was carried out *in situ* on a Bruker D8 Venture diffractometer. After first determining the specific unit-cell parameters for the as-synthesized crystal (270 K, Table S2) it was heated on the diffractometer to 435 K at a rate of 120 K h^{-1}, held at this temperature for 180 seconds and then cooled to 270 K at 120 K h^{-1}. A full data collection was carried out on the now activated crystal (form **1a**). The unit-cell parameters for both forms are shown in the table below.

Table S2. Selected crystallographic parameters for the *in situ* activation of **1** to **1a**.

	1	1a_insitu
Temperature/ K	270(2)	270(2)
Wavelength/ Å	0.71073	0.71073
Crystal system	Monoclinic (Primitive)	Monoclinic
Space group	not determined	$P2_1/n$
a / Å	7.69	7.852(1)
b / Å	26.14	17.583(4)
c / Å	16.65	14.848(3)
α / °	90	90
β / °	99.48	101.21(1)
γ / °	90	90
V/ Å^3	3300	2010.9(7)

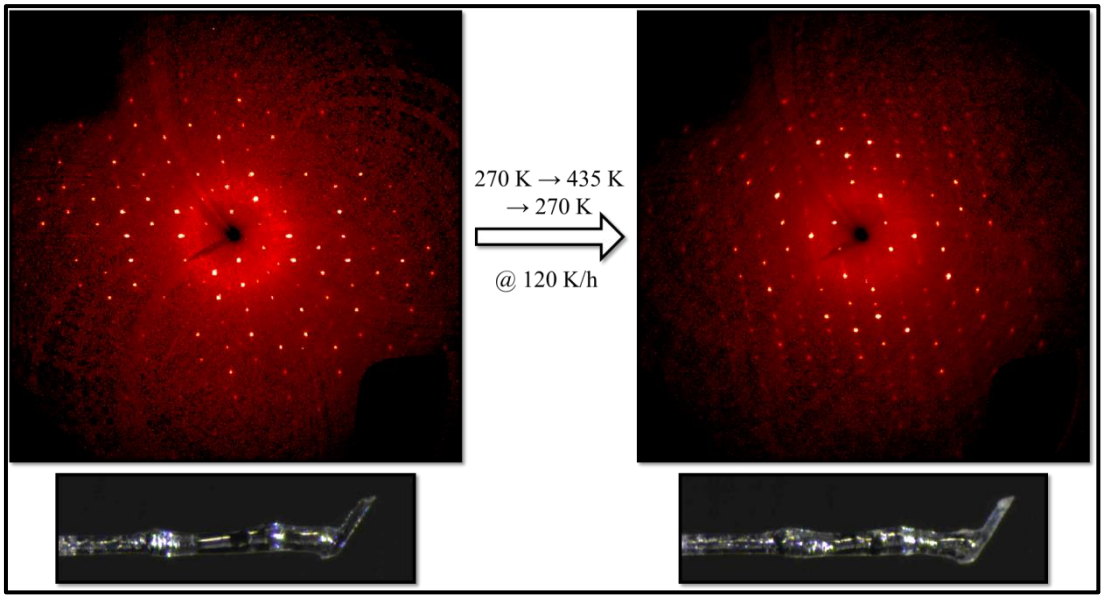

Figure S1. Precession images and photographs of the *in situ* activation of a crystal of **1** (left) to **1a** (right). Precession images show the *h*0*l* plane.

Table S3. Change in the crystal size before and after *in situ* activation of a two single crystals of **1**.

	Crystal 1		Crystal 2	
	1	1a	1	1a
Crystal size min (mm)	0.060	0.040	0.084	0.055
Crystal size mid (mm)	0.085	0.089	0.172	0.191
Crystal size max (mm)	0.321	0.291	0.254	0.208
Crystal volume (mm^3)	0.00164	0.00104	0.00367	0.00219
Change in crystal volume (%)	-	37	-	40

2.2. Probe-Accessible Volume (PAV) maps

The PAV[24] for each species was investigated in Mercury[35–37] using a probe radius of 1.5 Å and a grid spacing of 0.2 Å.

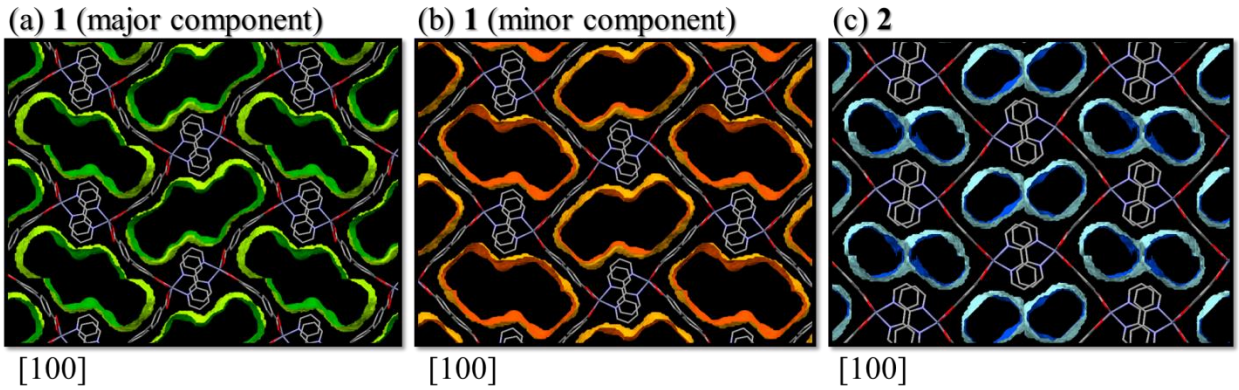

Figure S2: PAV of **1** with only the **(a)** major or **(b)** minor component of bpdc disorder present (45 and 46% SAS, respectively) and **(c)** **2** (32% PAV). In **(a)** and **(b)** only the major component of the bpy disorder is shown. Hydrogen atoms are omitted for clarity.

2.3. Comparison of the asymmetric units of the as-synthesized and activated materials, and the ensuing Cambridge Structural Database (CSD)[45] search.

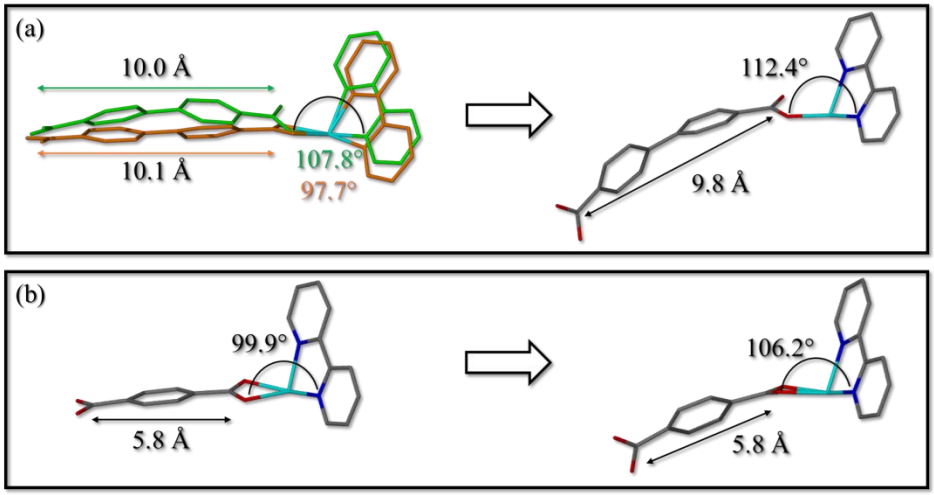

Figure S3. Comparison of the asymmetric units (ASUs) of the as-synthesized (left) and activated forms (right) of **1**/**1a** **(a)** and **2**/**2a** **(b)**. In **(a)** the ligand disorder in **1** shows the major component (for both bpdc and bpy disorder) in green and the minor component in orange. This coloring scheme is reflected in the individual measurements as well. For all ASUs hydrogen atoms are omitted for clarity.

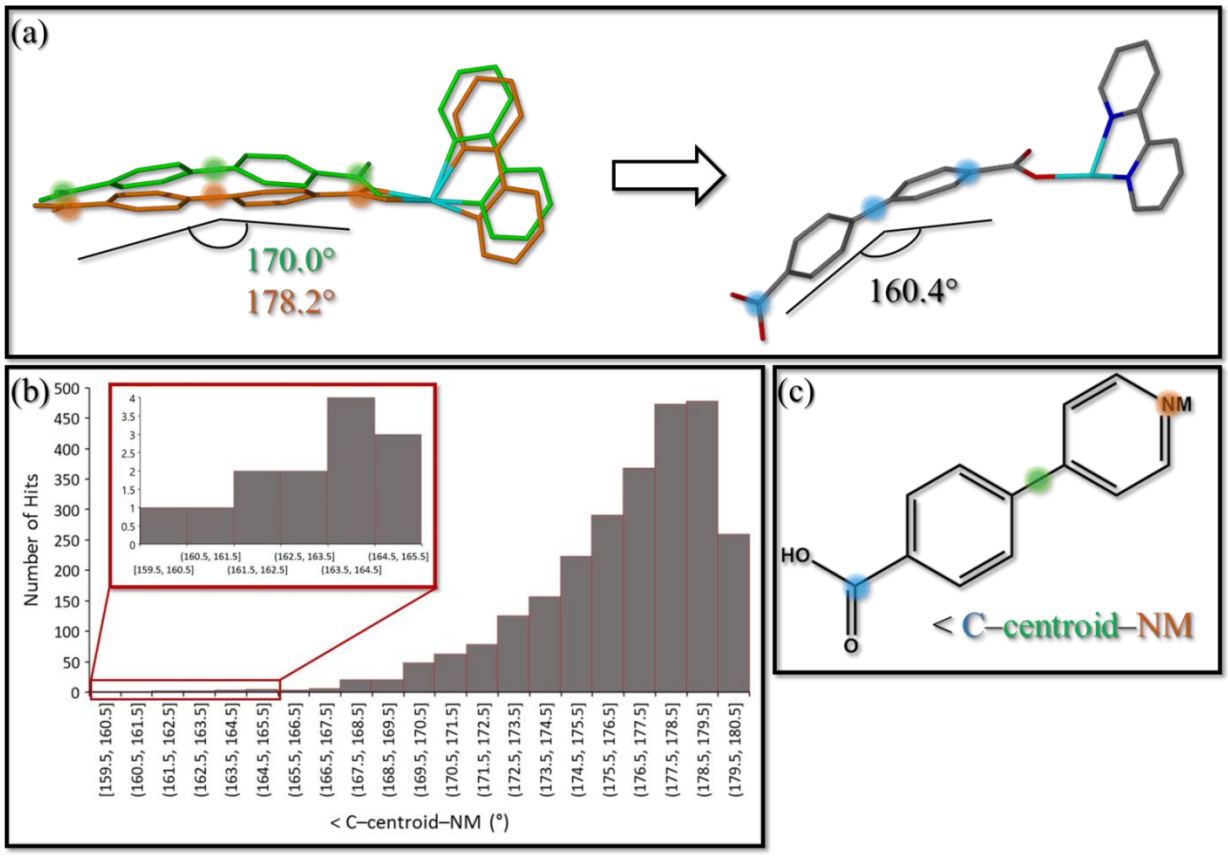

Figure S4. The change in bending angle of the bpdc ligand in **1** (left) and **1a** (right), measured as: carbon–centroid–carbon, is shown in **(a)**. In **(a)** the ligand disorder in **1** shows the major component (for both bpdc and bpy disorder) in green and the minor component in orange. This coloring scheme is reflected in the individual measurements as well. For all ASUs in **(b)** hydrogen atoms are omitted for clarity. A search of comparative bending angles in similar ligands was carried out in the CSD the results of which are shown as histograms in **(b)**, with the search criterion shown in **(c)**. The search criteria defined the angle between the carboxylate carbon, a centroid between the phenyl ring and any para positioned non-metal (NM). Note that multiple hits may originate from a single structure.

Please note that although there is one reported structure where the bending angle exceeds that within this work, this angle is in actuality the result of disorder and thus not a real angle, but an artefact of the modelling of the disorder (CSD refcode: BAJYES).

Table S4. Descriptive statistics for the CSD searches carried out for comparative bending angles in similar ligands. Note that multiple hits may originate from a single structure.

	entire CSD	only angles 155 ≤ ° ≤ 165
Number of hits	2630	13
Minimum	159.52	159.52
Maximum	180	164.95
Mean	176.53	163.10
Median	177.26	163.67
Lower quantile	175.11	162.17
Upper quantile	178.66	164.47

3. Fourier transform infrared spectrophotometry (FT-IR)

IR spectra were recorded using a Bruker Alpha P ATR-IR instrument. A background measurement was performed before each experimental spectrum was recorded.

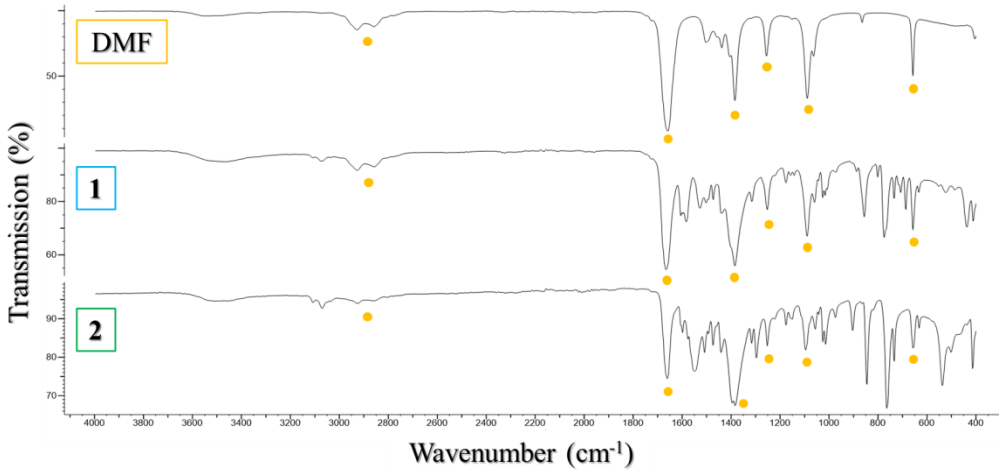

Figure S5. IR spectra of neat DMF (top), **1** (middle) and **2** (bottom). Yellow dots indicate characteristic peaks of DMF.

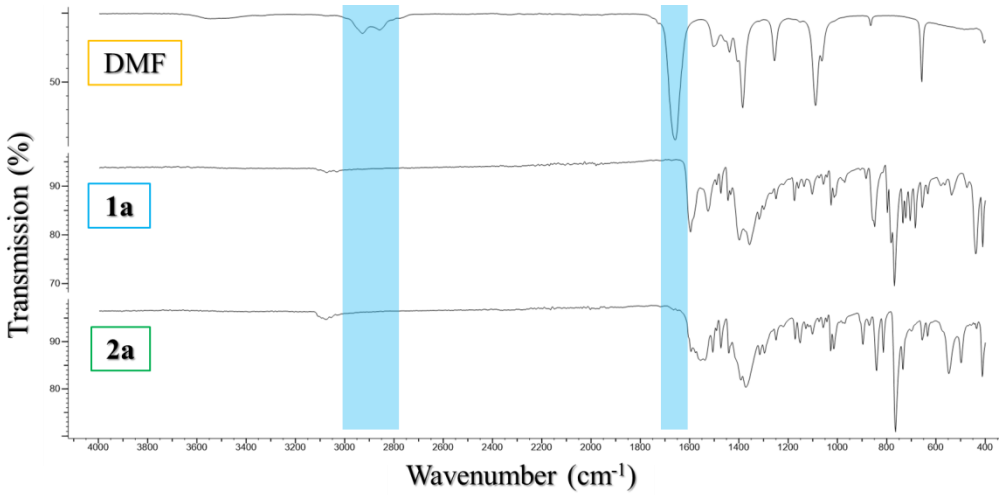

Figure S6. IR spectra of neat DMF (top), **1a** (middle) and **2a** (bottom). Blue areas indicate the loss the characteristic peaks of DMF (sp^3 C–H and C=O stretches at *ca* 2900 and 1650 cm^{-1}, respectively, both vanish).

4. Thermogravimetric analysis (TGA)

A TGA trace was generated by measuring the percentage mass as the sample was heated at a constant rate. A TA Instruments Q500 thermogravimetric analyzer was used. Samples were contained in aluminum pans and sample weights typically ranged from 1 to 5 mg. N_2 gas (flow rate 40 ml min^{-1}) was used to purge the furnace. The temperature was ramped from room temperature to *ca.* 600 °C at a constant heating rate of 10 °C min^{-1}. The resulting thermograms were analyzed using the TA Instruments Universal Analysis program.

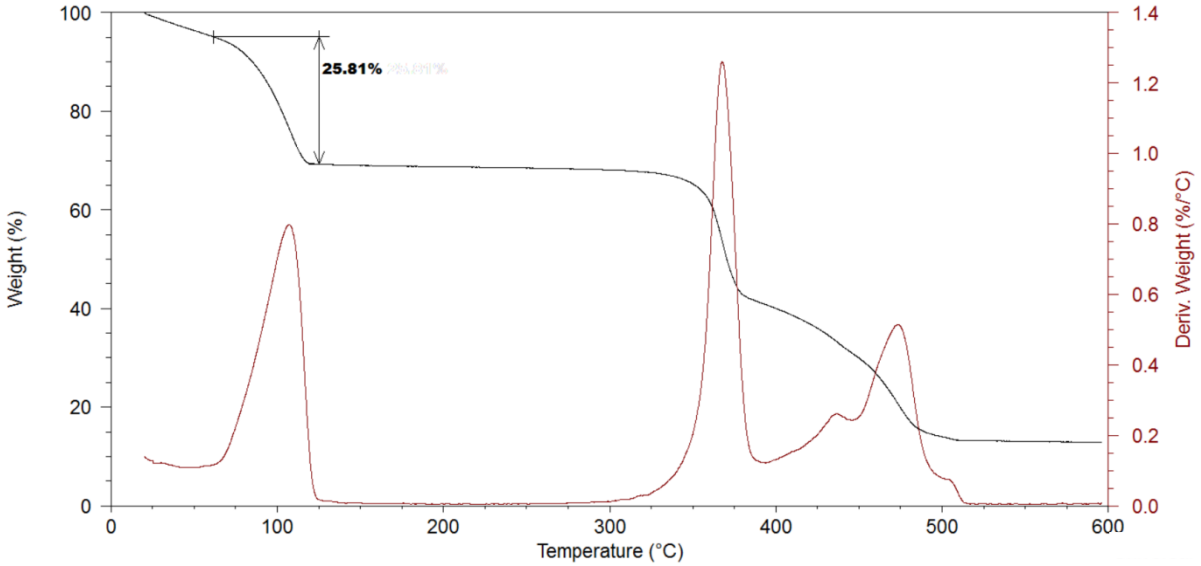

Figure S7: Thermogram of **1**. The weight loss of 25.8% is equal to *ca* 2 DMF molecules per ASU.

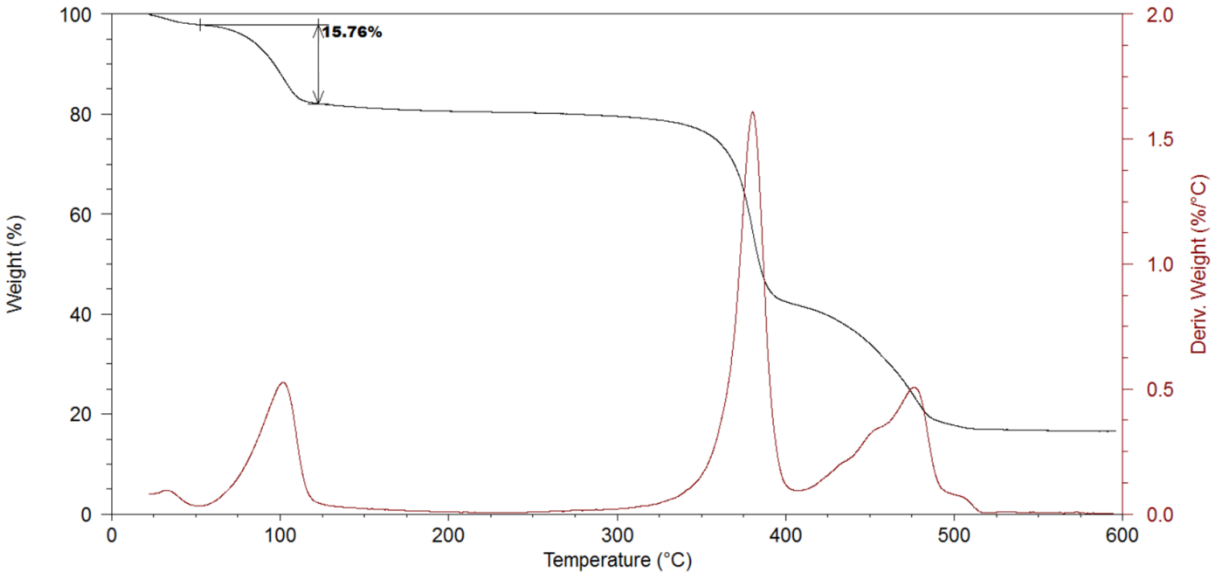

Figure S8: Thermogram of **2**. The weight loss of 15.8% is equal to *ca* 1 DMF molecule per ASU.

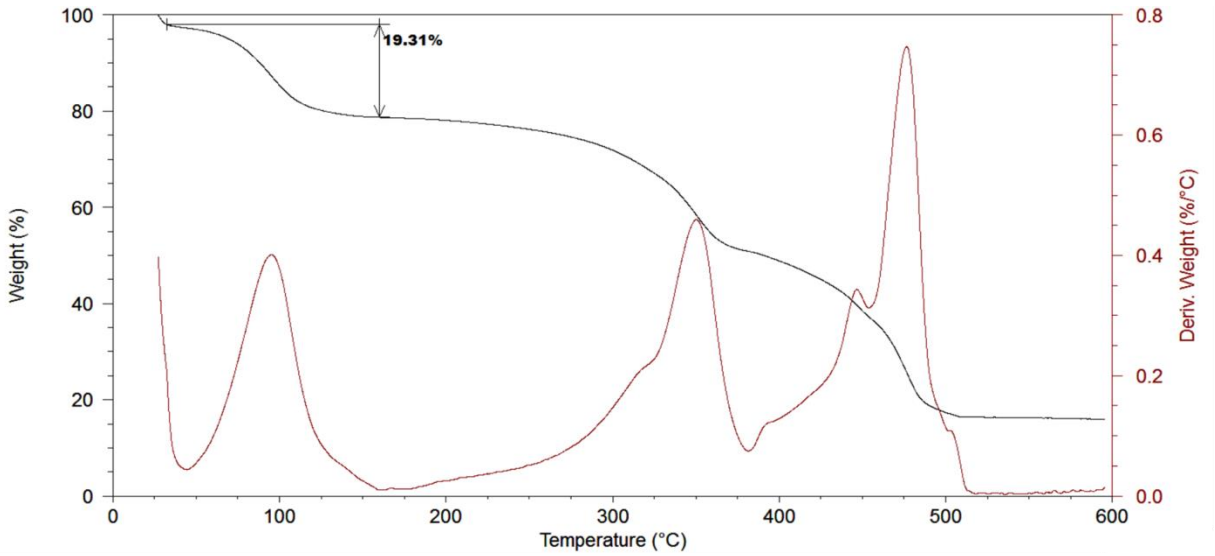

Figure S9: Thermogram of **1′**. The weight loss of 19.3% is equal to *ca* 1.5 DMF molecules per ASU. This is less than in **1**, however, once resolvated the material becomes paste-like in consistency making drying difficult. Rigorous drying to remove surface solvent may have resulted in the loss of a portion of the guest.

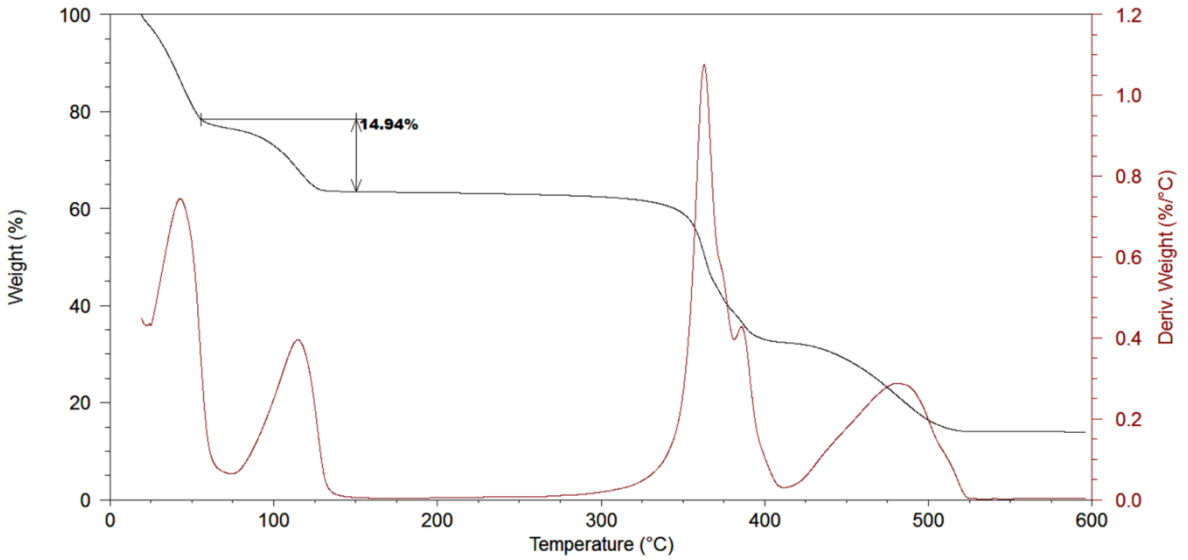

Figure S10: Thermogram of **2′**. The weight loss of 14.9% is equal to *ca* 1 DMF molecule per ASU. Less rigorous drying of the resolvated paste resulted in a large surface solvent peak (onset to *ca* 55 °C), however the guest occupancy matches well with that of **2**.

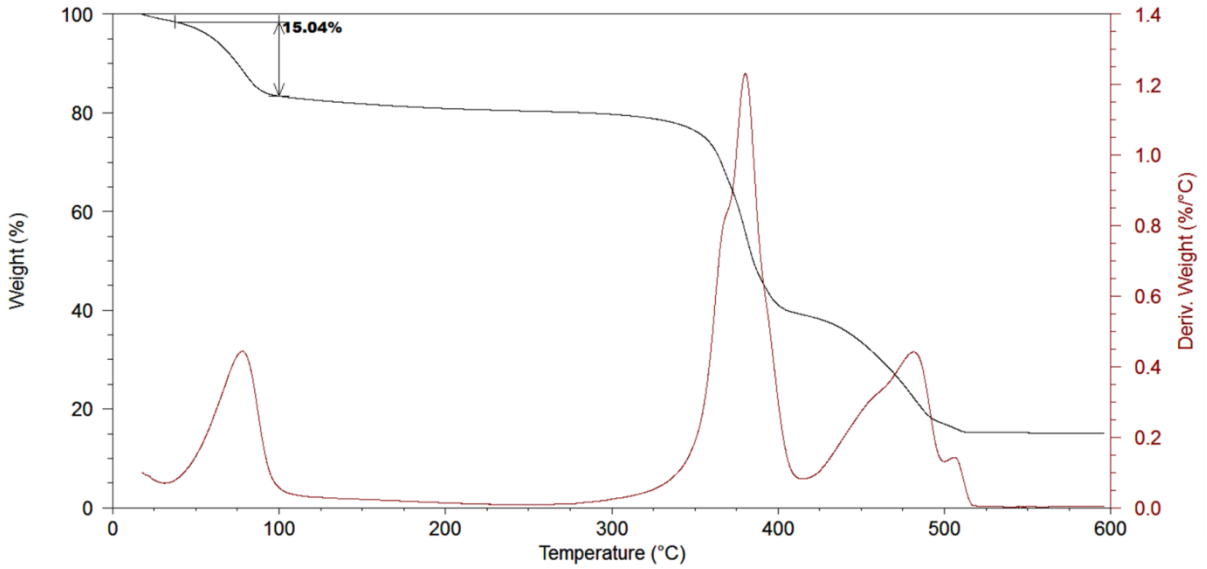

Figure S11: Thermogram of **2** after solvent exchange with THF. The weight loss of 15.0% is equal to *ca* 1 THF molecule per ASU.

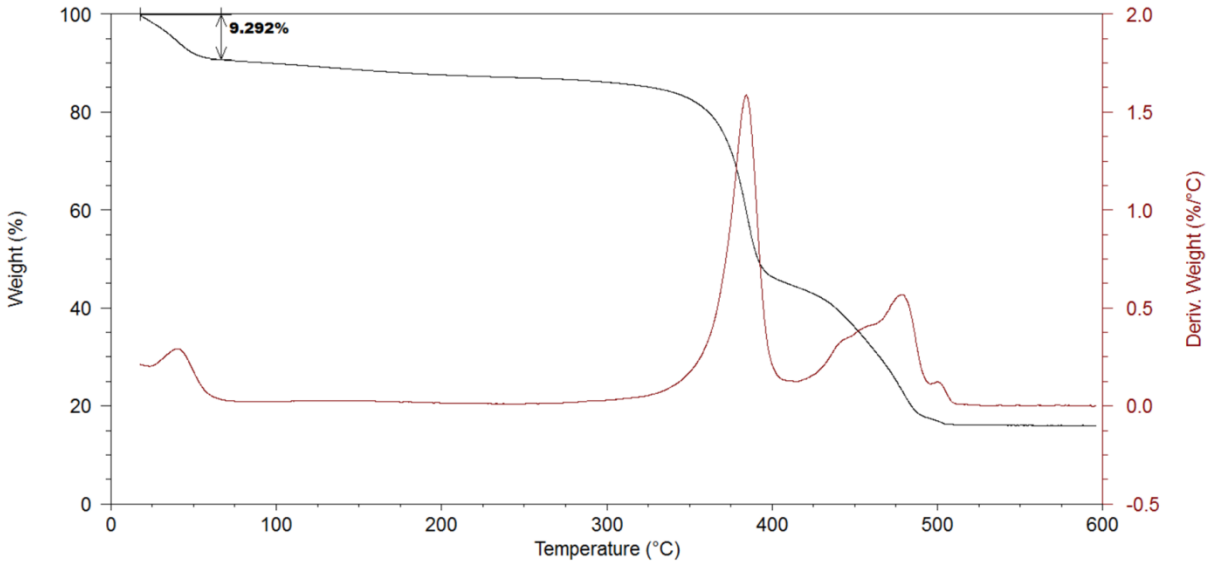

Figure S12: Thermogram of **2** after solvent exchange with DE. The weight loss of 9.3% is equal to *ca* 0.5 DE molecules per ASU.

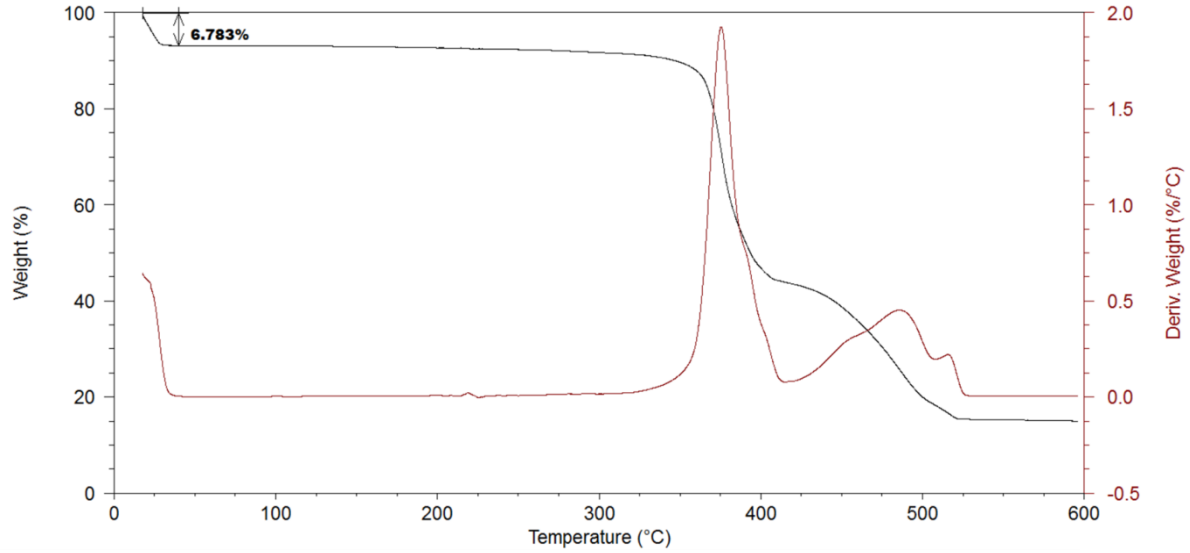

Figure S13: Thermogram of **2** after solvent exchange with MeOH. The weight loss of 6.8% is equal to *ca* 1 MeOH molecule per ASU.

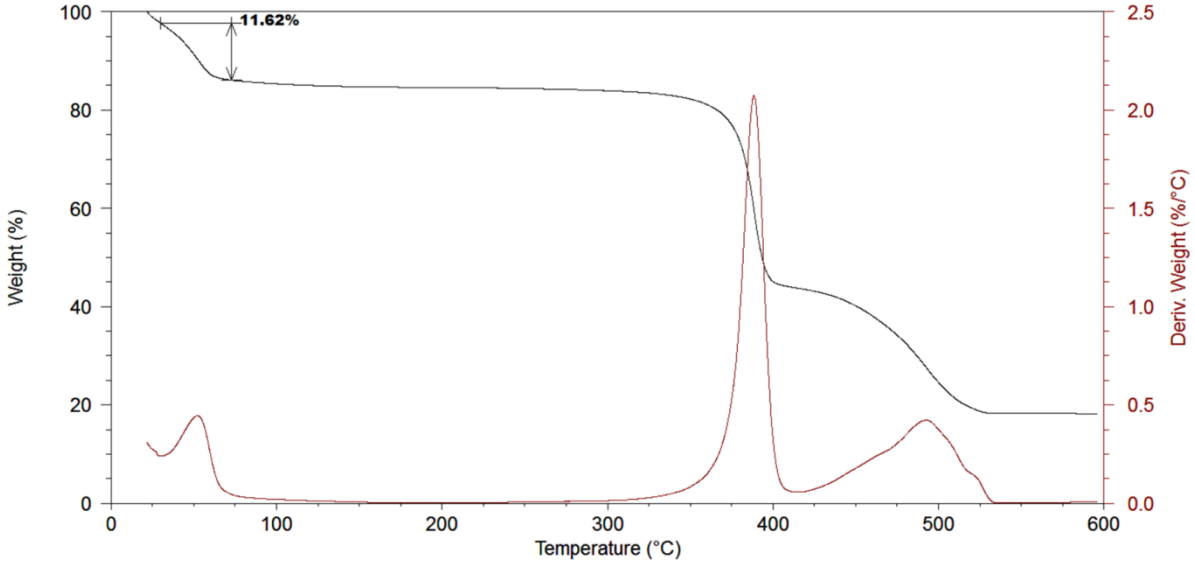

Figure S14: Thermogram of **2** after solvent exchange with EtOH. The weight loss of 11.6% is equal to *ca* 1 EtOH molecule per ASU.

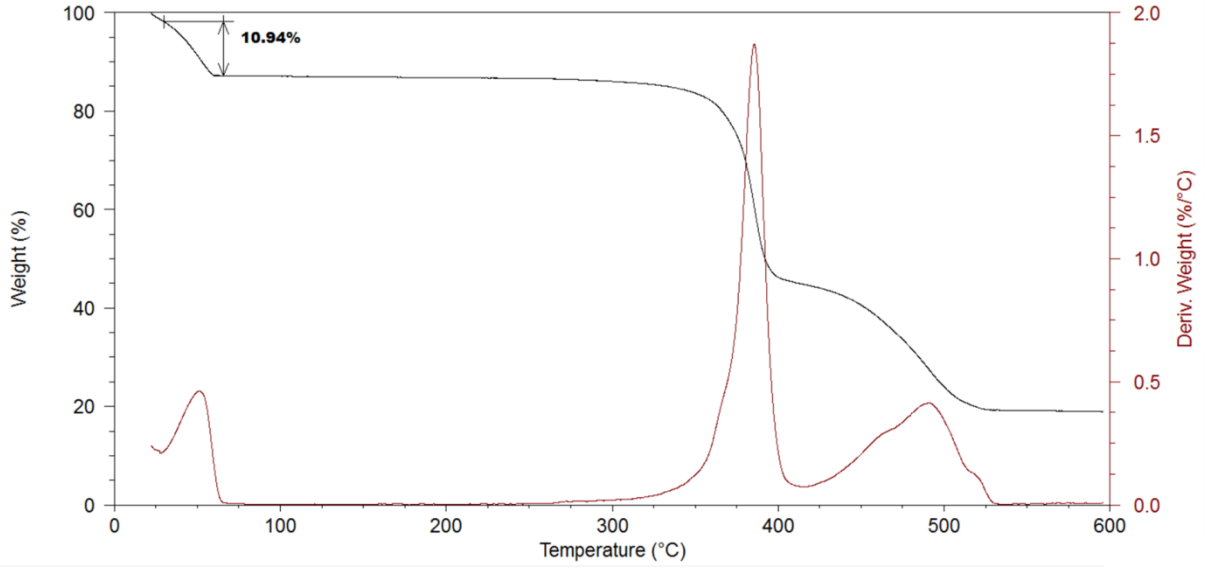

Figure S15: Thermogram of **2** after solvent exchange with ACN. The weight loss of 10.9% is equal to *ca* 1 ACN molecule per ASU.

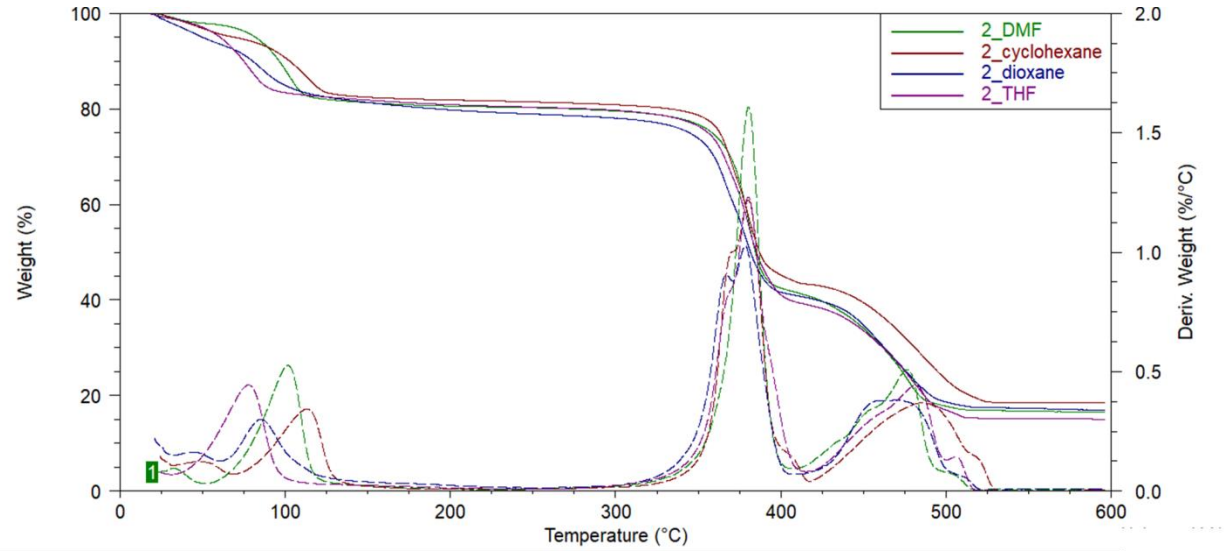

Figure S16: Thermograms of **2** (green trace) after solvent exchange with cyclohexane (red), 1,4-dioxane (blue) and THF (purple). While the solvent exchange with THF is determined to be successful owing to the shift in the peak mass loss closer to the boiling point of THF and peak resolution. The attempted solvent exchanges with cyclohexane and 1,4-dioxane are ambiguous owing to their small peak shifts (event though their respective boiling points differ substantially from that of DMF) as well as the lack of peak resolution.

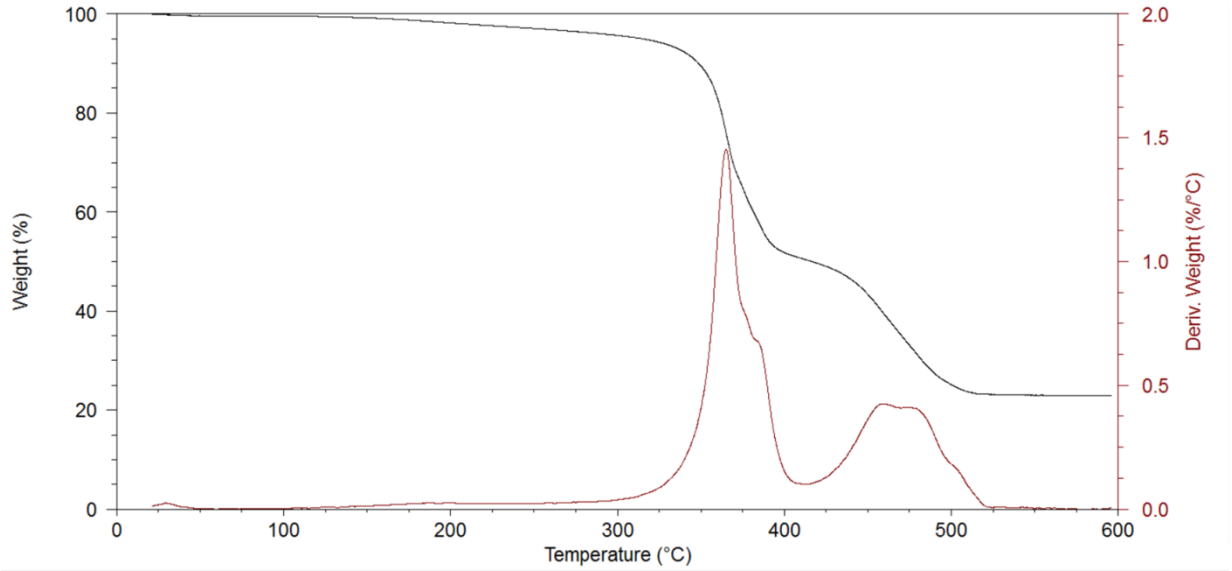

Figure S17: Thermogram of **2a** post vapor sorption and heat treatment at 75 °C for several hours under reduced pressure.

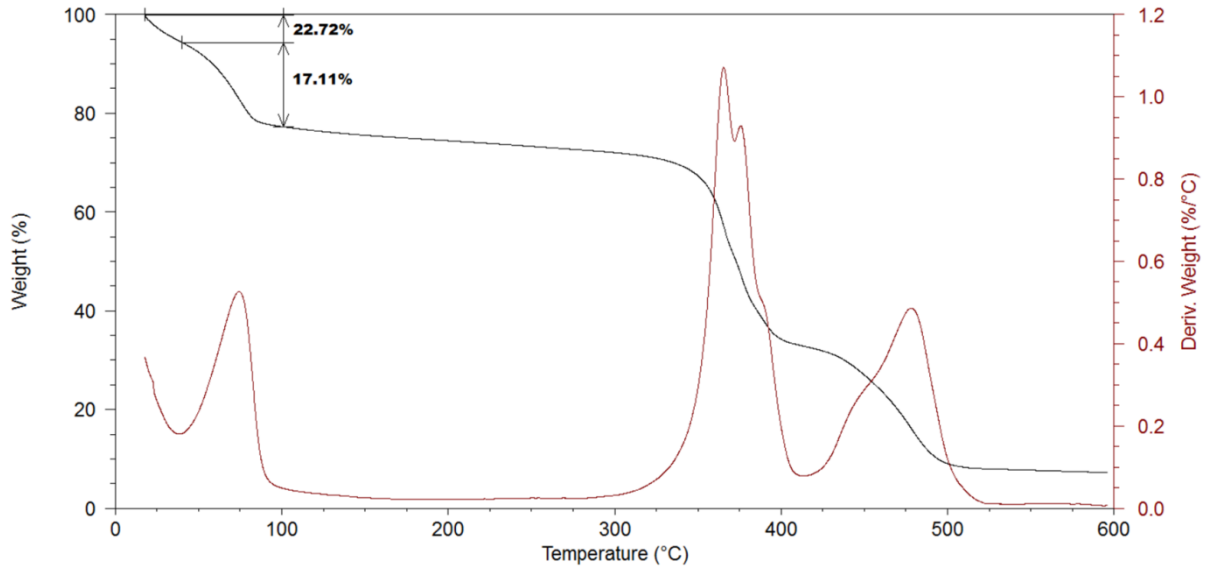

Figure S18: Thermogram of **2a** post THF vapor sorption. The weight loss of 17.1% is equal to *ca* 1 THF molecule per ASU. However, the total initial weight loss of *ca* 22.7% is equal to *ca* 1.6 molecules per ASU. This illustrates the effect of solvent condensation on the sample during vapor sorption.

5. Powder X-ray diffraction (PXRD)

A Bruker D2 Phaser diffractometer was used to determine experimental diffractograms. The diffractometer utilises Bragg-Brentano geometry and Cu Kα radiation (λ = 1.5418 Å) as the incident beam. The diffractometer was operated at 30 kV and 10 mA. Intensity data were recorded with a Lynxeye detector using a rotating flat stage (30° min^{-1}). Samples were finely ground (where necessary) using a mortar and pestle, loaded onto a zero-background sample holder and levelled with a glass slide. The diffractograms were determined under ambient conditions with a scanning range of 5–40°, a step size of 0.016° and a 0.8 second scan speed.

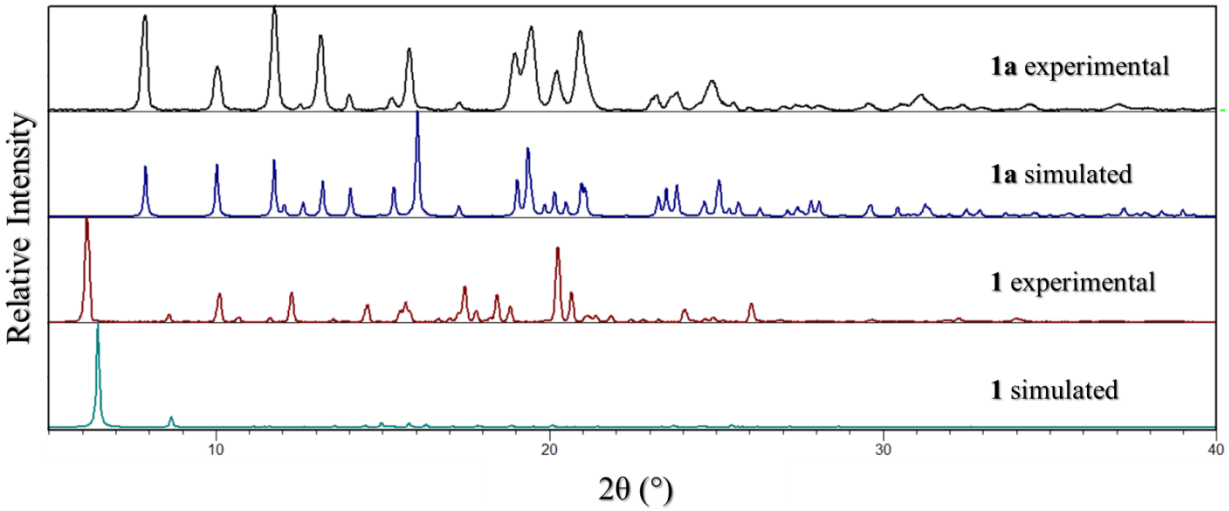

Figure S19: Diffractograms of **1** and **1a**. The small shift between the simulated and experimental diffractograms of **1** may be attributed to thermal effects as the simulated diffractogram is generated from structural data collected at 100 K.

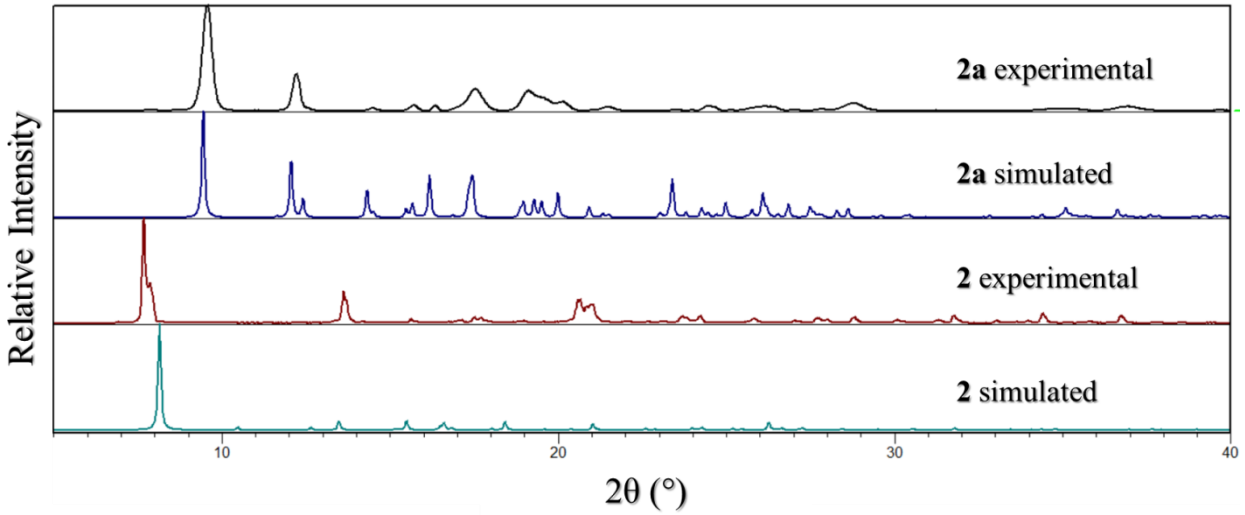

Figure S20: Diffractograms of **2** and **2a**. The small shift between the simulated and experimental diffractograms of **2** may be attributed to thermal effects as the simulated diffractogram is generated from structural data collected at 100 K.

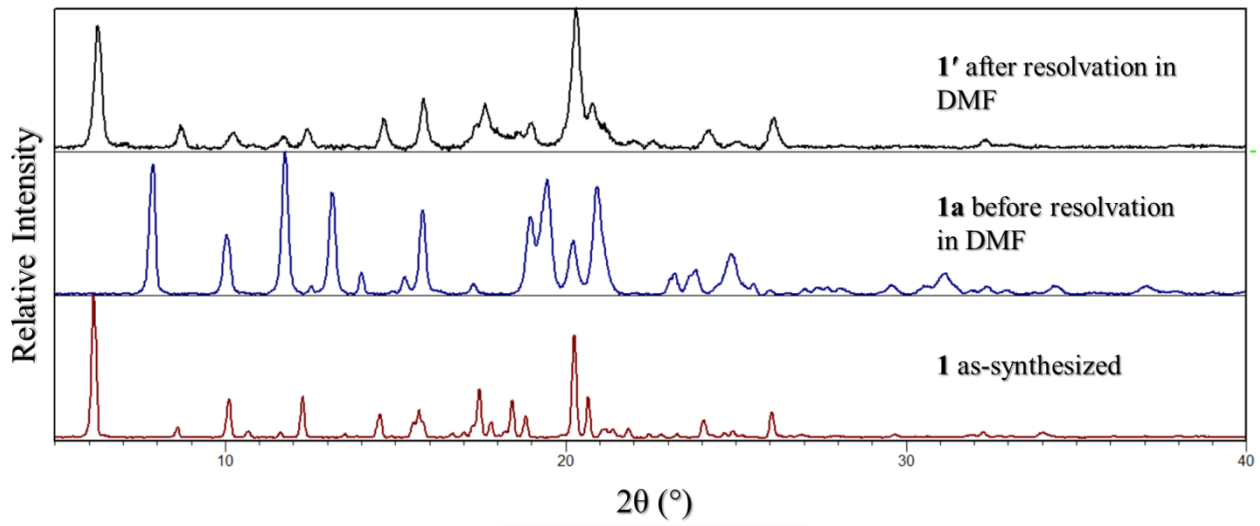

Figure S21: Experimental diffractograms of 1, 1a and 1′ (prepared by immersing 1a in DMF overnight).

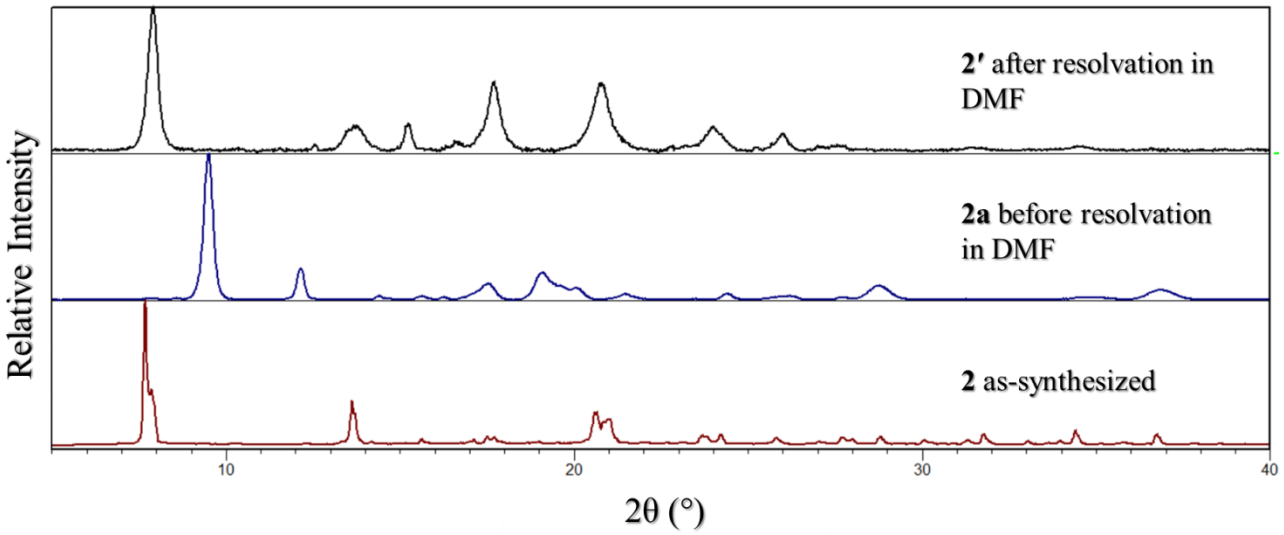

Figure S22: Experimental diffractograms of 2, 2a and 2′ (prepared by immersing 2a in DMF overnight).

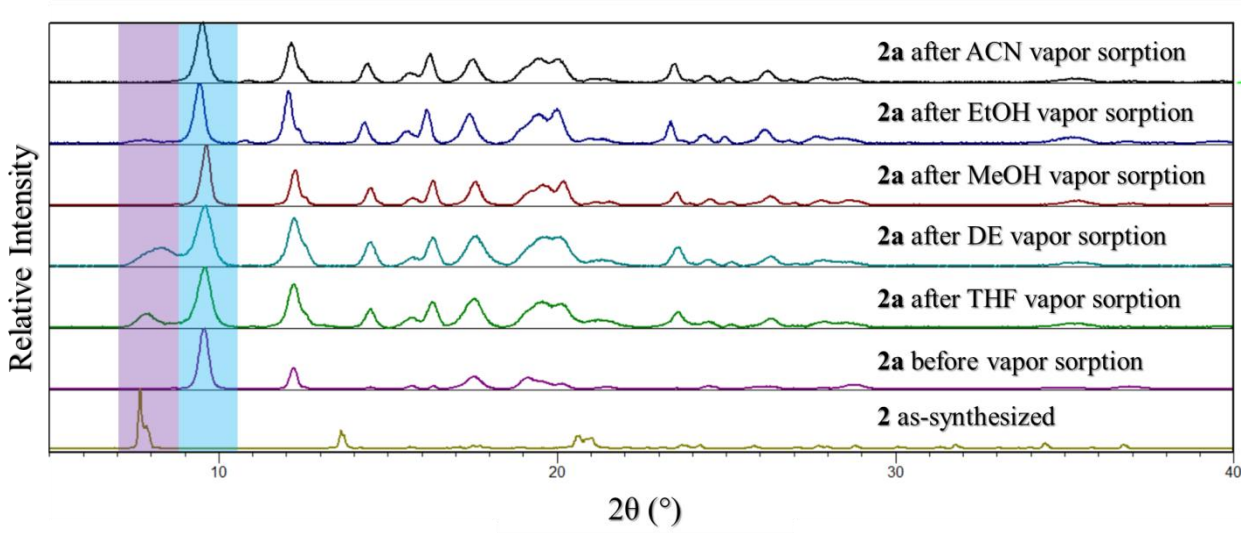

Figure S23: Experimental diffractograms of 2, 2a and 2a after each cycle of vapor sorption-desorption. The purple area highlights peaks which are characteristic of an open phase, while the blue area highlights those of a closed phase.

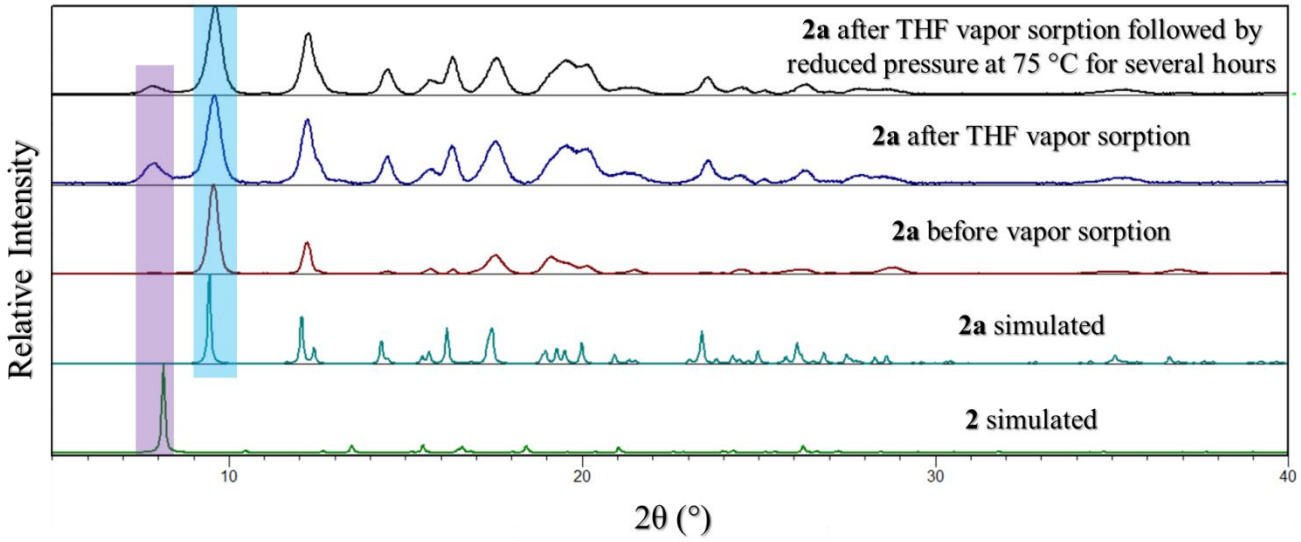

Figure S24: Experimental and simulated diffractograms of 2 and 2a, along with those of 2a after THF vapor sorption-desorption and subsequent heat treatment. The purple area highlights peaks which are characteristic of an open phase, while the blue area highlights those of a closed phase.

6. Pressure Gradient Differential Scanning Calorimetry (PG-DSC)

This set-up measures the change in heat flow of the sample as a function of pressure. PG-DSC experiments were carried out on a Setaram µDSC7 Evo instrument equipped with a high pressure sample holder (that can withstand up to 1000 bar). A Teledyne ISCO 260D syringe pump coupled to a D-series pump controller was used to increase the pressure throughout the measurement. ISCO software developed by Prof. L. J. Barbour was used to control the pressure gradient. Calisto Data Acquisition software was used to record the data. Calisto Processing software was used to process the raw data before plotting. A graphic representation of this set-up is shown in Figure S25.[46,50]

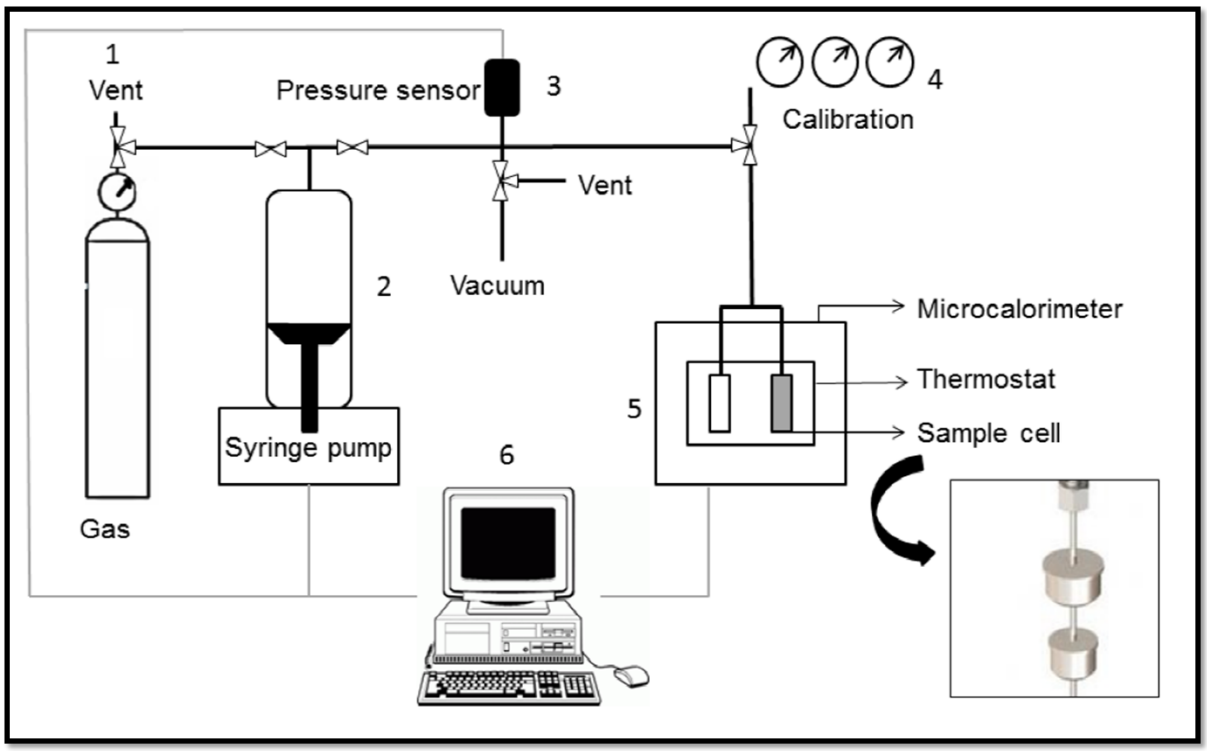

Figure S25: Diagrammatic representation of the PG-DSC instrumentation set-up. Numbers represent key structures: 1 – gas inlet, 2 – Teledyne ISCO 260D syringe pump, 3 – pressure sensor, 4 – calibration gauges, 5 – Setaram µDSC7 Evo and 6 – computer.[15]

Samples were activated *in-situ* under dynamic vacuum overnight (approximately 12 hours) to ensure the absolute activation. The vacuum pressure reached was 6.97 x 10^{-2} mbar. After each cycle the samples were activated under the same conditions for *ca.* 1–2 hours. The initial pressure is required to be slightly higher than the desired starting pressure as the pressure may drop slightly once the sample valve is opened owing to the void volume of the system lines. Once the pressure and temperature were set, the sample was exposed to the pre-set pressure by opening the sample valve. The sample was then left to equilibrate for *ca.* 15–30 minutes. Thereafter the manual flow-rate program was started once the heat flow

baseline was stable. After program completion, the sample was left for a further 10 minutes to return to its original equilibrium point, after which an activation cycle was initiated.

In materials that undergo phase changes to accommodate gaseous guests a peak is expected in the heat flow during the PG-DSC measurement. This heat flow peak subsequently corresponds to an inflection in the corresponding gas sorption isotherm. Since **1a** and **2a** are 'virtually nonporous' a phase change is indeed expected in order for sorption to take place. Since no peaks were observed in the PG-DSC experiments, no phase changes occurred over the pressure range for the gases trialled, and it may be inferred that no sorption occurred.

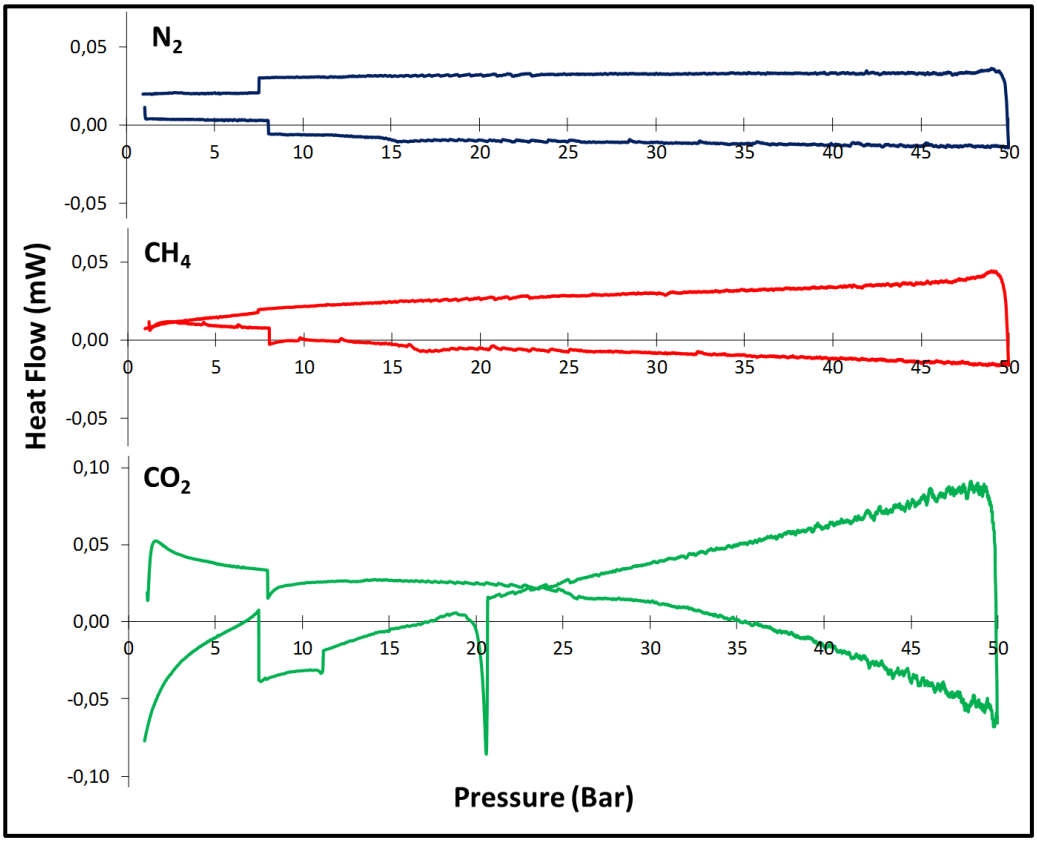

Figure S26: PG-DSC plots of **1a** with N_2 (blue), CH_4 (red) and CO_2 (green). Although there appears to be a peak around 20 bar CO_2 (desorption), one should note the small scale of the plot.

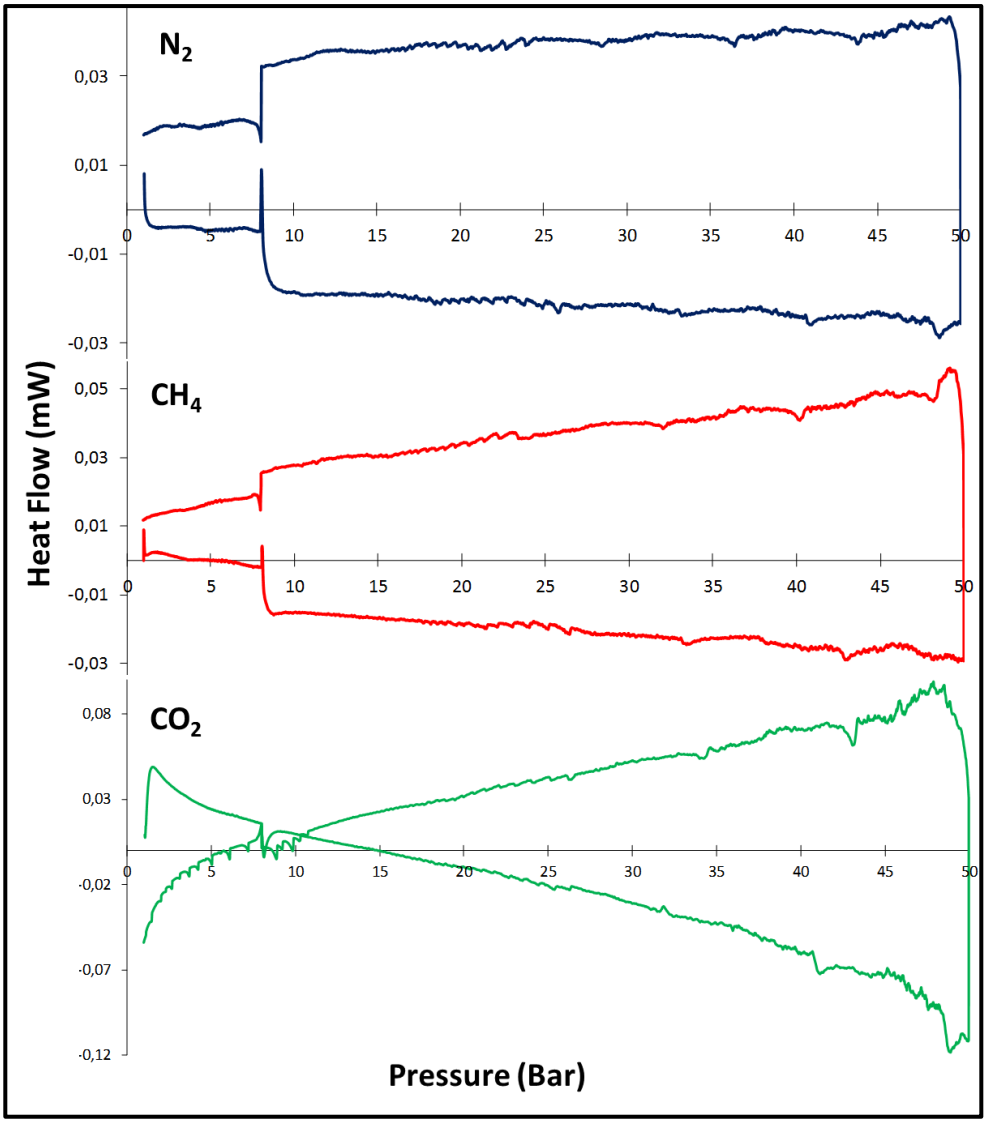

Figure S27: PG-DSC plots for **2a** with N_2 (blue), CH_4 (red) and CO_2 (green).

7. Vapor sorption

A modified version of the vapor balance setup reported by Barbour and co-workers[38] was used to carry out vapor sorption experiments. The system provides an accurate measure of the change in sample weight as a function of time. A wooden cabinet encloses the system to aid temperature regulation, in addition to two Edison light bulbs and an integral fan. The sample is suspended by a thin steel wire in an aluminum basket from the microelectronic balance with a counterweight suspended on the adjacent end. A vacuum pump and pressure sensor allow the system to be placed under reduced pressure (0.1 mbar). This reduced pressure environment allows both for the preparation of the sample vapor along with the evacuation of the apparatus and sample after an experiment is complete. Typically sample

sizes range from 15-30 mg, and the temperature is maintained at 23 °C. After introduction of the sample vapor to the system the experiment is allowed to run until the sample weight reaches a plateau (indicating an equilibrium state). When required, the desorption profile can also be recorded by applying reduced pressure to a sorbed system at equilibrium. Once more the experiment is continued until an equilibrium state was reached.

8. Vapor pressures and kinetic diameters of select solvents

Table S5. Vapor pressures of select solvents calculated from the Antoine equation.[51,52]

Solvent	Vapor pressure at 20 °C (mbar)	Vapor pressure at 25 °C (mbar)
THF	$T < T_{min}$	216
DE	583	710
MeOH	130	169
EtOH	58	78
ACN	97	122

Table S6. Kinetic diameters of select solvents.

Solvent	Kinetic diameter (Å)
1,4-dioxane	7.0[53]
p-xylene	6.5[54]
toluene	5.9[54]
DE	5.2[55,56]
THF	4.9[55,56]
EtOH	4.3[55,56]
ACN	4.3[55,56]
MeOH	3.8[55,56]

References

1 MiTeGen, MiTeGen, https://www.mitegen.com/, (accessed 25 June 2018).

2 Bruker AXS Inc., 2016.

3 Bruker AXS Inc., 2016.

4 G. M. Sheldrick, *Acta Cryst.*, 2015, **A71**, 3–8.

5 G. M. Sheldrick, *Acta Cryst.*, 2015, **C71**, 3–8.

6 L. J. Barbour, *J. Supramol. Chem.*, 2001, **1**, 189–191.

7 L. J. Barbour, *J. Appl. Cryst.*, 2020, **53**, 1–6.

8 Persistence of Vision Raytracer Pty. Ltd., 2004.

9 C. F. Macrae, P. R. Edgington, P. McCabe, E. Pidcock, G. P. Shields, R. Taylor, M. Towler and J. Van De Streek, *J. Appl. Crystallogr.*, 2006, **39**, 453–457.

10 C. F. Macrae, I. J. Bruno, J. A. Chisholm, P. R. Edgington, P. McCabe, E. Pidcock, L. Rodriguez-Monge, R. Taylor, J. Van De Streek and P. A. Wood, *J. Appl. Crystallogr.*, 2008, **41**, 466–470.

11 C. F. MacRae, I. Sovago, S. J. Cottrell, P. T. A. Galek, P. McCabe, E. Pidcock, M. Platings, G. P. Shields, J. S. Stevens, M. Towler and P. A. Wood, *J. Appl. Crystallogr.*, 2020, **53**, 226–235.

12 A. L. Spek, *Acta Crystallogr.*, 2015, **C71**, 9–18.

13 D. P. van Heerden and L. J. Barbour, *Chem. Soc. Rev.*, 2021, **50**, 735–749.

14 C. R. Groom, I. J. Bruno, M. P. Lightfoot and S. C. Ward, *Acta Crystallogr.*, 2016, **B72**, 171–179.

15 K.-A. White, MSc. Thesis, University of Stellenbosch, 2017.

16 W. K. Feldmann, K.-A. White, C. X. Bezuidenhout, V. J. Smith, C. Esterhuysen and L. J. Barbour, *ChemSusChem*, 2020, **13**, 102–105.

17 L. J. Barbour, K. Achleitner and J. R. Greene, *Thermochim. Acta*, 1992, **5**, 171–177.

18 Dortmund Data Bank, Saturated Vapor Pressure, http://ddbonline.ddbst.com/AntoineCalculation/AntoineCalculationCGI.exe, (accessed 28 March 2019).

19 R. C. M. D. Rodgers and G. E. M. D. Hill, *Br. J. Anaesth.*, 1978, **50**, 415–424.

20 S. D. Bhat and T. M. Aminabhavi, *Microporous Mesoporous Mater.*, 2006, **91**, 206–214.

21 D. Fairén-Jiménez, F. Carrasco-Marín and C. Moreno-Castilla, *Langmuir*, 2007, **23**, 10095–10101.

22 T. C. Bowen, S. Li, R. D. Noble and J. L. Falconer, *J. Memb. Sci.*, 2003, **225**, 165–176.

23 M. E. Van Leeuwen, *Fluid Phase Equilib.*, 1994, **99**, 1–18.

Chapter 5 – Tuning Extreme Anisotropic Thermal Expansion in 1D Coordination Polymers through Metal Selection and Solid Solutions

"Once you can accept the universe as matter expanding into nothing that is something, wearing stripes with plaid comes easy." — Albert Einstein

4.1. Article in preparation

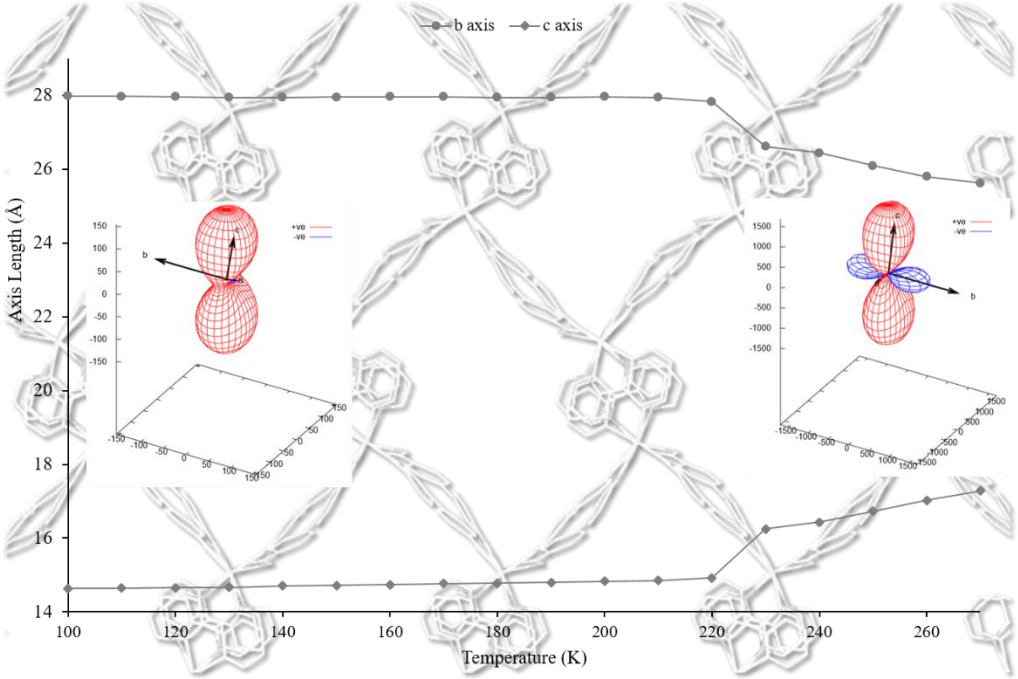

4.1.1. Contributions by author

- Design of the project
- Preparation and handling of crystals
- Collection of single-crystal X-ray diffraction data with Dr Leigh Loots
- Structure solution and refinement
- Modelling of disorder
- Recording TGA and DSC thermograms
- Collection of powder X-ray diffraction data
- Interpretation of results
- Writing of the first draft of the article

ARTICLE

Tuning Extreme Anisotropic Thermal Expansion in 1D Coordination Polymers through Metal Selection and Solid Solutions

Lisa M. van Wyk, Leigh Loots and Leonard J. Barbour*

Received 00th January 20xx,
Accepted 00th January 20xx

DOI: 10.1039/x0xx00000x

The thermal expansion behaviour of a series of 1D coordination polymers has been investigated. Variation of the metal centre allows tuning of the thermal expansion behaviour from colossal positive volumetric to extreme anomalous thermal expansion. Preparation of solid solutions increased the magnitude of the anomalous thermal expansion further, producing two species displaying supercolossal anisotropic thermal expansion (**ZnCoCP^{HT}** α_{V2} = -712 MK^{-1}, α_{V3} = 1632 MK^{-1} and **ZnCdCP^{HT}** α_{V2} = -711 MK^{-1}, α_{V3} = 1216 MK^{-1}).

Introduction

Owing to increased thermal motion of their constituent atoms, solids usually expand upon heating;[1–3] this is known as positive thermal expansion (PTE).[1,3,4] However, some materials display anomalous thermal expansion behaviour, including negative and zero thermal expansion (NTE and ZTE, respectively), exceptional magnitudes of PTE, as well as extreme anisotropy.[1,3] Anisotropic thermal expansion is characterised by significantly different linear thermal expansion coefficients for the individual principal axes.[1] Although anisotropy is expected for materials that do not possess cubic symmetry, extreme anisotropy is uncommon. There have been relatively few reports of anomalous thermal expansion behaviour,[4–7] but such materials are of great interest in materials science owing to possible applications in optical devices, semiconductor materials and space exploration vehicles.[1,2,8,9] Furthermore, controlled tuning of the thermal expansion behaviour of solids is desirable for tailoring materials to specific applications.[1,7,8,10]

Previous studies on thermal expansion of crystalline solids have explored molecular crystals, co-crystals and mineral-type compounds.[3,11–13] However, recent interest in extended materials such as metal-organic frameworks, coordination polymers (CPs), and covalent and hydrogen bonded frameworks have inspired new avenues of investigation.[10,14,15,16] Flexible one dimensional CPs have received little attention in this regard, but may prove to be excellent candidates for studies of solid-state dynamics.

Recent studies have shown that compounds with "wine-rack" or "lattice-fence" solid-state packing often exhibit anomalous thermal expansion (Fig. 1a-c)[3,5,7,10,17] as a consequence of hinging and twisting around the metal nodes.[3,5,10] We have also seen that solid solutions show promise for tuning thermal expansion.[7,9,18] Here we describe the thermal expansion behaviour of a series of isotypical[19] CPs and their solid solutions, which all employ packing reminiscent of ideal "wine-rack" or "lattice-fence" motifs (Fig. 1d).

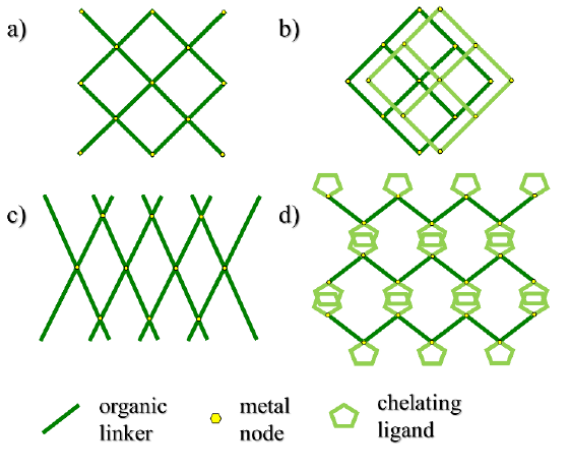

Figure 1 Simplified packing motifs commonly associated with anomalous thermal expansion behaviour, including **(a)** wine-rack, **(b)** interpenetrated/offset-layered square-lattice and **(c)** lattice-fence packing. A simplified depiction of the similar packing motif generated by the 1D materials in this study is shown in **(d)**. Note that, although it appears that the 1D strands in **(d)** run parallel to the plane of the page, they traverse it.

Results and Discussion

Four CPs with the general formula [M(bpdc)(bpy)·2DMF]$_n$ (**MCP**, M = Zn, Ni, Co and Cd) were prepared solvothermally from a solution of metal nitrate, 4,4′-biphenyldicarboxylic acid (bpdc) and 2,2′-bipyridine (bpy) in *N,N*-dimethylformamide (DMF). **ZnCP** was the first of these to be characterised structurally, but the low-temperature (100 K) single-crystal

Department of Chemistry and Polymer Science, University of Stellenbosch, 7602 Matieland, South Africa. Email: ljb@sun.ac.za

Electronic supplementary information (ESI) available: Synthetic procedure, TGA, additional figures, SCXRD, PXRD, DSC and PAS results. CCDC: 1940578, 2036084-2036096. For ESI and crystallographic data in CIF or other electronic format. See DOI: 10.1039/x0xx00000x

X-ray diffraction (SCXRD) data were of poorer quality than we had expected (Fig. S8). SCXRD at 270 K (the crystals lose solvent at room temperature) yielded better data (Fig. S8), but notably different unit-cell parameters relative to those at 100 K. Differential scanning calorimetry (DSC) revealed that this discrepancy is due to a subtle phase transition, which occurs with an onset temperature of 250–240 K upon cooling (Fig. S17). Comparison of the high- and low-temperature crystal structures of **ZnCP** (**ZnCP^{HT}** and **ZnCP^{LT}**, respectively) reveals that the space group ($P2_1/n$) remains unchanged and that, although highly reminiscent of one another, their corresponding unit cell parameters differ by more than can be expected for normal thermal expansion (Table S1). Nevertheless, the two crystal structures can be considered isotypical.[19]

ZnCP^{HT} is comprised of infinite 1D "zigzag" chains (∠Zn···Zn···Zn = 125.34(3)°) that propagate along [602]. Successive metal nodes are linked by means of chelating bpdc ligands (disordered over two positions with site occupancies of 0.53 and 0.47). Each metal centre is also bound to a chelating bpy ligand (disordered over two positions with site occupancies of 0.67 and 0.33), resulting in an overall highly distorted octahedral coordination environment. The 1D strands interdigitate *via* offset π···π interactions between bpy moieties of adjacent CP strands. This arrangement produces 1D guest-accessible channels that propagate along [100] and that contain DMF guest molecules (Figs 2 and S10). We have explored the transient porosity[20] of **ZnCP** as part of a separate study,[21] and a view along the 1D channels serves as a convenient frame of reference with respect to comparing the crystal structures.

The phase transition from **ZnCP^{HT}** to **ZnCP^{HT}** (based on the crystal structures determined at 270 and 100 K, respectively) involves a relatively minor structural rearrangement. The connectivity of **ZnCP^{HT}** is maintained in **ZnCP^{LT}**, and the disorder of the ligands remains similar (50:50 and 62:38 for bpdc and bpy, respectively). However, after the phase change the zigzag angle is markedly different. These changes lead to slight distortion of the 1D channel, with lengthening along [010] and shortening along [001] (Figs. 2, S9 and S14).

The phase change experienced by **ZnCP** upon cooling is due to an abrupt decrease in the M···M···M zigzag angle from 123.89(3)° at 250 K to 121.66(3) at 240 K (Fig. S16 and Table S13). This is accompanied by elongation of the channels along [010], with concomitant narrowing along the vector perpendicular to (001) (*cf* Figs 2 and S8). These changes are manifested as elongation of the crystallographic *a* and *b* axes, a small increase in the β angle, and shortening of the *c* axis (Fig. S13).

Determination of unit-cell parameters at 10 K intervals from 270 to 100 K shows that both phases of **ZnCP** undergo dramatic anisotropic thermal expansion (Fig. S14). Respectively, the linear thermal expansion coefficients[22] α_{y1}, α_{y2} and α_{y3} for **ZnCP^{HT}** are 100, −462 and 882 MK^{-1}, while those for **ZnCP^{LT}** are 69, −57 and 275 MK^{-1}. The matrices relating the principal axes to the unit-cell axes are given in Figs S25, S26 and S39 of the ESI. Taken together, the linear thermal expansion coefficients of **ZnCP^{HT}** and **ZnCP^{LT}** represent some of the most extreme anisotropic values recorded to date for any known crystalline materials (Table S17). Moreover, both phases also undergo colossal (α > 100 MK^{-1}) volumetric PTE (α_V = 575 and 292 MK^{-1}, respectively). Since the 1D channels propagate along [100] (Fig. 2), we can infer that most of the thermal expansion anisotropy is due to distortion of the host around the channels. In both phases the expansion coefficient approximately along [100] (i.e., α_{Y1}) is relatively modest, while that along [010] (i.e., α_{Y2}) is highly negative. The expansion coefficient normal to (001) is very highly positive in both cases. These observations comport with gradual narrowing (see ESI) of the zigzag angle

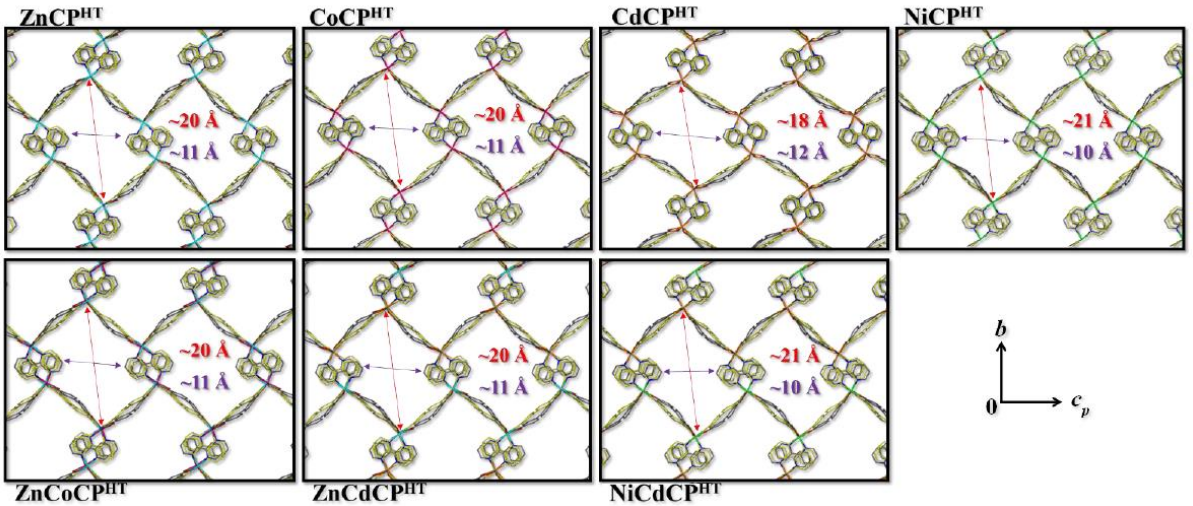

Figure 2 Packing of the high-temperature phases (270 K) of all CPs described in this study, viewed along [100]. In all cases both ligands are disordered over two positions. The minor component of disorder for each ligand is shown in yellow. The approximate atom-to-atom dimensions are indicated for each CP. Both metal atoms are shown in the representations of the solid solutions, but may be superimposed. Guest molecules and hydrogen atoms have been omitted for clarity. Note that the red arrow runs approximately along the *b* axis and the purple arrow approximately along the *c* axis.

with decreasing temperature, as also occurs abruptly during the phase transition.

Previously we[23,24] and others[3,6,25–27] were successful in tuning the thermal expansion behaviour of structural analogues by modulating their composition. In this context we explored metal node substitution for facile modification of the coordination geometries about various metal centres; a series of **MCP** analogues was prepared with M = Ni, Co and Cd. Using SCXRD, we established that all of these materials are isotypes[19] of **ZnCP** (Fig. 2 and Table S1). They also undergo subtle low temperature phase transitions in the ranges 250-240, 260-250 and 200-190 K, respectively (Fig. S14).

Multiple attempts were made to determine successive crystal structures across the phase change with slow cooling. However, in all cases the crystals fractured during the transition, thus yielding poor quality diffraction data from which it was only possible to determine unit cell parameters, the space group and estimates of M···M···M angles (with the exception of **CoCP**).

Upon cooling, the changes in the unit-cell parameters of **NiCP** across the phase change are similar to those of **ZnCP**, with expansion along [010] and concomitant contraction along [001]. Moreover, the M···M···M zigzag angle in **NiCP** also narrows across the phase change (from 123.31(3)° at 250 K to 116.38(3)° at 240 K, Table S13, Fig. S16b). Interestingly, in the cases of **CoCP** and **CdCP,** cooling across the phase-change results in shortening of the *b* axis and narrowing of the *β* angle, with elongation of the *c* axis (Fig. S14). Therefore, with regard to these parameters, the phase changes in **CoCP** and **CdCP** are inversely related to those of **ZnCP** and **NiCP**. This is also reflected in the increase of the M···M···M zigzag angle in **CdCP** from 140.24(1)° at 200 K to 145.29(1)° at 190 K (Table S13 and Fig. S16). The phase change temperatures for **CoCP** and **CdCP** are significantly different (*ca* 260 and 200 K, respectively).

Variable-temperature unit-cell determinations for **CdCP** were carried out as for **ZnCP**. Owing to facile desolvation and relatively high phase-change temperatures of **CoCP^{HT}** and **NiCP^{HT}** (both *ca* 250 K), an environmental solvent cell was used for unit cell determinations in the range 280 to 310 K (see ESI). **NiCP^{HT}** exhibits colossal linear thermal expansion along *Y2* and *Y3*, while **CoCP^{HT}** exhibits linear NTE along *Y3* (Figs 3, S30, Table S14). Both exhibit colossal volumetric PTE (α_V = 371 MK^{-1} for **NiCP^{HT}** and 239 MK^{-1} **CoCP^{HT}**). In **CoCP^{HT}** both linear PTE and NTE occur in the *ac* plane between adjacent 1D strands (Fig. 4b). The magnitudes of thermal expansion (both linear and volumetric) of **NiCP^{HT}** and **CoCP^{HT}** are substantially lower than that of **ZnCP**. Both phases of **CdCP** exhibit extreme anisotropic thermal expansion (Figs 3, S40, Table S16), similar to **ZnCP** (**CdCP^{HT}** α_{Y2} = 778 MK^{-1}, α_{Y3} = −389 MK^{-1} and α_V = 531 MK^{-1}).

Tuning of thermal expansion behaviour in metal containing materials may also be achieved by the preparation of solid solutions.[7–9,18] Three solid solutions were prepared by the addition of equimolar amounts of two metal nitrates to the crystallisation solution (**MM'CP**, MM' = ZnCo, ZnCd, NiCd). However, energy dispersive X-ray analysis showed that each of the resulting materials contains substantially different amounts of metal ions (Table S18). All of the solid solutions have similar packing arrangements and phase change behaviour to those observed for **ZnCP**. As expected, the structure of **ZnCoCP** ($[Zn_{0.92}Co_{0.08}(bpdc)(bpy)\cdot 2DMF]_n$) and **ZnCdCP** ($[Zn_{0.92}Cd_{0.08}(bpdc)(bpy)\cdot 2DMF]_n$) are most similar to that of **ZnCP**; the packing is likely directed by the major metal component. This holds true for both the **HT** and **LT** phases of these materials. The structure of **NiCdCP^{HT}** ($[Ni_{0.83}Cd_{0.17}(bpdc)(bpy)\cdot 2DMF]_n$) is also closer to that of **NiCP^{HT}**. However, owing to the notable difference in packing between **NiCP^{LT}** and **CdCP^{LT}** (Fig. S9), **NiCdCP^{LT}** adopts an intermediate packing arrangement, which is similar to that of the other solid solutions.

Variable-temperature unit-cell determinations were carried out to determine the thermal behaviour of the solid solutions. With regard to changes in their unit cell parameters, all three solid solutions exhibit phase-change behaviour similar to that of **ZnCP**, albeit at different onset temperatures. **ZnCoCP^{HT}** exhibits

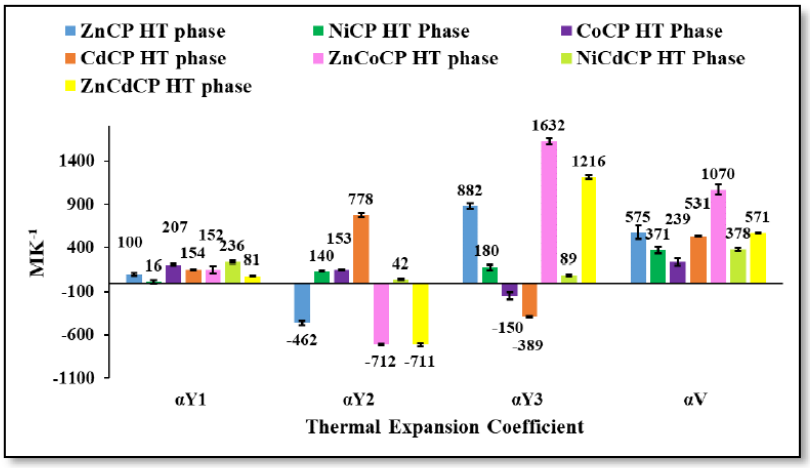

Figure 3 Thermal expansion coefficients for the high-temperature phases of the CPs. Error bars and specific values are indicated.

colossal linear NTE along *Y2* (α_{Y2} = –712 MK^{-1}) and supercolossal (an order of magnitude larger than colossal)[28] PTE along *Y3* (α_{Y3} = 1632 MK^{-1}). **ZnCoCP^{HT}** also displays supercolossal volumetric PTE (α_V = 1070 MK^{-1}, Figs 3, Table S16). Both α_V and the degree of anisotropy are far greater for **ZnCoCP^{HT}** than for **ZnCP^{HT}** or **CoCP^{HT}**, and both *Y2* and *Y3* are nearly twice those for **ZnCP^{HT}** and many times larger than for **CoCP^{HT}**. Furthermore, *Y1* experiences moderate NTE in **ZnCoCP^{HT}**, as opposed to moderate linear PTE in **ZnCP^{HT}**. Interestingly, the thermal expansion behaviour of **ZnCoCP^{LT}** is more similar to that of **CoCP^{LT}**; it undergoes linear ZTE along *Y2* and PTE along the other principal axes (Table S16 and Fig. S40), resulting in colossal volumetric PTE.

The thermal expansion of **ZnCdCP^{HT}** is analogous to that of the **ZnCoCP^{HT}** (Fig. 3, Table S16). Similarly, to **ZnCoCP^{HT}** the linear NTE along *Y2* is colossal and the PTE along *Y3* is supercolossal (α_{Y2} = –711 MK^{-1}, α_{Y3} = 1216 MK^{-1}). However, its volumetric PTE is colossal (α_V = 571 MK^{-1}). The orientations of the principal axes and thus the mechanism for thermal expansion in **ZnCdCP^{HT}** are analogous to those of **ZnCoCP^{HT}** (Fig. S39). The linear thermal expansion behaviour of **NiCdCP^{HT}** differs from that of both **NiCP^{HT}** and **CdCP^{HT}** (Fig. 3); the magnitudes of the coefficients along *Y2* and *Y3* for **NiCdCP^{HT}** are notably smaller than those for **NiCP^{HT}** and **CdCP^{HT}**.

During the course of this study we noted a discrepancy between the unit-cell parameters at 100 K obtained after incremental cooling (periodic unit-cell determinations) and flash-cooling the crystal (rapid cooling from ambient to 100 K) – see Tables S1 and S2, and Fig. S14. The thermal expansion behaviour appears to be attenuated when the crystal is flash-cooled. This observation was further investigated by means of differential scanning calorimetry at different cooling rates and in triplicate, which supports the assertion that higher cooling rates lead to attenuation of the phase-change.

Conclusions

All of the CPs display interesting thermal expansion behaviour, ranging from colossal volumetric PTE to supercolossal linear thermal expansion. Their thermal expansion coefficients are comparable to the highest reported values for anisotropic thermal expansion (Tables 1, S17). An overview of reports of colossal (and supercolossal) anisotropic thermal expansion is presented in Table 1 and a more comprehensive survey of the literature is given in Table S17. Almost all of the materials in this study exceed reports of both linear and volumetric thermal expansion in 1D CPs (Table S17). The only material exceeding (dramatically) the values reported here requires a spin-crossover transition to effect exceptional thermal expansion of a 2D framework.[7] It is interesting to note that the best performing materials in this study (**ZnCoCP^{HT}** and **ZnCdCP^{HT}**) and two of the four best performing materials in the literature are all solid solutions. Therefore, solid solutions should be considered a viable method of increasing the thermal expansion properties of a given class of material.

Table 1 Examples of extreme anisotropic thermal expansion.

Material	α_{Y1} (MK^{-1})	α_{Y2} (MK^{-1})	α_{Y3} (MK^{-1})	α_V (MK^{-1})	Ref.
CA-Pyz	–1375	196	1524	245	28
[Zn_2(fu-L^1)$_2$dabco]*n*	–380	1161	14.6	837	6
[$Fe_{0.84}Ni_{0.16}$(bpac)($Au(CN)_2)_2$]·2EtOH	–3200	5200	1500	3200	7
($Mn_{0.95}Ni_{0.05}$)CoGe	–1804	1265	46	–624	18
ZnCoCP^{HT}	152	–712	1632	1070	This work
ZnCdCP^{HT}	81	–711	1216	570	This work

Conflicts of interest

There are no conflicts to declare.

ACKNOWLEDGMENTS

We thank the National Research Foundation (NRF) of South Africa for financial support and the Central Analytical Facilities at Stellenbosch University for EDX analyses.

Notes and references

1 J. Chen, L. Hu, J. Deng and X. Xing, *Chem. Soc. Rev.*, 2015, **44**, 3522–3567.
2 K. Takenaka, *Sci. Technol. Adv. Mater.*, 2012, **13**, 013001.
3 Z. Liu, Q. Gao, J. Chen, J. Deng, K. Lin and X. Xing, *Chem. Commun.*, 2018, **54**, 5164–5176.
4 D. Das, T. Jacobs and L. J. Barbour, *Nat. Mater.*, 2010, **9**, 36–39.
5 W. Cai and A. Katrusiak, *Nat. Commun.*, 2014, **5**, 1–8.
6 S. Henke, A. Schneemann and R. A. Fischer, *Adv. Funct. Mater.*, 2013, **23**, 5990–5996.
7 B. R. Mullaney, L. Goux-Capes, D. J. Price, G. Chastanet, J.-F. Létard and C. J. Kepert, *Nat. Commun.*, 2017, **8**, 1053.
8 J. Chen, Q. Gao, A. Sanson, X. Jiang, Q. Huang, A. Carnera, C. G. Rodriguez, L. Olivi, L. Wang, L. Hu, K. Lin, Y. Ren, Z. Lin, C. Wang, L. Gu, J. Deng, J. P. Attfield and X. Xing, *Nat. Commun.*, 2017, **8**, 14441.
9 H. Yamamoto, T. Imai, Y. Sakai and M. Azuma, *Angew. Chem., Int. Ed.*, 2018, **57**, 8170–8173.
10 L. D. Devries, P. M. Barron, E. P. Hurley, C. Hu and W. Choe, *J. Am. Chem. Soc.*, 2011, **133**, 14848–14851.
11 T. A. Mary, J. S. Evans, T. Vogt and A. W. Sleight, *Science*, 1996, **272**, 90–92.
12 J. S. O. Evans, Z. Hu, J. D. Jorgensen, D. N. Argyriou, S. Short and A. W. Sleight, *Science*, 1997, **275**, 61–65.
13 A. L. Goodwin, M. Calleja, M. J. Conterio, M. T. Dove, J. S. O. Evans, D. A. Keen, L. Peters and M. G. Tucker, *Science*, 2008, **319**, 794–797.
14 J. P. Zhang, P. Q. Liao, H. L. Zhou, R. B. Lin and X. M. Chen,

Chem. Soc. Rev., 2014, **43**, 5789–5814.
15 Z. Chang, D. H. Yang, J. Xu, T. L. Hu and X. H. Bu, *Adv. Mater.*, 2015, **27**, 5432–5441.
16 S. R. Batten, N. R. Champness, X. Chen, J. Garcia-Martinez, S. Kitagawa, L. Ohrstrom, M. O'Keeffe, M. Paik Suh and J. Reedijk, *CrystEngComm*, 2012, **14**, 3001–3004.
17 S. J. Hunt, M. J. Cliffe, J. A. Hill, A. B. Cairns, N. P. Funnell and A. L. Goodwin, *CrystEngComm*, 2015, **17**, 361–369.
18 Q. Ren, W. Hutchison, J. Wang, A. Studer, G. Wang, H. Zhou, J. Ma and S. J. Campbell, *ACS Appl. Mater. Interfaces*, 2019, **11**, 17531–17538.
19 L. J. Barbour, D. Das, T. Jacobs, G. O. Lloyd and V. J. Smith, in *Supramolecular Chemistry: From Molecules to Nanomaterials*, eds. P. A. Gale and J. W. Steed, John Wiley & Sons, Ltd., Hoboken, 2012.
20 L. J. Barbour, *Chem. Commun.*, 2006, 1163.
21 L. M. van Wyk and L. J. Barbour, In Preparation.
22 M. J. Cliffe and A. L. Goodwin, *J. Appl. Crystallogr.*, 2012, **45**, 1321–1329.
23 I. Grobler, V. J. Smith, P. M. Bhatt, S. A. Herbert and L. J. Barbour, *J. Am. Chem. Soc.*, 2013, **135**, 6411–6414.
24 E. R. Engel, V. J. Smith, C. X. Bezuidenhout and L. J. Barbour, *Chem. Mater.*, 2016, **28**, 5073–5079.
25 L. Hu, J. Chen, J. Xu, N. Wang, F. Han, Y. Ren, Z. Pan, Y. Rong, R. Huang, J. Deng, L. Li and X. Xing, *J. Am. Chem. Soc.*, 2016, **138**, 14530–14533.
26 J. S. Ovens and D. B. Leznoff, *Inorg. Chem.*, 2017, **56**, 7332–7343.
27 H. L. Zhou, R. B. Lin, C. T. He, Y. B. Zhang, N. Feng, Q. Wang, F. Deng, J. P. Zhang and X. M. Chen, *Nat. Commun.*, 2013, **4**, 1–8.
28 H. Liu, M. J. Gutmann, H. T. Stokes, B. J. Campbell, I. R. Evans and J. S. O. Evans, *Chem. Mater.*, 2019, **31**, 4514–4523.

5.2. Supplementary Information

Electronic Supporting Information:

Tuning Extreme Anisotropic Thermal Expansion in 1D Coordination Polymers through Metal Selection and Solid Solutions

Lisa M. van Wyk, Leigh Loots and Leonard J. Barbour*

Department of Chemistry and Polymer Science, University of Stellenbosch, 7602 Matieland, South Africa.

* Correspondence to Professor Leonard J. Barbour (Email: ljb@sun.ac.za)

Contents

1. Crystallisation procedures

1.1. Crystallisation of ZnCP

{[Zn(bpdc)(bpy)]·2DMF}$_n$ (**ZnCP**) was prepared solvothermally. In a scintillation vial, equimolar amounts of the ligands 4,4′-biphenyldicarboxylic acid (bpdc, 0.10 mmol, 24 mg) and 2,2′-bipyridine (bpy, 0.10 mmol, 16 mg), along with $Zn(NO_3)_2{\cdot}6H_2O$ (0.15 mmol, 45 mg) were added to 3 ml DMF and sonicated until partially dissolved. The vial was placed in an 80 °C preheated oven for 3 days. Clear, rod-shaped crystals were produced in quantitative yield (**Fig. S1**).

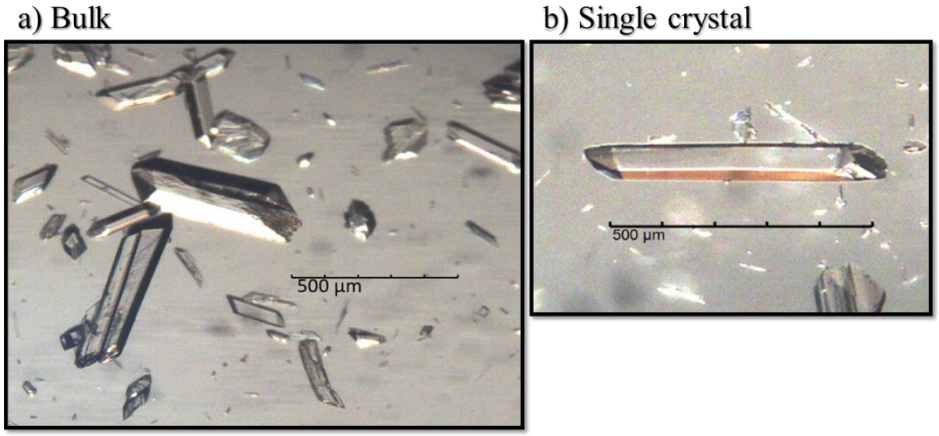

Figure S1: Photomicrographs of the bulk crystallisation **(a)** and a single crystal **(b)** of **ZnCP**.

1.2. Crystallisation of CoCP

Single crystals of {[Co(bpdc)(bpy)]·2DMF}$_n$ (**CoCP**) were prepared similarly to the procedure in **§1.1**. However, $Co(NO_3)_2{\cdot}6H_2O$ (0.15 mmol, 30 mg) was utilised in place of $Zn(NO_3)_2{\cdot}6H_2O$. Clusters of dark pink rod-shaped crystals were produced in quantitative yield (**Fig. S2**).

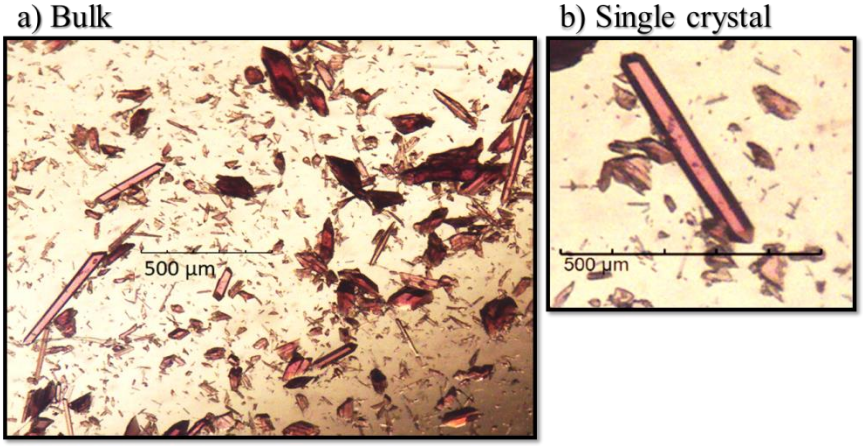

Figure S2: Photomicrographs of the bulk crystallisation **(a)** and a single crystal **(b)** of **CoCP**.

1.3. Crystallisation of CdCP

Single crystals of {[Cd(bpdc)(bpy)]·2DMF}$_n$ (**CdCP**) were prepared similarly to the procedure in §1.1. However, $Cd(NO_3)_2{\cdot}4H_2O$ (0.15 mmol, 46 mg) was utilised in place of $Zn(NO_3)_2{\cdot}6H_2O$. The solvothermal temperature was also adjusted to 100 °C. Clear, rod-shaped crystals were produced in quantitative yield (Fig. S3).

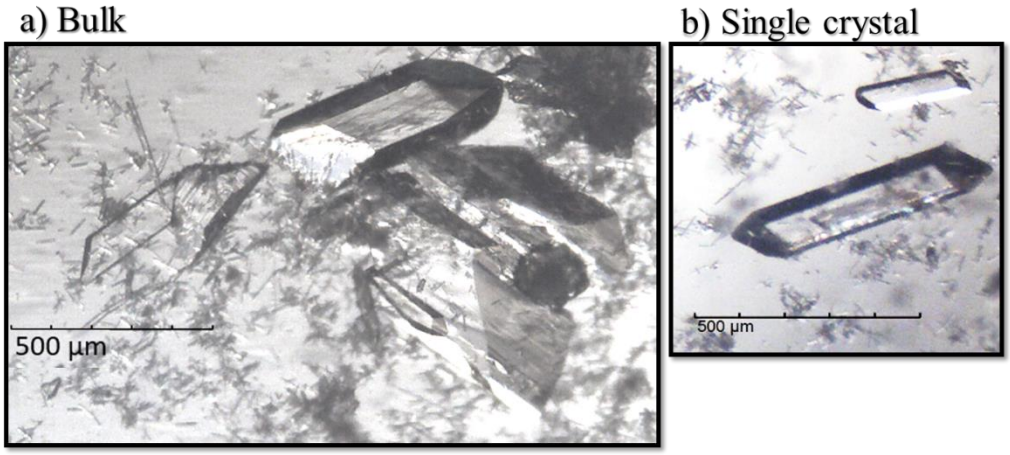

Figure S3: Photomicrographs of the bulk crystallisation **(a)** and single crystals **(b)** of **CdCP**.

1.4. Crystallisation of NiCP

Single crystals of {[Ni(bpdc)(bpy)]·2DMF}$_n$ (**NiCP**) were prepared similarly to the procedure in §1.1. However, $Ni(NO_3)_2{\cdot}6H_2O$ (0.15 mmol, 44 mg) was utilised in place of $Zn(NO_3)_2{\cdot}6H_2O$. Intergrown teal rod-shaped crystals were produced in quantitative yield (Fig. S4).

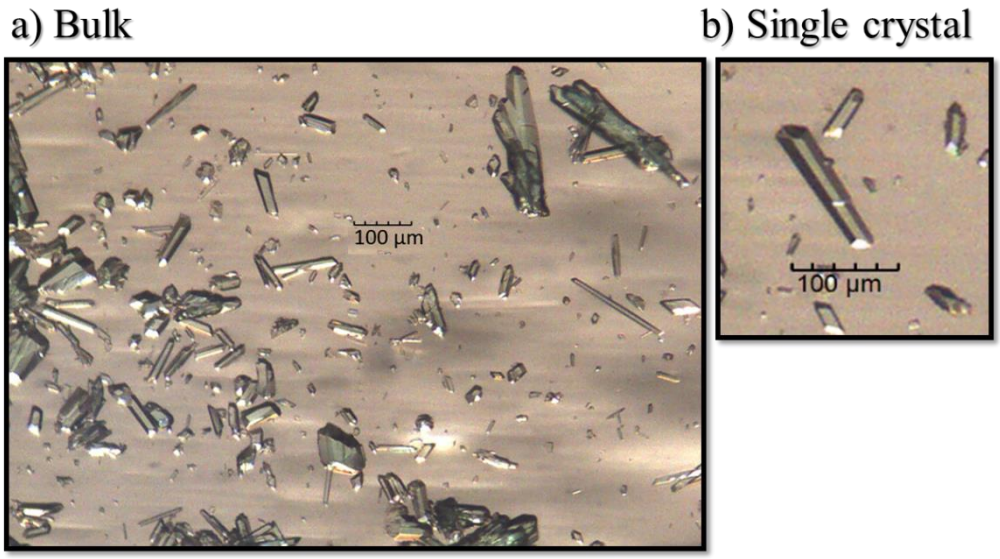

Figure S4: Photomicrographs of the bulk crystallisation **(a)** and single crystals **(b)** of **NiCP**.

1.5. Crystallisation of ZnCoCP

Single crystals of $\{[Zn_{0.92}Co_{0.08}(bpdc)(bpy)]\cdot 2DMF\}_n$ (**ZnCoCP**) were prepared similarly to the procedure in **§1.1**. However, both $Zn(NO_3)_2\cdot 6H_2O$ (0.08 mmol, 22 mg) and $Co(NO_3)_2\cdot 6H_2O$ (0.08 mmol, 15 mg) were utilised. Clusters of light pink rod-shaped crystals were produced in quantitative yield (**Fig. S5**).

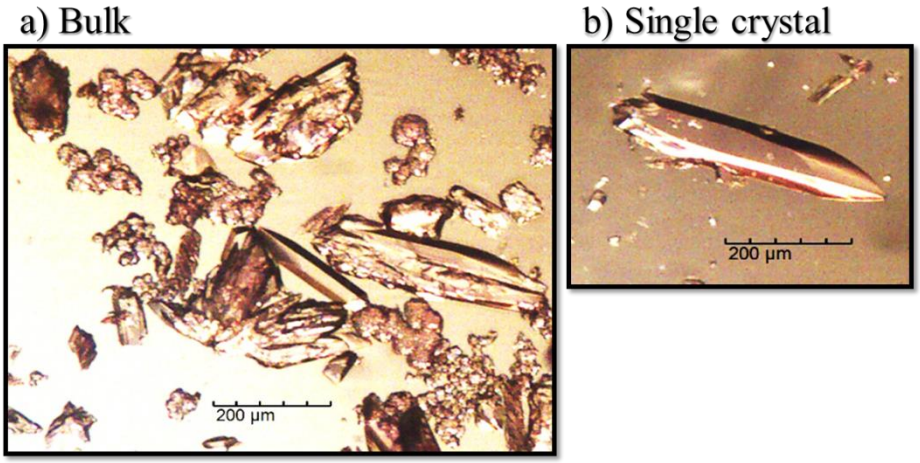

Figure S5: Photomicrographs of the bulk crystallisation **(a)** and a single crystal **(b)** of **ZnCoCP**.

1.6. Crystallisation of NiCdCP

Single crystals of $\{[Ni_{0.17}Cd_{0.83}(bpdc)(bpy)]\cdot 2DMF\}_n$ (**NiCdCP**) were prepared similarly to the procedure in **§1.1**. However, both $Cd(NO_3)_2\cdot 4H_2O$ (0.08 mmol, 23 mg) and $Ni(NO_3)_2\cdot 6H_2O$ (0.08 mmol, 22 mg) were utilised. The solvothermal temperature was also adjusted to 100 °C. Green rod-shaped crystals were produced in quantitative yield (**Fig. S6**).

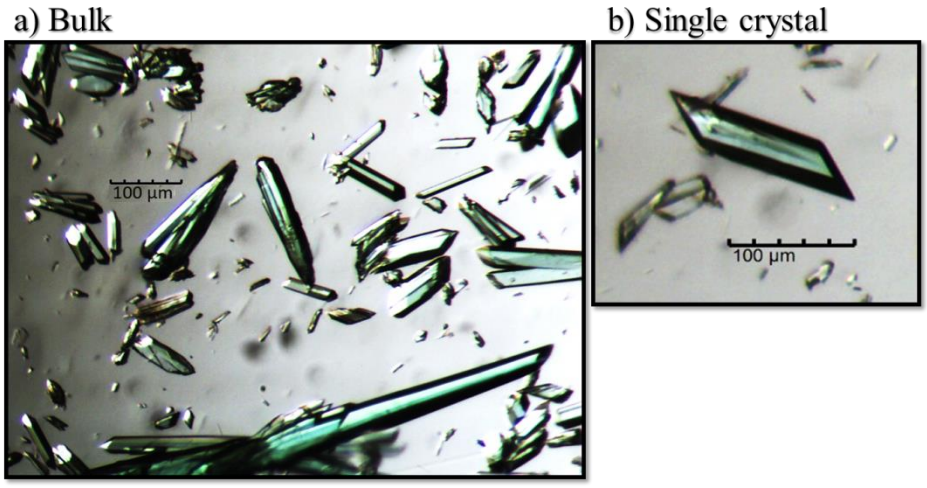

Figure S6: Photomicrographs of the bulk crystallisation **(a)** and a single crystal **(b)** of **NiCdCP**.

1.7. Crystallisation of ZnCdCP

Single crystals of $\{[Zn_{0.92}Cd_{0.08}(bpdc)(bpy)]\cdot 2DMF\}_n$ (**ZnCdCP**) were prepared similarly to the procedure in **§1.1**. However, both $Zn(NO_3)_2\cdot 6H_2O$ (0.08 mmol, 22 mg) and $Cd(NO_3)_2\cdot 4H_2O$ (0.08 mmol, 23 mg) were utilised. The solvothermal temperature was also adjusted to 100 °C. Clear rod-shaped crystals were produced in a quantitative yield (**Fig. S7**).

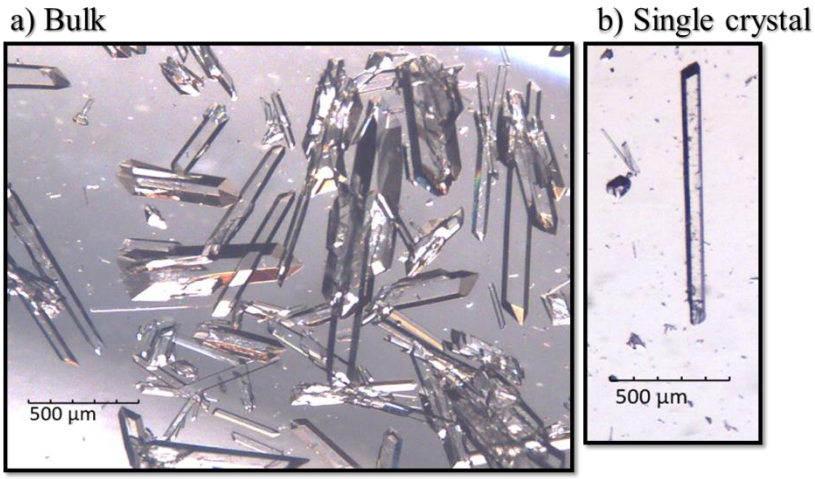

Figure S7: Photomicrographs of the bulk crystallisation **(a)** and a single crystal **(b)** of **ZnCdCP**.

2. Single-crystal X-ray diffraction (SCXRD)

Crystals of appropriate size and morphology, and the ability to extinguish plane-polarized light were attached to the tip of a MiTeGen mount[1] using Paratone®N oil. The crystal mount was then attached to a goniometer head, which was in turn mounted on a diffractometer. X-ray intensity data were recorded using either a Bruker APEX II DUO or a Bruker D8 Venture diffractometer. The DUO instrument is equipped with Incoatec IμS molybdenum (λ = 0.71073 Å) and copper (λ = 1.5418 Å) microfocus X-ray sources and a CCD area detector. The Venture instrument is equipped with an Incoatec IμS 3.0 molybdenum (λ = 0.71073 Å) microfocus X-ray source and a Photon II CPAD detector. Each diffractometer is equipped with an Oxford Cryosystems cryostat (700 Series Cryostream Plus for the DUO instrument and 800 Series Cryostream Plus for the Venture instrument), which is used to control the sample temperature. Both the frame exposure time and the number of frames collected for each experiment were varied, depending on the diffraction quality and characteristics of the mounted crystal.

Data reduction and absorption corrections were carried out using the SAINT[2] and SADABS[3] programs, respectively. The unit-cell dimensions were refined on all data and space groups were assigned based on systematic absences and intensity statistics. The structures were solved with a dual-space algorithm or direct methods using SHELXT[4] or SHELXS-2016/1,[5] respectively. Structure refinement was carried out with SHELXL-2018/3[5] using the X-Seed[6,7] graphical user interface. Non-hydrogen atoms were refined anisotropically. Hydrogen atoms were placed in calculated positions. Illustrations of all crystal structures were generated using the programs POV-Ray[8] and Mercury.[9–11]

Please note that the structural determinations of the separate phases for each material were carried out on different crystals.

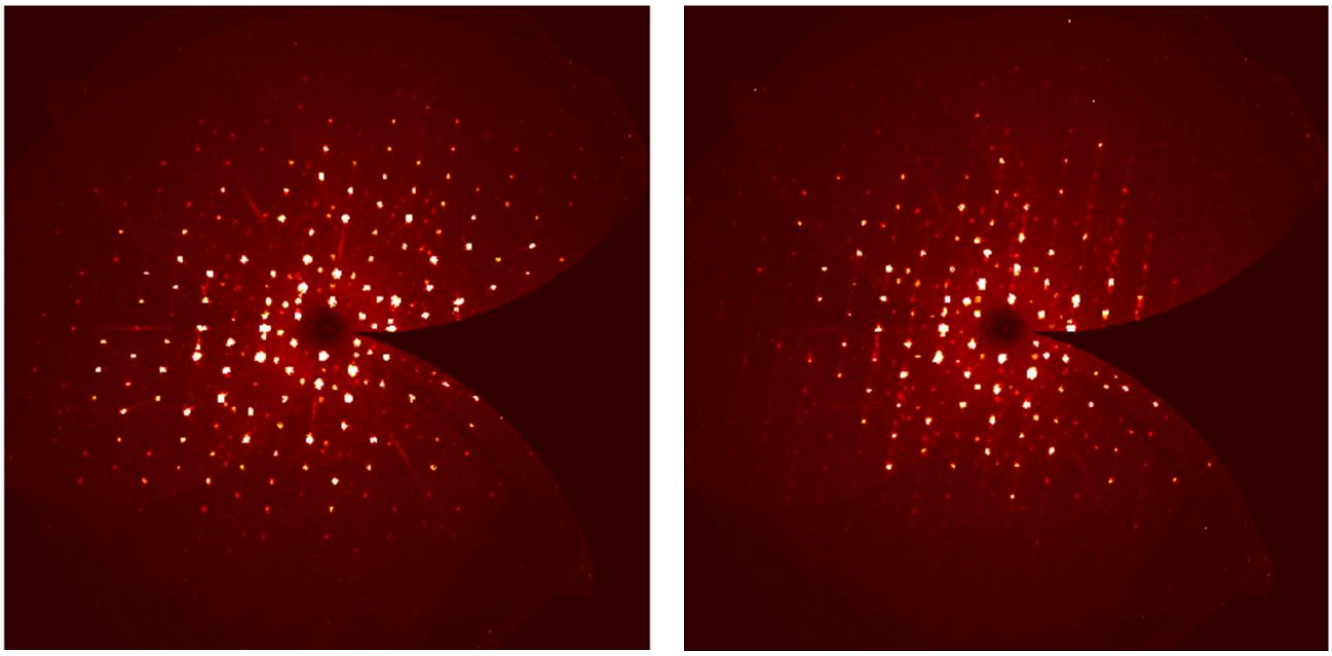

Figure S8: Precession images of a single crystal of **ZnCP** showing the *h0l* plane. The image on the left shows the crystal at 270 K while the image on the right shows the same crystal at 100 K (fast cooling so as not to shock the crystal). The crystal exhibits poorer diffraction at 100 K.

Table S1. Crystallographic parameters for the full structural determination of the materials studied.

	ZnCP^{HT}	ZnCP^{LT}	NiCP^{HT}	NiCP^{LT}	CoCP^{HT}	CoCP^{LT}	CdCP^{HT}	CdCP^{LT}
Empirical Formula	$C_{30}H_{30}N_4O_6Zn$	$C_{30}H_{30}N_4O_6Zn$	$C_{30}H_{30}N_4O_6Ni$	$C_{30}H_{30}N_4O_6Ni$	$C_{30}H_{30}N_4O_6Co$	$C_{30}H_{30}N_4O_6Co$	$C_{30}H_{30}N_4O_6Cd$	$C_{30}H_{30}N_4O_6Cd$
Formula weight (g mol^{-1})	607.94	607.94	601.28	601.28	601.50	601.50	654.97	654.97
Temperature (K)	270(2)	100(2)	270(2)	100(2)	270(2)	100(2)	270(2)	100(2)
Wavelength (Å)	0.71073	0.71073	0.71073	0.71073	0.71073	0.71073	0.71073	0.71073
Crystal system	Monoclinic	Monoclinic	Monoclinic	Monoclinic	Monoclinic	Monoclinic	Monoclinic	Monoclinic
Space group	$P2_1/n$	$P2_1/n$	$P2_1/n$	$P2_1/n$	$P2_1/n$	$P2_1/n$	$P2_1/n$	$P2_1/n$
a (Å)	7.700(4)	7.598(1)	7.587(1)	7.696(1)	7.672(5)	7.580(3)	7.751(1)	7.635(1)
b (Å)	25.487(13)	26.508(5)	26.025(1)	28.012(6)	25.683(18)	25.608(11)	23.773(1)	22.768(3)
c (Å)	17.427(8)	16.115(3)	16.934(6)	14.695(3)	17.291(13)	16.702(7)	19.044(1)	19.177(2)
α (°)	90	90	90	90	90	90	90	90
β (°)	99.18(1)	99.22(3)	99.26(1)	99.71(1)	98.63(2)	97.96(1)	96.40(1)	94.90(1)
γ (°)	90	90	90	90	90	90	90	90
V (Å^3)	3376.0(30)	3204.0(11)	3301.0(2)	3122.6(11)	3369.0(40)	3211.0(20)	3487.3(4)	3321.5(7)
Z	4	4	4	4	4	4	4	4
Calculated density / (g cm^{-3})‡	0.908	0.957	0.916	0.968	0.898	0.942	0.969	1.017
Absorption coefficient (mm^{-1})	0.748	0.788	0.609	0.644	0.530	0.556	0.646	0.679
F_{000}	944.0	944.0	936.0	936.0	932.0	932.0	1016.0	1016.0
θ range for data collection (°)	2.37–26.02	2.00–28.38	1.42–26.02	1.58–25.08	2.38–25.03	1.47–26.48	2.74–27.88	2.31–28.31
Miller index ranges	-8 ≤ h ≤ 9 -31 ≤ k ≤ 31 -21 ≤ l ≤ 21	-10 ≤ h ≤ 10 -35 ≤ k ≤ 35 -21 ≤ l ≤ 21	-9 ≤ h ≤ 9 -32 ≤ k ≤ 31 -20 ≤ l ≤ 20	-9 ≤ h ≤ 9 -33 ≤ k ≤ 33 -17 ≤ l ≤ 17	-9 ≤ h ≤ 8 -30 ≤ k ≤ 30 -20 ≤ l ≤ 20	-9 ≤ h ≤ 9 -31 ≤ k ≤ 32 -20 ≤ l ≤ 19	-10 ≤ h ≤ 8 -31 ≤ k ≤ 31 -25 ≤ l ≤ 25	-10 ≤ h ≤ 10 -30 ≤ k ≤ 30 -25 ≤ l ≤ 25
Reflections collected	34409	85516	57798	27343	21224	21695	73044	48126
Independent reflections	6651	8016	6499	5760	5944	6485	8298	8254
Completeness to θ_{max} (%)	99.9	99.8	99.9	98.9	99.9	97.6	99.9	99.7
Max. and min. transmission	0.260, 0.216	0.746, 0.700	0.260, 0.233	0.745, 0.576	0.260, 0.208	0.745, 0.647	0.263, 0.224	0.746, 0.665
Refinement Method	Full-matrix least-squares on F^2	Full-matrix least-squares on F^2	Full-matrix least-squares on F^2	Full-matrix least-squares on F^2	Full-matrix least-squares on F^2	Full-matrix least-squares on F^2	Full-matrix least-squares on F^2	Full-matrix least-squares on F^2
Data / restraints / parameters	6651 / 1512 / 552	8016 / 1837 / 552	5499 / 1533 / 552	5491 / 1563 / 552	5944 / 1524 / 552	6485 / 1503 / 552	8298/ 1539 / 552	8254 / 1509 / 552
Goodness-of-fit on F^2	1.010	1.020	1.040	1.129	1.013	1.033	1.016	1.117
Final R indices [$I > 2\sigma(I)$]	$R1$ = 0.0514 $wR2$ = 0.1455	$R1$ = 0.0405 $wR2$ = 0.1040	$R1$ = 0.0358 $wR2$ = 0.1004	$R1$ = 0.0850 $wR2$ = 0.1952	$R1$ = 0.0693 $wR2$ = 0.1754	$R1$ = 0.0530 $wR2$ = 0.1333	$R1$ = 0.0410 $wR2$ = 0.0991	$R1$ = 0.0469 $wR2$ = 0.1046
Largest diff. peak and hole (e A^{-3})	0.418, -0.427	0.467, -0.513	0.211, -0.199	0.653, -1.077	0.405, -0.554	0.531, -0.580	0.316, -0.587	0.932, -1.281

‡Densities calculated with structures that have had the guest electron density removed by the Platon/SQUEEZE[12] routine

Table S2. Crystallographic parameters for the full structural determination of the CPs studied (cont'd).

	ZnCoCP^{HT}	ZnCoCP^{LT}	NiCdCP^{HT}	NiCdCP^{LT}	ZnCdCP^{HT}	ZnCdCP^{LT}
Empirical Formula	$C_{30}H_{30}N_4O_6Zn_{0.92}Co_{0.08}$	$C_{30}H_{30}N_4O_6Zn_{0.92}Co_{0.08}$	$C_{30}H_{30}N_4O_6Ni_{0.83}Cd_{0.17}$	$C_{30}H_{30}N_4O_6Ni_{0.83}Cd_{0.17}$	$C_{30}H_{30}N_4O_6Zn_{0.92}Cd_{0.08}$	$C_{30}H_{30}N_4O_6Zn_{0.92}Cd_{0.08}$
Formula weight (g mol^{-1})	607.42	607.42	610.4	610.4	611.7	611.7
Temperature (K)	270(2)	100(2)	270(2)	100(2)	270(2)	100(2)
Wavelength (Å)	0.71073	0.71073	0.71073	0.71073	0.71073	0.71073
Crystal system	Monoclinic	Monoclinic	Monoclinic	Monoclinic	Monoclinic	Monoclinic
Space group	$P2_1/n$	$P2_1/n$	$P2_1/n$	$P2_1/n$	$P2_1/n$	$P2_1/n$
a (Å)	7.716(2)	7.600(1)	7.632(1)	7.501(1)	7.696(1)	7.604(1)
b (Å)	25.819(6)	26.519(1)	26.288(6)	25.985(1)	25.461(1)	26.523(1)
c (Å)	17.144(4)	16.029(1)	16.739(4)	16.598(1)	17.429(1)	16.123(1)
α (°)	90	90	90	90	90	90
β (°)	99.26(1)	99.21(1)	98.90(1)	98.15(1)	99.02(1)	99.05(1)
γ (°)	90	90	90	90	90	90
V (Å^3)	3370.8(14)	3189.2(1)	3317.9(12)	3202.5(2)	3373.1(4)	3211.1(3)
Z	4	4	4	4	4	4
Calculated density / (g cm^{-3})‡	0.909	0.961	0.929	0.963	0.917	0.963
Absorption coefficient (mm^{-1})	0.732	0.774	0.618	0.641	0.742	0.780
F_{000}	943	943	949.6	949.6	950	949.8
θ range for data collection (°)	1.44–25.35	1.50–26.02	2.58–25.03	1.47–26.02	2.50–26.73	1.49–26.41
Miller index ranges	$-9 \le h \le 9$ $-31 \le k \le 31$ $-20 \le l \le 20$	$-9 \le h \le 9$ $-32 \le k \le 32$ $-19 \le l \le 19$	$-9 \le h \le 8$ $-31 \le k \le 31$ $-19 \le l \le 19$	$-9 \le h \le 9$ $-32 \le k \le 32$ $-20 \le l \le 20$	$-9 \le h \le 9$ $-32 \le k \le 32$ $-22 \le l \le 22$	$-9 \le h \le 9$ $-33 \le k \le 33$ $-20 \le l \le 20$
Reflections collected	69300	67084	48308	55707	66170	58598
Independent reflections	6175	6283	5839	6303	7157	6582
Completeness to θ_{max} (%)	100	99.9	99.8	99.9	99.8	99.7
Max. and min. transmission	0.260, 0.202	0.745, 0.698	0.259, 0.191	0.746, 0.659	0.263, 0.218	0.745, 0.707
Refinement Method	Full-matrix least-squares on F^2	Full-matrix least-squares on F^2	Full-matrix least-squares on F^2	Full-matrix least-squares on F^2	Full-matrix least-squares on F^2	Full-matrix least-squares on F^2
Data / restraints / parameters	6175 / 1590 / 561	6283 / 1620 / 561	5839 / 1595 / 561	6303 / 1610 / 561	7157 / 1583 / 555	6582 / 1579 / 561
Goodness-of-fit on F^2	1.050	1.055	1.038	1.120	1.032	1.090
Final R indices [$I > 2\sigma(I)$]	$R1$ = 0.0627 $wR2$ = 0.1936	$R1$ = 0.0415 $wR2$ = 0.1238	$R1$ = 0.0694 $wR2$ = 0.1862	$R1$ = 0.0628 $wR2$ = 0.1500	$R1$ = 0.0461 $wR2$ = 0.1314	$R1$ = 0.0397 $wR2$ = 0.1180
Largest diff. peak and hole (e A^{-3})	0.398, -0.511	0.513, -0.257	0.323, -0.650	0.874, -1.053	0.507, -0.384	0.429, -0.318

‡Densities calculated with structures that have had the guest electron density removed by the Platon/SQUEEZE[12] routine

2.1. Packing diagrams of the low temperature phases

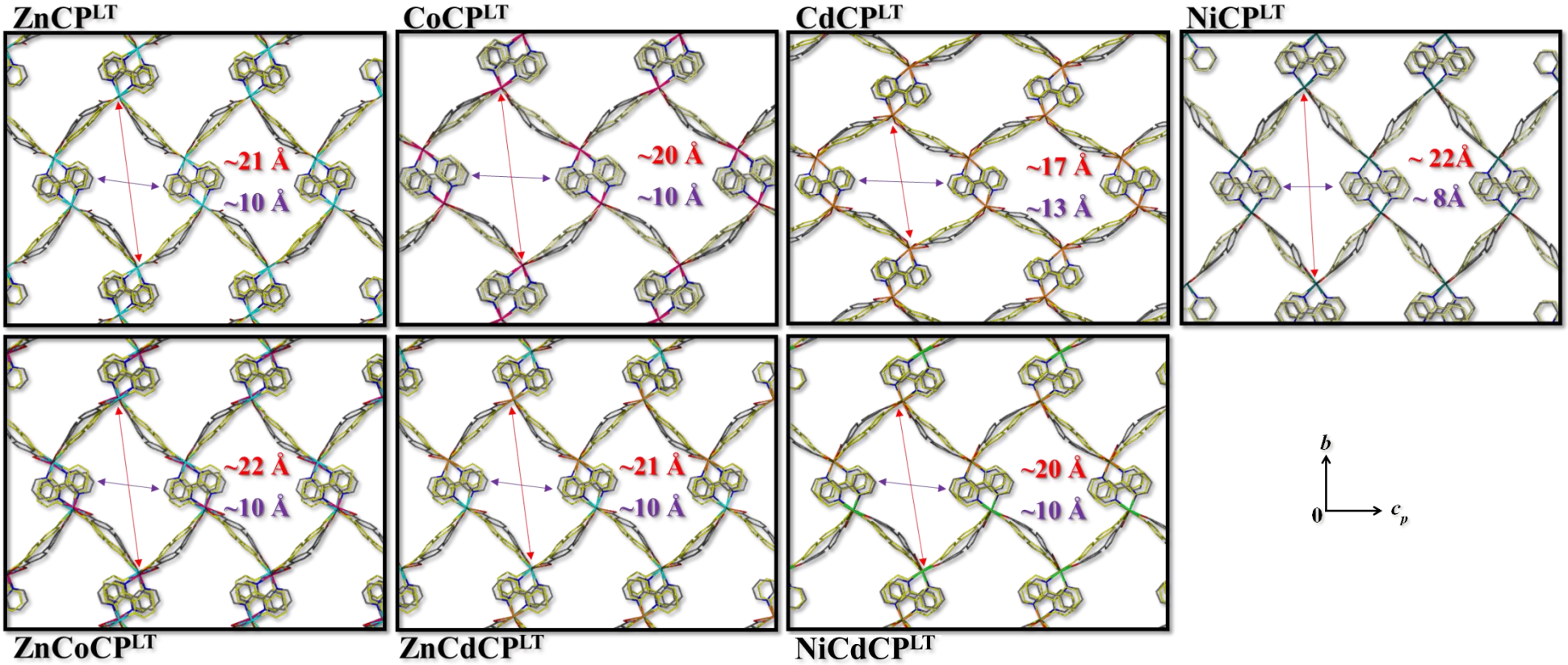

Figure S9: Packing of the low temperature phase (determined at 100 K) of each material studied viewed down the *a* axis. In each material both ligands are disordered over two positions. The minor component of disorder for each ligand is shown in yellow for clarity. The approximate channel aperture dimensions are indicated for each species. Both metal atoms are shown in the representations of the solid solutions, but may be superimposed. Guest molecules and hydrogen atoms have been omitted for clarity.

2.2. Probe-accessible volume (PAV) maps

The PAV[13] for each species was investigated in Mercury[9–11] using a probe radius of 1.5 Å and a grid spacing of 0.2 Å.

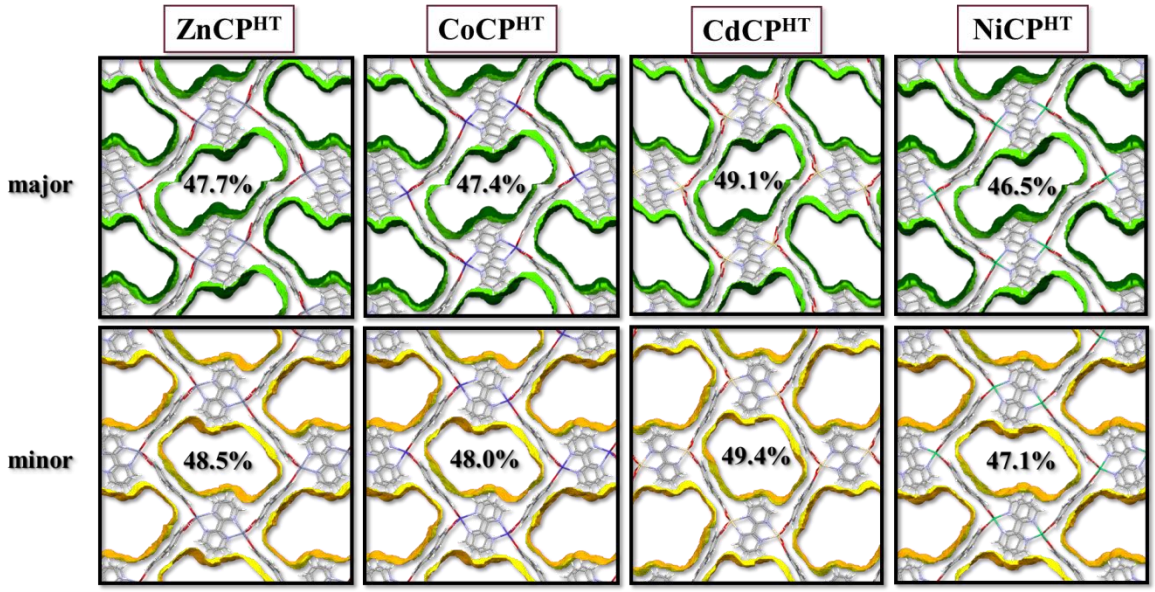

Figure S10: PAV of the high temperature phase (270 K) of the materials studied viewed down the *a* axis. The PAV for the major components of ligand disorder are shown in the top row, while the minor components are shown in the bottom row. The percentage PAV of the unit-cell volume is also given in each case. Guest molecules have been omitted.

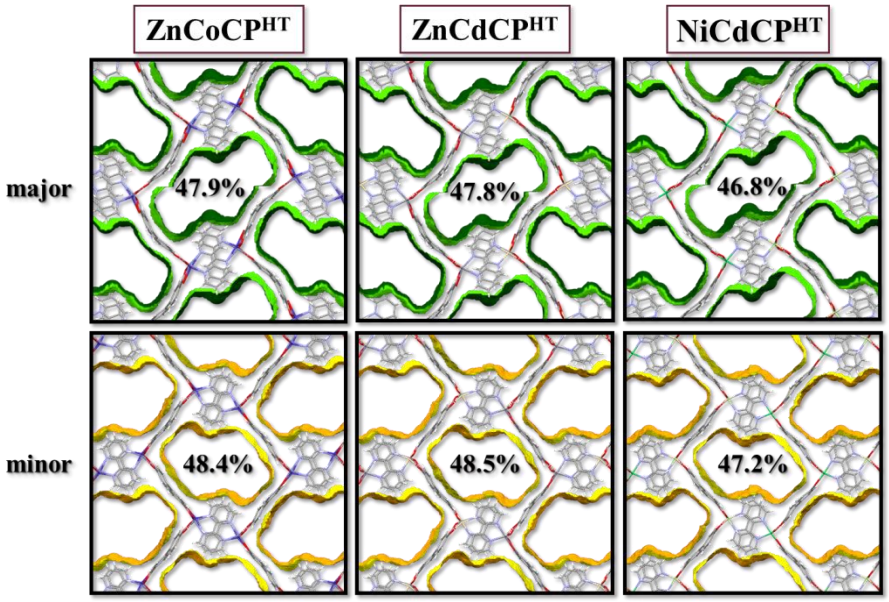

Figure S11: PAV of the high temperature (270 K) phase of the solid-solutions studied viewed down the *a* axis. The PAV for the major components of ligand disorder are shown in the top row, while the minor components are shown in the bottom row. The percentage PAV of the unit-cell volume is also given in each case. Both metal centres are shown, but may be superimposed. Guest molecules have been omitted.

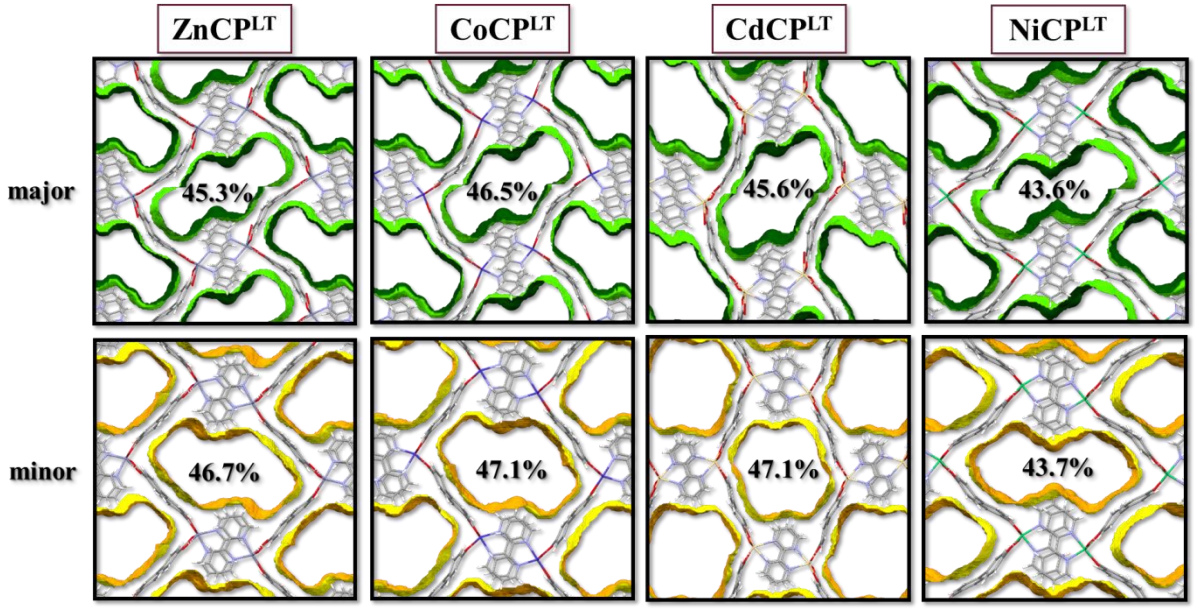

Figure S12: PAV of the low temperature phase (100 K) of the materials studied viewed down the *a* axis. The PAV for the major components of ligand disorder are shown in the top row, while the minor components are shown in the bottom row. The percentage PAV of the unit-cell volume is also given in each case. Guest molecules have been omitted.

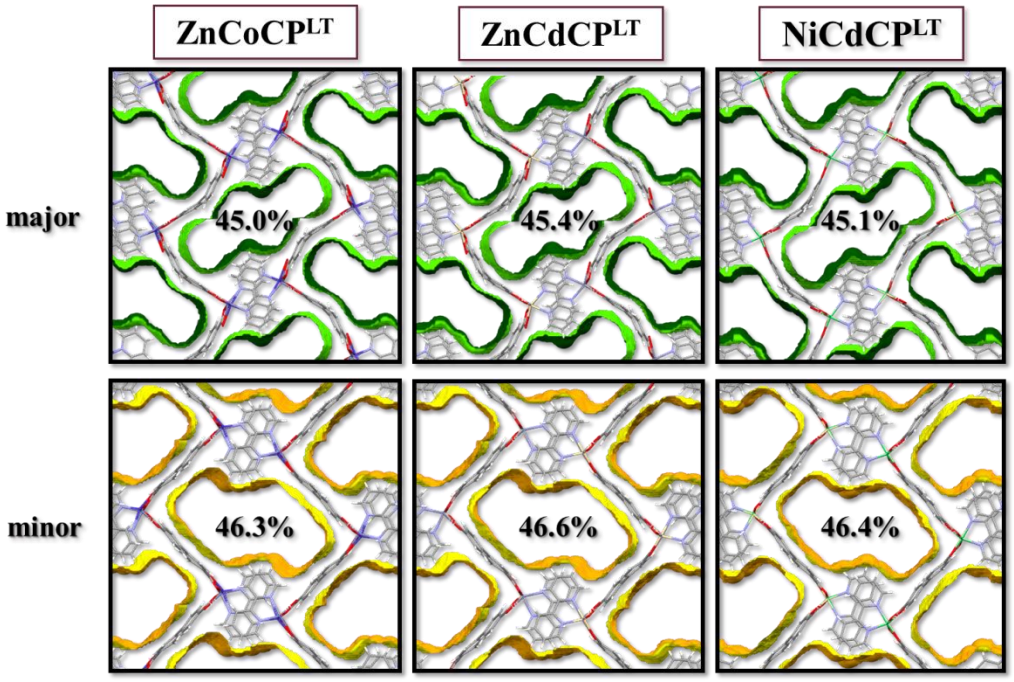

Figure S13: PAV of the low temperature phase (100 K) of the solid solutions studied viewed down the *a* axis. The PAV for the major components of ligand disorder are shown in the top row, while the minor components are shown in the bottom row. The percentage PAV of the unit-cell volume is also given in each case. Both metal centres are shown, but may be superimposed. Guest molecules have been omitted.

2.3. Variable-temperature unit-cell determinations

Variable-temperature unit-cell data were determined at 10 K intervals over a temperature range of 270–100 K. 270 K was chosen as the upper temperature limit owing to the facile desolvation of the compounds studied. These data were processed in the unit-cell tab of APEX3[14] as well as reduced with the SAINT[2] program (three iterations). Care was taken to remove anomalous scattering from the reciprocal lattice. In most cases the reduced data are presented. However, in the case of **CoCP** the loss of single crystal quality below 250 K led to the unreduced data presenting a more accurate depiction.

In cases where materials desolvate under the required experimental temperature an environmental solvent cell was employed. The solvent cell consists of a 1 mm diameter glass Lindemann Capillary attached to a steel nut with epoxy, which is then screwed into a placeholder body (allowing the solvent cell to be mounted to the goniometer). The capillary was filled with the same solvent that is the guest in the material of interest (*i.e.* DMF). A crystal was then positioned in the capillary on cotton wool (to keep it stationary). The capillary was capped by the placeholder body and attached to the goniometer. Subsequently, the data collection procedure was followed as above.

An environmental solvent cell was used to expand the upper temperature range in data collections for **CoCP**, **NiCP** and **NiCdCP** as their phase change temperature are high relative to the other CPs. Therefore, more data was required to accurately quantify the thermal expansion coefficients. Unit-cell determinations were carried out as above using the solvent cell in the temperature range 280–310 K. The solvent cell was heated to 310 K and cooled to provide cooling data for comparison to the low temperature experiments. However, we do note that this may lead to preconditioning of the crystals, resulting in differences in the unit-cell data as extrapolated from the differences from the 270–100 K.

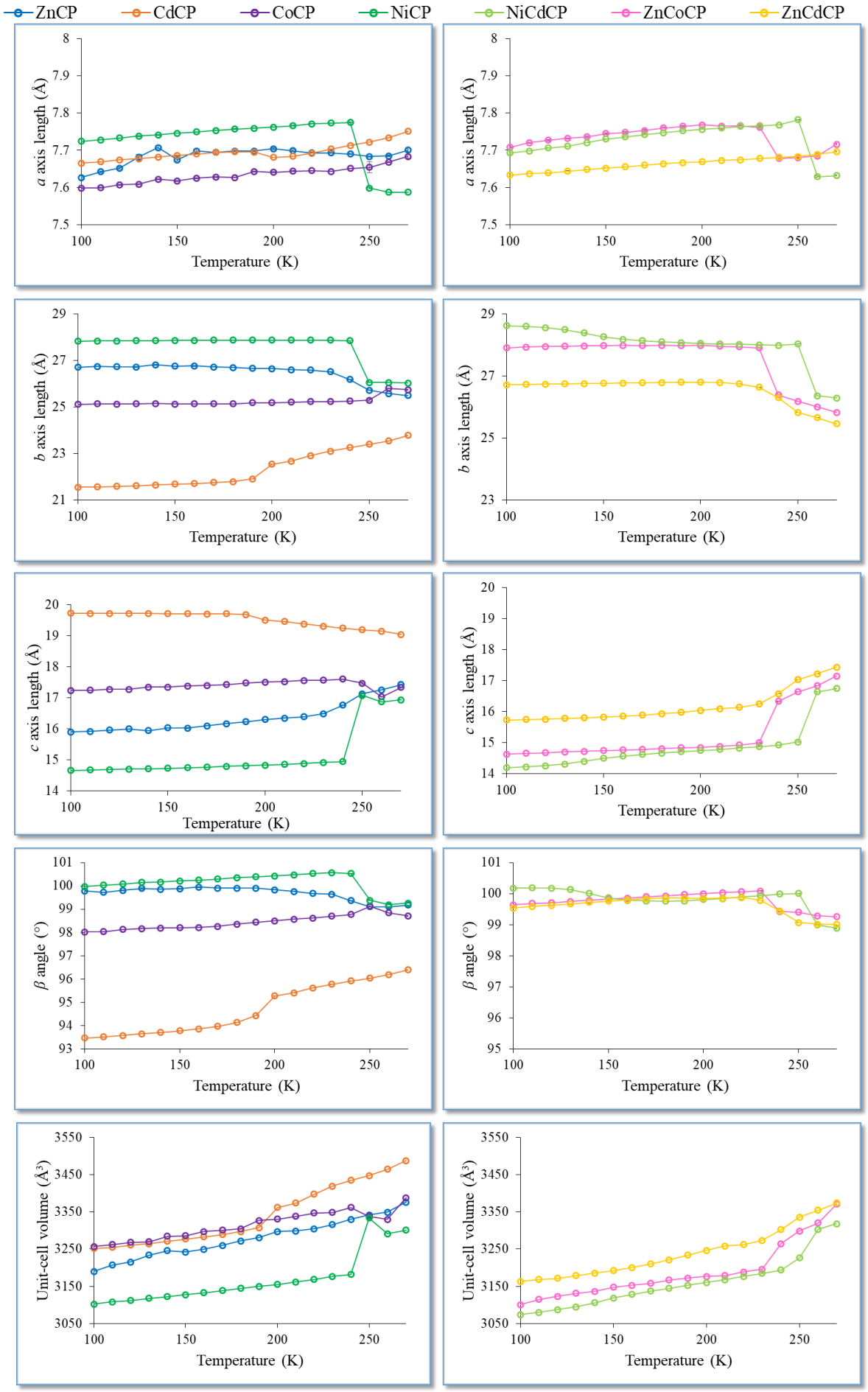

Figure S14: Variation of the unit-cell parameters over temperature of the materials in this study. Error bars are shown, but may be too small to discern.

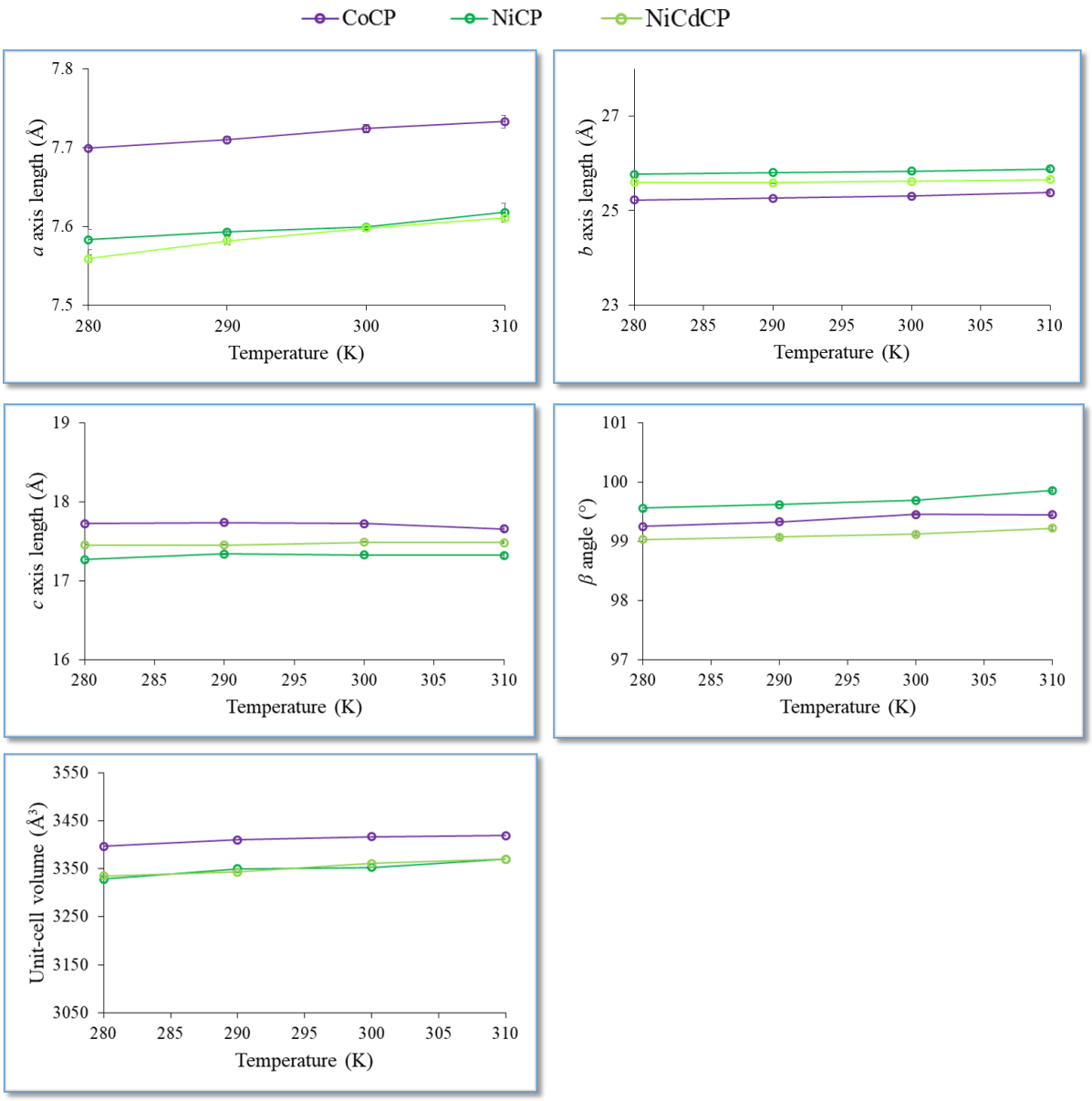

Figure S15: Variation of the unit-cell parameters over temperature for the environmental solvent cell experiments. Error bars are shown, but may be too small to discern.

Table S3. Variable-temperature unit-cell parameters as determined for **ZnCP**.

Temperature (K)	*a* axis (Å)	*b* axis (Å)	*c* axis (Å)	*β* angle (°)	Volume (Å^3)
270	7.700(4)	25.487(13)	17.427(8)	99.18(1)	3376.3
260	7.685(2)	25.578(7)	17.254(5)	99.11(1)	3349.0
250	7.683(1)	25.720(5)	17.128(4)	99.11(1)	3341.9
240	**7.690(1)**	**26.181(8)**	**16.763(5)**	**99.37(1)**	**3330.0**
230	**7.693(2)**	**26.511(7)**	**16.490(4)**	**99.64(1)**	**3315.6**
220	7.693(2)	26.581(7)	16.393(4)	99.68(1)	3304.5
210	7.699(3)	26.592(10)	16.348(6)	99.76(1)	3298.7
200	7.704(3)	26.646(12)	16.301(7)	99.83(1)	3297.2
190	7.698(3)	26.652(13)	16.233(8)	99.90(1)	3280.9
180	7.698(4)	26.691(15)	16.166(9)	99.91(2)	3271.8
170	7.694(4)	26.718(17)	16.096(10)	99.91(2)	3259.6
160	7.698(5)	26.763(19)	16.021(11)	99.95(2)	3249.5
150	7.674(3)	26.752(10)	16.031(7)	99.88(3)	3242.0
140	7.707(6)	26.810(21)	15.944(12)	99.86(2)	3245.6
130	7.682(6)	26.710(30)	15.994(16)	99.89(3)	3234.0
120	7.652(3)	26.724(13)	15.958(8)	99.81(2)	3215.0
110	7.642(2)	26.743(12)	15.920(5)	99.73(1)	3207.0
100	7.627(3)	26.703(14)	15.896(9)	99.78(2)	3190.0
100[‡]	7.598(1)	26.508(5)	16.115(3)	99.22(3)	3204.0

*Values in bold indicate the phase transition region

[‡]Parameters determined from flash cooling (different crystal)

Table S4. Variable-temperature unit-cell parameters as determined for **NiCP**.

Temperature (K)	*a* axis (Å)	*b* axis (Å)	*c* axis (Å)	*β* angle (°)	Volume (Å^3)
270	7.587(1)	26.025(1)	16.938(1)	99.26(1)	3301.0
260	7.587(1)	26.047(1)	16.872(1)	99.19(1)	3291.3
250	**7.598(2)**	**26.049(9)**	**17.073(6)**	**99.38(4)**	**3333.8**
240	**7.775(1)**	**27.849(4)**	**14.947(3)**	**100.54(1)**	**3182.0**
230	7.773(1)	27.865(4)	14.919(2)	100.57(1)	3176.6
220	7.771(1)	27.868(3)	14.884(2)	100.54(1)	3168.8
210	7.766(1)	27.866(3)	14.856(2)	100.48(1)	3161.6
200	7.762(1)	27.867(2)	14.831(1)	100.43(1)	3155.3
190	7.759(1)	27.868(1)	14.809(1)	100.39(1)	3149.5
180	7.757(1)	27.868(2)	14.790(1)	100.36(1)	3144.8
170	7.753(1)	27.865(2)	14.768(1)	100.30(1)	3138.9
160	7.749(1)	27.859(2)	14.748(1)	100.25(1)	3133.0
150	7.746(1)	27.853(2)	14.731(1)	100.22(1)	3127.8
140	7.741(1)	27.846(2)	14.715(1)	100.17(1)	3122.2
130	7.738(1)	27.842(2)	14.703(1)	100.16(1)	3118.0
120	7.733(1)	27.831(2)	14.688(1)	100.08(1)	3112.1
110	7.728(1)	27.830(2)	14.675(1)	100.04(1)	3107.9
100	7.724(1)	27.827(2)	14.656(1)	99.98(1)	3102.6
100[‡]	7.696(1)	28.012(5)	14.695(3)	99.71(3)	3122.6

*Values in bold indicate the phase transition region

[‡]Parameters determined from flash cooling (different crystal)

Table S5. Variable-temperature unit-cell parameters as determined for **CoCP**.

Temperature (K)	*a* axis (Å)	*b* axis (Å)	*c* axis (Å)	*β* angle (°)	Volume (Å^3)
270	7.672(5)	25.683(18)	17.291(13)	98.63(2)	3368.8
260	**7.668(2)**	**25.795(7)**	**17.036(5)**	**98.85(1)**	**3329.6**
250	**7.654(14)**	**25.291(50)**	**17.468(35)**	**98.13(5)**	**3338.3**
240	7.651(1)	25.253(4)	17.605(3)	98.78(1)	3361.7
230	7.643(1)	25.223(3)	17.570(2)	98.70(1)	3348.4
220	7.645(1)	25.222(3)	17.557(2)	98.62(1)	3347.1
210	7.644(1)	25.198(4)	17.527(3)	98.57(1)	3338.3
200	7.641(1)	25.179(4)	17.503(3)	98.50(1)	3330.6
190	7.643(1)	25.179(5)	17.476(3)	98.44(1)	3326.9
180	7.627(1)	25.137(5)	17.423(3)	98.36(1)	3304.8
170	7.628(1)	25.131(5)	17.398(4)	98.26(1)	3300.7
160	7.625(1)	25.131(5)	17.385(3)	98.22(1)	3297.0
150	7.618(1)	25.125(5)	17.348(3)	98.20(1)	3286.2
140	7.622(2)	25.148(6)	17.348(4)	98.19(1)	3284.7
130	7.609(1)	25.133(5)	17.275(3)	98.17(1)	3269.9
120	7.607(1)	25.121(6)	17.274(4)	98.13(1)	3267.9
110	7.599(1)	25.137(5)	17.250(3)	98.04(1)	3262.4
100	7.598(2)	25.105(6)	17.242(4)	98.02(1)	3256.7
100[‡]	7.580(3)	25.608(11)	16.702(7)	97.96(1)	3211.0

*Values in bold indicate the phase transition region

[‡]Parameters determined from flash cooling (different crystal)

Table S6. Variable-temperature unit-cell parameters as determined for **CdCP**.

Temperature (K)	*a* axis (Å)	*b* axis (Å)	*c* axis (Å)	*β* angle (°)	Volume (Å^3)
270	7.751(1)	23.773(2)	19.044(1)	96.40(1)	3487.3
260	7.734(1)	23.535(1)	19.144(1)	96.19(1)	3464.4
250	7.722(1)	23.391(1)	19.191(1)	96.04(1)	3447.1
240	7.713(1)	23.258(1)	19.248(1)	95.92(1)	3434.4
230	7.703(1)	23.100(1)	19.311(1)	95.78(1)	3418.8
220	7.692(1)	22.902(1)	19.380(1)	95.62(1)	3397.5
210	7.684(1)	22.666(1)	19.459(1)	95.41(1)	3373.9
200	**7.681(1)**	**22.540(2)**	**19.501(2)**	**95.28(1)**	**3361.8**
190	**7.695(1)**	**21.903(2)**	**19.683(2)**	**94.43(1)**	**3307.6**
180	7.696(1)	21.794(2)	19.706(1)	94.13(1)	3296.9
170	7.694(1)	21.749(2)	19.704(1)	93.97(1)	3289.0
160	7.690(1)	21.711(2)	19.707(1)	93.86(1)	3282.7
150	7.686(1)	21.676(2)	19.711(1)	93.78(1)	3276.9
140	7.682(1)	21.643(1)	19.715(1)	93.70(1)	3270.8
130	7.677(2)	21.614(1)	19.715(1)	93.64(1)	3264.7
120	7.674(1)	21.590(1)	19.719(1)	93.58(1)	3260.6
110	7.669(1)	21.563(1)	19.719(1)	93.52(1)	3254.8
100	7.665(1)	21.547(1)	19.726(1)	98.47(1)	3251.9
100[‡]	7.635(1)	22.768(3)	19.177(2)	94.90(1)	3321.5

*Values in bold indicate the phase transition region

[‡]Parameters determined from flash cooling (different crystal)

Table S7. Variable-temperature unit-cell parameters as determined for **ZnCoCP**.

Temperature (K)	*a* axis (Å)	*b* axis (Å)	*c* axis (Å)	*β* angle (°)	Volume (Å^3)
270	7.716(2)	25.819(6)	17.144(4)	99.26(1)	3370.8
260	7.685(1)	26.001(1)	16.836(1)	99.29(2)	3319.9
250	7.680(1)	26.179(1)	16.632(1)	99.40(1)	3298.9
240	**7.678(4)**	**26.386(13)**	**16.335(9)**	**99.43(2)**	**3264.6**
230	**7.761(2)**	**27.902(8)**	**14.992(5)**	**100.09(1)**	**3196.2**
220	7.766(2)	27.937(5)	14.923(3)	100.06(1)	3188.2
210	7.765(1)	27.955(5)	14.874(3)	100.04(1)	3179.2
200	7.768(1)	27.981(5)	14.843(3)	100.00(1)	3177.0
190	7.764(2)	27.977(6)	14.828(3)	99.97(1)	3172.0
180	7.760(2)	27.984(6)	14.804(4)	99.93(1)	3166.7
170	7.753(2)	27.977(7)	14.780(4)	99.90(1)	3158.2
160	7.748(2)	27.979(7)	14.760(4)	99.86(1)	3152.5
150	7.745(2)	27.977(7)	14.744(4)	99.83(1)	3147.7
140	7.736(2)	27.961(7)	14.713(4)	99.79(1)	3136.1
130	7.732(2)	27.959(7)	14.695(4)	99.75(1)	3131.0
120	7.727(2)	27.945(7)	14.675(4)	99.71(1)	3123.3
110	7.720(2)	27.933(7)	14.654(4)	99.69(1)	3115.0
100	7.708(2)	27.904(7)	14.623(4)	99.64(1)	3101.0
100‡	7.600(1)	26.519(1)	16.029(1)	99.21(1)	3189.2

*Values in bold indicate the phase transition region

‡Parameters determined from flash cooling (different crystal)

Table S8. Variable-temperature unit-cell parameters as determined for **NiCdCP**.

Temperature (K)	*a* axis (Å)	*b* axis (Å)	*c* axis (Å)	*β* angle (°)	Volume (Å^3)
270	7.632(2)	26.288(5)	16.739(4)	98.89(1)	3317.9
260	**7.629(1)**	**26.358(2)**	**16.632(1)**	**98.99(1)**	**3303.3**
250	**7.782(1)**	**28.029(3)**	**15.019(2)**	**100.01(1)**	**3266.3**
240	**7.768(1)**	**27.986(1)**	**14.918(1)**	**99.99(1)**	**3193.9**
230	7.766(1)	28.002(1)	14.868(1)	99.94(1)	3184.9
220	7.764(1)	28.014(1)	14.825(1)	99.89(1)	3176.4
210	7.760(1)	28.024(1)	14.783(1)	99.84(1)	3167.4
200	7.756(1)	28.043(1)	14.744(1)	99.81(1)	3160.2
190	7.752(1)	28.068(1)	14.704(1)	99.77(1)	3152.9
180	7.747(1)	28.096(2)	14.661(1)	99.76(1)	3144.9
170	7.742(1)	28.131(1)	14.615(1)	99.77(1)	3137.0
160	7.736(1)	28.178(1)	14.563(1)	99.79(1)	3128.3
150	7.730(1)	28.259(1)	14.492(1)	99.87(1)	3118.7
140	7.720(2)	28.382(1)	14.394(1)	100.01(1)	3105.8
130	7.711(2)	28.491(1)	14.310(1)	100.13(1)	3094.9
120	7.706(1)	28.555(1)	14.256(1)	100.18(1)	3087.5
110	7.698(1)	28.595(1)	14.214(1)	100.19(1)	3079.6
100	7.693(1)	28.617(1)	14.187(1)	100.18(1)	3074.2
100‡	7.501(1)	25.985(1)	16.598(1)	98.15(1)	3202.5

*Values in bold indicate the phase transition region

‡Parameters determined from flash cooling (different crystal)

Table S9. Variable-temperature unit-cell parameters as determined for **ZnCdCP**.

Temperature (K)	*a* axis (Å)	*b* axis (Å)	*c* axis (Å)	*β* angle (°)	Volume (Å^3)
270	7.696(1)	25.460(2)	17.433(1)	99.01(1)	3373.9
260	7.689(1)	25.656(1)	17.216(1)	99.02(1)	3354.5
250	**7.683(1)**	**25.821(2)**	**17.027(1)**	**99.07(1)**	**3335.6**
240	**7.681(1)**	**26.299(2)**	**16.576(1)**	**99.45(1)**	**3302.7**
230	**7.678(1)**	**26.631(2)**	**16.245(1)**	**99.79(1)**	**3273.3**
220	7.674(1)	26.744(1)	16.134(1)	99.88(1)	3262.4
210	7.673(1)	26.788(1)	16.090(1)	99.86(1)	3258.2
200	7.669(1)	26.797(2)	16.035(1)	99.85(1)	3246.9
190	7.667(1)	26.798(2)	15.977(1)	99.86(1)	3234.0
180	7.664(1)	26.786(2)	15.926(1)	99.86(1)	3220.9
170	7.660(1)	26.776(2)	15.885(1)	99.74(1)	3210.3
160	7.656(1)	26.768(2)	15.849(1)	99.80(1)	3200.5
150	7.652(1)	26.759(2)	15.819(1)	99.76(1)	3192.0
140	7.648(1)	26.753(2)	15.795(1)	99.72(1)	3185.6
130	7.644(1)	26.744(2)	15.774(1)	99.67(1)	3178.9
120	7.639(1)	26.729(2)	15.753(2)	99.63(1)	3171.5
110	7.637(1)	26.726(2)	15.743(1)	99.59(1)	3168.2
100	7.633(1)	26.717(11)	15.728(1)	99.54(1)	3163.0
100‡	7.604(1)	26.523(1)	16.123(1)	98.05(1)	3211.1

*Values in bold indicate the phase transition region

‡Parameters determined from flash cooling (different crystal)

Table S10. Variable-temperature unit-cell parameters as determined for **NiCP** (HT range, solvent cell).

Temperature (K)	*a* axis (Å)	*b* axis (Å)	*c* axis (Å)	*β* angle (°)	Volume (Å^3)
310	7.618(11)	25.880(40)	17.320(30)	99.86(3)	3370
300	7.599(3)	25.833(10)	17.327(8)	99.69(1)	3353
290	7.593(3)	25.803(11)	17.341(8)	99.62(1)	3350
280	7.583(13)	25.770(40)	17.270(30)	99.56(4)	3328

Table S11. Variable-temperature unit-cell parameters as determined for **CoCP** (HT range, solvent cell).

Temperature (K)	*a* axis (Å)	*b* axis (Å)	*c* axis (Å)	*β* angle (°)	Volume (Å^3)
310	7.733(8)	25.380(30)	17.655(20)	99.44(2)	3419
300	7.724(5)	25.309(14)	17.722(10)	99.46(1)	3417
290	7.710(4)	25.266(13)	17.737(10)	99.33(1)	3410
280	7.699(2)	25.223(7)	17.723(5)	99.25(1)	3397

Table S12. Variable-temperature unit-cell parameters as determined for **NiCdCP** (HT range, solvent cell).

Temperature (K)	*a* axis (Å)	*b* axis (Å)	*c* axis (Å)	*β* angle (°)	Volume (Å^3)
310	7.611(6)	25.660(18)	17.483(14)	99.22(3)	3370
300	7.598(4)	25.621(12)	17.489(10)	99.12(3)	3361
290	7.582(5)	25.588(15)	17.452(11)	99.07(3)	3343
280	7.559(5)	25.600(11)	17.452(10)	99.03(4)	3335

2.4. Variable-temperature single-crystal structure determinations

Many attempts were made to determine successive structures of a single crystal over the phase change event. However, this process results in significant stress on the crystal and in all cases the data were deemed to be of insufficient quality for satisfactory structure solution and refinement. Nonetheless, in the case of **ZnCP**, **CdCP** and **NiCP** the data were adequate to model the metal atoms and measure the M···M···M distance in the 1D chain. The solid solutions were excluded from this analysis since the partial occupancy of either metal node would complicate this determination. This distance was then plotted in an attempt to illustrate the changes effected by the phase change in each material.

Table S13. Change in the M···M···M angle in **ZnCP**, **NiCP** and **CdCP** over the phase change.

Temperature (K)	M···M···M ZnCP (°)	M···M···M NiCP (°)	M···M···M CdCP (°)
270	125.34(3)	123.144(7)	135.999(7)
260	124.63(3)	122.956(14)	136.861(10)
250	**123.89(3)**	**123.310(30)**	137.385(10)
240	**121.66(3)**	**116.380(30)**	137.860(13)
230	**120.12(3)**	116.270(20)	138.379(13)
220	119.80(3)	116.200(20)	139.025(13)
210	119.69(4)	116.170(20)	139.818(13)
200	119.53(5)	116.146(19)	**140.242(16)**
190	119.31(5)	116.106(19)	**145.286(13)**
180	119.03(5)	116.085(19)	145.837(10)
170	118.76(6)	116.053(19)	146.077(10)
160	118.46(6)	116.023(19)	146.244(10)
150	118.78(9)	116.000(19)	146.378(10)
140	118.21(8)	115.970(19)	146.487(10)
130	118.12(7)	115.924(19)	146.573(10)
120	118.08(7)	115.907(19)	146.650(10)
110	118.10(7)	115.876(19)	146.720(10)
100	118.56(11)	115.840(19)	146.774(10)

*Values in bold indicate the phase transition region

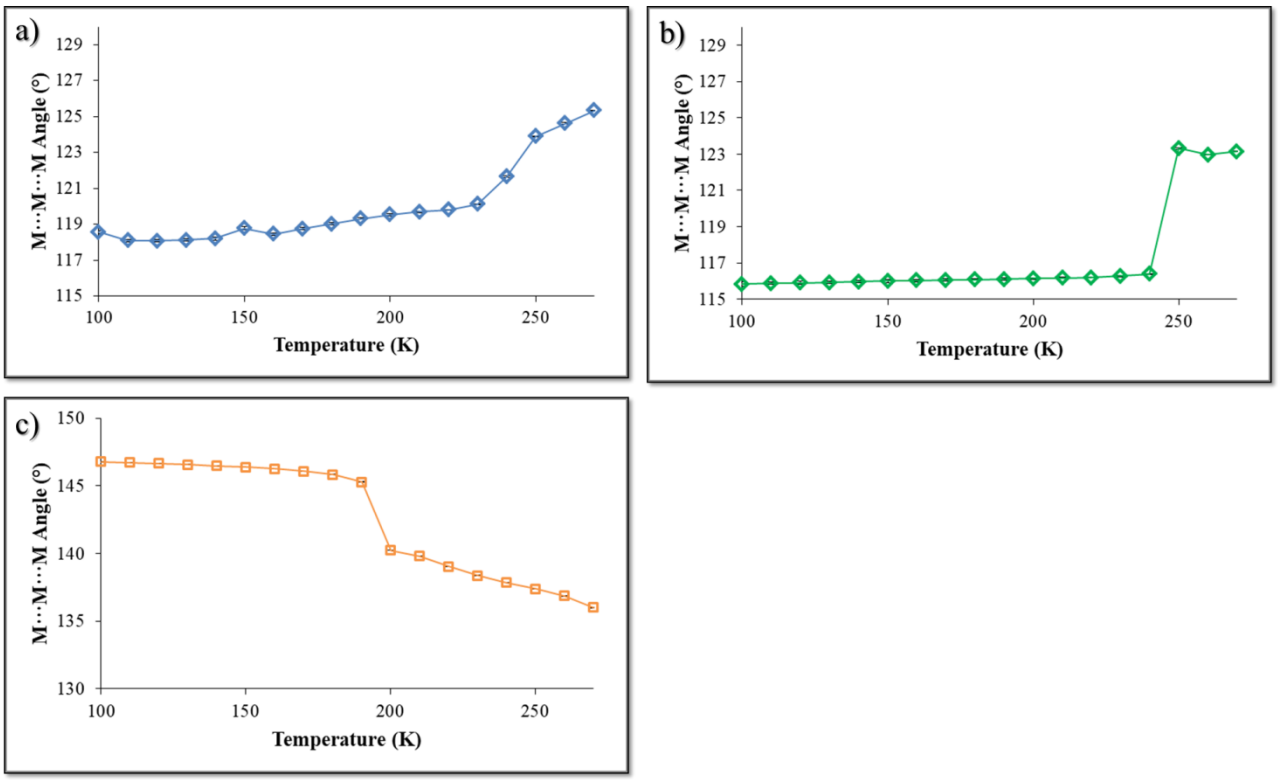

Figure S16: Variation in the M···M···M angle of the 1D chain as a function of temperature for **(a) ZnCP**, **(b) NiCP** and **(c) CdCP**. Error bars are shown, but may be too small to discern.

2.5. Temperature cycling of ZnCP to investigate flash cooling effect

To investigate possible attenuation of the phase change by changes in cooling rate, a SCXRD experiment was carried where the crystal was first cooled rapidly from 270 to 100 K (at a rate of 360 K h^{-1}) and its unit-cell parameters subsequently determined. Following this the crystal was heated to 270 K and then slowly cooled to 100 K (at a rate of 50 K h^{-1}) and the unit-cell parameters were determined again. Although this is not as dramatic as that seen in the variable temperature data it is important to note that the cooling rate is much lower in that case. However, the expected trend is observed, where the extent of the phase change is reduced with the higher cooling rate.

Table S14. Unit-cell parameters obtained from temperature cycling of **ZnCP**.

Temperature (K)	*a* axis (Å)	*b* axis (Å)	*c* axis (Å)	*β* angle (°)	Volume (Å^3)
270 (initial)	7.711(8)	25.516(30)	17.603(31)	99.28(6)	3418.3
100 (cooled at 360 K h^{-1})	7.605(1)	26.524(1)	16.027(1)	99.24(1)	3191.2
270 (heated at 360 K h^{-1})	7.703(1)	25.446(2)	17.489(2)	99.24(1)	3383.8
100 (cooled at 50 K h^{-1})	7.623(1)	26.644(2)	15.910(1)	99.47(1)	3187.2

3. Differential Scanning Calorimetry (DSC)

DSC was performed on either a TA Q20 instrument (analysis of **ZnCP**, **NiCP** and **CoCP**) or a TA Q100 instrument equipped with a Liquid Nitrogen Cooling System (analysis of **CdCP**). Samples of **ZnCP**, **NiCP**, **CoCP** and **CdCP** ranging in weight between 7 and 10 mg were placed in aluminium pans. The ramp rate was set at either 5 or 2 K min^{-1} to ascertain if a change in the rate of cooling would attenuate the energy of the phase transition. Each experiment was carried out in triplicate with a fresh sample used for each repetition. An N_2 gas flow rate of 50 ml min^{-1} was used. The resultant data were analysed using the TA Instruments Universal Analysis program.

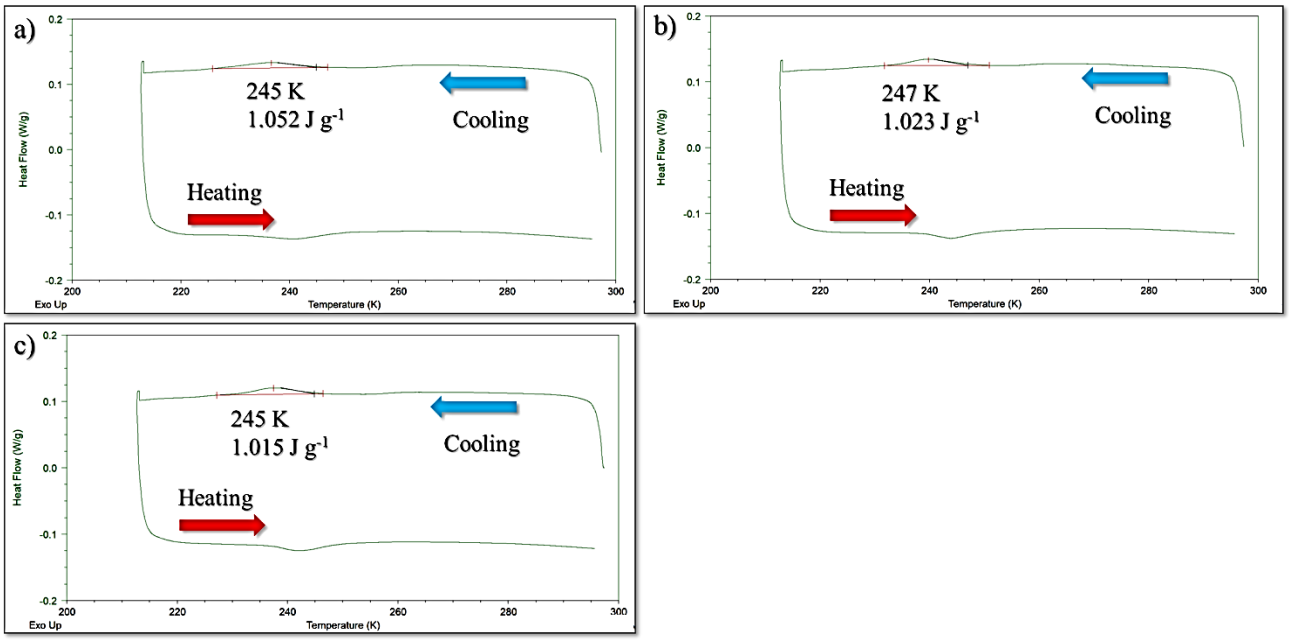

Figure S17: DSC thermograms for **ZnCP** cooled at 5 K min^{-1}. The onset temperature of the phase change and the peak integral are shown in each figure.

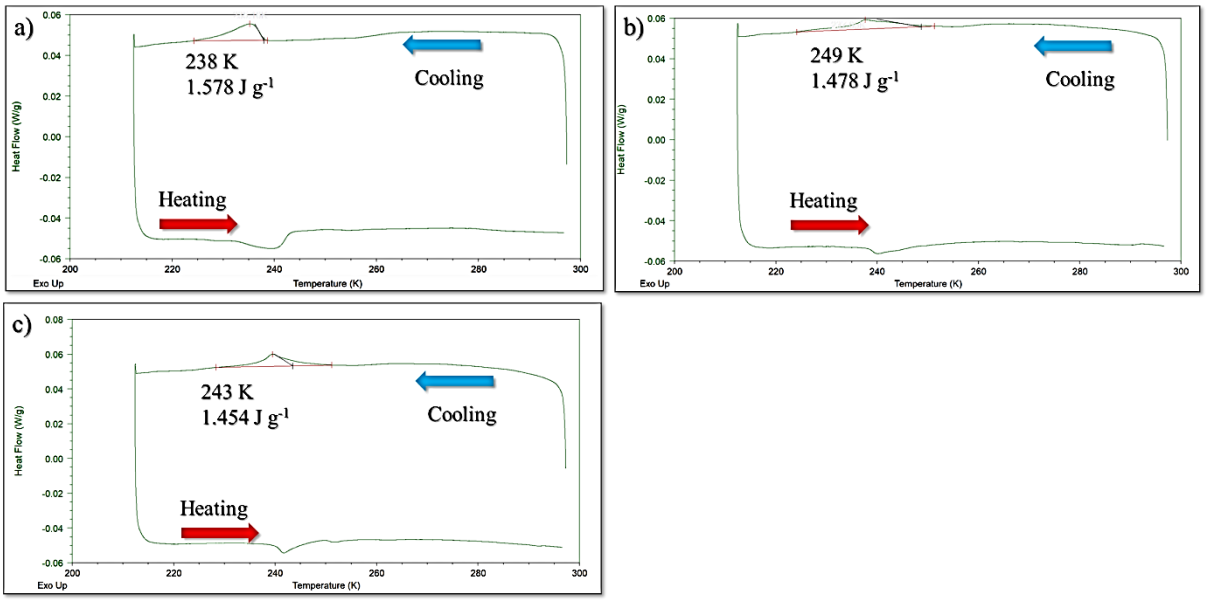

Figure S18: DSC thermograms for **ZnCP** cooled at 2 K min^{-1}. The onset temperature of the phase change and the peak integral are shown in each figure.

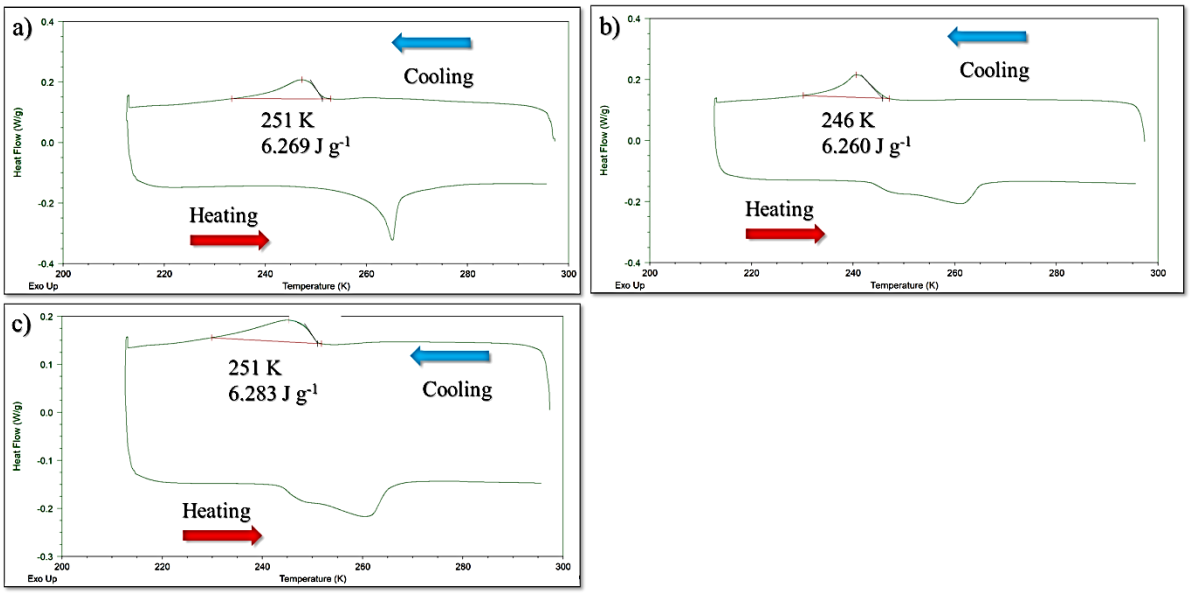

Figure S19: DSC thermograms for **NiCP** cooled at 5 K min^{-1}. The onset temperature of the phase change and the peak integral are shown in each figure.

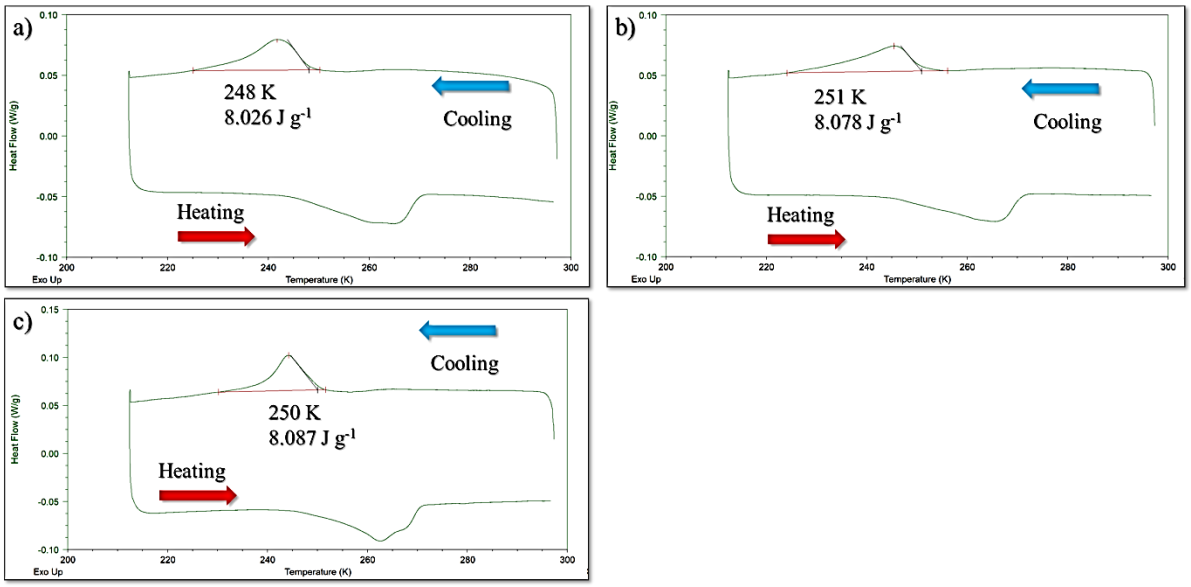

Figure S20: DSC thermograms for **NiCP** cooled at 2 K min^{-1}. The onset temperature of the phase change and the peak integral are shown in each figure.

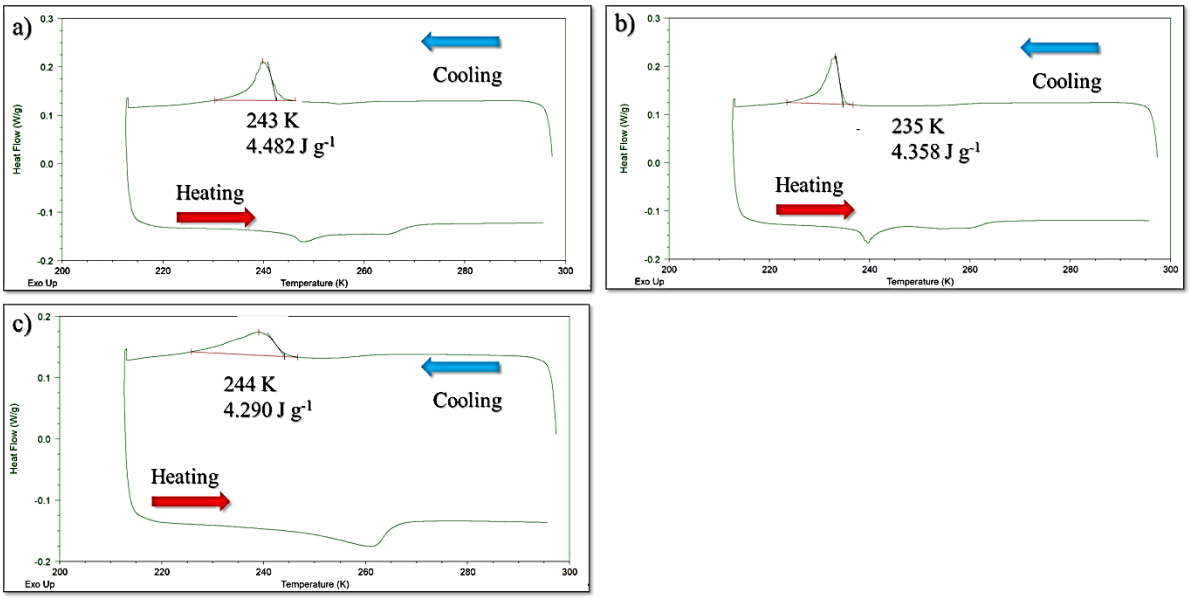

Figure S21: DSC thermograms for **CoCP** cooled at 5 K min^{-1}. The onset temperature of the phase change and the peak integral are shown in each figure.

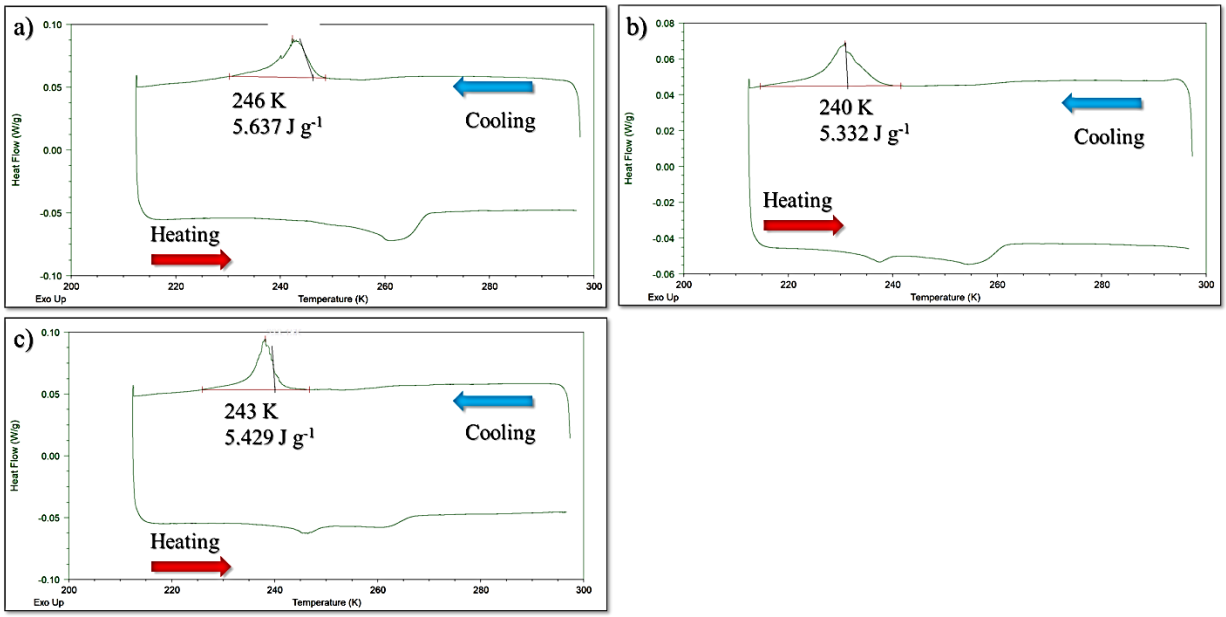

Figure S22: DSC thermograms for **CoCP** cooled at 2 K min^{-1}. The onset temperature of the phase change and the peak integral are shown in each figure.

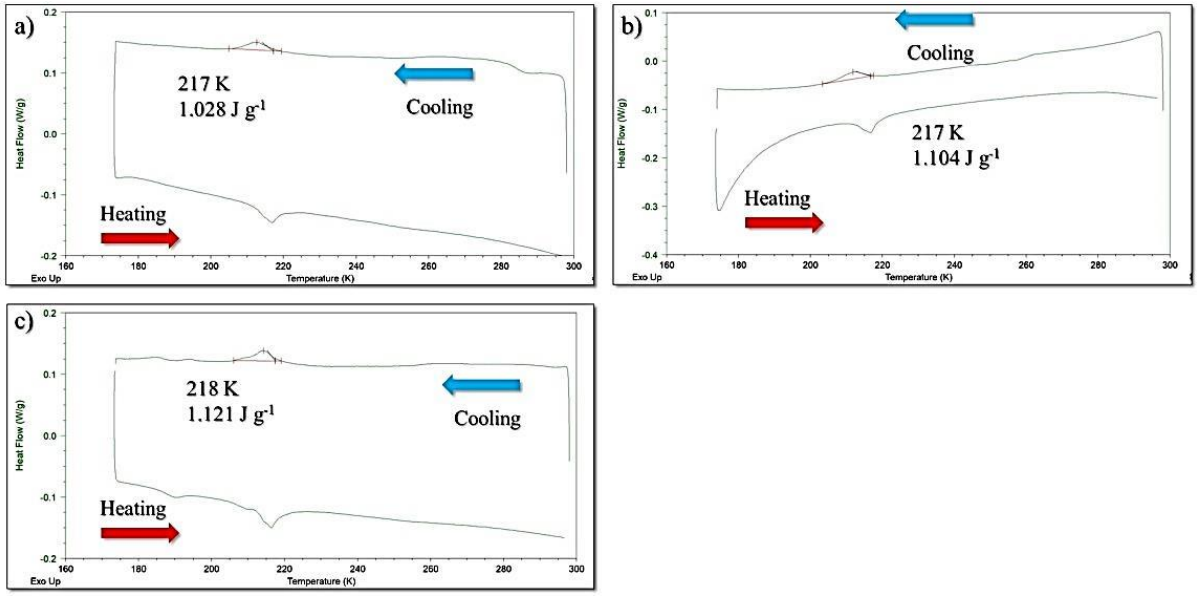

Figure S23: DSC thermograms for **CdCP** cooled at 5 K min^{-1}. The onset temperature of the phase change and the peak integral are shown in each figure.

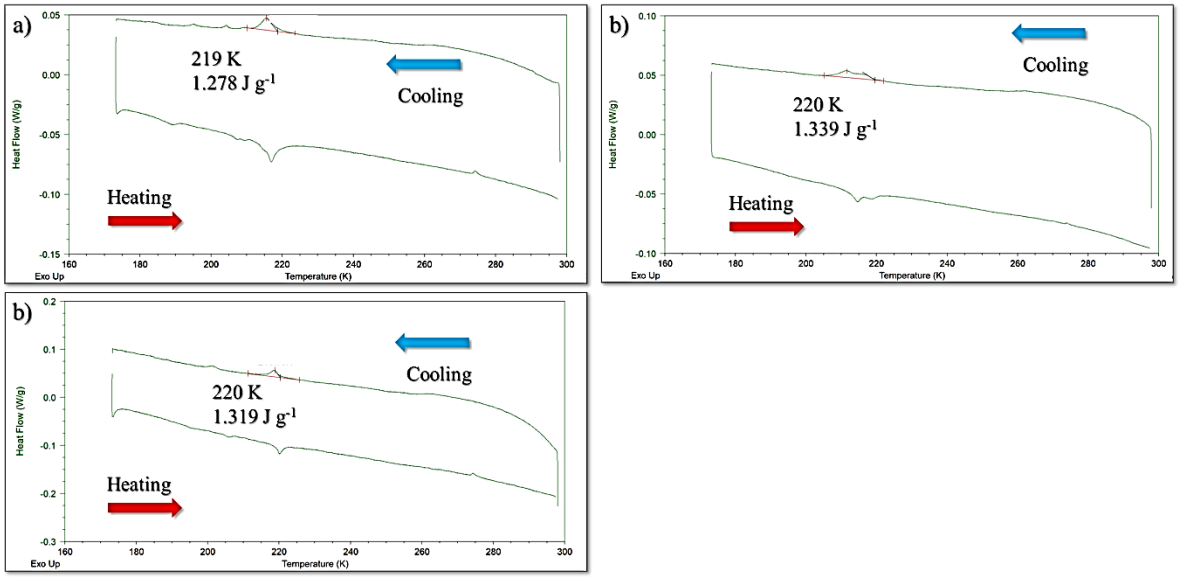

Figure S24: DSC thermograms for **CdCP** cooled at 2 K min^{-1}. The onset temperature of the phase change and the peak integral are shown in each figure.

Table S15. Analysis of DSC data.

Material		Cooling at 5 K min^{-1}			Cooling at 2 K min^{-1}		
		Energy (J g^{-1})	Onset temperature (K)	Peak temperature (K)	Energy (J g^{-1})	Onset temperature (K)	Peak temperature (K)
ZnCP	Experiment 1	1.052	245	237	1.578	238	235
	Experiment 2	1.023	237	240	1.478	249	238
	Experiment 3	1.015	245	237	1.454	243	239
Average		1.030	242	238	1.503	243	237
Standard deviation		0.019	5	2	0.066	6	2
NiCP	Experiment 1	6.269	251	247	8.026	248	242
	Experiment 2	6.260	246	241	8.078	251	245
	Experiment 3	6.283	250	245	8.087	250	244
Average		6.271	249	244	8.064	250	244
Standard deviation		0.012	3	3	0.033	2	2
CoCP	Experiment 1	4.482	243	240	5.637	246	242
	Experiment 2	4.358	235	233	5.332	240	231
	Experiment 3	4.290	244	239	5.429	243	238
Average		4.377	241	237	5.466	243	237
Standard deviation		0.097	5	4	0.156	3	6
CdCP	Experiment 1	1.028	217	213	1.279	219	216
	Experiment 2	1.104	217	212	1.339	220	212
	Experiment 3	1.121	218	218	1.319	220	218
Average		1.084	217	213	1.312	220	215
Standard deviation		0.050	1	1	0.031	1	3

4. Principal Axis Strain (PAS) Calculations

The web-based tool PASCal[15] (Principal Axis Strain Calculator, http://pascal.chem.ox.ac.uk) was used to determine a set of principal axes and calculate the linear and volumetric coefficients of thermal expansion. The thermal expansion coefficients were calculated from the lattice parameters obtained from variable temperature single-crystal diffraction data.

4.1. Expansivity indicatrixes and transformation matrices of principal axes to unit-cell axes

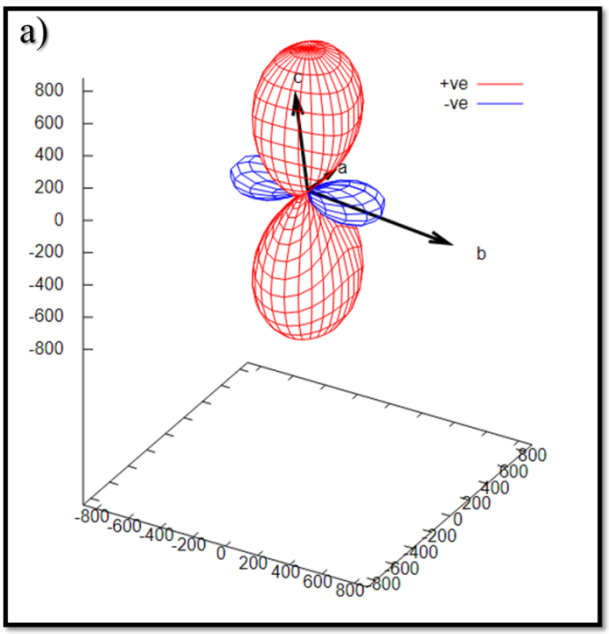

c)

	a	*b*	*c*
X_1	0.0679	0.9906	0.1191
X_2	0.9994	-0.0005	0.0355
X_3	0.1778	0.0524	0.9827

Figure S25: Thermal expansion data for **ZnCP^{HT}** (250–270 K). The expansivity indicatrix is shown in **(a)**, while **(b)** illustrates the percentage change in the principal axes (relative to 250 K) as a function of temperature. The matrix relating the principal axes to the crystallographic axes is shown in **(c)**.

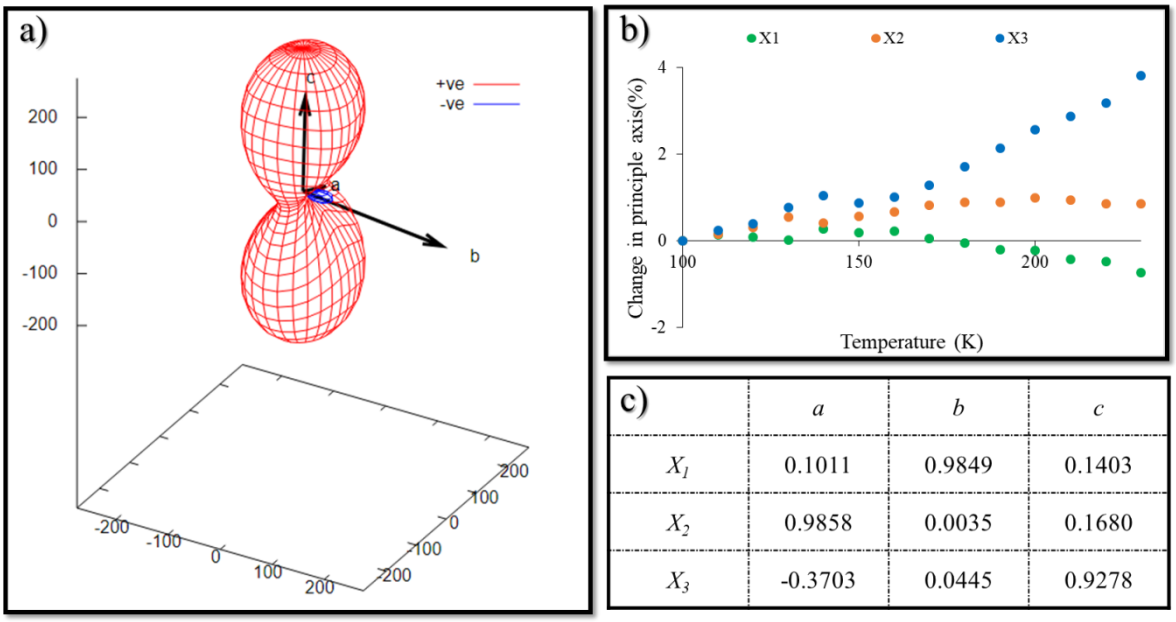

c)

	a	*b*	*c*
X_1	0.1011	0.9849	0.1403
X_2	0.9858	0.0035	0.1680
X_3	-0.3703	0.0445	0.9278

Figure S26: Thermal expansion data for **ZnCP^{LT}** (100–230 K). The expansivity indicatrix is shown in **(a)**, while **(b)** illustrates the percentage change in the principal axes (relative to 100 K) as a function of temperature. The matrix relating the principal axes to the crystallographic axes is shown in **(c)**.

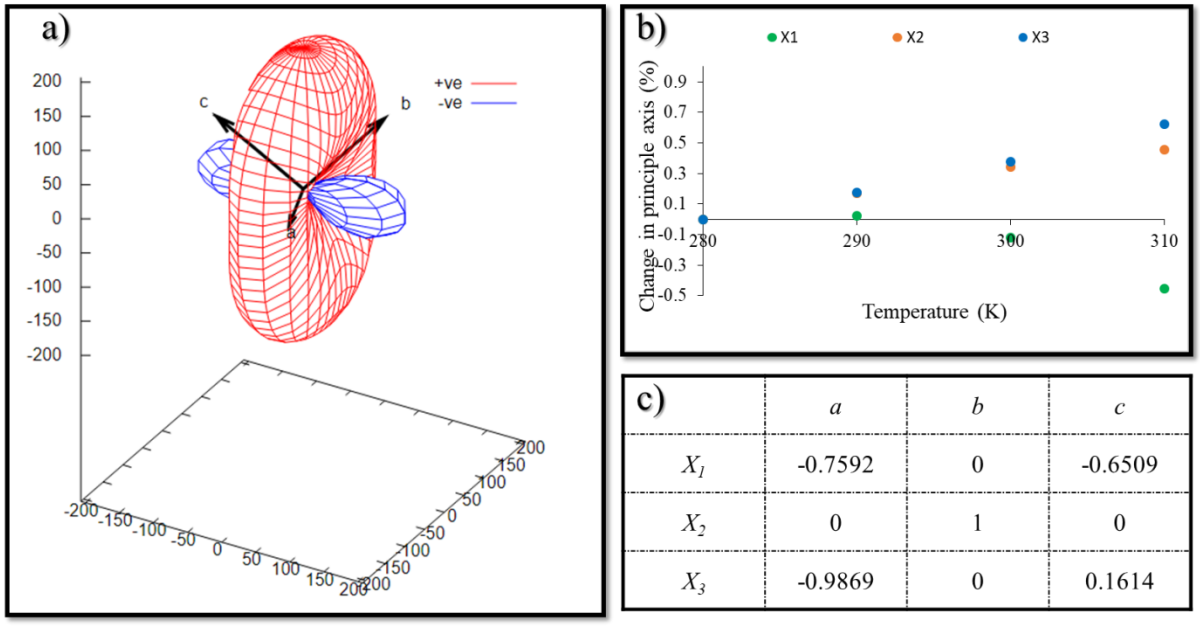

c)

	a	*b*	*c*
X_1	-0.7592	0	-0.6509
X_2	0	1	0
X_3	-0.9869	0	0.1614

Figure S27: Thermal expansion data for **CoCP^{HT}** (280–310 K). The expansivity indicatrix is shown in **(a)**, while **(b)** illustrates the percentage change in the principal axes (relative to 280 K) as a function of temperature. The matrix relating the principal axes to the crystallographic axes is shown in **(c)**.

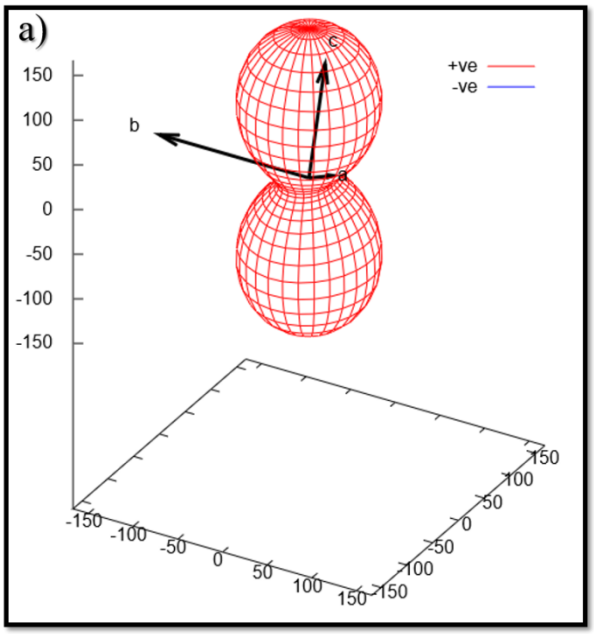

c)	*a*	*b*	*c*
X_1	0	-1	0
X_2	0.9833	0	0.182
X_3	-0.5603	0	0.8283

Figure S28: Thermal expansion data for **CoCP^{LT}** (100–240 K). The expansivity indicatrix is shown in **(a)**, while **(b)** illustrates the percentage change in the principal axes (relative to 100 K) as a function of temperature. The matrix relating the principal axes to the crystallographic axes is shown in **(c)**.

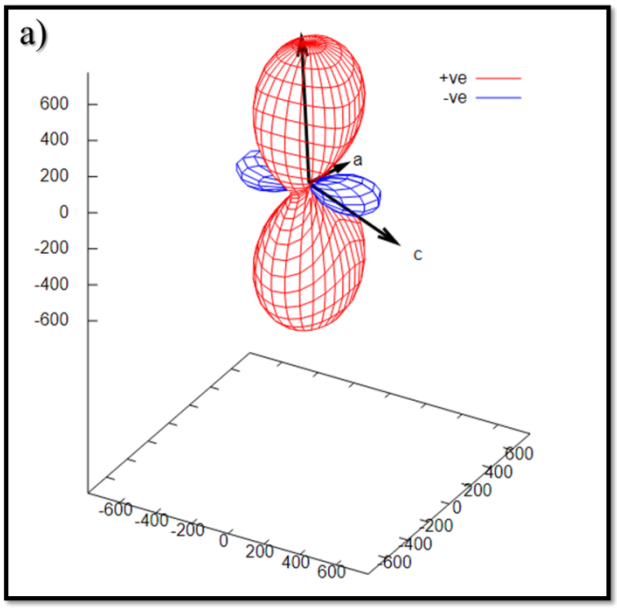

c)	*a*	*b*	*c*
X_1	0.6413	0.0524	0.7655
X_2	0.9952	-0.0015	-0.0975
X_3	-0.0188	0.9953	0.0949

Figure S29: Thermal expansion data for **CdCP^{HT}** (200–270 K). The expansivity indicatrix is shown in **(a)**, while **(b)** illustrates the percentage change in the principal axes (relative to 200 K) as a function of temperature. The matrix relating the principal axes to the crystallographic axes is shown in **(c)**.

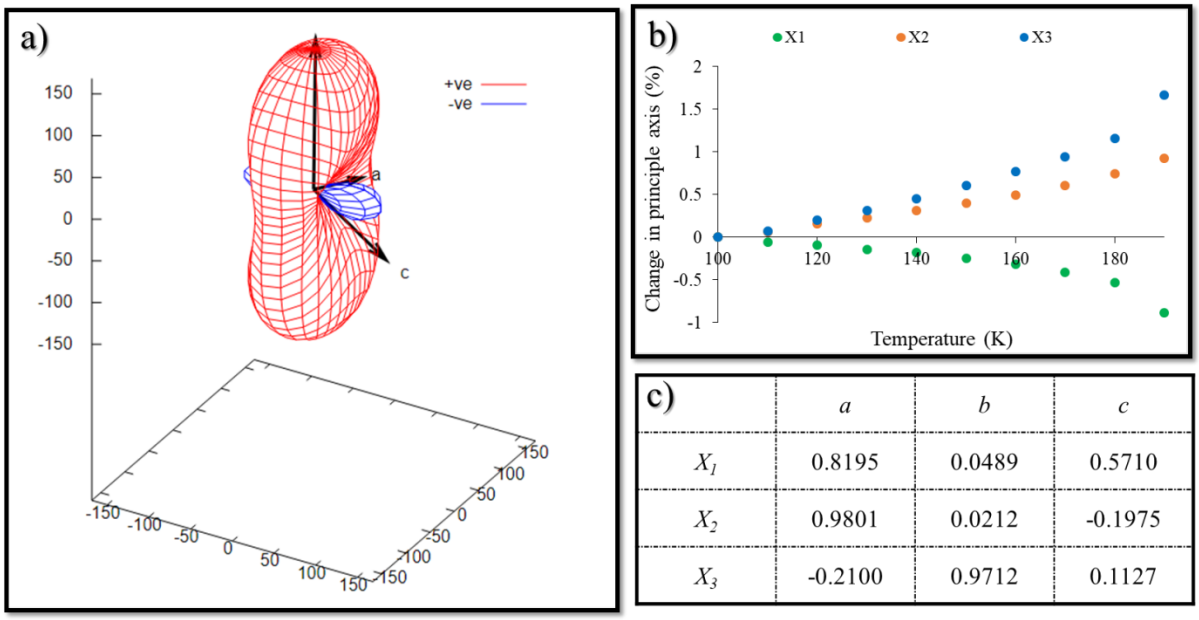

c)	*a*	*b*	*c*
X_1	0.8195	0.0489	0.5710
X_2	0.9801	0.0212	-0.1975
X_3	-0.2100	0.9712	0.1127

Figure S30: Thermal expansion data for **CdCP**^{LT} (100–190 K). The expansivity indicatrix is shown in **(a)**, while **(b)** illustrates the percentage change in the principal axes (relative to 100 K) as a function of temperature. The matrix relating the principal axes to the crystallographic axes is shown in **(c)**.

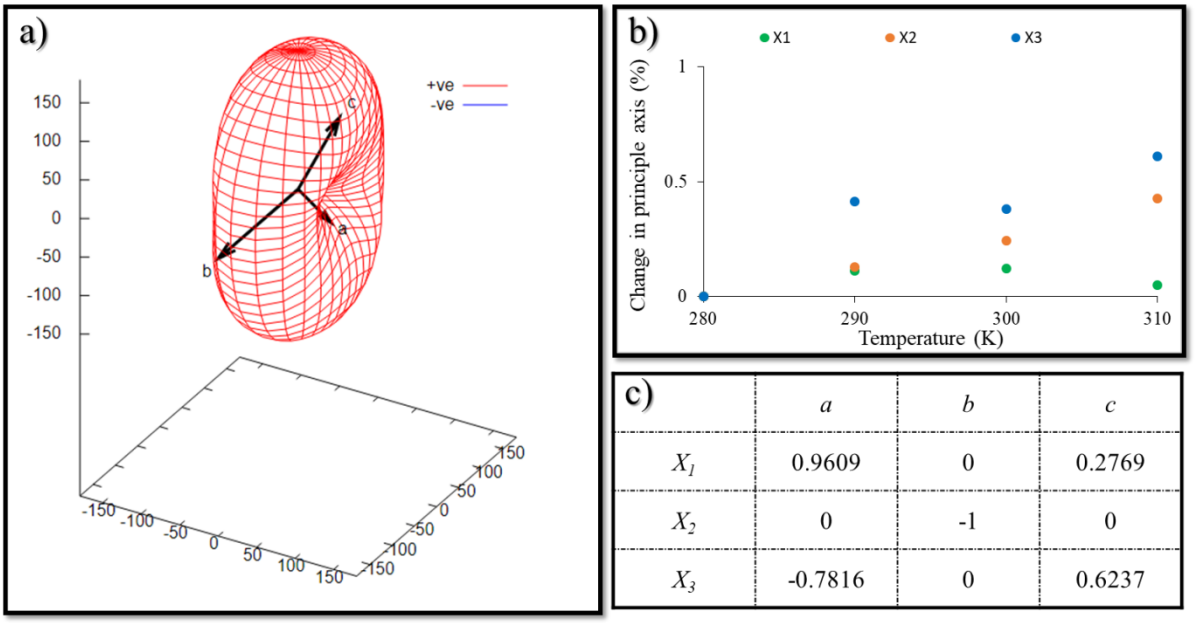

c)	*a*	*b*	*c*
X_1	0.9609	0	0.2769
X_2	0	-1	0
X_3	-0.7816	0	0.6237

Figure S31: Thermal expansion data for **NiCP**^{HT} (280–310 K). The expansivity indicatrix is shown in **(a)**, while **(b)** illustrates the percentage change in the principal axes (relative to 280 K) as a function of temperature. The matrix relating the principal axes to the crystallographic axes is shown in **(c)**.

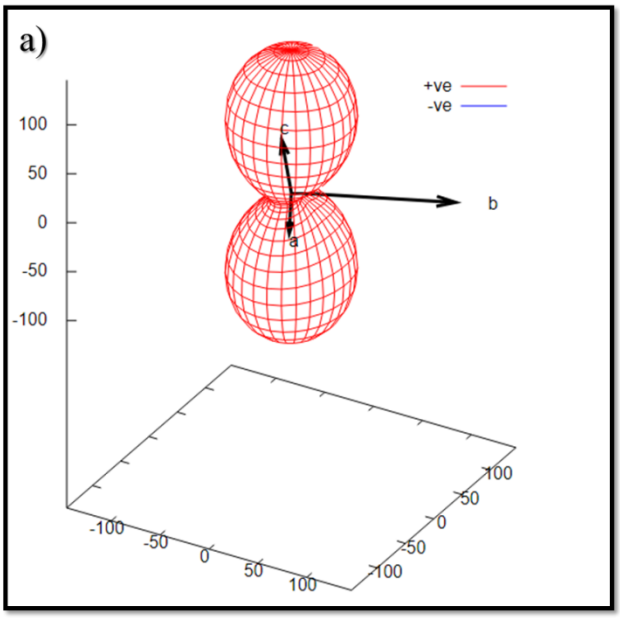

c)

	a	*b*	*c*
X_1	0.8179	0.4840	0.3112
X_2	-0.9589	0.1301	-0.2797
X_3	-0.6219	0.0359	0.7574

Figure S32: Thermal expansion data for **NiCP^{LT}** (100–240 K). The expansivity indicatrix is shown in **(a)**, while **(b)** illustrates the percentage change in the principal axes (relative to 100 K) as a function of temperature. The matrix relating the principal axes to the crystallographic axes is shown in **(c)**.

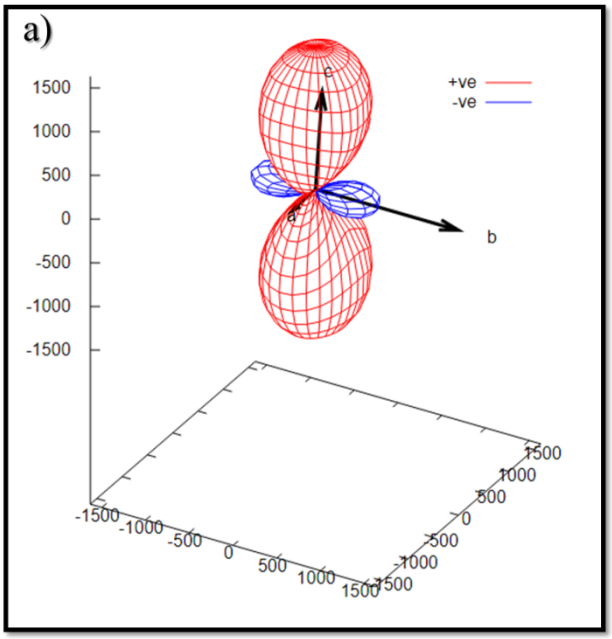

c)

	a	*b*	*c*
X_1	0	1	0
X_2	-0.9998	0	-0.0179
X_3	0.2603	0	0.9655

Figure S33: Thermal expansion data for **ZnCoCP^{HT}** (240–270 K). The expansivity indicatrix is shown in **(a)**, while **(b)** illustrates the percentage change in the principal axes (relative to 240 K) as a function of temperature. The matrix relating the principal axes to the crystallographic axes is shown in **(c)**.

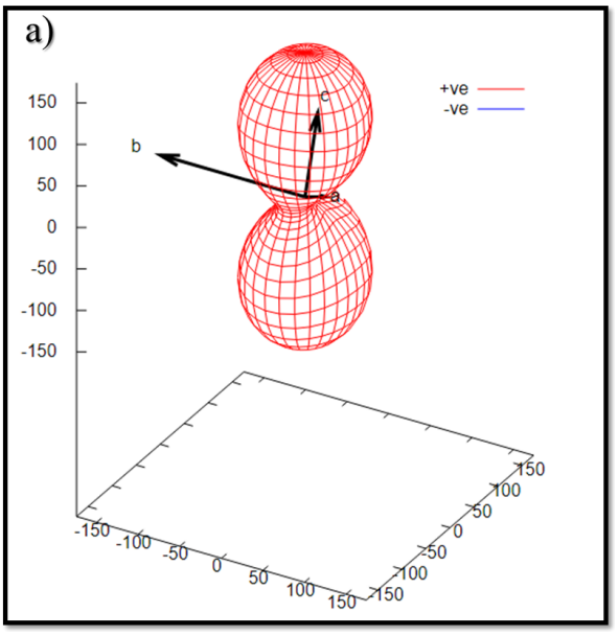

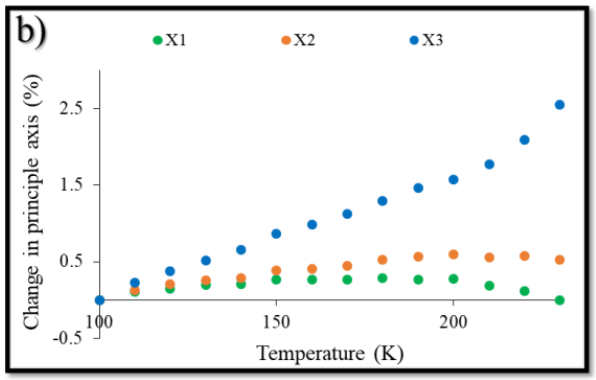

c)	*a*	*b*	*c*
X_1	0	-1	0
X_2	0.9714	0	0.2376
X_3	-0.5209	0	0.8536

Figure S34: Thermal expansion data for **ZnCoCP**^{LT} (100–230 K). The expansivity indicatrix is shown in **(a)**, while **(b)** illustrates the percentage change in the principal axes (relative to 100 K) as a function of temperature. The matrix relating the principal axes to the crystallographic axes is shown in **(c)**.

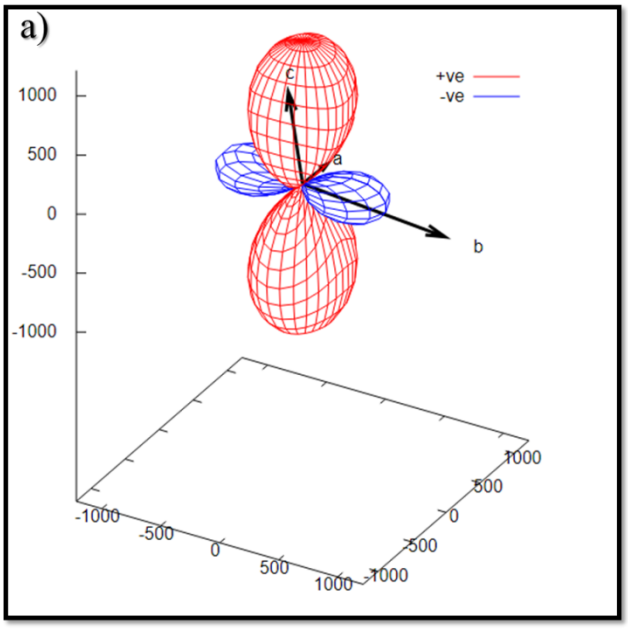

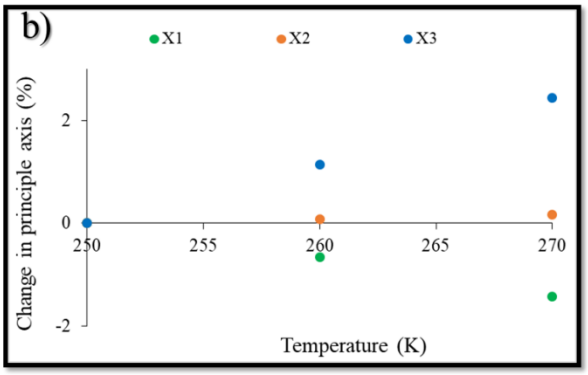

c)	*a*	*b*	*c*
X_1	0.0557	0.9914	0.1184
X_2	0.9999	-0.0004	0.0162
X_3	0.2622	0.0513	0.9636

Figure S35: Thermal expansion data for **ZnCdCP**^{HT} (250–270 K). The expansivity indicatrix is shown in **(a)**, while **(b)** illustrates the percentage change in the principal axes (relative to 250 K) as a function of temperature. The matrix relating the principal axes to the crystallographic axes is shown in **(c)**.

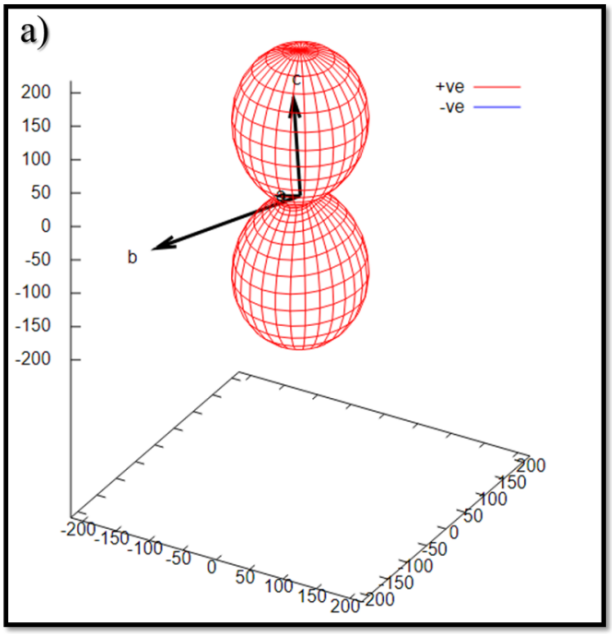

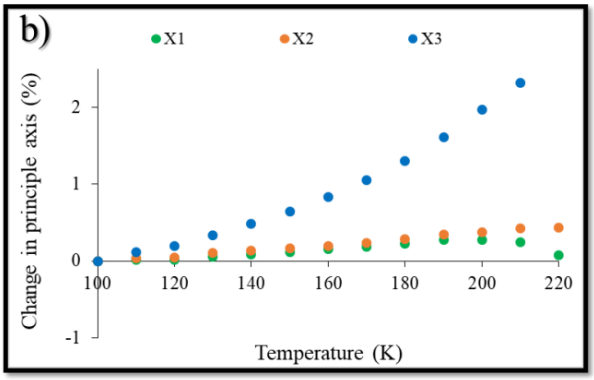

c)

	a	*b*	*c*
X_1	-0.9534	-0.1803	-0.2417
X_2	0.8854	-0.4381	0.1552
X_3	-0.5641	0.0419	0.8247

Figure S36: Thermal expansion data for **ZnCdCP^{LT}** (100–230 K). The expansivity indicatrix is shown in **(a)**, while **(b)** illustrates the percentage change in the principal axes (relative to 100 K) as a function of temperature. The matrix relating the principal axes to the crystallographic axes is shown in **(c)**.

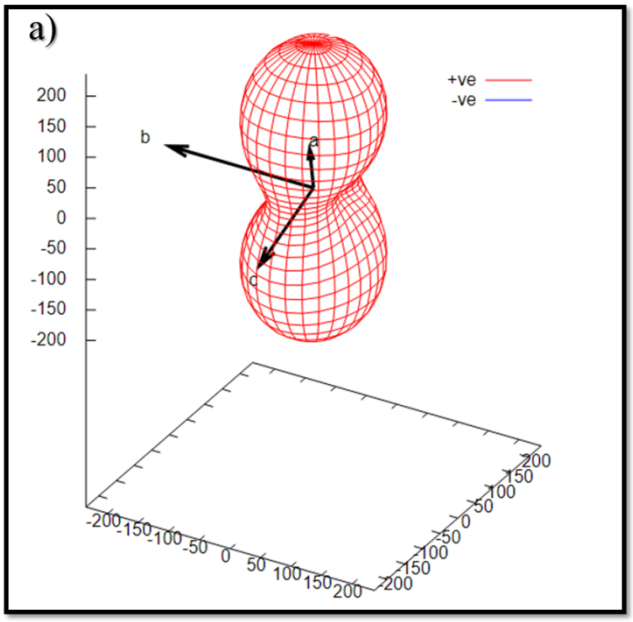

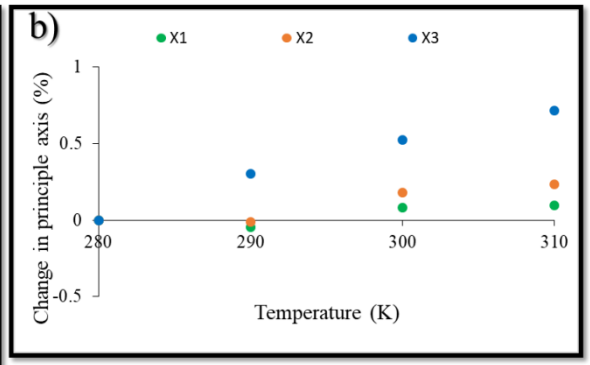

c)

	a	*b*	*c*
X_1	0	-1	0
X_2	-0.5896	0	-0.8077
X_3	0.9974	0	-0.0724

Figure S37: Thermal expansion data for **NiCdCP^{HT}** (280–310 K). The expansivity indicatrix is shown in **(a)**, while **(b)** illustrates the percentage change in the principal axes (relative to 280 K) as a function of temperature. The matrix relating the principal axes to the crystallographic axes is shown in **(c)**.

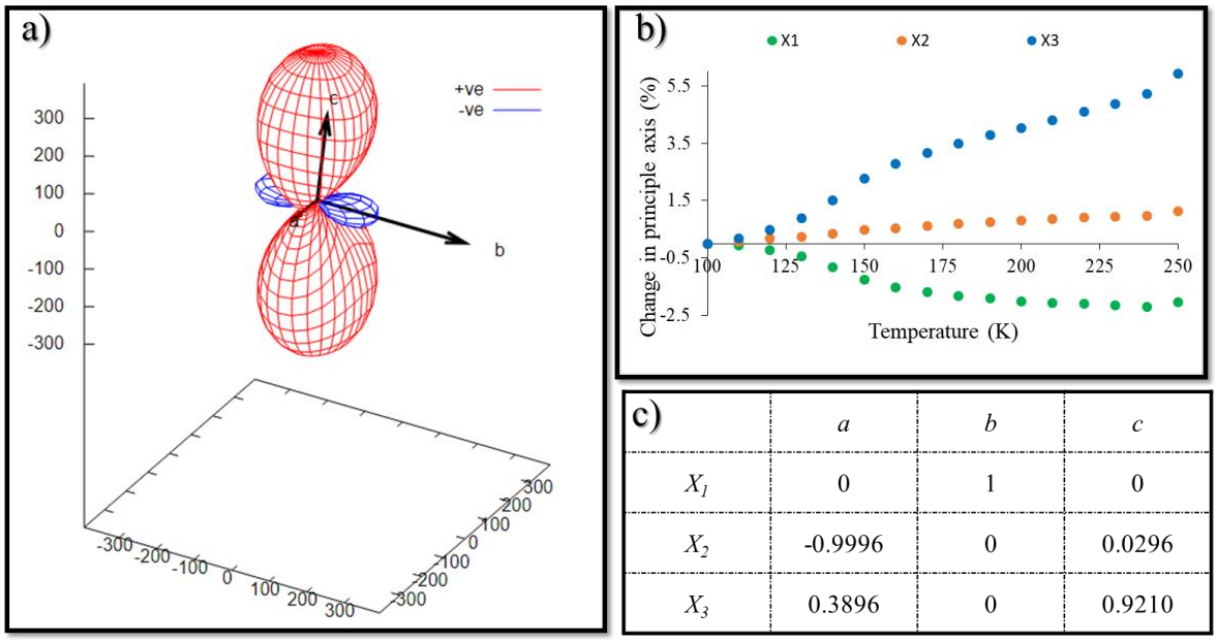

c)

	a	*b*	*c*
X_1	0	1	0
X_2	-0.9996	0	0.0296
X_3	0.3896	0	0.9210

Figure S38: Thermal expansion data for **NiCdCP^{LT}** (100–250 K). The expansivity indicatrix is shown in **(a)**, while **(b)** illustrates the percentage change in the principal axes (relative to 100 K) as a function of temperature. The matrix relating the principal axes to the crystallographic axes is shown in **(c)**.

4.2. Transformation to comparable principal axes

Although principal axes are generated automatically by PasCAL, the authors determined that the inconsistent assignment of these axes inhibited direct comparison of the thermal expansion properties of the CPs. Therefore, an alternative set of principal axes (denoted *Y1*, *Y2* and *Y3*) was determined for each CP so that the principal axes for all forms can be compared directly to one another. Accordingly, the linear thermal expansion coefficients are also denoted α_{Y1}, α_{Y2} and α_{Y3}.

ZnCP^{HT}	*a*	*b*	*c*
Y_1	-0.9994	0.0005	-0.0355
Y_2	0.0679	0.9906	0.1191
Y_3	0.1778	0.0524	0.9827

ZnCP^{LT}	*a*	*b*	*c*
Y_1	-0.9858	-0.0035	-0.1680
Y_2	0.1011	0.9849	0.1403
Y_3	-0.3703	0.0445	0.9278

NiCP^{HT}	*a*	*b*	*c*
Y_1	0.9609	0	0.2769
Y_2	0	-1	0
Y_3	-0.7816	0	0.6237

NiCP^{LT}	*a*	*b*	*c*
Y_1	0.9512	-0.1301	0.2798
Y_2	0.8179	0.4840	0.3112
Y_3	-0.6519	0.0359	0.7574

CoCP^{HT}	*a*	*b*	*c*
Y_1	-0.9869	0	0.1614
Y_2	0	1	0
Y_3	0.7592	0	0.6509

CoCP^{LT}	*a*	*b*	*c*
Y_1	0.9833	0	0.182
Y_2	0	1	0
Y_3	-0.5603	0	0.8283

CdCP^{HT}	*a*	*b*	*c*
Y_1	-0.9952	0.0015	0.0975
Y_2	0.0188	-0.9953	-0.0949
Y_3	0.6413	0.0524	0.7655

CdCP^{LT}	*a*	*b*	*c*
Y_1	-0.9801	-0.0212	0.1975
Y_2	0.2100	-0.9712	-0.1127
Y_3	0.8195	0.0489	0.5710

ZnCoCP^{HT}	*a*	*b*	*c*
Y_1	0.9998	0	0.0179
Y_2	0	1	0
Y_3	0.2603	0	0.9655

ZnCoCP^{LT}	*a*	*b*	*c*
Y_1	0.9714	0	0.2376
Y_2	0	1	0
Y_3	-0.5209	0	0.8536

NiCdCP^{HT}	*a*	*b*	*c*
Y_1	0.9974	0	-0.0724
Y_2	0	1	0
Y_3	0.5896	0	0.8077

NiCdCP^{LT}	*a*	*b*	*c*
Y_1	0.9996	0	-0.0296
Y_2	0	1	0
Y_3	0.3896	0	0.9210

ZnCdCP^{HT}	*a*	*b*	*c*
Y_1	-0.9999	0.0004	-0.0162
Y_2	0.0557	0.9914	0.1184
Y_3	0.2622	0.0513	0.9636

ZnCdCP^{LT}	*a*	*b*	*c*
Y_1	-0.9534	-0.1803	-0.2417
Y_2	0.8854	-0.4381	0.1552
Y_3	-0.5641	0.0419	0.8247

Figure S39: Transformed matrices for the principal axes of each CP and their individual forms

Table S16. Summary of the thermal expansion coefficients for the materials studied.

Material	α_{Y1} (MK^{-1})	α_{Y2} (MK^{-1})	α_{Y3} (MK^{-1})	α_{V} (MK^{-1})
ZnCP^{HT}	100(18)	−462(23)	882(32)	575(81)
ZnCP^{LT}	69(10)	−57(13)	275(16)	292(10)
NiCP^{HT}*	16(20)	140(7)	180(30)	371(36)
NiCP^{LT}	27(1)	8(2)	146(5)	182(3)
CoCP^{HT}*	207(7)	153(7)	−150(40)	239(36)
CoCP^{LT}	37(2)	26(2)	168(4)	237(6)
CdCP^{HT}	154(8)	778(19)	−389(11)	531(12)
CdCP^{LT}	98(6)	169(18)	−81(14)	189(10)
ZnCoCP^{HT}	152(43)	−712(11)	1632(36)	1070(60)
ZnCoCP^{LT}	42(6)	3(8)	176(10)	224(9)
ZnCdCP^{HT}	81(1)	−711(14)	1216(19)	571(3)
ZnCdCP^{LT}	20(6)	38(1)	218(15)	285(12)
NiCdCP^{HT}*	236(13)	42(11)	89(13)	378(24)
NiCdCP^{LT}	73(3)	−160(16)	394(11)	306(16)

*Data determined by means of solvent cell (temperature range 280–310 K)

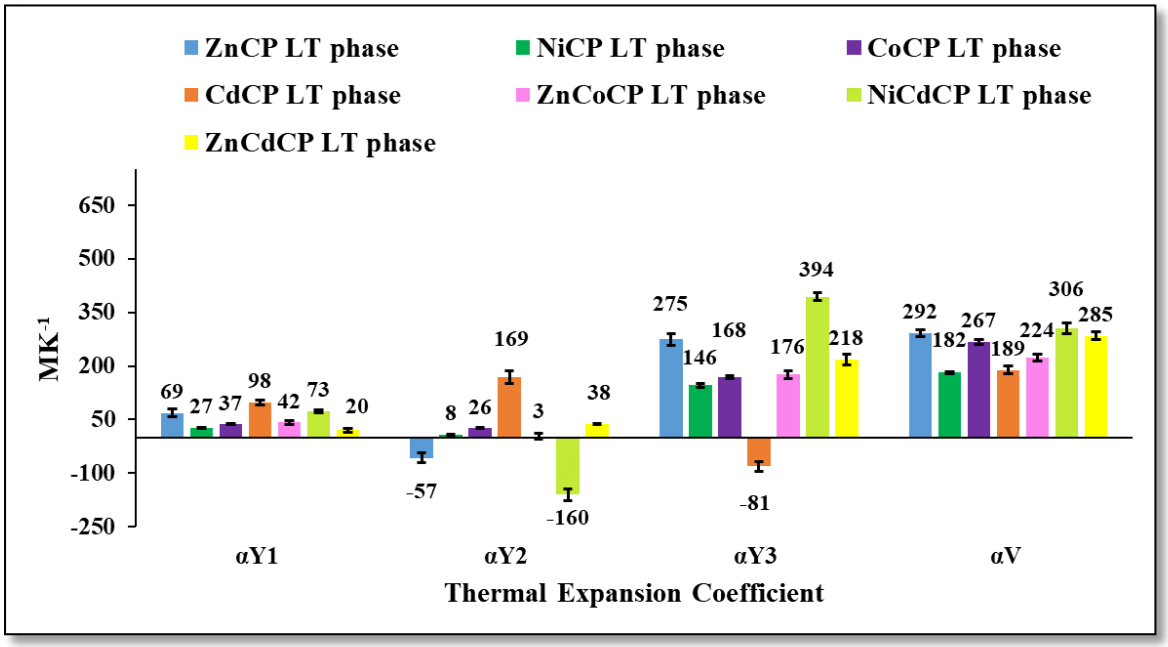

Figure S40: Thermal expansion coefficients determined for the low temperature phases of the CP series. Error bars and specific values are indicated.

Table S17. Reported extreme and/or anisotropic coefficients of thermal expansion

	Material	Temperature range (K)	α_{X1} (MK^{-1})	α_{X2} (MK^{-1})	α_{X3} (MK^{-1})	α_V (MK^{-1})	Reference
Organic materials	IMD-HBC	100–360	-115	18	210	110	16
	(S,S)-octa-3,5-diyn-2,7-diol	225–330	515	-85	-204	47	17
	18C6N	90–273	-129(15)	144(14)	282(16)	311(17)	18
	$C_{12}H_{24}O_6{\cdot}2CH_3NO_2$	180–273	-198(12)	215(16)	369(20)	378(22)	19
	$CD_3OD{\cdot}D_2O$	20–155	-64(4)	462(4)	93(4)	494(6)	20
	β L-PGA	320–420	-54.5(8)	303(1)	-3.62(8)	245(2)	21
	CA-Pyz	250–300	-1375(30)	196(30)	1524(30)	245(30)	22
Metal-organic frameworks	$[Zn_2(fu\text{-}L^1)_2dabco]n$	303–463	-380	1161	14.6	837	23
	$[Zn_2(fu\text{-}L^2)_2dabco]n$	303–463	-186	674	17.1	524	23
	$[Fe_{0.84}Ni_{0.16}(bpac)(Au(CN)_2)_2]{\cdot}2EtOH$	160–215	-3200	5200	1500	3200	24
	α-Cu(tcm)	20–240	591(28)	-407(28)	-13.6(11)	-*	25
	FJI-H11-Me	100–300	-37.8(2)	=X1	653.2(5)	568.1(7)	26
	FJI-H11-Me	100–300	-33.2(3)	=X1	489.4(10)	416.8(11)	26
	[Cd(34pba)(44pba)]	112–300	61(1)	482(12)	-218(3)	319(13)	27
	$\{[FeTp(CN)_3]_2Co\text{-}(Bib)_2\}{\cdot}5H_2O$	300–350	-656	-18	197	-489	28
	$\{[FeTp(CN)_3]_2Co\text{-}(Bib)_2\}{\cdot}5H_2O$	180–240	85	278	1089	1498	28
1D coordination polymers	$[ZnCl_2(\mu\text{-bipy})]_\infty$ 1D-α	170–295	1(2)	36(3)	92(7)	134(7)	29
	$[ZnCl_2(\mu\text{-bipy})]_\infty$ 1D-β	155.5–295	-10(3)	39(3)	77(2)	108(3)	29
	$Ag[AuCl_2(CN)_2]$	100–300	49.4(13)	23.6(10)	-4.7(14)	88(3)	30
	$Ag[AuBr_2(CN)_2]$	100–300	52.1(9)	25.3(6)	5.1(5)	97.7(9)	30
	$Cu[AuBr_2(CN)_2]$	100–300	45.9(5)	-11.3(2)	73.6(6)	103.1(12)	30
	$[Cu_3(cdm)_4]$	120–350	-18.8(6)	=X1	46.8(19)	9.3(9)	31
Other	$Ag_3[Co(CN)_6]$	20–300	150	=X1	-130	-*	32
	$[Ag(en)]NO_3$-I	120–360	-89.7(15)	37.9(12)	149.2(12)	95.8(20)	33
	$(Mn_{0.95}Ni_{0.05})CoGe$	270–320	-1804(105)	1265(71)	46(2)	-621(35)	34

*Value not reported

5. Powder X-ray diffraction (PXRD)

A Bruker D2 Phaser diffractometer was used to determine experimental diffractograms. The diffractometer utilises Bragg-Brentano geometry and Cu Kα radiation (λ = 1.5418 Å) as the incident beam. The diffractometer was operated at 30 kV and 10 mA. Intensity data were recorded with a Lynxeye detector using a rotating flat stage (30° min^{-1}). The diffractograms were determined under ambient conditions with a scanning range of 5–35°, a step size of 0.016° and a 0.8 second scan speed. Slight shifts between the simulated (from 270 K data) and the experimental (ambient temperature) diffractograms are related to thermal expansion of the materials. Differences in peak intensity are attributed to preferred orientation since grinding of the samples aided desolvation.

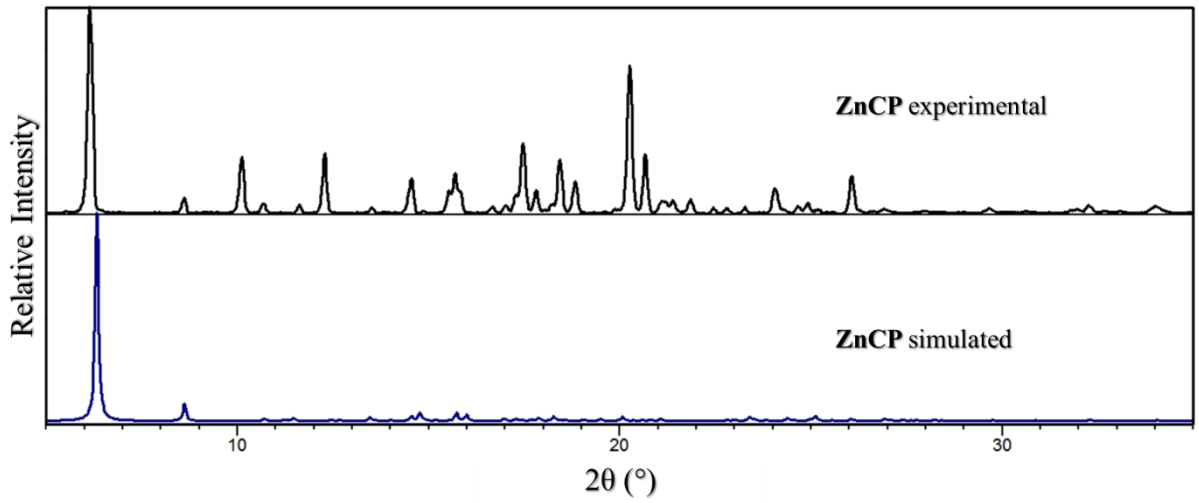

Figure S41: Simulated and experimental diffractograms for **ZnCP^{HT}**.

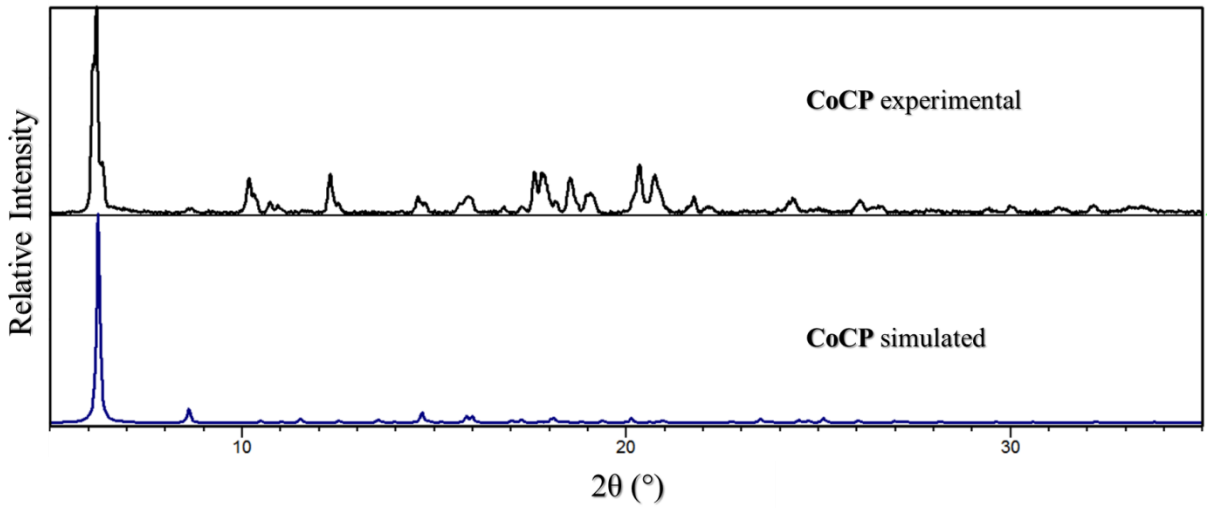

Figure S42: Simulated and experimental diffractograms for $CoCP^{HT}$.

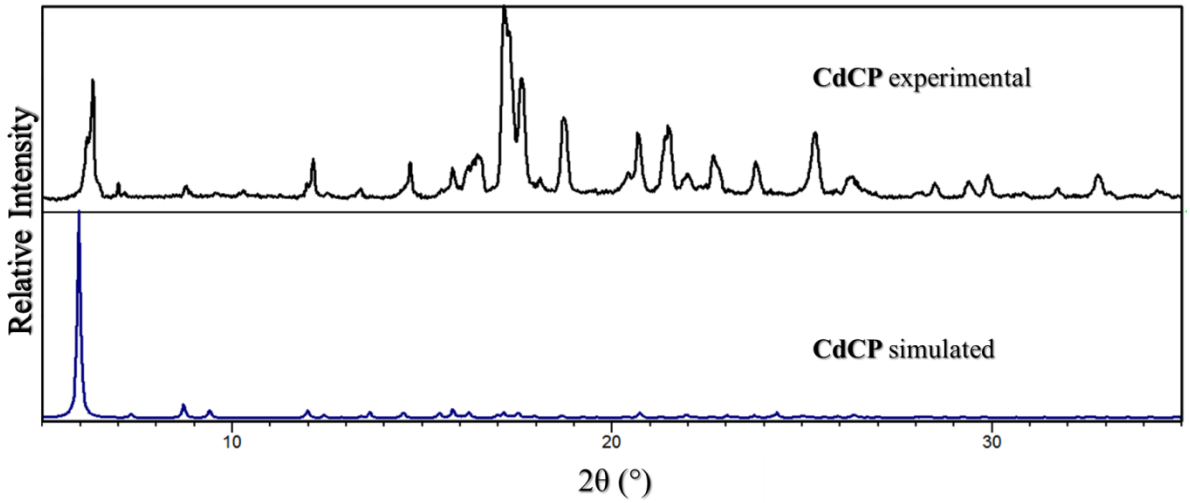

Figure S43: Simulated and experimental diffractograms for $CdCP^{HT}$.

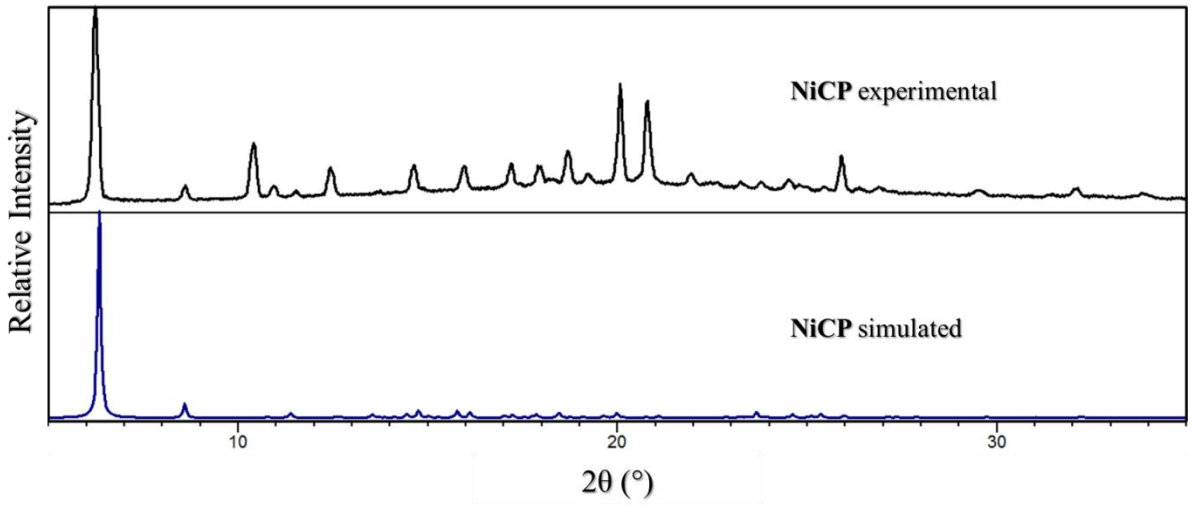

Figure S44: Simulated and experimental diffractograms for NiCP^{HT}.

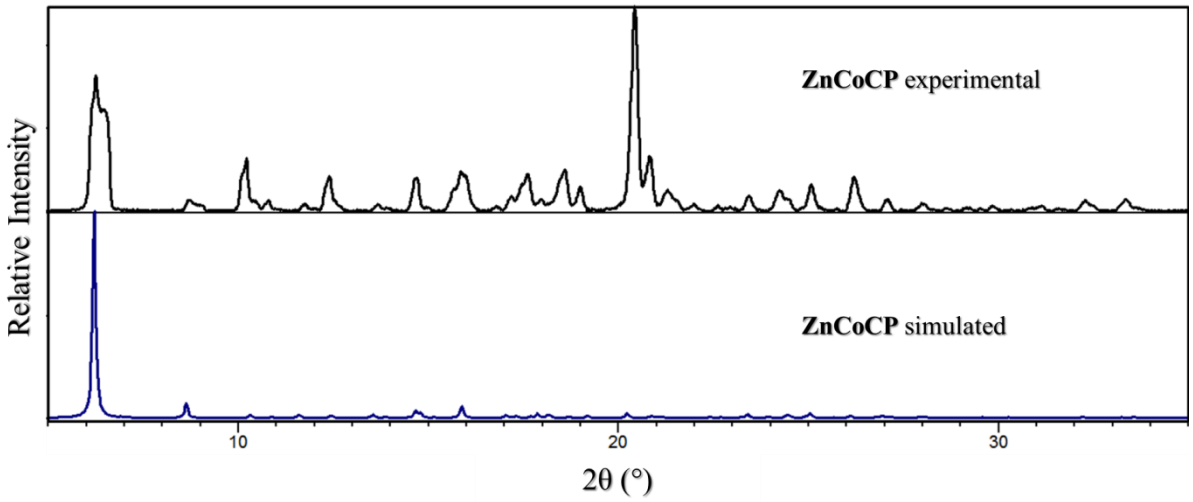

Figure S45: Simulated and experimental diffractograms for ZnCoCP^{HT}.

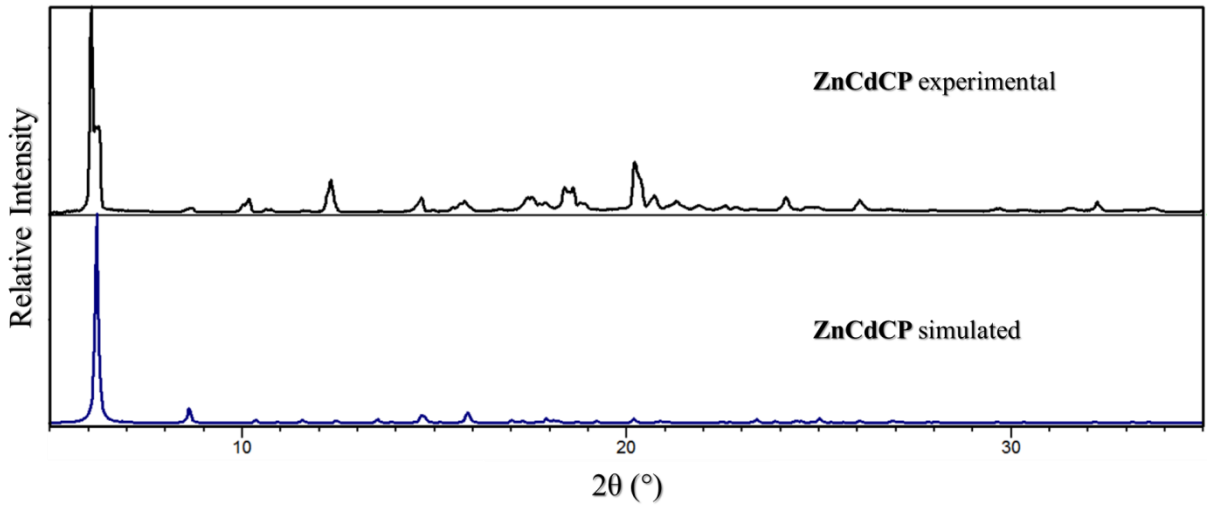

Figure S46: Simulated and experimental diffractograms for ZnCdCP^{HT}.

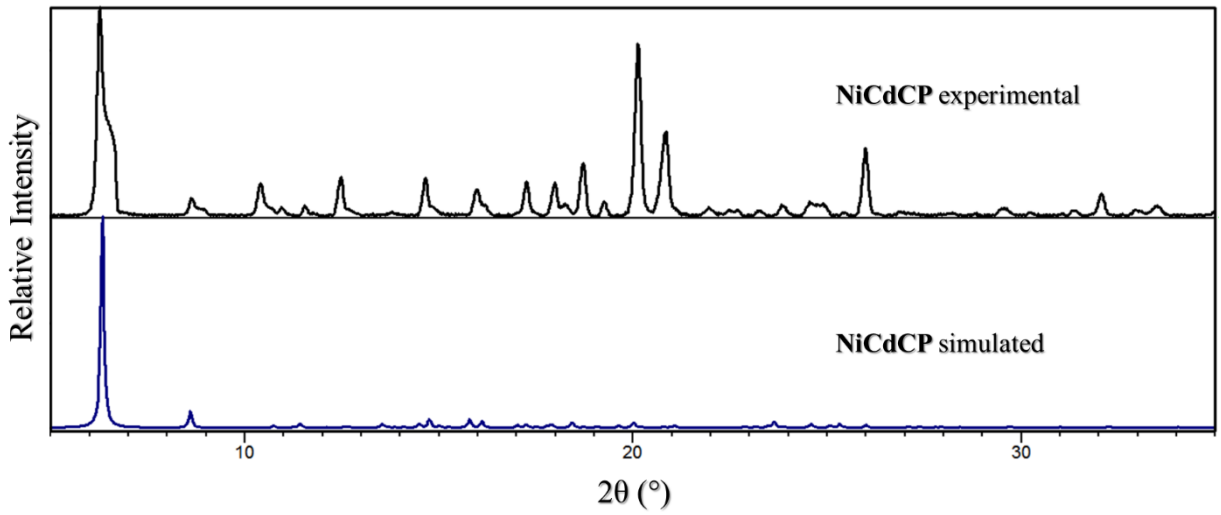

Figure S47: Simulated and experimental diffractograms for NiCdCP^{HT}.

6. Fourier-transform infrared spectrophotometry (FT-IR)

IR spectra were recorded using a Bruker Alpha P ATR-IR instrument. A background measurement was performed before each spectrum was recorded. Samples were briefly dried on filter paper before measurement to remove any surface solvent.

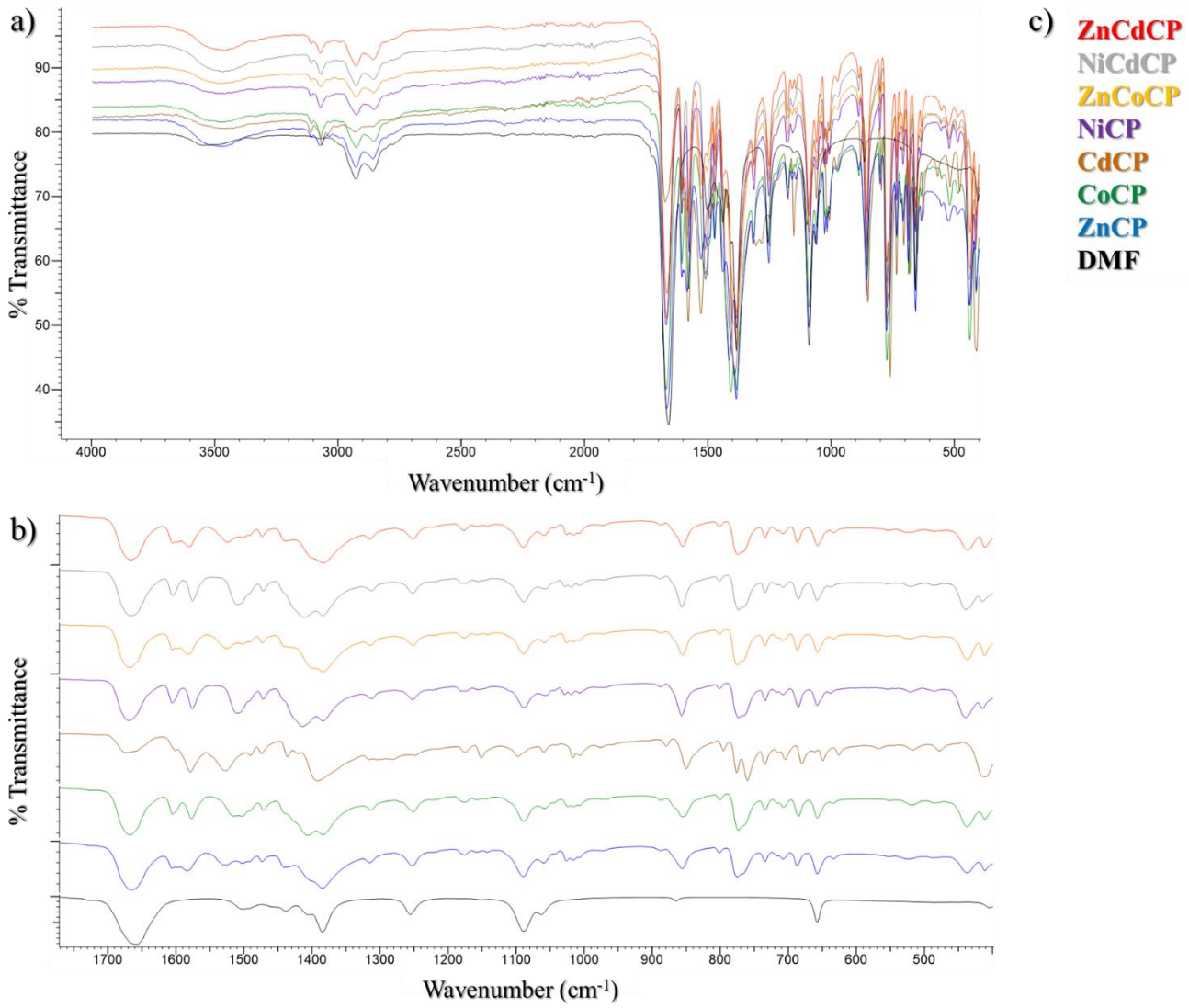

Figure S48: FT-IR spectra of all the compounds studied compared to pure DMF. In **(a)** the entire IR range is shown with spectra overlayed (slight offset from baseline). Note that the sp^3 C–H stretching bands (*ca* 3000–2800 cm^{-1}) are purely derived from the guest, while the aromatic sp^2 C–H stretching bands (*ca* 3200–3000 cm^{-1}) are in turn derived from the host system. The fingerprint region of the spectra are shown stacked in **(b)**. The legend for both **(a)** and **(b)** is represented in **(c)**.

7. Thermogravimetric analysis (TGA)

TGA data were recorded by measuring the percentage mass as the sample was heated at a constant rate. A TA Instruments Q500 thermogravimetric analyser was used. Samples were placed in aluminium pans and sample weights typically ranged from 1 to 5 mg. N_2 gas (flow rate 40 ml min^{-1}) was used to purge the furnace. The temperature was ramped from room temperature to *ca.* 600 °C at a constant heating rate of 10 °C min^{-1}. The resulting thermograms were analysed using the TA Instruments Universal Analysis program.

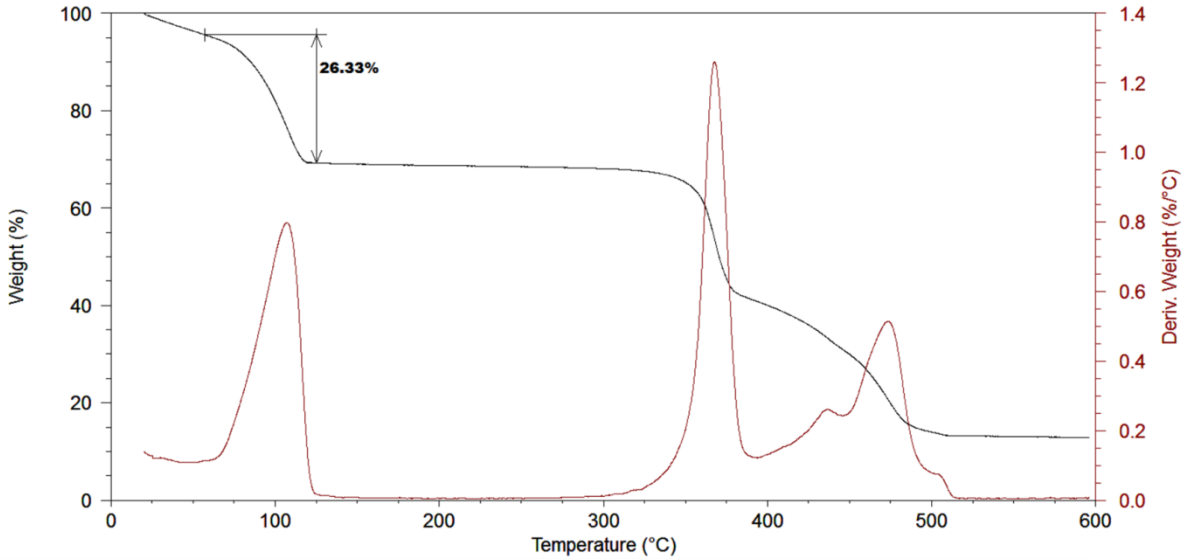

Figure S49: Thermogram of **ZnCP^{HT}**. The weight loss of 26.3% corresponds to *ca* two DMF molecules per host formula unit (calculated 24.0%).

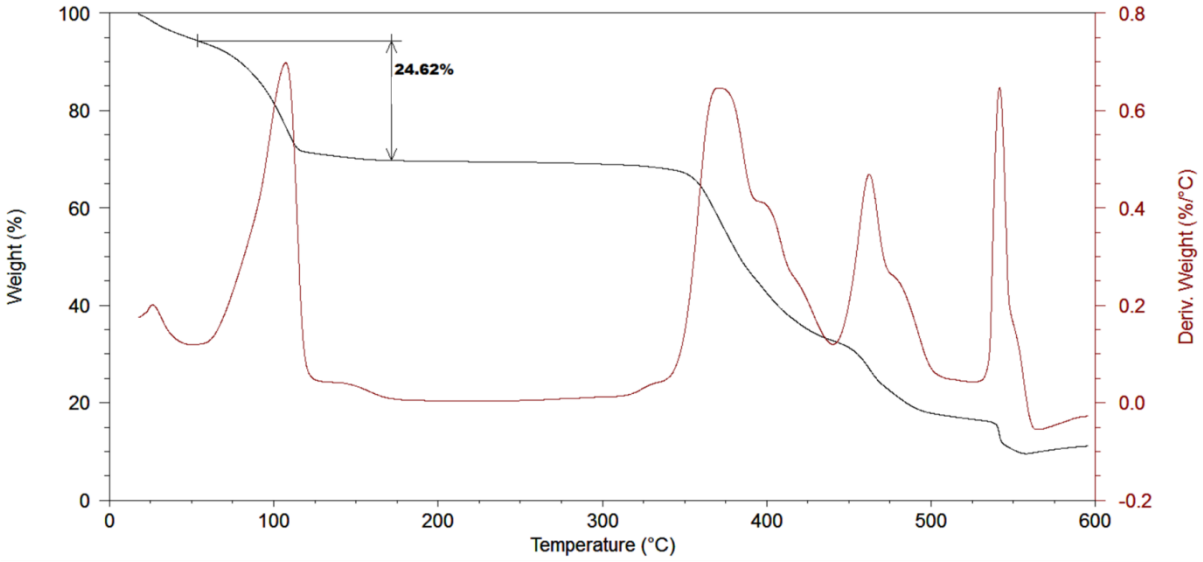

Figure S50: Thermogram of **CoCP^{HT}**. The weight loss of 24.6% corresponds to *ca* two DMF molecules per host formula unit (calculated 24.3%).

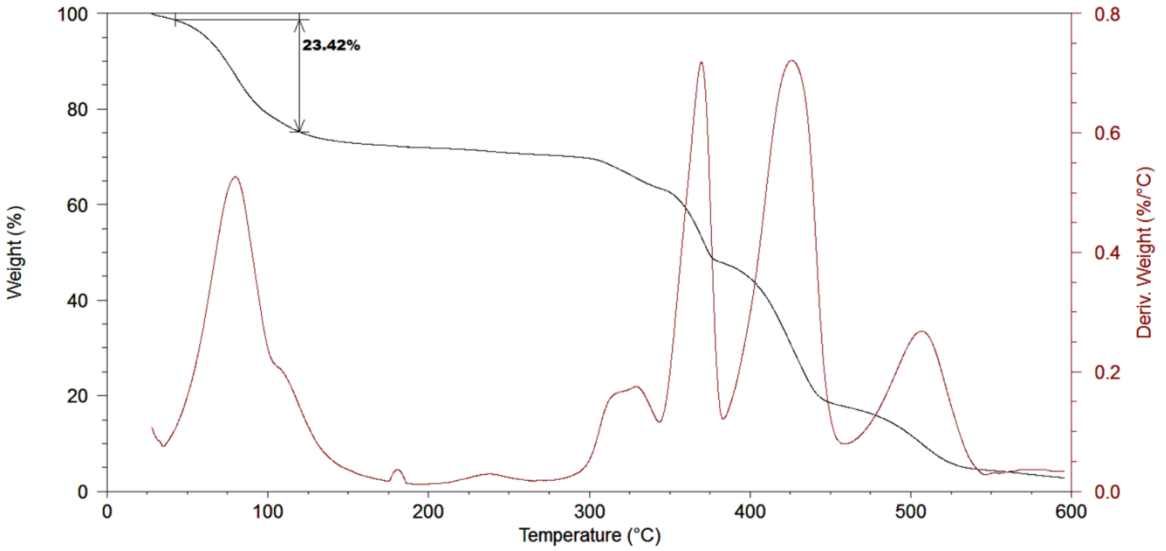

Figure S51: Thermogram of **CdCP^{HT}**. The weight loss of 23.4% corresponds to *ca* two DMF molecules per host formula unit (calculated 22.3%).

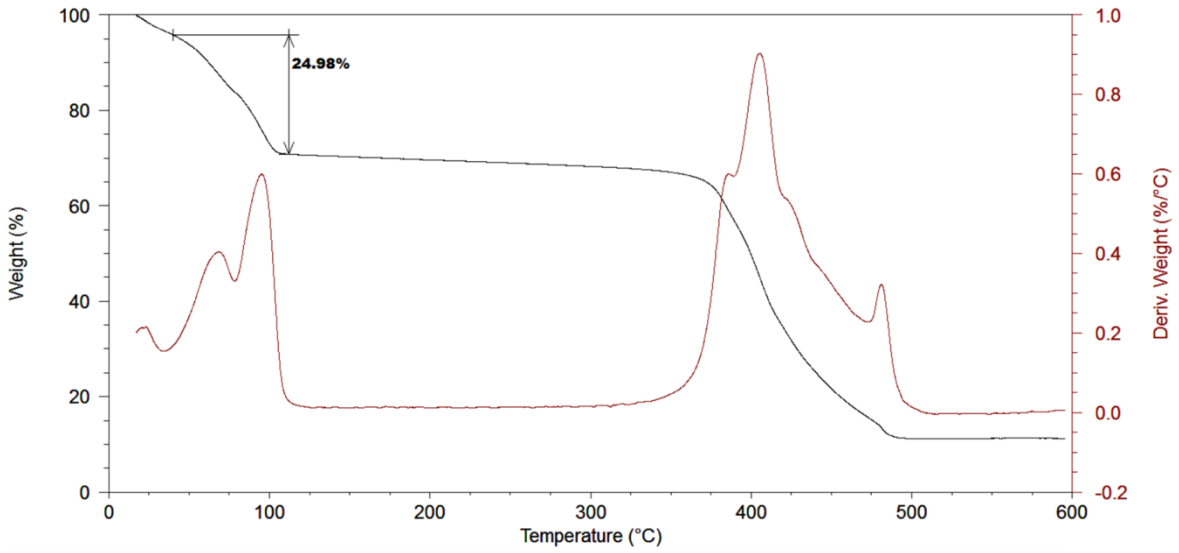

Figure S52: Thermogram of **NiCP^{HT}**. The weight loss of 25.0% corresponds to *ca* two DMF molecules per host formula unit (calculated 24.3%).

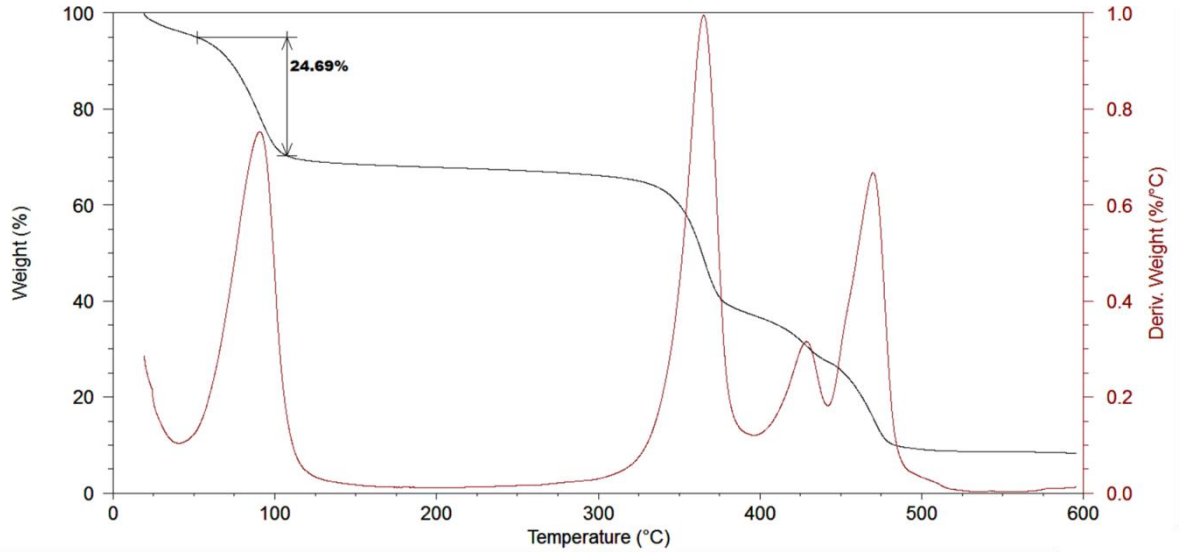

Figure S53: Thermogram of **ZnCoCP^{HT}**. The weight loss of 24.7% corresponds to *ca* two DMF molecules per host formula unit (calculated 24.1%).

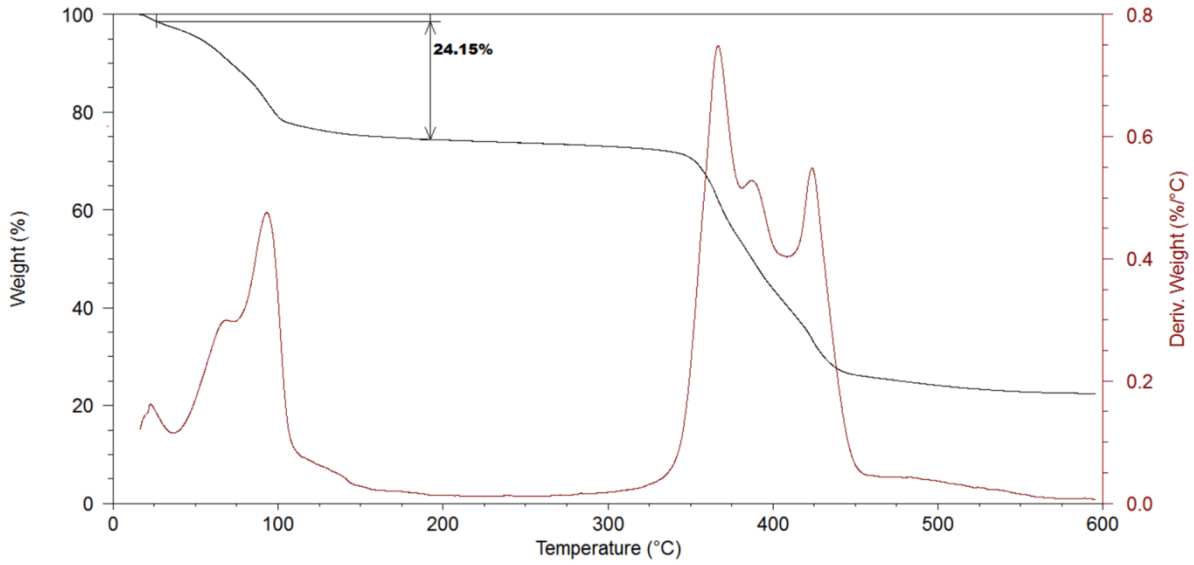

Figure S54: Thermogram of **NiCdCP^{HT}**. The weight loss of 24.2% corresponds to *ca* two DMF molecules per host formula unit (calculated 23.8%).

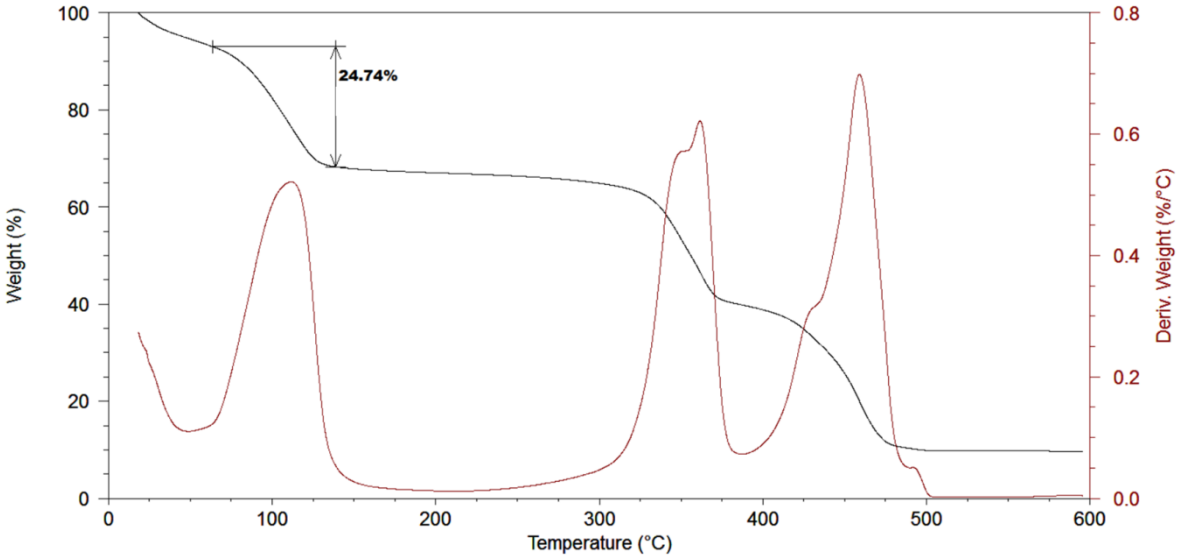

Figure S55: Thermogram of **ZnCdCP^{HT}**. The weight loss of 24.7% corresponds to *ca* two DMF molecules per host formula unit (calculated 23.9%).

8. Energy dispersive X-ray spectroscopy (EDX)

Samples of **ZnCoCP**, **ZnCdCP** and **NiCdCP** were prepared for EDX analysis by removing the guest in a thermogravimetric furnace (T_{max} = 150 °C, ramp rate = 5 °C min^{-1}, N_2 purge = 40 ml min^{-1}). This produced single crystals of the guest-free phases of these materials – denoted **ZnCoCPa**, **ZnCdCPa** and **NiCdCPa**. Samples were attached to aluminium scanning electron microscope (SEM) stubs using double sided carbon tape. The samples were allowed to dry in an oven, after which a gold sputter coating (10 nm) was applied. Images were recorded out with a Zeiss EVO SEM equipped with both a backscattered electron detector (Carl Zeiss Microscopy, Germany) and an energy dispersive X-ray spectroscopy (EDX) detector (Oxford Instruments® XMax 20 mm^2). Accelerating voltage (EHT): 20 kV, working distance: 8.5 mm and beam current: 11 nA. Measurements were carried out in triplicate.

Table S18. Molar ratios for solid solutions determined by EDX.

Material	Ratio in crystallisation solution (Zn:Co:Cd:Ni)	Zinc	Cobalt	Cadmium	Nickel
ZnCoCPa	1:1:0:0	0.145(5)	0.012(1)	0	0
ZnCdCPa	1:0:1:0	0.149(12)	0	0.012(1)	0
NiCdCPa	0:0:1:1	0	0	0.029(1)	0.156(9)

The final ratios were determined to be approximately 12:1 Zn:Co, 12:1 Zn:Cd and 5:1 Ni:Cd for **ZnCoCP**, **ZnCdCP** and **NiCdCP**, respectively.

8.1. EDX mapping

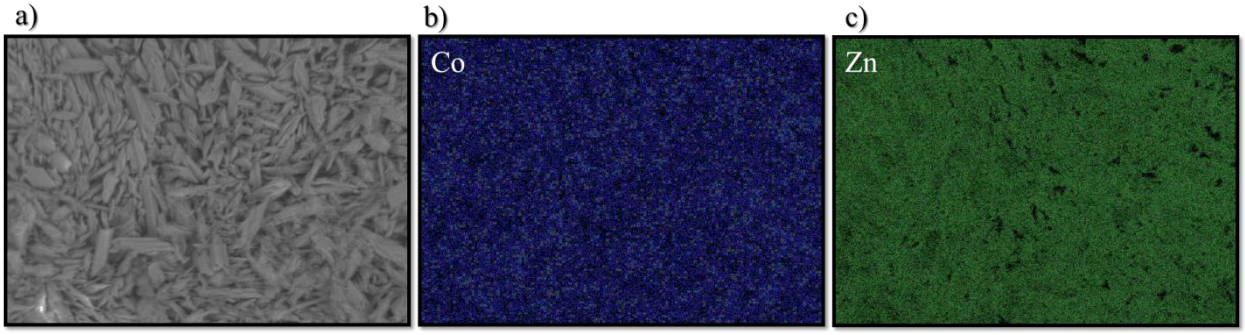

Figure S56: SEM imaging of **ZnCoCPa (a)** along with EDX mapping showing the distribution of the cobalt **(b)** and zinc **(c)** atoms in the sample. The metal atoms are evenly distributed throughout the sample, with a higher concentration of zinc.

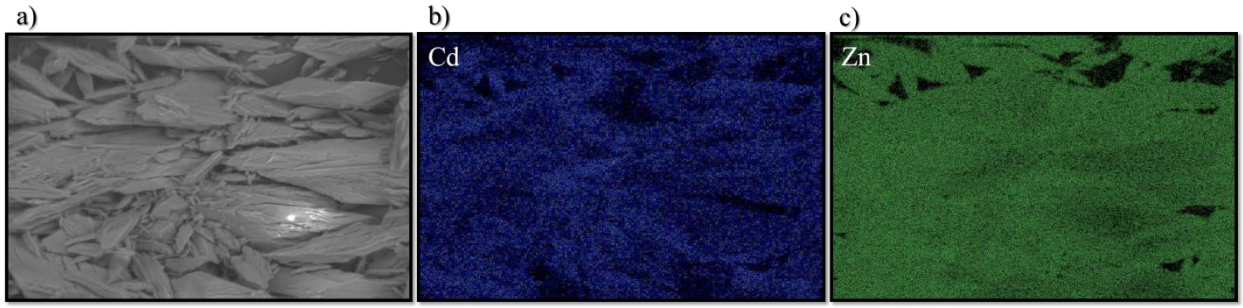

Figure S57: SEM imaging of **ZnCdCPa (a)** along with EDX mapping showing the distribution of the cadmium **(b)** and zinc **(c)** atoms in the sample. The metal atoms are evenly distributed throughout the sample, with a higher concentration of zinc.

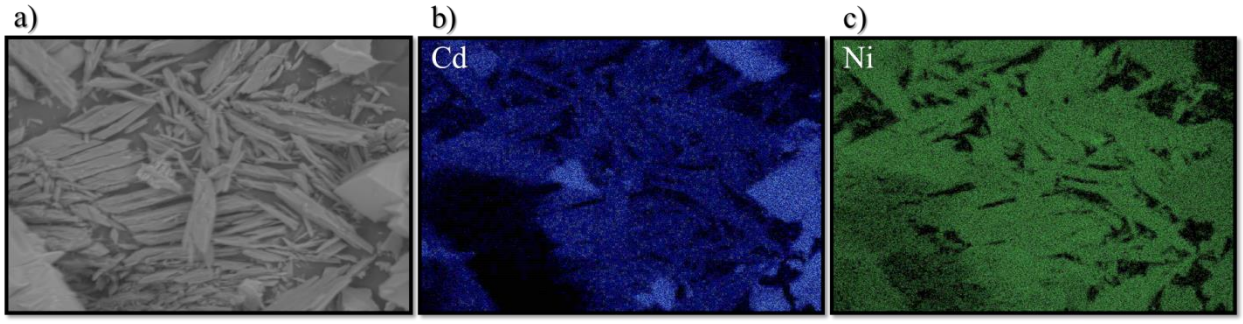

Figure S58: SEM imaging of **NiCdCPa (a)** along with EDX mapping showing the distribution of the cadmium **(b)** and nickel **(c)** atoms in the sample. The metal atoms are evenly distributed throughout the sample, with a higher concentration of nickel.

References

1 MiTeGen, MiTeGen, https://www.mitegen.com/, (accessed 25 June 2018).

2 Bruker AXS Inc., 2016.

3 Bruker AXS Inc., 2016.

4 G. M. Sheldrick, *Acta Cryst.*, 2015, **A71**, 3–8.

5 G. M. Sheldrick, *Univ. Göttingen, Ger.*, 2018.

6 L. J. Barbour, *J. Supramol. Chem.*, 2001, **1**, 189–191.

7 L. J. Barbour, *J. Appl. Crystallogr.*, 2020, **53**, 1141–1146.

8 Persistence of Vision Raytracer Pty. Ltd., 2004.

9 C. F. Macrae, P. R. Edgington, P. McCabe, E. Pidcock, G. P. Shields, R. Taylor, M. Towler and J. Van De Streek, *J. Appl. Crystallogr.*, 2006, **39**, 453–457.

10 C. F. Macrae, I. J. Bruno, J. A. Chisholm, P. R. Edgington, P. McCabe, E. Pidcock, L. Rodriguez-Monge, R. Taylor, J. Van De Streek and P. A. Wood, *J. Appl. Crystallogr.*, 2008, **41**, 466–470.

11 C. F. MacRae, I. Sovago, S. J. Cottrell, P. T. A. Galek, P. McCabe, E. Pidcock, M. Platings, G. P. Shields, J. S. Stevens, M. Towler and P. A. Wood, *J. Appl. Crystallogr.*, 2020, **53**, 226–235.

12 A. L. Spek, *Acta Crystallogr.*, 2015, **C71**, 9–18.

13 D. P. van Heerden and L. J. Barbour, *Chem. Soc. Rev.*, 2021, **50**, 735–749.

14 Bruker AXS Inc., *Bruker AXS Inc., Wisconsin, USA*, 2016.

15 M. J. Cliffe and A. L. Goodwin, *J. Appl. Crystallogr.*, 2012, **45**, 1321–1329.

16 B. Dwivedi, A. Shrivastava, L. Negi and D. Das, *Cryst. Growth Des.*, 2019, **19**, 2519–2524.

17 D. Das, T. Jacobs and L. J. Barbour, *Nat. Mater.*, 2010, **9**, 36–39.

18 E. R. Engel, V. J. Smith, C. X. Bezuidenhout and L. J. Barbour, *Chem. Commun.*, 2014, **50**, 4238–4241.

19 E. R. Engel, V. J. Smith, C. X. Bezuidenhout and L. J. Barbour, *Chem. Mater.*, 2016, **28**, 5073–5079.

20 A. D. Fortes, E. Suard and K. S. Knight, *Science*, 2011, **331**, 742–746.

21 M. K. Panda, T. Runčevski, A. Husain, R. E. Dinnebier and P. Naumov, *J. Am. Chem. Soc.*, 2015, **137**, 1895–1902.

22 H. Liu, M. J. Gutmann, H. T. Stokes, B. J. Campbell, I. R. Evans and J. S. O. Evans, *Chem. Mater.*, 2019, **31**, 4514–4523.

23 S. Henke, A. Schneemann and R. A. Fischer, *Adv. Funct. Mater.*, 2013, **23**, 5990–5996.

24 B. R. Mullaney, L. Goux-Capes, D. J. Price, G. Chastanet, J.-F. Létard and C. J. Kepert, *Nat. Commun.*, 2017, **8**, 1053.

25 S. J. Hunt, M. J. Cliffe, J. A. Hill, A. B. Cairns, N. P. Funnell and A. L. Goodwin, *CrystEngComm*, 2015, **17**, 361–369.

26 J. Pang, C. Liu, Y. Huang, M. Wu, F. Jiang, D. Yuan, F. Hu, K. Su, G. Liu and M. Hong, *Angew. Chem., Int. Ed.*, 2016, **55**, 7478–7482.

27 H. L. Zhou, Y. B. Zhang, J. P. Zhang and X. M. Chen, *Nat. Commun.*, 2015, **6**, 1–7.

28 J. X. Hu, Y. Xu, Y. S. Meng, L. Zhao, S. Hayami, O. Sato and T. Liu, *Angew. Chem., Int. Ed.*, 2017, **56**, 13052–13055.

29 B. K. Saha, S. A. Rather and A. Saha, *Eur. J. Inorg. Chem.*, 2017, **28**, 3390–3394.

30 J. S. Ovens and D. B. Leznoff, *Inorg. Chem.*, 2017, **56**, 7332–7343.

31 J. E. Auckett, S. G. Duyker, E. I. Izgorodina, C. S. Hawes, D. R. Turner, S. R. Batten and V. K. Peterson, *Chem. Eur. J.*, 2018, **24**, 4774–4779.

32 A. L. Goodwin, M. Calleja, M. J. Conterio, M. T. Dove, J. S. O. Evans, D. A. Keen, L. Peters and M. G. Tucker, *Science*, 2008, **319**, 794–797.

33 W. Cai and A. Katrusiak, *Nat. Commun.*, 2014, **5**, 1–8.

34 Q. Ren, W. Hutchison, J. Wang, A. Studer, G. Wang, H. Zhou, J. Ma and S. J. Campbell, *ACS Appl. Mater. Interfaces*, 2019, **11**, 17531–17538.

Chapter 6 – Concluding Remarks & Future Work

"Nothing in life is to be feared, it is only to be understood. Now is the time to understand more, so that we may fear less."— Marie Curie

In this work, the solid-state dynamics of a novel family of 1D coordination polymers was investigated. These materials exhibit dramatic flexibility, upon which nearly all of the studied structure-property relationships were based. The high degree of flexibility results in unique and interesting physicochemical properties, but may induce sufficient stress for the crystal to disintegrate. Some modes of flexibility allow for various possible solid-state architectures to co-exist. These pose problems the phase purity required for bulk phase property determinations (*e.g.,* sorption analyses, calorimetry, magnetism, *etc.*). Nonetheless, if these concerns can be balanced effectively by careful experimental design and some luck, the results may yield exciting new avenues of exploration in materials science.

The work presented in Chapter 3 approaches the problem of resolving a system wherein two solvates crystallise concomitantly under conventional solvothermal techniques. Since the materials possess different guest systems, attempts at solvothermal separation of these isomers focussed on changes in temperature, solvent water composition and crystallisation duration. Although this methodology was partially successful at resolving form **1b**, **1a** remained elusive.

Mechanochemistry was investigated as an alternative method of preparation as opposed to conventional solvothermal methods. Indeed, mechanochemistry has recently been shown to resolve polymorphs in metal-organic materials.[1–3] Mechanochemistry also provides the added benefit of a greener approach to conventional chemistry owing to a reduction in the amount of solvent used. The use of mechanochemistry allowed selective preparation of either **1a** or **1b**, depending on the grinding procedure and composition of the solvent system employed. Slurry grinding immediately after solvent addition resulted in **1b**, while aging of the solvent and starting materials prior to grinding produced **1a**. Further variation of the solvent system produced a third supramolecular isomer (**1c**). Additional changes in the water content of the solvent system used during slurry grinding allowed for further means of selective preparation of both **1a** and **1b**.

Solvent exchange in the appropriate solvent system allowed for interconversion between the isomers. Interestingly, form **1a** reproducibly converts to form **1b** within two days when

immersed in fresh solvent. This time-dependent conversion between forms is not observed (within several weeks) in single crystals. Furthermore, no temperature-mediated conversion is observed between forms **1a** and **1b** in the temperature range −80 to 70 °C.

Chapters 4 and 5 present studies on two similar series of compounds (with one compound in common). While Chapter 4 focuses on apohost materials and their sorption properties, Chapter 5 describes the dynamics of the host-guest materials in response to temperature.

In Chapter 4 the activation of the materials results in a dramatic uniaxial or biaxial contraction, resulting in a reduction of the unit-cell volume of up to 39%. Very few examples of SC-SC transformations of such magnitude exist,[4–7] with even fewer exceeding it.[8] This dramatic contraction produces apohost materials that are nonporous owing to collapse of the 1D channels upon guest removal. The structural transformation to afford the apohost material produces an unusual degree of contortion of the conceptually rigid ligand that far exceeds any other reports for the deviation from linearity of similar ligands in the solid-state.

While the apohost materials do not sorb gases, both readily sorb DMF and **2a** sorbs solvent vapour. The inclusion of either liquid or vapour requires reopening of the 'virtually nonporous' apohost form. **2a** sorbs volatile organic vapours and surface deposition, coupled to the sorption process, allows the material to sorb up to twice as much vapour as would be expected from the host-guest ratio of the corresponding solvate. Furthermore, although there is a latent period before the apohost framework reopens during vapour sorption, this period is reduced in consecutive sorption cycles. Investigation of this phenomenon revealed that a component of the framework remains open upon consecutive cycles (even once the guest has been entirely removed) and this likely facilitates greater ease of reopening in the following sorption cycle. It is also postulated that the duration of the latent period may be attributed to the kinetic diameters and vapour pressures of the guests in question. Shorter latent periods were observed for small guest molecules with high vapour pressures, and longer latent periods for large guest molecules with low vapour pressures.

Chapter 5 describes the thermal expansion behaviour of a series of materials where the metal node is varied. The variation in the metal centre produces slight changes in crystal packing in the analogous series. Each material undergoes a low-temperature phase change. The phase-change behaviour is governed by the chemistry of the metal centre since materials with more divergent solid-state packing undergo similar phase change behaviour (and *vice versa*). Similarly, the choice of metal node (and the resultant supramolecular packing) affects the thermal expansion behaviour of each material. Variation of the metal node from nickel or

cobalt to zinc or cadmium results in a change from colossal positive linear and volumetric thermal expansion to extreme anisotropic linear thermal expansion. Furthermore, by preparing solid solutions of two metal species one can induce supercolossal anisotropic thermal expansion, the magnitude and anisotropic nature of which are comparable to the best reported values in the literature (Table 6.1). Interestingly, two of the materials with the highest reported thermal expansion coefficients are solid solutions. This highlights the dramatic effect that even a minor component of a second metal can have on the physicochemical properties of a material. Additionally, to the best of our knowledge, these materials represent the largest anisotropic thermal expansion behaviour ever reported for 1D coordination polymers.

Table 6.1. Examples of extreme anisotropic thermal expansion

Material	α_{Y1} (MK^{-1})	α_{Y2} (MK^{-1})	α_{Y3} (MK^{-1})	α_{V} (MK^{-1})	Reference
CA-Pyz	-1375	196	1524	245	9
$[Fe_{0.84}Ni_{0.16}(bpac)(Au(CN)_2)_2]\cdot 2EtOH$	-3200	5200	1500	3200	10
$(Mn_{0.95}Ni_{0.05})CoGe$	-1804	1265	46	-624	11
$ZnCoCP^{HT}$	152	-712	1632	1070	This work
$ZnCdCP^{HT}$	81	-711	1216	570	This work

The mechanism of thermal expansion differs from material to material, even within the analogous series, and is related to deformation of the 1D channel, variation in the distance between 1D strands, variation in the extent of the offset in π···π stacking or a combination of these factors. This, once more, underpins the various modes of flexibility occurring in these materials.

We have prepared 9 novel 1D coordination polymers (including several forms of each) that form part of an extended family of materials exhibiting analogous solid-state packing. We have elucidated many structure-property relationships in these compounds and described the underlying mechanism where possible. This was achieved through the use of multiple techniques including, but not limited to: single-crystal X-ray diffraction, powder X-ray diffraction, sorption techniques, thermogravimetry, differential scanning calorimetry and infrared spectroscopy. We have assessed complications arising from bulk phase impurity, loss of single-crystal quality and extreme host disorder, and have found methods of either

addressing or circumventing these difficulties. We report several extreme structure-property relationships that exceed in magnitude those previously reported for 1D coordination polymers and add insights to crystal engineering and materials science that will hopefully spark further interest in these materials and techniques.

Future work should focus on expansion of the current series of materials. 1D coordination polymers seldom occur with such large guest-accessible channels, as the inherent flexibility of these materials may manifest in close-packing resulting in materials that are less dynamic in nature. However, the large guest-accessible channels in this series allow these materials freedom to undergo changes in their solid-state packing upon the application of specific stimuli. Furthermore, the groundwork has been established in terms of the techniques required to study these materials, which will enable future studies to proceed with greater ease.

During this study only slight changes were made to the metal centre and ligands. Greater variation in ligand size, shape and functionality may produce further analogous materials, possibly generating species with equally, if not more, interesting structure-property relationships. Several possible candidate molecules are identified in Figure 6.1.

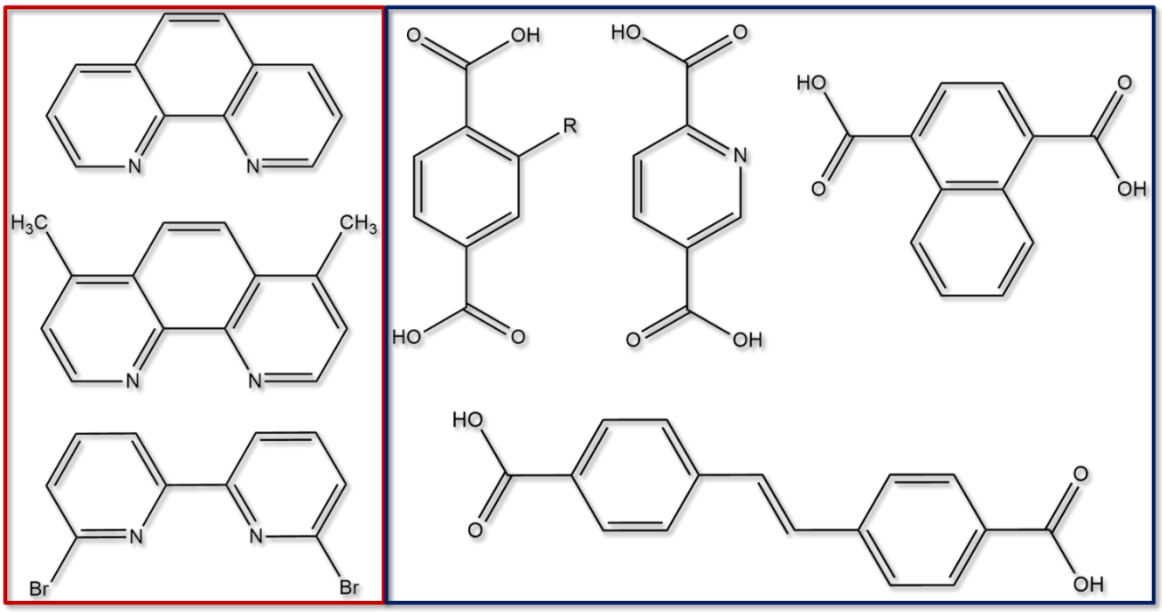

Figure 6.1. Proposed ligands for further expansion of the current coordination polymer series. R = Br, Cl, I, NH_2, NO_2, CH_3, *etc*.

Secondly, our foray into the chemistry of solid solutions was limited in scope. In this study only 1:1 ratios of two metal ions were employed in the crystallisation solution. Although the prepared solid solutions did not crystallise with a 1:1 ratio of metal centres, it is still unknown if changing the stoichiometry of the crystallisation solution would further influence the final

CP metal composition. Solid solutions of two or more metals should be investigated to determine if materials with more dramatic anomalous thermal expansion can be prepared. This part of the work lends itself to systematic studies on how the nature of the metal ions and their stoichiometry affect the properties of the resultant materials (even when the solid-state packing is not appreciably affected). Furthermore, isotypic materials may have their properties further modified by *epitaxy*, which describes the growth of one crystal on the surface of another (*i.e.,* one crystal essentially seeds the other).[12] When the two materials are isostructural this phenomenon is called *homoepitaxy*, otherwise it is known as *heteroepitaxy*.[12] Epitaxial growth may be utilised to seed specific crystal forms, develop self-healing materials, and to hone physical properties of the components (*i.e.,* producing task specific materials).[13,14]

The CPs reported in this study were all prepared in either DMF or DMA. Owing to the inherent flexibility of the materials, it is expected that they may exhibit solvatomorphic behaviour. Exchanging the current guest(s) with other solvents should produce new forms with further subtle differences in their structure-property relationships. If the group of solvates produced is large enough, it may be possible to start inferring trends in properties (*e.g.,* thermal expansion) from changes in guest size and electronics.

Once the CP series has been sufficiently expanded mechanical pressure could be investigated in addition to the stimuli already employed. Although still a niche technique, diamond-anvil cells are unique tools used to investigated the structural behaviour of crystalline materials at high pressures (up to 100 GPa, but more routinely between 0.1 and 6 GPa).[15,16] Indeed, recent studies have shown the close relationship between anomalous thermal expansion in crystalline materials and interesting compression behaviour.[15,17]

References

1 B. Karadeniz, Z. Dijana, I. Huskić, L. S. Germann, A. M. Fidelli, M. Etter, R. E. Dinnebier, D. Barišić, S. Muratović, I. Lončarić, N. Cindro, T. Islamoglu, O. K. Farha, T. Friščić and K. Užarević, *J. Am. Chem. Soc.*, 2019, **141**, 19214–19220.

2 T. Stolar, S. Lukin, M. Tireli, I. Sović, B. Karadeniz, I. Kereković, G. Matijašić, M. Gretić, Z. Katančić, I. Dejanović, M. Di Michiel, I. Halasz and K. Užarević, *ACS Sustain. Chem. Eng.*, 2019, **7**, 7102–7110.

3 T. Stolar and K. Užarević, *CrystEngComm*, 2020, **22**, 4503–4666.

4 C. Chen, A. M. Goforth, M. D. Smith, C.-Y. Su and H.-C. zur Loye, *Angew. Chem., Int. Ed.*, 2005,

44, 6673–6677.

5 W. Kaneko, M. Ohba and S. Kitagawa, *J. Am. Chem. Soc.*, 2007, **129**, 13706–13712.

6 M. C. Bernini, F. Gándara, M. Iglesias, N. Snejko, E. Gutiérrez-Puebla, E. V. Brusau, G. E. Narda and M. Á. Monge, *Chem. Eur. J.*, 2009, **15**, 4896–4905.

7 A. Demessence and J. R. Long, *Chem. Eur. J.*, 2010, **16**, 5902–5908.

8 Y. Zhang, X. Zhang, J. Lyu, K. Otake, X. Wang, L. R. Redfern, C. D. Malliakas, Z. Li, T. Islamoglu, B. Wang and O. K. Farha, *J. Am. Chem. Soc.*, 2018, **140**, 11179–11183.

9 H. Liu, M. J. Gutmann, H. T. Stokes, B. J. Campbell, I. R. Evans and J. S. O. Evans, *Chem. Mater.*, 2019, **31**, 4514–4523.

10 B. R. Mullaney, L. Goux-Capes, D. J. Price, G. Chastanet, J.-F. Létard and C. J. Kepert, *Nat. Commun.*, 2017, **8**, 1053.

11 Q. Ren, W. Hutchison, J. Wang, A. Studer, G. Wang, H. Zhou, J. Ma and S. J. Campbell, *ACS Appl. Mater. Interfaces*, 2019, **11**, 17531–17538.

12 L. J. Barbour, D. Das, T. Jacobs, G. O. Lloyd and V. J. Smith, in *Supramolecular Chemistry: From Molecules to Nanomaterials*, eds. P. A. Gale and J. W. Steed, John Wiley & Sons, Ltd., Hoboken, 2012.

13 C. R. R. Adolf, S. Ferlay, N. Kyritsakas and M. W. Hosseini, *J. Am. Chem. Soc.*, 2015, **137**, 15390–15393.

14 C. R. R. Adolf, S. Ferlay and M. W. Hosseini, *CrystEngComm*, 2018, **20**, 2233–2236.

15 M. Kaźmierczak, E. Patyk-Kaźmierczak and A. Katrusiak, *Cryst. Growth Des.*, 2021, **21**, 2196–2204.

16 A. Katrusiak, *Acta Crystallogr. Sect. A Found. Crystallogr.*, 2008, **64**, 135–148.

17 W. Cai and A. Katrusiak, *Nat. Commun.*, 2014, **5**, 4337.